UNIVERSITY OF MODENA AND REGGIO EMILIA
"ENZO FERRARI" ENGINEERING DEPARTMENT

PHD COURSE IN INDUSTRIAL AND ENVIRONMENTAL ENGINEERING

XXXIII CYCLE

Development of numerical methodologies for the analysis of the piston liner interaction in high-performance engines

Sviluppo di modelli numerici per l'analisi dell'interazione canna pistone in motori ad elevate prestazioni.

Supervisor:
Prof. Matteo Giacopini

Candidate:
Saverio Giulio Barbieri

Co-supervisor:
Prof. Elena Bassoli

Course Coordinator:
Prof. Alberto Muscio

Index

Abstract (English)

There is no single choice regarding the materials commonly employed in the automotive industry. The most common metallic materials are steel, cast iron, aluminium and titanium. The choice is guided by the thermomechanical performances required, by the technological constraints and by the production costs. In particular for high-performance engines, the most common materials used for piston and cylinder liner are steel and aluminium.

This thesis aims at analysing and comparing the effects of possible material choices on the interaction between piston and cylinder liner. The main tool adopted for performing these analyses is the Finite Element simulation.

First, a motorcycle engine is considered and two possible pistons are examined: one in aluminium and the second variant in steel. This engine is equipped with both aluminium piston and cylinder liner as standard. It is therefore necessary to design a steel piston that is structurally equivalent to the aluminium one with a comparable mass. The technology designated for the production of the steel piston is Additive Manufacturing. This production technique grants wide design freedom to the shape of the component concerned. For this reason, a methodology for the design of a new piston is developed and applied using Topological Optimization techniques. The steel piston is structurally comparable to the aluminium one, but with the advantage of being able to withstand higher pressures and temperatures in the combustion chamber.

At the same time, the geometry of the steel cylinder liner is achieved simply by thinning the aluminium component in order to obtain two structurally equivalent components.

Having identified the system and the four possible combinations of coupling between piston and cylinder liner, each considered in the two variants of applied material, Finite Element simulations are performed. The components required for this analysis are the engine head, the engine block, the bolts, the gasket, the upper part of the crank mechanism and the cylinder liner.

First of all, it is necessary to carry out a thermal analysis of the assembly, because the interaction between the components, in particular gap, interference fit and contact pressures, depends on their thermal deformation. Consequently, it is necessary to obtain the temperature field of the assembly considering both the heat generated by combustion and friction and the heat removed by the oil, by the water circuit and by the air surrounding the engine. Thereafter, a thermo-structural analysis is carried out simulating both the assembly of the engine and its operating condition. This last analysis shows great complexity from a computational point of view; for this reason, a methodology is developed and applied to lighten these calculations without losing the accuracy of the solutions.

From the results of these simulations, it is possible to evaluate gap and interference with the variation of the materials and it is also possible to evaluate the stress field and the fatigue safety factor of the components involved in the analyses.

The methodologies explained in this work show results that can guide the choice of materials to be used in the piston-cylinder liner coupling. Furthermore, the simplifying techniques illustrated in this thesis can be applied to any traditional engine also to speed up the thermomechanical analyses of other components such as engine head and block.

Abstract (Italian)

Non esiste una scelta univoca riguardo ai materiali impiegati in ambito motoristico. I materiali metallici più comuni sono acciaio, ghisa, alluminio e titanio. La scelta viene guidata dalle performance termomeccaniche richieste, dai vincoli tecnologici e dai costi di produzione. In particolare per motori ad elevate prestazioni, i materiali più comuni usati per pistone e canna cilindro sono acciaio e alluminio.

Questo lavoro di tesi si pone l'obiettivo di analizzare e confrontare gli effetti delle possibili scelte di materiale sull'interazione tra pistone e canna cilindro. Lo strumento principale in queste analisi è la simulazione agli Elementi Finiti.

Per cominciare è stato considerato un motore motociclistico e sono stati esaminati due possibili pistoni: uno in alluminio ed una seconda variante in acciaio. Questo motore viene equipaggiato di serie con pistone e canna cilindro in alluminio. È stato quindi necessario progettare un pistone in acciaio che fosse strutturalmente equivalente a quello in alluminio e che presentasse una massa equiparabile al pistone di serie. La tecnologia designata per la realizzazione del pistone in acciaio è l'Additive Manufacturing. Questa tecnica produttiva concede una vasta libertà progettuale alla forma del componente interessato. Per questo motivo è stata ideata ed applicata una metodologia per la progettazione di nuovo pistone utilizzando tecniche di Ottimizzazione Topologica. Il pistone in acciaio è strutturalmente equiparabile a quello in alluminio, ma con il vantaggio di poter sopportare pressioni e temperature in camera di combustione più elevate.

Allo stesso tempo, la geometria della canna cilindro in acciaio è stata ottenuta semplicemente assottigliando il componente in alluminio al fine di ottenere due componenti strutturalmente equivalenti.

Identificato il sistema e le quattro possibili combinazioni di accoppiamento tra pistone e canna cilindro, ognuna considerata nelle due varianti di materiale applicato, si è passati alla simulazione agli Elementi Finiti. I componenti necessari a questa analisi sono la testata motore, il basamento, le viti prigionieri, la guarnizione, la parte alta del manovellismo di spinta e la canna cilindro.

Innanzitutto, è necessario svolgere un'analisi termica dell'assieme, perché l'interazione tra i componenti, in particolare giochi, interferenze e pressioni di contatto, dipendono dalla loro deformazione termica. Di conseguenza è stato necessario ricavare una mappa termica dell'assieme considerando sia i contributi dei flussi termici entranti, come combusione e attriti, sia i flussi di calore uscente asportato ad esempio dall'olio, dal circuito di raffreddamento e dall'aria che circonda il motore. In seguito, è stata svolta un'analisi termostrutturale simulando sia l'assemblaggio del motore, sia il funzionamento dello stesso. Quest'ultima analisi mostra una grande complessità dal punto di vista computazionale, per questo motivo è stata ideata ed applicata una metodologia per alleggerire questi calcoli senza perdere accuratezza nelle soluzioni.

Dai risultati di queste simulazioni è stato possibile valutare giochi ed interferenze al variare dei materiali ed è stato anche possibile valutare lo stato tensionale e i coefficienti di sicurezza a fatica dei componenti coinvolti nelle analisi.

Le metodologie esposte in questo lavoro mostrano risultati che possono guidare la scelta dei materiali da utilizzare nell'accoppiamento del pistone con la canna cilindro. Inoltre, le tecniche semplificative illustrate in questo lavoro di tesi potranno essere applicate a qualsiasi motore tradizionale per velocizzare le analisi termomeccaniche anche di altri componenti come testata e basamento.

Introduction

In this thesis, the engine of the Panigale 959 is examined, Figures 0.1 (a) and (b), data in Table 0.1, but all the explained considerations are generally valid for any high-performance engine and are even more pertinent in the analysis of wet cylinder liner engines.

The piston and the cylinder liner form a sliding cylindrical coupling. These two components play a crucial role in transforming the pressure in the chamber into useful work and at the same time they must not allow the combustion gases to leak into the crankcase to maximize engine efficiency. Therefore, the piston-cylinder coupling must perform two fundamental tasks: sealing the burnt gases inside the combustion chamber and withstanding mechanical loadings and their fatigue damage.

In this thesis, both aspects are examined.

First, the thermal and mechanical loads acting on the piston and cylinder are evaluated to retrieve the deformation of these two components during the operating conditions. Once the deformation of the cylinder liner is known, it is possible to consequently choose the most suitable ring pack to seal the gases in the combustion chamber.

Secondly, the fatigue life coefficient of these components is evaluated.

It is easy to see how these analyses strongly depend on the materials used to make the piston and cylinder liner. For this reason, piston and liner are considered made of steel and aluminium, generating four possible coupling combinations.

While it is common usage to have steel or aluminium cylinders for motorcycle engines, it is not so easy to observe the use of steel pistons. For this reason, the research activity is also focused on the development of a methodology for the design of steel pistons based on Topological Optimization techniques.

In addition, the Finite Element calculations performed to study the interaction between the liner and the piston are particularly onerous from a computational point of view. Therefore, this thesis explains a methodology that aims at simplifying simulations without losing details in the results.

The engine analyzed has an aluminium liner and piston; starting from the geometries of the standard components, the geometries of the piston and cylinder liner are proposed in the other three possible configurations: aluminium piston and steel liner, steel piston and aluminium liner, steel piston and steel liner.

The thesis is subdivided into two parts, chapters 1 to 5 describe the background knowledge to be understood to deal with the second part. In fact, chapters 6 to 10 present the calculations and simulation adopted to investigate the piston-liner contact interaction based on the different material combination of these two components.

Chapter 1 addresses the piston. The different main tasks and requirements are explained, the main layouts of this component are shown, both for gasoline and Diesel engines, and the main materials employed are displayed focusing on the main advantages and disadvantages. In particular, a section is dedicated to the piston profile, the drawing of the piston is explained and the purposes of such a complicated profile are illustrated.

Chapter 2 focuses on the cylinder block. The different layouts are shown, the most common materials employed are explained and the function of the head gasket is briefly explained.

Chapter 3 addresses the calculation of the thermal boundary conditions. The boundary conditions applied to the piston and to the liner are described in detail. In particular, the most complicated aspect is the effect of the motion of the piston on the thermal boundary conditions of the liner.

Chapter 4 concerns Additive Manufacturing technologies. In fact, the new steel piston is designed using Additive Manufacturing as a productive technique. In particular, techniques suitable for metals are taken into accounts, such as powder bed fusion and selective laser melting.

Chapter 5 focuses on optimization techniques. Additive Manufacturing techniques offer wide freedom to the designer so that it is necessary to find a scientific methodology to define the optimal geometry of the new steel piston. In this chapter, the theory of the optimization techniques is briefly explained, while the topology optimization is debated in detail.

Chapter 6 shows the settings and the results of the Finite Element analysis of the original aluminium piston. In particular, a thermal analysis is performed to obtain the regime thermal field of the crank mechanism. Then thermal-structural analyses are computed to verify the structural resistance of the piston and to evaluate the deformation of the piston caused by the thermal field. These results are used in the following to retrieve the design constraints of the topology optimization and to define the profile of the new steel piston.

Chapter 7 shows the topology optimizations performed to define the new steel piston. Besides, the design process based on the results is described and the first proposal for the new steel piston is presented.

Chapter 8 focuses on the Finite Elements analyses performed on the new steel piston. Both thermal and structural simulations are performed and the piston profile of the new piston is defined.

Chapter 9 describes the analyses and the results of the simulation of the engine using the original configuration of aluminium piston and aluminium cylinder liner. These calculations reveal themselves to be very heavy from a computation point of view so that methodologies to speed up the calculations are invented and applied. In particular, thermal, thermo-structural and fatigue simulations are performed. The simulations are not lightened by using a coarser mesh, but by removing the unnecessary sources of nonlinearity. The head, the gasket and the upper part of the bolts are removed and substituted by a suitable pressure distribution mimicking the contact pressure generated by these components. Besides, the fatigue analysis has been simplified by selecting the border of the fatigue cycle based on the bending moment of the cylinder liner generated by the piston lateral thrust force. Finally, a methodology to further simplify the fatigue analysis is proposed, the piston is removed and substituted by a pressure distribution mimicking the contact interaction with the liner.

Chapter 10 shows the simulations performed for the remaining three different combinations: aluminium piston and steel liner, steel piston and aluminium liner, and steel piston and steel liner. First, the geometry of the steel liner is simply defined by simply thinning this component. Then, for each combination, thermal, thermo-structural

and fatigue analyses are performed. In particular, the shape of the contact forces between the piston and the liner is described to obtain the information necessary to guide the improvement of the design of the new steel piston. In addition, gaps and interferences between the piston and the liner are considered to understand the requirements needed for practical usage of each configuration.

(a) (b)

Figure 0.1. (a) Ducati Panigale 959; (b) the engine under investigation.

Table 0.1. Engine data.

Engine configuration	L-twin
Displacement	955 cm^3
Bore	100 mm
Stroke	60.8 mm
Maximum power	115 kW @11000 rpm
Maximum torque	107 Nm @ 9000 rpm
Maximum ccombustion pressure	9100 kPa @11000 rpm

Chapter 1: The piston

1.1 Introduction

Figures 1.1(a) and (b) and Figure 1.2 shows the piston under investigation.

The piston is a crucial element in the transmission of power [1]. In the combustion chamber of an engine, the chemical energy contained in the fuel is rapidly converted into heat and pressure during the combustion phase. The piston, which is the moving part of the combustion chamber, has to convert this energy into mechanical work.

The basic structure of a piston is a hollow cylinder closed on one side, with the addition of the slots for the segments, the bosses for the gudgeon pin and the skirt.

The first geometric parameters of the piston to be considered are the bore of the engine B and the height of the piston H_{tot}, Figure 1.3. The value of their ratio guides the intended use of the piston. For racing engines H_{tot}/B is less than 0.5, petrol engines generally have H_{tot}/B between 0.8 and 1 while for Diesel engines H_{tot}/B it is between 1 and 1.5. In recent years there has been a decrease in the H_{tot}/B ratio as a result of research in the motor industry.

Now, the tasks, that the piston must perform, and the requirements, that it must fulfil, are listed.

The most important tasks that the piston must fulfil are:

- transmission of force from the working gas (power stroke) and to the working gas (compression stroke);
- variable lower bounding of the working chamber;
- sealing off the working chamber;
- linear guiding of the connecting rod;
- heat dissipation;
- support (4 strokes engine) or controlling (2 strokes engine) of the charge exchange;
- support of mixture formation (with a suitable shape of the piston top);
- housing the sealing components (ring pack);
- guiding the connecting rod (for top-guided connecting rods).

The most common requirements of the piston are:

- structural strength;
- adaptability to operating conditions;
- low friction;
- low wear;
- low oil consumption;
- low pollutant emissions.

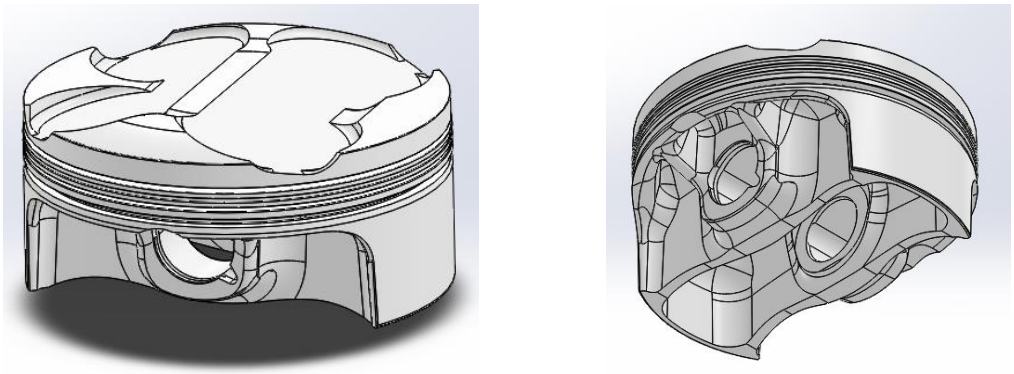

(a) (b)

Figure 1.1. (a), (b) aluminium piston of Ducati Panigale 959.

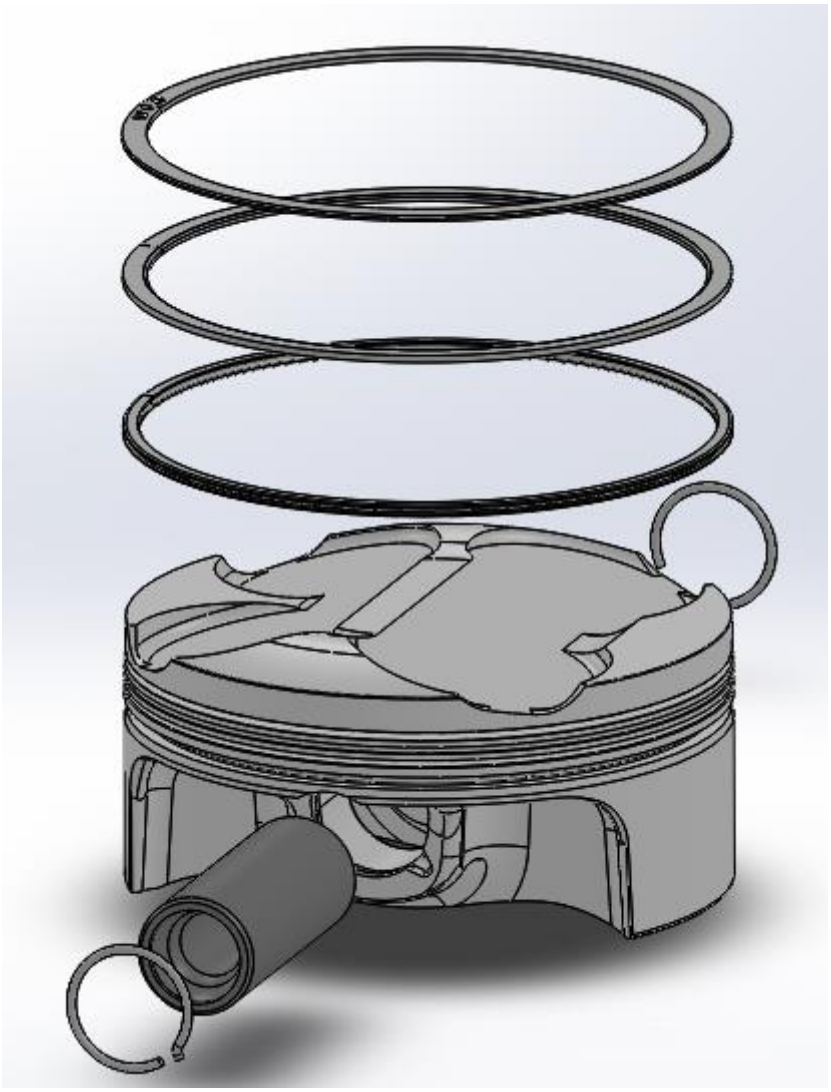

Figure 1.2. The reciprocating masses of the crack mechanism.

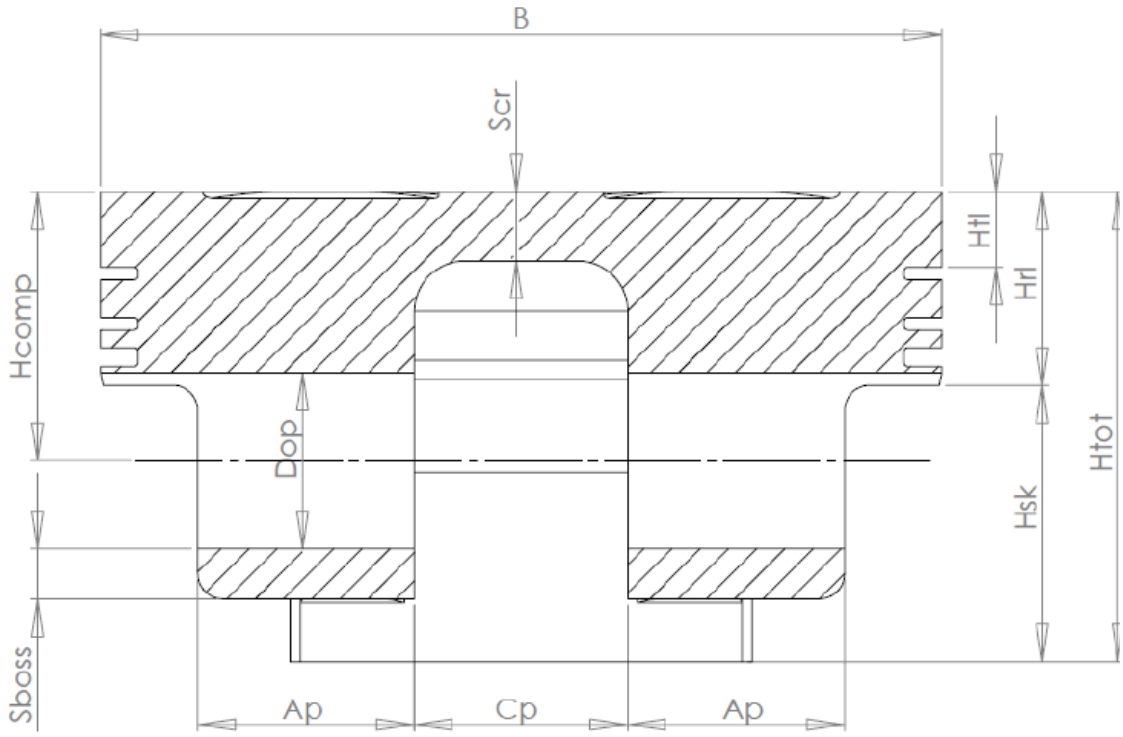

Figure 1.3. Piston main parameters.

1.1.1 Piston top

The piston crown is the mobile part of the combustion chamber and for this reason, different geometries have been designed [2,3] according to the specific application, Figure 1.4.

Geometry 1 shows a flat crown, it is the simplest geometry. Geometry 2 (cap) has very marked valve tracks to reduce the dead volume at the top dead centre. Figure 3 shows a piston with a flat cavity, this cavity allows reducing the dead volume using a simple geometry. Piston 4 is used in direct injection petrol engines with stratified charge, the piston crown contributes to the turbulence generated in the cylinder. Pistons 5 and 6 are similar, they are used in Diesel engines and the hollow called bowl ha helps to create the necessary turbulence [4–6]. The only difference lies in the manufacturing technique used to produce these two pistons. The cavity of piston 5 is an undercut and requires processing after forging or moulding which, on the other hand, may be sufficient to achieve the geometry of the piston crown 6.

Figure 1.4. Piston crown geometries.

1.1.2 Piston lands

The cylindrical area of the piston that goes from the edge of the piston top to the groove of the first ring is called top land. The height of this area is linked to several parameters: the combustion process, the material of the first segment and the geometry of the slot of the first segment. For petrol engines, the top land has a height of 4-10% of the bore or even less to reduce the emission of hydrocarbons caused by the gap [7]. While the top land of diesel engine pistons generally has a height equal to 8-15% of the bore.

The area of the rings is generally composed of 3 hollows that house as many elastic rings. The sealing rings must seal the combustion chamber and regulate oil consumption [8]. Their surfaces must therefore be suitably machined. Poor sealing leads to a gas leakage (blow-by) in the case, to heating of the components from contact with hot gases and to the destruction of the oil film on the liner, necessary for the lubrication of the sliding contact. Besides, the elastic rings must never touch the internal part of the groove and therefore a radial play is required. Common lubricating oils allow piston groove temperatures to be higher than 200 ° C in petrol engines and higher than 280 ° C in Diesel engines without the segments blocking due to carbon residues accumulated in the seat of the first segment.

The segments do not simply have to conform to a cylindrical surface, in fact, the cylinder has a surface deformed by the mechanical and thermal loads suffered during the assembly of the engine and during its operation. The segment must have a geometry that easily flexes and adheres correctly to the deformation of the barrel. The ability of a segment to follow the geometric distortion of the cylinder is called elastic ring conformability. The conformity of an elastic ring is expressed by the conformability coefficient K_c:

$$K_c = \frac{F_t(d-2t)^2}{4EJ} \tag{1.1}$$

where t is the radial distance from the neutral axis to the sliding surface of the segment, d is the nominal diameter of the cylinder liner, E is the Young modulus of the segment material, J is the moment of inertia of the segment section, and F_t is the tangential load on the segment. The tangential force is often measured using a flexible tape that closes the ring.

The conformability index must be compared with the geometry of the liner deformed by the loads resulting from the assembly of the engine and its temperature gradient. In fact, it is possible to read how much the shape of the barrel differs from a perfect circumference by measuring its internal profile at different heights along its axis or by simulating the hot assembly procedure with the Finite Elements. The deformation of the barrel at each height is generally written using the Fourier series decomposition. Considering a specific order *i*, the amplitude of the deformation U_i can be retrieved. The maximum width that a ring with a conformability K_c can tolerate is:

$$U_{max,i} = \frac{d \cdot K_c}{2(i^2 - 1)^2} \tag{1.2}$$

Therefore, it is necessary to choose an elastic ring such that $U_{max,\,i}$ is less than U_i of the liner. From equation (1.2), it is clear that high orders can be particularly critical. Fortunately, the cylinder liners show deformations with important amplitudes up to the fourth order and then suddenly decrease. So if a segment has sufficient conformability up to the fourth order, it will probably be sufficient to support the deformations of the next order.

The topics related to the cylinder liner and its deformation will be expanded in the following dedicated sections.

1.1.3 Piston Skirt

The piston skirt is the lower part of the piston and it guides the piston in the cylinder. Sufficient skirt length and tight guidance keep the tipping of the piston low during contact alteration from one cylinder wall to the other. In the past, a preliminary attempt to define the length of the piston skirt, H_{skr}, was:

$$H_{skr} = \frac{F_{thr,max}}{B \cdot p_{adm}} \tag{1.3}$$

where $F_{thr,max}$ is the maximum thrust force between the piston and the liner, B is the engine bore a p_{adm} is the admissible contact pressure between piston and liner. This design guideline usually overestimated the skirt extend and it is only marginally employed nowadays. Nowadays it is common to use FEM simulation software to identify the contact area with the cylinder.

Figure 1.5 shows how the area of the skirt in contact with the cylinder is limited to its central area. Furthermore, the contact zone changes according to the load and temperature (and deformation) of the piston and cylinder. These aspects will be extended in the dedicated section.

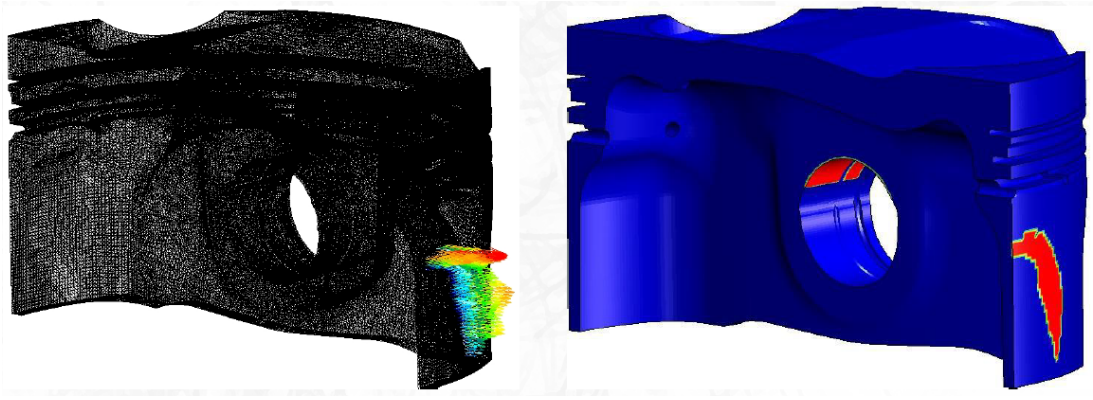

(a) (b)

Figure 1.5. (a) Piston-liner contact pressure; (b) piston-liner contact area.

1.1.4 Pin bosses

Figure 1.6 shows the most common geometries for the piston pin bosses. Their geometry depends on some factors, including: the ratio between the piston pin length and the bore (Lp/B), the loads that the component must support from the production technology used to make the piston. Figure 1.6 also shows that the shape of the bosses is constrained by the need not to have undercuts in order to be made using traditional technologies. It is also noted that the bosses for the pin have an often massive geometry and a non-negligible volume. Only when very high load are encountered and very high durations are required, a bush is press-fitted into the pin bosses in order to mitigate possible direct contacts Figure 1.7. With the introduction of Additive Manufacturing techniques, the possibility of creating more varied and performing geometries opens up. In this doctoral thesis a methodology for the determination of the optimal geometry of the piston pin flows using Topological Optimization techniques will be presented.

$L_p/D=0.8$ standard pistons | $L_p/D=0.6$ standard and box-n-box pistons | $L_p/D=0.4$ box-n-box pistons

Figure 1.6. Pin boss geometries.

(a) (b)

Figure 1.7. Detail of bush for pin bosses.

1.2 Piston profile

The surfaces of the skirt and the lands of the segments are machined to have a particular intentionally non-cylindrical surface. The purpose of this process is to obtain a specific hot deformed shape. In fact, the piston has a high thermal gradient in the axial direction (Figure 1.8) which leads to a highly inhomogeneous deformed shape (Figure 1.9). The lands are machined to exhibit a truncated cone geometry to avoid contact between these areas and the liner and to have a hot shape as cylindrical as possible to obtain reduced dead volume. The machining on the skirt aims at obtaining a particular form of contact in order to damage the piston and barrel as little as possible. For low lateral thrust, the skirt must touch the cylinder only in a small central portion, with

increasing lateral thrust this contact area increases and for the maximum contact pressures encountered during the operation conditions, the contact must move towards the peripheral area of the skirt near the area of the skirt supports, see Figure 1.10 (a) and (b). More details will be provided in the dedicated section of this thesis.

Figure 1.11 contains all the information useful for creating the machined profile of the piston. This information is essential for a correct representation of this component using Finite Element simulations. Figure 1.11 (a) describes the profile of the piston section along a plane passing through the axis of the cylinder and perpendicular to the axis of the pin. The profile of the piston is also divided into two main areas: the crown with a truncated cone shape and the skirt with a barrel shape.

The axial coordinate of the crown is expressed in absolute form and for each identified height the amount of the reduction in diameter to be made on the nominal diameter is specified. It should be noted that the land between the second segment and the oil scraper has a much smaller diameter than the others.

The lower part refers instead to the skirt. The vertical coordinate is indicated incrementally and, for each dimension, a value is supplied to correct the nominal diameter. It is interesting to note that the dimensions with zero correction approximately identify the contact area between the piston and the cylinder liner for low lateral thrust forces.

To carry out the machining on the entire piston it is not sufficient to create a circular revolution of this profile around the axis of the cylinder. In fact, it must be considered that the diameter in the direction of the pin axis expands more due to the lower stiffness of the piston in this direction. Therefore, it is necessary to further reduce the diameter progressively and give the piston an oval shape. Figure 1.11 (b) contains all the details of this machining. For each circumferential dimension, three diameter reduction values are indicated and refer to three different areas of the piston. To locate the reference zone, pay attention to the tolerance value indicated next to the 90° diameter correction. The innermost values refer to the crown, the outermost values refer to the upper part of the mantle, while the values in the middle refer to the lower part of the mantle. It is useful to note that the correction for 0 ° is zero, the variations in diameter indicated in Figure 1.11 (a) do not need to be corrected along the frontal plane.

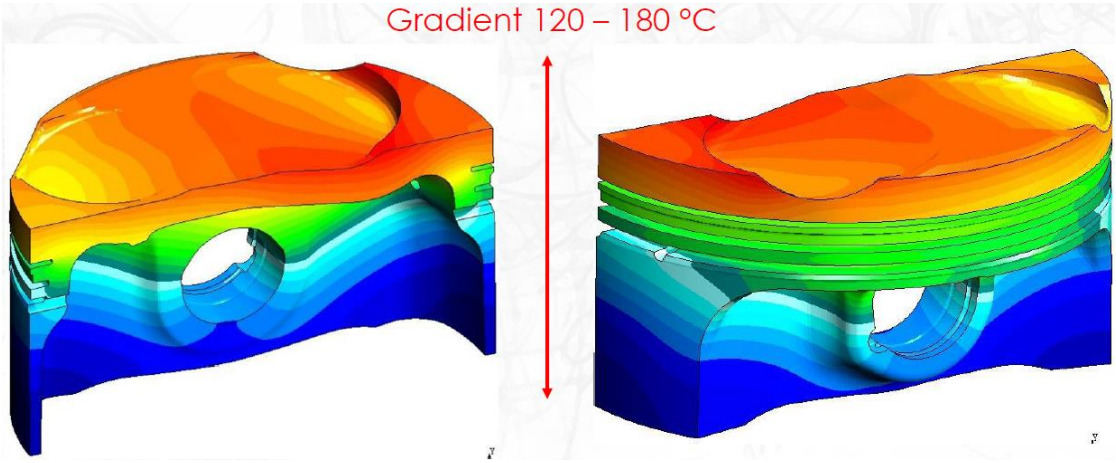

Figure 1.8. Thermally deformed shape of the piston.

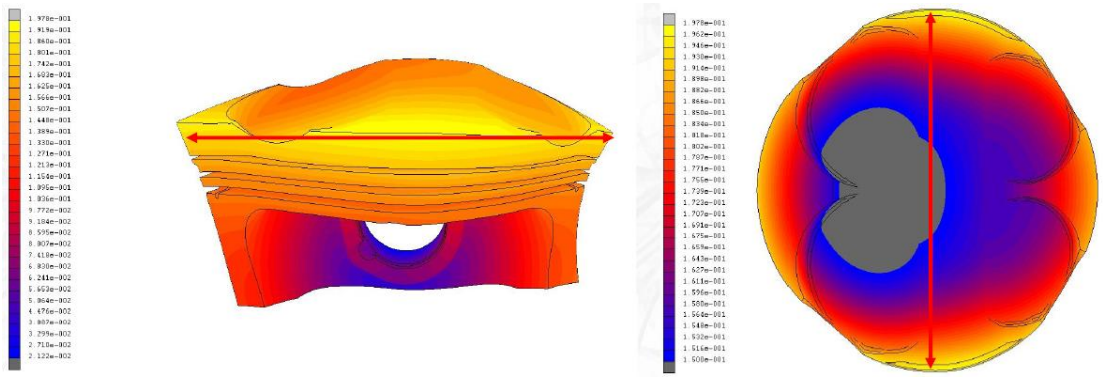

Figure 1.9. Thermally deformed shape of the piston.

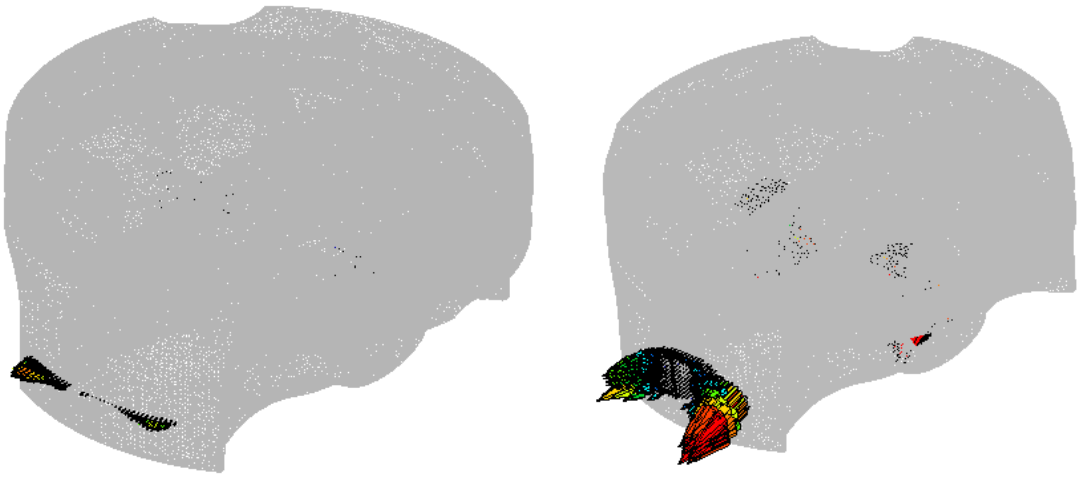

(a) (b)

Figure 1.10. Different contact areas depending on the contact force.

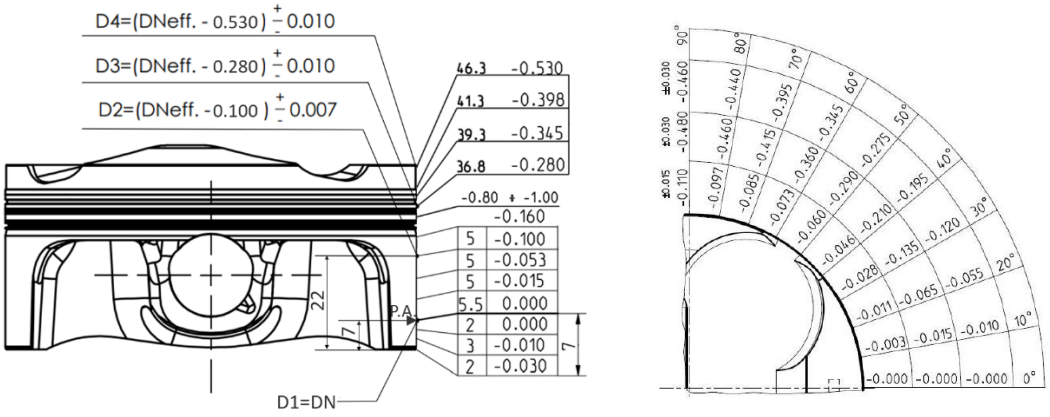

(a) (b)

Figure 1.11. Drawing of the piston profile.

1.3 Piston Material

Aluminium is undoubtedly the most used material for pistons as it has low density, good heat dispersion and a low friction coefficient with the cylinder liner. The only exceptions are present in fields far from series applications: in slow Diesel engines, cast iron is used, while, in competitions, magnesium alloys are used, which have less mass, but also less resistance and a higher friction coefficient. Considering the production technologies, the most common are casting (cheaper but also riskier due to the possible formation of porosity which reduces the resistance of the piece) and moulding (more expensive, but which ensures greater resistance, which is why it is used in competitions).

Machining from solid is less common. The production of the component is necessarily followed by machining on machine tools, in which all the details are taken care of such as the connecting radii and particularly important surfaces (even with grinding operations) such as the skirt or the pin seat are machined.

One could think of adopting steel for the production of the piston. This material has a density and a Young modulus three times higher than aluminium. As a first approximation, one could think of reducing the characteristic dimensions of the piston geometries to one third, unfortunately, these shapes are too thin and achievable only through Additive Manufacturing technologies.

1.3.1 Advantages of steel for pistons

The increasingly stringent regulations regarding CO2 emissions [9] have prompted the use of steel pistons in fast Diesel engines. The greatest advantage of adopting this material is found in the reduction of friction between piston and cylinder.

The advantages of the steel piston that lead to a reduction in CO2 emissions and consumption are attributed to these characteristics of the material

- low thermal conductivity;
- high structural strenght;
- lo thermal expanzion coefficient.

The low thermal conductivity leads to an increase in the piston crown temperature. Furthermore, the heat emitted by the component is less and therefore the adiabatic efficiency increases. At the same time, the high temperature of the top improves combustion. Unfortunately, these temperatures can generate carbon deposits and can degrade the oil.

The greater strength of the steel allows reducing the overall height of the piston, in particular the compression height, Figure 1.12 (a). This allows the adoption of more compact engines or longer connecting rods, with the resulting benefits in terms of less lateral thrust, Figure 1.12 (b).

The steel piston has a lower thermal expansion than the aluminium one, Figure 1.13.

During the operation conditions, the traditional piston can incur interference with the cylinder and therefore considerable friction losses. The same steel component expands less and always retains the clearance necessary for the correct functioning of the coupling.

Schreer et al. [10] investigated this topic and in particular the friction losses, the combustion process and the piston temperature.

If the clearance between piston and cylinder is too large, an excessively noisy engine is obtained, whereas if the clearance is too small there will be considerable friction losses, especially for aluminium pistons. This latter aspect is accentuated at low speeds and loads: in order not to penalize the organic and adiabatic efficiency, the piston cooling pump tends to be switched off, this increases the difference between thermal expansion of the piston and the cylinder causing further friction losses. For steel pistons, it is not recommended to switch off its cooling system due to the high temperatures it reaches during operation.

The advantages in the combustion process are primarily determined by a lower blow-by, the lower thermal deformation of the steel piston allows a greater optimization of the characteristics of the rings. Combustion is also aided by a higher combustion chamber wall temperature. Finally, the steel piston can have a narrower crown and consequently, a reduction in the deadvolume and a reduction in the production of CO is obtained.

Schreer, in his study, states that the temperature distribution in the aluminium piston is profoundly different from that of the steel piston. In the aluminium component, the heat is distributed evenly, thanks to its high thermal conductivity, and then dissipated through the cooling oil. While the diffusion of heat in the steel piston occurs mainly through the action of oil. Due to its thin thickness and low conductivity, thermal conduction plays a less important role in this case.

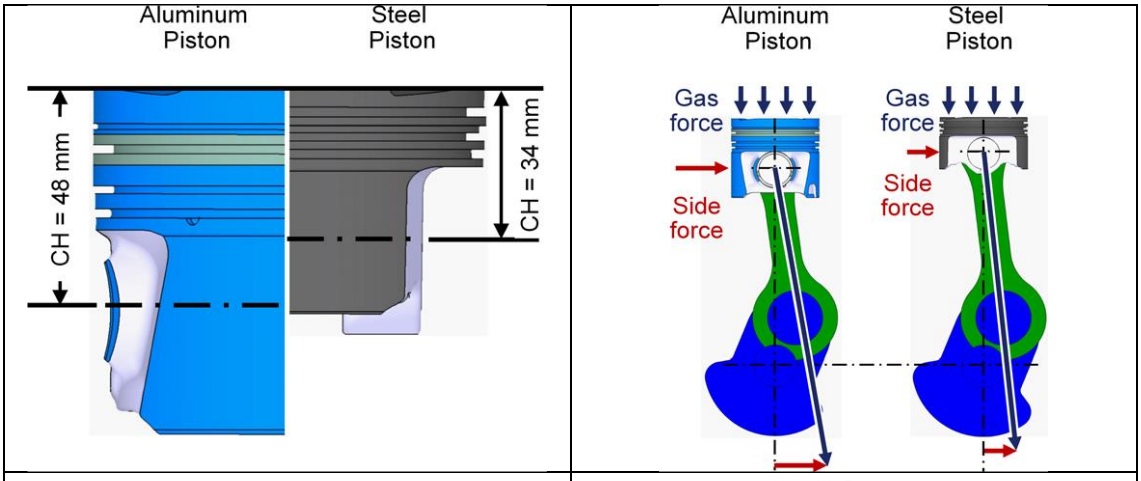

Figure 1.12. [10] Comparison between aluminium and steel piston.

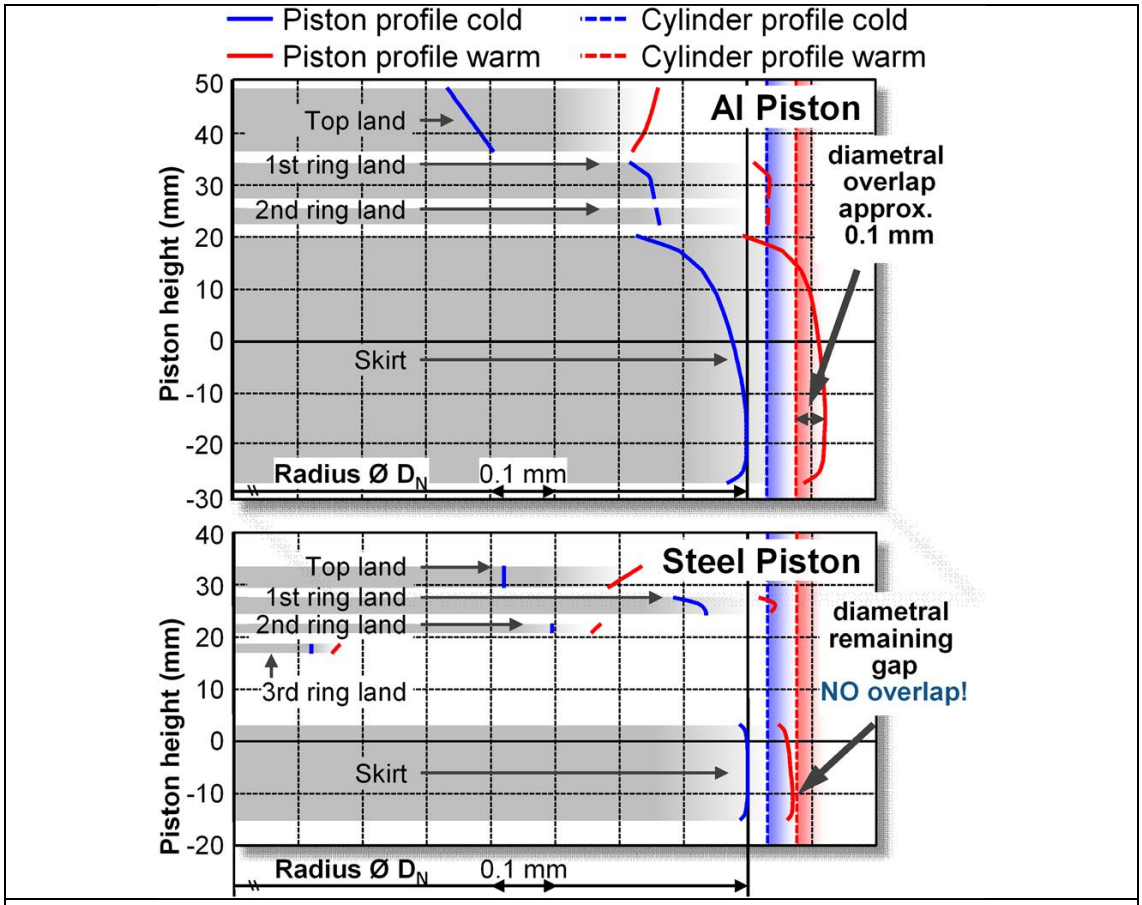

Figure 1.13. [10] Different thermal expansion for aluminium and steel piston.

1.3.2 The disadvantage of steel for pistons

Steel generally has a density equal to 3 times that of aluminium and a Young modulus equal to one third. Naively, designing a steel piston might seem simple, it might be enough to appropriately reduce all the thicknesses to obtain a steel piston with the same mass and stiffness as the aluminium piston. Unfortunately, the thicknesses that would be obtained could not be made with traditional technologies, but we need to switch to Additive Manufacturing technologies. In the motorsport field, there are pistons with a shape that recalls the traditional one of aluminium pistons, Figure 1.14. In addition, the use of Additive Manufacturing techniques gives the designer enormous design freedom and it is, therefore, possible to design a piston with a geometry that is far from the traditional one. This thesis will describe a methodology for identifying the structurally optimal geometry of the steel piston using topological optimization techniques.

Figure 1.14. A classical steel piston for high-performance engines.

Chapter 2: The Cylinder Block

2.1 Introduction

The cylinder block is the foundation of the engine [11], and supports the piston, cranktrain, cylinder head, and sometimes the valvetrain. It also houses the lubrication and cooling systems It provides mounting points for the charging system, starting system, power take off (PTO), and typically has mounts that support the entire powertrain.

The engine may be rigidly mounted as a structural member of the chassis, such as in a racecar or motorcycle. The cylinder block supports a variety of static, dynamic, and thermal loads, and must provide stiffness and alignment for many components.

Because of the complexity of geometry, and complexity of loading, hand calculations are rarely used while numerical Finite Element simulations are usually employed to verify the mechanical strength of the engine block.

The cylinder block must utilize the given space at the lowest possible part mass, while maintaining sufficient structural stiffness and the shape accuracy of bearing bores and cylinder fit (for replaceable cylinder liners).

Cylinder blocks support the internal forces and moments and transfer them to the engine mounts. They also need to withstand external loadings, such as:

- forces from accessory equipment;
- forces form the engine mounts;
- assembly forces (bolt tightening);
- thermal loading (thermal gradient).

The type of cylinder block is based on the size and application of the engine, the operating principle (four-stroke or two-stroke), the coolant employed (water/air), the number of cylinders, their design and arrangement, the material, and production process.

A crankcase consists of intermediate walls, the side and end walls, cylinder surfaces or liners, and, depending on the design, an upper cover plate. The intermediate walls house the crankshaft and, sometimes, also the camshaft(s). In addition, it contains channels for coolant and lubricant. The cylinder block is closed at the bottom by an oil pan and at the top by the gasket and then the cylinder head.

Two different parts of the cylinder block can be identified depending on the function, Figure 2.1:

- (a) the upper portion actually called cylinder block;
- (b) the lower portion, called crankcase.

Two main solutions exist:

- an integral solution in which these two parts are obtained in the same cast (this is our case study, Figure 2..2, the block of the Panigale 959 has a complex geometry, but it exhibits a high stiffness);
- a split solution, in which the cylinder block and the crankcase are separated.

(a) (b)

Figure 2.1. (a) Cylinder block; (b) crankcase.

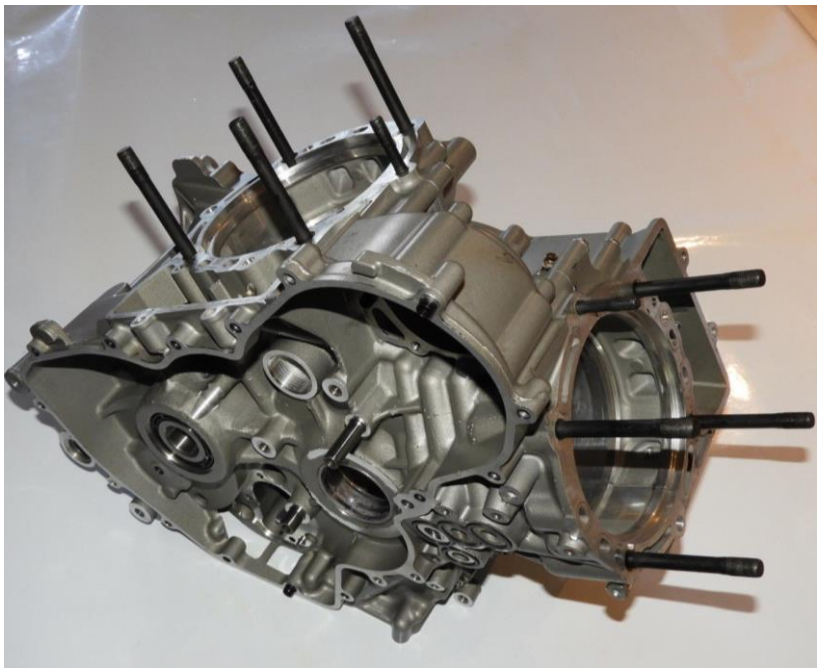

Figure 2.2. The engine block of the Panigale 959.

2.1 Liner design

The goal of the cylinder liner is to provide a good wear surface for the piston rings and to maintain cylindricity to aid piston ring sealing. If the liner deviates from round through machining, static head bolt loads dynamic firing loads, or thermal stresses, the engine will experience higher oil consumption, higher blow by, and higher engine friction

There are three general approaches to the cylinder liner:

- integral liner;
- dry liner;
- wet liner.

2.1.1 Integral liner

For automobile engines, the most common approach is the integral liner design, in which the cylinder walls are cast integrally with the cylinder block. This is most common in cast iron blocks. The cylinders are surrounded by a cooling jacket, which in turn is surrounded by the outer wall of the block. This design minimizes the cylinder bore spacing, and shortens the total length of the block. It has the further advantages of good heat transfer from the cylinder surface to the coolant, and reduced cylinder bore distortion compared to dissimilar materials used in other applications. An integral cylinder liner is the least expensive to manufacture, but offers the least flexibility for an engine overhaul.

2.1.2 Dry liner

A dry cylinder liner is made from separate material than the block and is inserted or cast into the crankcase. No contact with the coolant occurs. This reduces the opportunity for leaks, but reduces the heat transfer from the liner through the block to the coolant. If the block is cast from aluminium, cylinder liners made of a higher hardness material may form the running surface Material choices are typically iron, steel, or high silicon aluminium alloy and it is critical to make sure the aluminium adheres to the liner so that proper thermal contact is maintained.

2.1.3 Wet liner

Most heavy-duty diesel engines and (high performance) gasoline engines use wet liners. In such engines, the cylinder liners are pressed or slip fit into the surrounding structure such that they are in direct contact with the coolant and sealed at the top and bottom. In order to provide sufficient structural rigidity, the block casting includes walls separating the cooling jackets for each cylinder. The wet liner engine holds the advantages of having the cylinders easily replaced when the engine is rebuilt, and direct contact of the cylinders with coolant for optimum temperature control. However, the cylinder spacing and thus the overall length of the engine must be increased and the possibility of coolant leakage is increased. The engine studied in this thesis is equipped with wet liners.

2.1.4 Cooling

The cylinder block design strongly depends on the cooling targets.

In fact, the temperature must be maintained within a certain range for some reasons, such as:

- high-temperature gradients cause thermal stresses;
- high temperatures reduce static and fatigue resistance in the employed alloys;

- high temperatures cause large deformations in the crankcase and deformed the cylinder surfaces;

For these reasons, the cylinder surfaces must be properly cooled to minimize cylinder deformation and overheating of the lubricating oil, in particular in the area involved in the movement of the first compression ring. In addition, high temperatures of the cylinder surfaces could force shift the ignition point reducing the thermal efficiency.

2.2 Cylinder block material

Cylinder blocks are generally cast in iron, aluminium or magnesium materials, in addition, various alloys are employed depending on the specific targets of the engine.

The most important cast iron materials are GJL (cast iron with lamellar graphite also known as gray cast iron), GJV (cast iron with vermicular graphite also known as compacted graphite iron or CGI), and GJS (cast iron with spheroidal graphite also known as ductile iron).

GJL is adopted to obtain economical blocks and easy to manufacture. Besides, these components are stable in term of deformation of both the surfaces of the cylinder and of the bearings. GJL can also be used as a cylinder surface and supports noise dampening. Unfortunately, GJL shows greater density, lower thermal conductivity if compared to aluminium, and lower mechanical resistance if compared to GJV and GJS.

GJV can afford higher loadings than GJL, but due to its low content sulphur (manganese sulphate acts as a lubricant during machining), it is harder to machine than GJL. Moreover, GJV is not economical and therefore it is used only in high-performance turbocharged diesel engines.

GJS has a greater load capacity than GJV (tensile strengths of up to 900 MPa). However, its cost is higher, it is more difficult to be cast, and it exhibits poor thermal conductivity.

The engine of the Panigale 959 is made of aluminium, this material shows a combination of good thermal conductivity, low-density good machinability, and sufficient mechanical properties. If aluminium is used for cylinder surface, the clearance between the piston and the cylinder surface can be smaller than if gray cast-iron liners are employed, because of the similar thermal expansion coefficient. Consequently, the noise caused by the motion of the piston is reduced. On one hand, low density and better thermal conductivity of aluminium improve the thermal efficiency, thus reducing fuel consumption and exhaust gas emission. On the other hand, aluminium exhibits a higher cost of the manufacturing process and of the material itself. Moreover, its reduced strength values get worse above 200°C.

2.3 The gasket

The gasket is the element interposed between the head and the crankcase and must ensure the tightness of the gases, refrigerant and lubricant. When designing the gasket it is important to take into account the different local stiffnesses of the head and crankcase which entail a substantial change in the pressure distribution on the gasket caused by the tightening of the studs.

For optimal gasket design, a suitable model based on the Kelvin model (Figure 2.3) must be used which simulates the correct behaviour of the gasket during an engine cycle [12,13]. This is because the surface pressure on the gasket varies overtime during an engine cycle, with a minimum value during the combustion phase in which the high pressure in the combustion chamber tends to separate the head and crankcase and with a maximum value in the intake phase in which the pressure of the gases in the chamber is equal to the ambient one. These maximum and minimum values depend on the stiffness of the gasket, the head and the stem of the screws and must always be such as to always ensure a perfect seal of the gases under pressure (the minimum pressure on the gasket must be greater than the maximum pressure of the gases in the chamber) [14,15].

The modern head gaskets belong to the multi-layer type (figure 2.3), consisting of an alternation of flat and shaped sheets.

The latter must have, in correspondence with the individual seals, a characteristic of differentiated stiffness in the case of a gas seal or in the case of a water and oil seal. This can be done by profiling the buckle differently, thus obtaining different seals (Full-Bead for sealing the gases on the cylinders, Half-Bead for sealing the coolant and engine lubricant).

The internal flat sheet, which makes up the body of the gasket, on the other hand, must adapt to the head and base surfaces.

The last characteristic element of the multi-layer gaskets is the stopper, a structure necessary to avoid the complete flattening of the profiles and therefore the loss of seal. This element can simply be an end of the body folded on itself or an additional flat sheet. The stopper is usually positioned on the inner end of the gasket, in correspondence with the cylinder liners and avoids excessive crushing of the Full-Bead.

Each typical element of a multi-layer gasket is visible in the diagram in Figure 2.4.

The gaskets used in automotive engines are made of different types of steel, possibly with external coatings that improve sealing.

Figure 2.3. A multi-layer gasket.

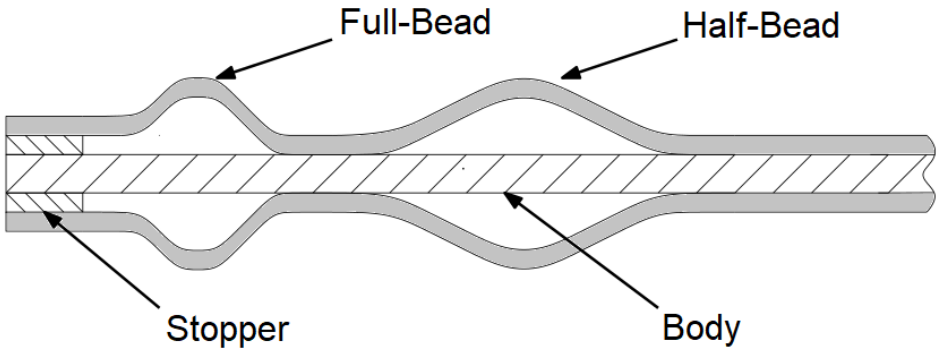

Figure 2.4. The functional layers of the gasket.

2.3.1 Multi-layer steel gasket

The gasket is manufactured with multi-layer (three/five) metal sheets (usually manufactured with harmonic spring steel). Contact areas are reduced in the region of the combustion seal and fluid seal. Layers can be divided into functional layers (the external ones) and carrier layer (the structural internal one).

Functional layers present several beads to properly distribute the load on the sealing areas, they can be subdivided into full beads and half beads. A full bead generates a suitable sealing contact pressure around the circumference of the combustion chamber. This elastic sealing element enables the sealing of very high gas pressures, even in the presence of large dynamic sealing gap oscillations. The half bead generates a suitable sealing pressure (lower than full bead pressure) along the coolant and oil passages, around the bolt holes and along the outer sealing contour.

The carrier layer gives adequate structural stiffness to the gasket, defines the proper gasket thickness (carrier layer thickness can be employed to control the compression ratio of the engine) and includes the internal rings (stopper ring). This stopper ring has crucial importance for the correct behaviour of the head gasket: it allows the correct pretension of the cylinder head, it limits the bead deflection (actually it behaves as a stopper for the bead crushing) and it enhances bead durability reducing bead movements and oscillations induced by gas forces. In addition, external coatings are adopted for surface micro sealing to obtain perfect adhesion with the mating surfaces of the engine head and block.

To better understand the function of the stopper, see Figure 2.5 and 2.6, a gasket without the stopper is displayed. Figure 2.5 is the initial condition, there is a loading related to the tightening of the bolt and there is no pressure in the combustion chamber. In Figure 2.6 a chamber pressure greater than zero is applied, a big gap around the bore and a high gap movement of the full bead is evident, this could lead to gas leaks and heavy damages of the full bead.

Figure 2.7 and 2.8 show the effect of the stopper. Figure 2.7 displays no combustion pressure. The engine head is preloaded by the bolt tightening and the pressure is transferred from the bolt to the combustion area through the stopper. Figure 2.8 depicts the effect of the application of combustion pressure. The contact pressure of the gasket is

reduced only in the stopper area and only there is only a small amplitude of the gap in the bead area.

Even if the advantages of adopting a gasket with the stopper are very clear, the gasket of the engine under investigation does not include any stopper. This choice is related to the low stiffness exhibited by the contact interaction between the gasket, head and block in the area of the flange of the cylinder liner. Figure 2.9 shows the engine after the application of the bolt tightening and of the temperature field. It is important to notice the contact between the gasket and the flange of the liner, the liner is pushed down as a cantilever beam. The flange is higher than the deck so that it behaves mimicking a stopper. Figure 2.10 displays the condition of maximum chamber pressure, the deformation of the head is followed by a consequent deformation of the liner flange, but the liner flange is still deformed. This deformation of the flange shield the full bead as the stopper acts in a more classical engine configuration.

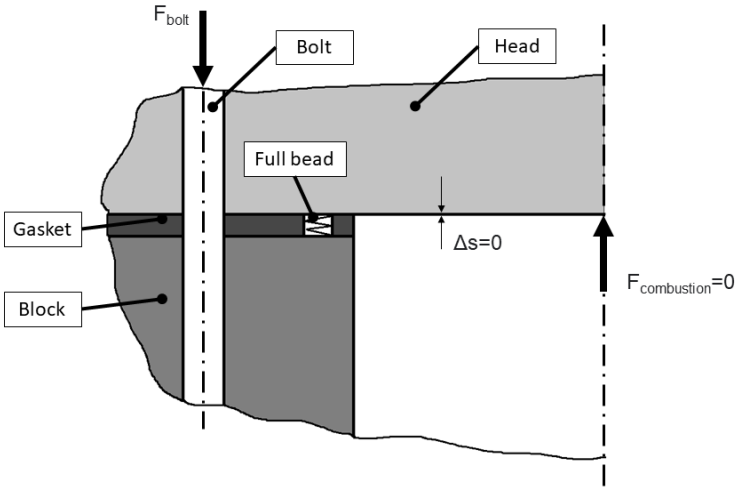

Figure 2.5. Gasket without the stopper, no combustion.

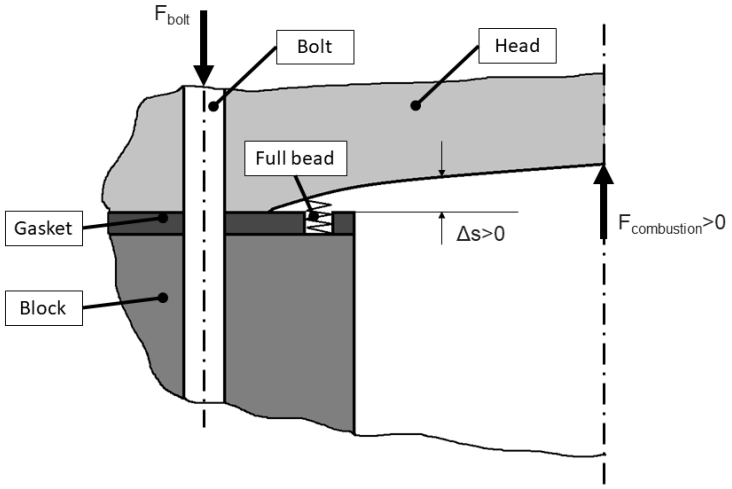

Figure 2.6. Gasket without the stopper, combustion loading.

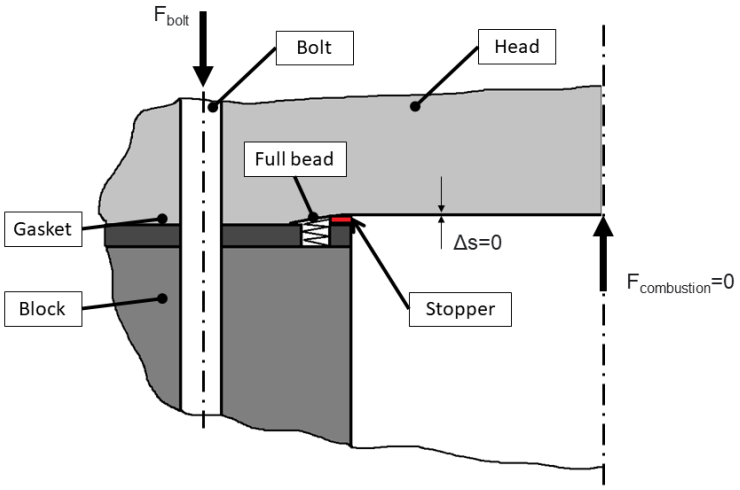

Figure 2.7. Gasket with the stopper, no combustion.

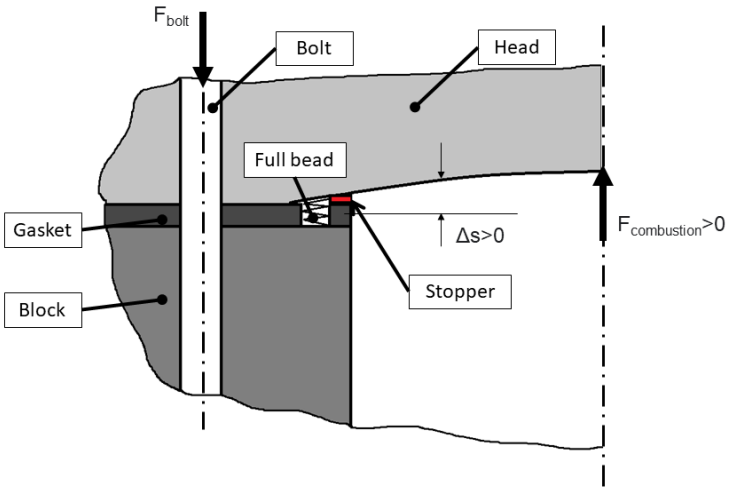

Figure 2.8. Gasket with the stopper, combustion loading.

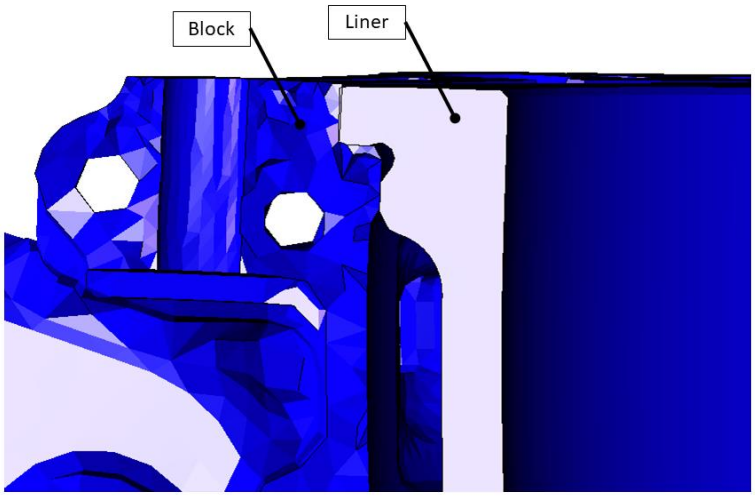

Figure 2.9. Detail of the deformed liner, amplified 20 times, no combustion.

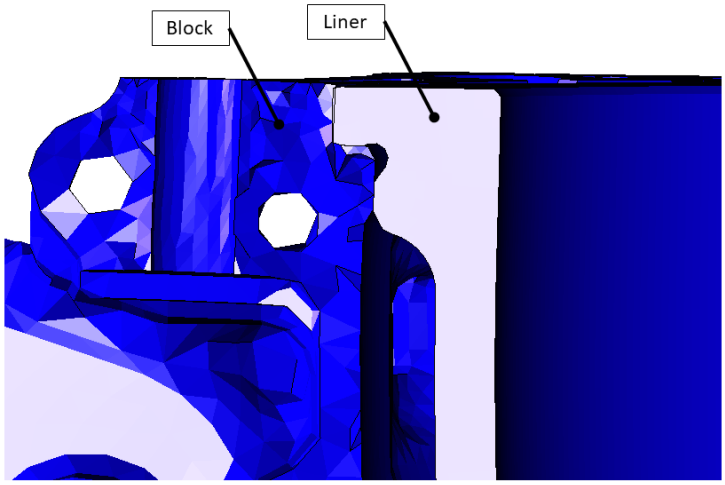

Figure 2.10. Detail of the deformed liner, amplified 20 times, combustion loading.

Chapter 3: Thermal Boundary Conditions

3.1 Introduction

The stress field of an engine component does not depend only on the mechanical loads to which it is subjected, but also on the non-uniform temperature field during the operation condition, which causes a non-negligible stress state. Moreover, as the temperature increases, the resistance of the materials decreases. Therefore, for each part of the component, it is necessary to know both the stress state and the temperature, in order to identify any critical issues. So, it is essential to determine the temperature field of the component, the real goal of the thermal analysis.

The temperature field of an engine during the operating condition can be considered stationary since the various mechanical parts have high thermal inertia and, in addition, the engine cycles follow one another with a high frequency. This consideration is exploited by considering the convection coefficients and temperatures averaged over a cycle, instead of considering the trend of these quantities over time. Thus, constant boundary conditions are considered, obtained by averaging over a cycle for most of the boundaries that are going to be defined.

To evaluate the temperatures, it is advisable to consider a thermal balance between the input and output thermal powers. The thermal power is generated by the burned gases and it is then disposed of by the oil that wets the lower part of the piston and by the water that wets the outside of the liner. Furthermore, other balances must be considered in detail, such as, for example, the thermal balances on the rings. Furthermore, the piston, during its motion, touches the liner, friction generates an additional source of heat, of a minor but not negligible entity, and it has to be also disposed of.

The final goal is to obtain the temperature field using Finite Element calculations. Suitable spreadsheets have been created as a support to the realization of the model and, specifically, to define the boundary conditions to be included in the simulations.

The steps for calculating the boundary conditions of the piston and cylinder liner separately are explained in the following.

3.1.1 In-cylinder heat transfer modelling: the Woschni model

The model used to calculate the instantaneous heat flux involving the various areas of the piston is the one formalized by Woschni [16]: one of the most used methods in the literature as it is not excessively complex and provides passing results. This model considers only the part concerning the forced convection, suitably increasing the convection coefficient *h* to take into account the part transmitted by radiation.

First, the relationship that links the Nusselt number to the Reynolds number has to be expressed:

$$Nu = C \cdot Re^{0.8} \tag{3.1}$$

consequently:

$$\frac{hB}{\lambda} = C\left(\frac{\rho u B}{\mu}\right)^{0.8} \tag{3.2}$$

where C indicates a constant, h is the convection coefficient, B the bore, λ the conductivity, ρ the density, u a characteristic speed and μ the dynamic viscosity of the gas. The physical meaning of the two dimensionless numbers just mentioned can be summarized as follows:

- the Nusselt number (*Nu*) provides a measure of the relative weight between the heat exchanged by convection h and that exchanged by conduction λ in the fluid;
- the Reynolds number (Re) defines the type of fluid motion (laminar or turbulent) and represents the ratio between the fluid dynamic forces ρu^2 and those due to viscous friction $\mu u/D$.

The model expresses the quantities just described as powers of the gas temperature:

$$\lambda \propto T^{0.75}, \rho \propto T^{-1}, \mu \propto T^{0.62} \tag{3.3}$$

thus the expression of the coefficient h is achieved from (3.2):

$$h = C_1 p^{0.8} B^{-0.2} T^{-0.53} u^{0.8} \tag{3.4}$$

where the coefficient C_1 depends on the units system adopted for the other quantities and is 3.26 in our case. The formula just described is valid instant by instant following the crank angle. Furthermore, the piston speed is described as the weighted average between the average speed of the same and a contribution of motion given by the density variation caused by combustion, proportional to the increase in pressure in the chamber. Thus, the formula for u can be obtained:

$$u = C_2 \bar{u}_p + C_3 \frac{V T_0}{p_0 V_0}(p - p_t) \tag{3.5}$$

where the values marked with the subscript *0* are reference values, u_p is the piston speed, p and V are the pressure and volume values at the instant considered and p_t is the pressure in the cylinder with the motor-driven, while the constants C_2 and C_3 take on different values depending on the engine phase:

- C_2 during compression, combustion and power phase is:

$$C_2 = 2.28 + 0.308\frac{u_s}{\bar{u}_p} \tag{3.6}$$

  where u_s is the swirl velocity;
- C_2 in the power phase is:

$$C_2 = 6.18 + 0.417\frac{u_s}{\bar{u}_p} \tag{3.7}$$

- C_3 is zero during the compression and intake phase, while during the power and combustion phase is:

$$C_3 = 3.24 \cdot 10^{-3} \tag{3.8}$$

3.2 Piston

The first boundary condition identified involves the piston top, which is in direct contact with the hot gases and transmits the heat to the rest of the piston. It transmits heat by conduction to the remaining parts of the piston, which will have different thermal resistances, depending on the material and geometry (Figure 3.1).

In particular, it distributes the incoming thermal power in equal parts to the water, through the segment and skirt, and to the oil through the lower part: 50% of the flow affects rings and skirt and 50% affects the lower surfaces. Considering the first 50%, 60% of heat exits through the rings and 40% through the skirt.

Considering the seats of the rings, each is divided into top and bottom, because they alternately come into contact with the moving rings. Then there is the oil scraper, always in contact with the lower and upper surface, the skirt on the thrust side, the counter-thrust side and the surfaces under the piston, divided into internal and external surfaces which, to define the heat exchange, can be indifferently horizontal or vertical: each of them will have its own way of exchanging heat with the shaking oil [17,18].

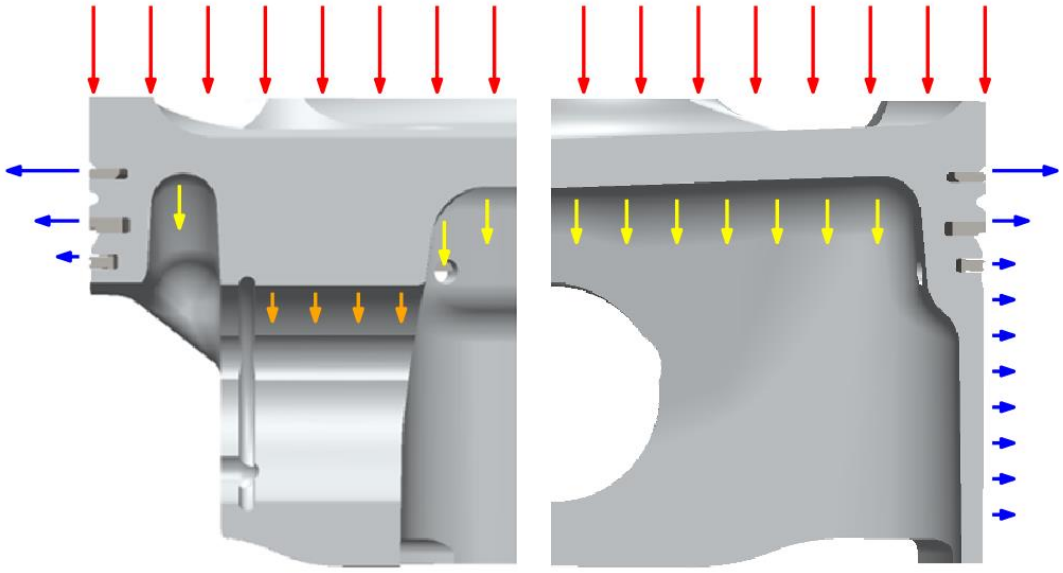

(a) (b)

Figure 3.1. The thermal flux path of the piston.

3.2.1 Piston top

The piston top is exposed to the hot gases of the combustion chamber, thus receiving an incoming heat flow.

$$P_{thermal} = HTC \cdot (T_g - T_w) \cdot A_{pist} \tag{3.9}$$

HTC is the heat exchange coefficient, T_g is the gas temperature averaged over an engine cycle, T_w is the piston crown temperature and A_{pist} is the surface of the piston crown exposed to gases. T_w is the unknown of our Finite Element problem, while *HTC* and T_g can be obtained using a spreadsheet and Woschni's theory.

First, the chamber pressure and temperature profiles during an engine cycle are taken into consideration. These values can be extracted from 1D or 3D CFD simulations or read from experimental tests, Figure 3.2.

Using this data it is possible to apply Woschni's theory and derive the HTC profile of the gases inside the cylinder, Figure 3.3.

Now it is necessary to obtain the HTC values and the average temperature of the gases during an engine cycle at full speed.

The average value of HTC is the compensation ordinate of the graph in Figure 3.3. The area underlying the graph is first calculated with the trapezoid method:

$$HTC_{mean} = \frac{\sum_1^{720} \frac{HTC_i + HTC_{i+1}}{2} \cdot (\theta_i - \theta_{i-1})}{720} \tag{3.10}$$

Where θ is the crank angle.

The average temperature is instead calculated considering the equivalence of heat flow per unit of surface for each crank angle.

$$T_{mean} = \frac{\sum_1^{720} \frac{HTC_i \cdot T_i + HTC_{i+1} \cdot T_{i+1}}{2} \cdot (\theta_i - \theta_{i-1})}{720 \cdot HTC_{mean}} \tag{3.11}$$

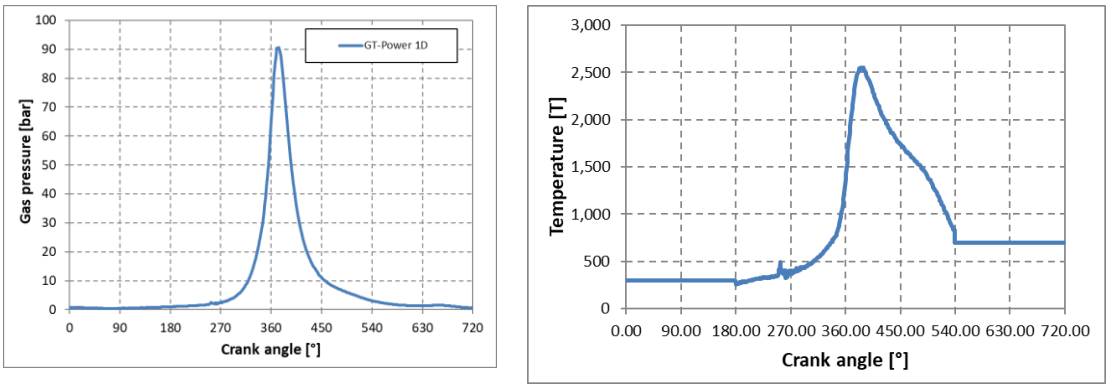

(a) (b)

Figure 3.2. (a) Pressure and (b) temperature profile.

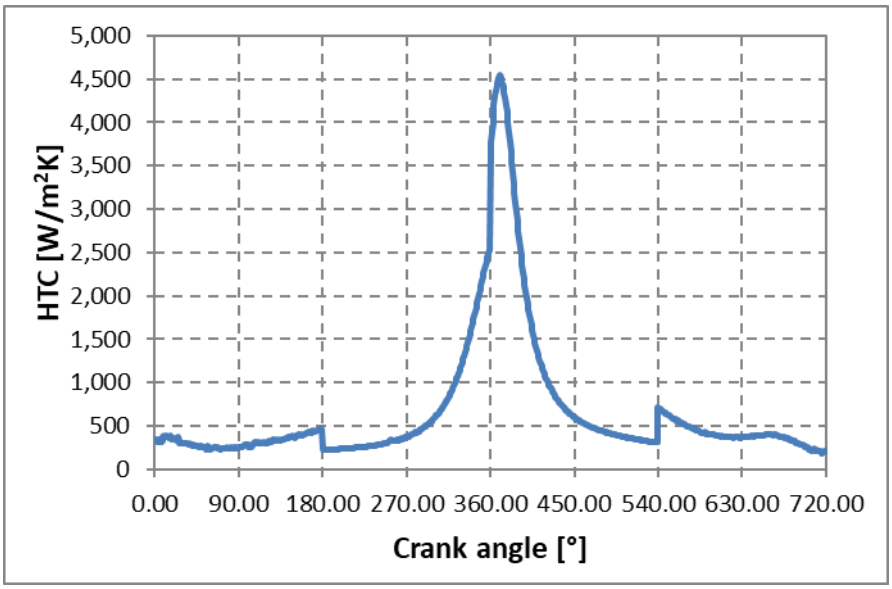

Figure 3.3. *HTC* profile.

3.2.2 Piston top land

The first land of the piston is exposed to gases, but the incoming heat flow which is generally low in the periphery of the combustion chamber is often neglected. This area is affected by a conductive exchange. The heat flow that entered the piston crown partly comes out of the first land and by conduction passes through the gases, the cylinder liner and it is removed by the water circuit that wets the cylinder liner. It is a consolidated methodology to create a thermal model to the FE that includes only the upper part of the crank mechanism, for this reason, the boundary condition is applied directly to the surface of the first land. Therefore, it is necessary to calculate an appropriate boundary condition that considers the path encountered by the heat flow, so it is necessary to calculate an HTC and the temperature of the body with which the heat exchange takes place. The simplest data to obtain is the temperature and the convective heat exchange coefficient of the water with the cylinder wall, through experimental tests and 3D CFD simulations. The temperature of the body with which the heat exchange takes place will therefore be the temperature of the water, but the HTC value must consider the type of heat exchange of the components crossed by the flow. For the calculation of this HTC the electrothermal analogy is used, Figure 3.4. Therefore, it is necessary to calculate the equivalent resistance of gas (R1), liner (R2) and water (R3). These three resistances are in series and therefore the total resistance is the sum of these. It is then immediate to calculate the HTC from the total resistance.

$$R_1 = \frac{gap_{land\ cyl}}{A_{land} k_{land}};\quad R_2 = \frac{ln\left(\frac{r_{e_{cyl}}}{r_{i_{cyl}}}\right)}{2\pi H_{stroke} k_{cyl}};\quad R_3 = \frac{1}{HTC_{w\ jacket} A_{w\ jacket}} \tag{3.12}$$

Where A_{land} is the area, k is the thermal conductivity of linear material, r are the radii involved in the calculation (e for external and i for internal) and $HTC_{w\ jacket}$ is the convective heat transfer coefficient of water. Now it is possible to calculate the HTC to be assigned to the surface of the first land.

$$HTC_{land} = \frac{1}{A_{land} \sum_1^3 R_i}; \tag{3.13}$$

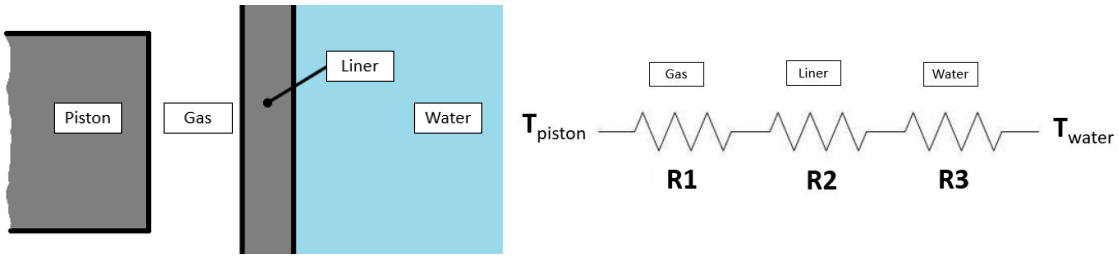

(a) (b)

Figure 3.4. Scheme of the electrothermal analogy.

3.2.3 Piston rings

The heat exchange mode is basically the same for rings and oil scraper, except for some details that will be illustrated below.

Piston rings can be inserted into the FEM simulation as physical bodies, or their effect can be simply taken into account without modelling them in the software. This second is used in this study.

A part of the heat flow that enters from the piston crown dissipates in the water after passing through part of the piston, the segment, the lubricating oil between the ring and the cylinder liner and the liner itself. Using once again the electrothermal analogy it is possible to calculate a heat exchange coefficient to be applied directly on the lower and upper surface of the groove, Figure 3.5.

The resistance exerted by the segment must be analyzed in two distinct ways for the portion of the ring inside the slot and the one outside.

The first section is a parallel of resistances, in fact, the flow enters along the entire contact surface between the segment and the piston and moves towards the outside of the ring.

This resistance R1 can be calculated as:

$$R_1 = \left[\int_{r_i}^{r_e - gap} \frac{2\pi k_{ring} h_{ring}}{ln\left(\frac{r_e}{r}\right)} dr \right]^{-1} \tag{3.14}$$

Where r_e and r_i are the inner and outer radius of the pressure ring, h is the axial thickness of the ring and k_{ring} is the thermal conductivity of the material. This formulation is strictly true when the heat flux is constant along the contact surface [19], the results of the Finite Element thermal calculations show that this assumption is not too far from reality.

The other resistances are those of hollow cylinders crossed by a flow in a radial direction and therefore R2, R3, R4 and R5 are:

$$R_2 = \frac{ln\left(\frac{r_e}{r_e - gap}\right)}{2\pi h_{ring} k_{ring}};\ R_3 = \frac{ln\left(\frac{r_{e_{oil}}}{r_{i_{oil}}}\right)}{2\pi H_{stroke} k_{oil}};$$
$$R_4 = \frac{ln\left(\frac{r_{e_{cyl}}}{r_{i_{cyl}}}\right)}{2\pi H_{stroke} k_{cyl}};\ R_5 = \frac{1}{HTC A_{w\ jacket}} \tag{3.15}$$

Each contact surface between grooves and rings exchanges up to the water and therefore the exchange temperature will be the one of the water jacket, while the HTC is:

$$HTC_{groove} = \frac{1}{2}\frac{1}{A_{groove}\sum_1^5 R_i}; \tag{3.16}$$

where A_{groove} is each contact area between groove and ring. The multiplicative coefficient ½ indicates that the exchange takes place for half the time on one side of the segment and for the other half of the time on the other side. This is strictly valid for the second ring and the oil scraper, the inertia of these components makes them change the contact area while the piston moves in the cylinder.

Considering the first segment, in addition to inertial phenomena, the pressure in the chamber also intervenes, pushing the segment downwards in the power stroke. So for ¾ of the time, the ring touches the bottom of the groove, while for the remaining quarter of the time it will touch the top. Therefore, the HTC to be assigned to the first segment is:

$$HTC_{grooveUP} = \frac{1}{4}\frac{1}{A_{grooveUP}\sum_1^5 R_i};$$
$$HTC_{grooveDOWN} = \frac{3}{4}\frac{1}{A_{grooveDOWN}\sum_1^5 R_i}; \tag{3.17}$$

From here it is possible to understand why it is preferable not to represent the rings in the FEM model. The motion of the segments cannot be inserted in the FEM model and therefore it would not be possible to distinguish in the first instance between the upper and lower surfaces. In fact, It is possible to appropriately modulate the contact resistance Rcont to obtain the same effect [20].

$$R_{tot+cont} = R_1 + R_2 + R_3 + R_4 + R_5 + R_{cont}\ ;$$

$$R_{cont} = R_{tot+cont} - (R_1 + R_2 + R_3 + R_4 + R_5)\ ;$$

$$k_{contUP} = \frac{1}{4}\frac{1}{R_{cont} \cdot A_{groove\ UP}} = \frac{1}{4}\frac{1}{\left(\frac{1}{h_{groove} \cdot A_{groove\ UP}} - \sum_1^5 R_i\right) \cdot A_{groove\ UP}} \tag{3.18}$$

$$k_{contDOWN} = \frac{3}{4}\frac{1}{R_{cont} \cdot A_{groove\ DOWN}} = \frac{3}{4}\frac{1}{\left(\frac{1}{h_{groove} \cdot A_{groove\ DOWN}} - \sum_1^5 R_i\right) \cdot A_{groove\ DOWN}}$$

K_{contUP} and $K_{contDOWN}$ are the contact conductivity to be assigned in the MSC Marc software between the groove and the appropriate side of the ring.

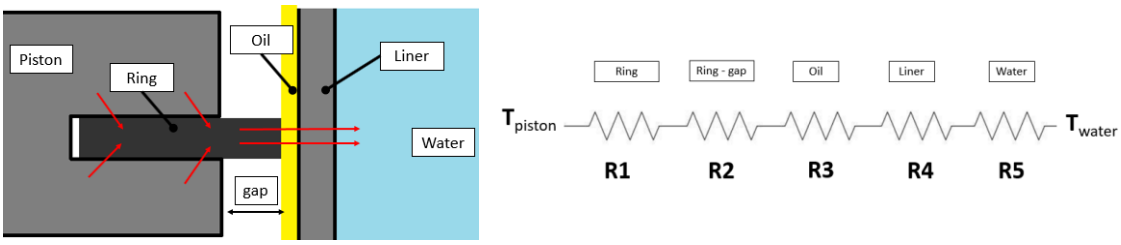

(a) (b)

Figure 3.5. Scheme of the electrothermal analogy.

3.2.4 Piston skirt

Part of the heat entering from the piston crown reaches the water passing through the skirt. In particular, this flow meets the lubrication oil, the cylinder liner and then reaches the water jacket. Also in this case the electrothermal analogy is applied to take into account three resistances in series: oil, cylinder and water, Figure 3.6.

$$R_1 = \frac{t_{oil}}{A_{skirt} k_{oil}};\ R_2 = \frac{ln\left(\frac{r_{e_{cyl}}}{r_{i_{cyl}}}\right)}{2\pi H_{stroke} k_{cyl}};\ R_3 = \frac{1}{HTC_{w\ jacket} A_{w\ jacket}} \tag{3.19}$$

where t_{oil} is the thickness of the oil film. The temperature of the fluid is the temperature of the water and the HTC to assign to the skirt is:

$$HTC_{skirt} = \frac{1}{A_{skirt} \sum_1^3 R_i} \tag{3.20}$$

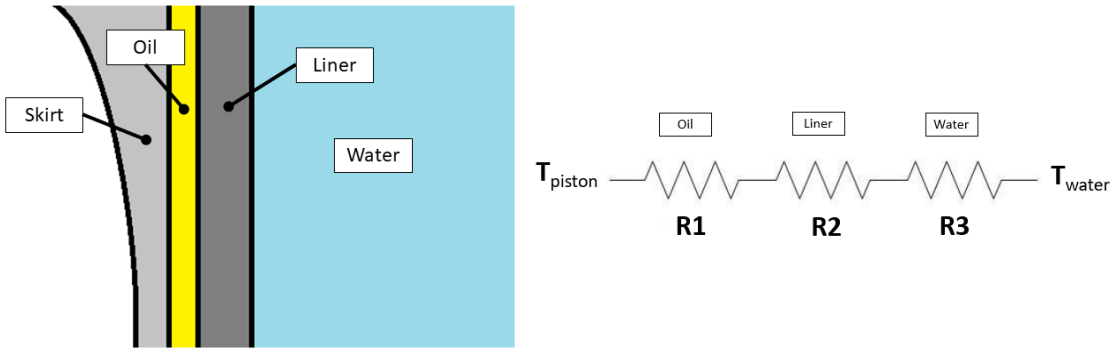

(a) (b)

Figure 3.6. Scheme of the electrothermal analogy.

3.2.5 Oil splash

Approximately, one half of the heat flow entering from the piston crown is dissipated by the cooling oil (and lubrication) which wets the lower surfaces of the piston [21].

For the evaluation of the heat transfer coefficients between the lower surfaces of the piston and the splashed oil, empirical expressions exist which usually distinguish between horizontal and vertical surfaces:

$$HTC_{horizontal} = 900 \left(\frac{n}{4600}\right)^{0.35} ; \; HTC_{vertical} = 240 \left(\frac{n}{4600}\right)^{0.35} \tag{3.21}$$

where n is the revving speed [rpm].

In fast engines, such as the one under consideration, the convective exchange of the oil cloud is not affected by the vertical or horizontal orientation of the lower piston surfaces. The HTC average of (3.21) is then applied to all surfaces wetted by splashing oil. This HTC value is also used to quantify the heat exchange of the connecting rod and pin with the oil.

In high-performance engines (as considered), one or more oil jets are used to remove heat from the lower part of the piston. In this case, other semi-empirical formulas must be used to calculate the HTC in the specific areas affected by the jet, while it is appropriate to correct the other areas. In fact, the oil jet intensifies the heat exchange and a different HTC must be applied between the external and external areas of the piston flow rates (Figure 3.7), because they benefit in different ways from the effect of the piston

jet. An HTC of 1.2 times the average between horizontal and vertical HTC is applied to the eternal surfaces, while a multiplicative coefficient 2.4 is used for the internal surfaces.

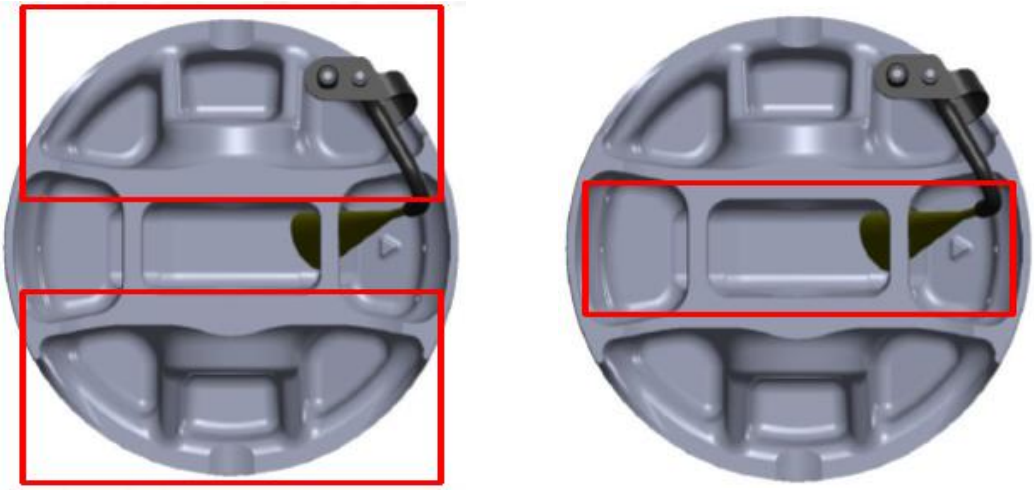

(a) (b)

Figure 3.7. Detail of the oil jet.

3.2.6 Oil jet

To intensify the removal of heat from the lower part of the piston, it is possible to install one (as in our case) or more jets in the base that point towards the piston [22–25]. The HTC to be assigned to the affected surfaces is calculated using an empirical formula:

$$HTC_{oil\ jet} = 68.17\left(r \cdot \omega \cdot \frac{D_{jet}}{\nu_{oil}}\right)^{0.5} \tag{3.22}$$

where r is the crank radius [m], ω is the angular velocity [rad/s], D_{jet} is the nozzle diameter [m] and v_{oil} is the kinematic viscosity of oil [m^2/s].

3.2.7 Heat flux due to friction

As already mentioned, another source of heat is the one that arises from the friction of the first compression ring and skirt with the cylinder liner; it is lower than the heat coming from combustion, but it is not negligible. To quantify this contribution, the lateral force that each of the components exerts on the liner is considered, it is multiplied by the piston speed to obtain the thermal power and the calculation is concluded by calculating the average value by performing a summation by trapezoid areas as in the case previously seen for the piston top.

The instantaneous friction loss generated at the interface between the piston skirt and the liner can be easily estimated as:

$$Q_{f_{skirt}}(\theta) = \mu_{skirt} F_{thr}(\theta)|v(\theta)| \tag{3.23}$$

where F_{thr} is the thrust force between the piston and the liner, v is the piston velocity and μ_{skirt} is the friction coefficient at the interface between the skirt and the liner. Note that the sign of F_{thr} defines which side of the skirt is in contact with the liner. As a consequence, left-skirt and right skirt friction losses can be defined:

$$\begin{aligned} Q_{f_{skirt\_left}}(\theta) &= \mu_{skirt} F_{thr\_pos}(\theta)|v(\theta)| \\ Q_{f_{skirt\_right}}(\theta) &= \mu_{skirt} \left|F_{thr\_neg}(\theta)\right| |v(\theta)| \end{aligned} \tag{3.24}$$

The instantaneous friction losses can then be cycle averaged in order to obtain the mean losses:

$$\begin{aligned} \overline{Q_{f_{skirt\_left}}} &= \frac{1}{720}\int_0^{720} \mu_{skirt} F_{thr\_pos}(\theta)|v(\theta)|d\theta \\ \overline{Q_{f_{skirt\_right}}} &= \frac{1}{720}\int_0^{720} \mu_{skirt} \left|F_{thr_{neg}}(\theta)\right| |v(\theta)|d\theta \end{aligned} \tag{3.25}$$

The instantaneous friction loss generated at the interface between the first compression ring and the liner can be easily estimated as:

$$Q_{f_{ring}}(\theta) = \mu_{ring} \alpha p(\theta) 2\pi r_{i,ring} H_{ring} |v(\theta)| \tag{3.26}$$

where p is gas pressure, $r_{i,ring}$ is the ring inner radius, H_{ring} is the ring width, v is the piston velocity, μ_{ring} is the friction coefficient at the interface between the ring and the liner and α is a coefficient which considers the pressure drop between the combustion chamber and the first ring groove.

The instantaneous friction loss can then be cycle averaged in order to obtain the mean loss:

$$\overline{Q_{f_{ring}}(\theta)} = \frac{1}{720}\int_0^{720} \mu_{ring} \alpha p(\theta) 2\pi r_{i,ring} H_{ring} |v(\theta)|d\theta \tag{3.27}$$

Finally, it must be considered that the heat flow is generated at the contact interface and therefore part of the flow will go into the ring (or skirt) to be dispersed in the oil and the remaining part will go into the cylinder to be dissipated in the water. To evaluate which element is most affected by this thermal flow, considerations are carried out on the thermal resistances involved. Through the conductivity values of the materials and the convective coefficient of the fluids, the total resistances on the cylinder side and shell side are defined. It has been estimated that, based on the entered values, the ratios of the resistances obtained produce a heat partition at the skirt of about 40% and of 60% for cylinder liner. Considering the ring, however, this subdivision is slightly different: with the same method, 20% of the heat produced by friction directed towards the ring and 80% towards the liner is evaluated. This evaluation is also carried out through the relative

resistances between liner and ring. In the latter, the flow rate that exits towards the splashing oil inside the pocket below the piston, the one that goes towards the second ring and the one towards the oil scraper are considered. Each of these three flows encounters its own resistance which contributes to the total resistance as a combination of resistors in parallel.

This division shows how the percentage of heat absorbed by the liner and then disposed of by the water circuit is much greater than that absorbed by the piston and then disposed of by the oil.

3.3 Cylinder Liner

To obtain the deformation of the cylinder liner and of the crankcase during the operation conditions, it is necessary to compute the temperature field of these components. The thermal loadings affecting the cylinder liner are: heat generated in the combustion chamber, heat generated by friction from the first compression ring and skirt and the heat that enters the piston crown and reaches the water jacket passing through the cylinder liner. Furthermore, it is necessary to consider the effect of the lubricating (and cooling) oil that wets the lower part of the cylinder liner.

The crucial aspect that must be considered to calculate the boundary conditions to be applied to the FEM model is the translatory motion of the piston. The piston, during its motion, covers or uncovers different areas of the liner making it non-trivial to calculate the quantities to be applied on the liner, in terms of HTC and heat fluxes.

3.3.1 Heat flux from the piston

The heat flux coming from the piston top because of the combustion process reaches the inner surface of the liner. In particular, this heat flux is transferred from the piston to the liner through the contact interaction of the rings and of the skirt with the cylinder liner.

Using the data already obtained for the piston calculation, the incoming flux from the piston crown can be obtained for each CA (crank angle) and then the average incoming heat flux for each cycle can be calculated.

Multiplying the value of the thermal flux on the piston crown by the factors 0.3 and 0.2, the thermal flow is obtained, at each crank degree, for the segment and for the skirt respectively. Graphing the series of values obtained, two curves similar to the previous one are retrieved, scaled by the aforementioned factors. Also in this case, the average value is the focus, so the logic seen so far is repeated: the trapezoid areas are added together and the result is averaged over the entire cycle. The formulas are those seen in the previous section.

Obtained the heat flux affecting the segment (or skirt), the heat flux per unit of area on the segment (or skirt) can be estimated, dividing the value just mentioned by the surface that sweeps the segment (or skirt) during the motion of the piston. Nevertheless, it can be possible to be more precise, this average value of heat flux could not be sufficient. The more velocity of the piston is slow, the more the heat

exchange is promoted so that it is necessary to correct the average value of the heat flux considering the instantaneous speed of the piston. Therefore, a different value of heat flux can be obtained based on the axial coordinate of the cylinder liner.

Finally, the heat flux is distinguished in the one generated by friction between the skirt and the cylinder and the one generated between the ring and the cylinder.

3.3.1.1 Heat flux of the rings

Starting from a crank angle equal to zero, it is necessary to calculate the position of the piston instant by instant, in order to evaluate the surface of the liner in contact with the rings and affected by the heat exchange, Figure 3.8.

A coarse vertical scale is used based on the axial mesh resolution of the liner so that the scale interval is 1 mm. For each section into which the cylinder liner has been divided, the thermal flux value is zero for all the heights of the liner in which the segment is not present. The heat dissipated by the segment is calculated per unit area:

$$Q_{ring} = \dot{Q}_{ring} \frac{\Delta t_{cycle}}{720} \frac{1}{A_{displced\_ring}} \tag{3.28}$$

This type of definition of the thermal flux must respect the fact that not always the entire surface of the liner is in contact with the ring, in fact the surface swept by the segment varies continuously. This implies that at each instant a different quantity of heat is exchanged (for this it must be considered $\frac{d\Delta t_{cycle}}{720}$ to evaluate the incidence of heat in a time interval of a crank angle).

To know the heat exchanged at each millimetre of the liner, the heat that enters that portion of the liner for each crank angle has to be added.

Therefore, each millimetre in which the liner has been divided represents an interval in which the ring releases heat; the subdivision in millimetres obtained from the different crank angles does not exactly coincide with the subdivision of the liner according to the coordinates on its axis, in fact, especially at the top dead centers, there are many crank angles in the same millimetre due to the trivially non-constant speed of the piston.

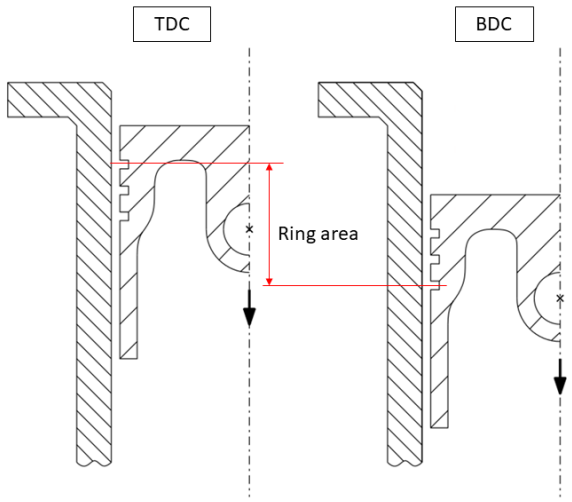

Figure 3.8. The region of application of the flux from the rings.

3.3.1.2 Heat flux of the skirt

Considering the flux coming from the skirt, the methodology is similar to that just seen for the rings. However, it is necessary to properly evaluate the geometries considered, for example, the cylindrical surface in contact with the liner at a given instant does not have a height equal to the axial thickness of the segment, but the height of the skirt must be considered, therefore for each crank angle a much larger area is affected by the heat flux, Figure 3.9.

Furthermore, the highest and lowest border of the skirt is different from the ones of the rings, therefore the translated coordinate must have an appropriate displacement.

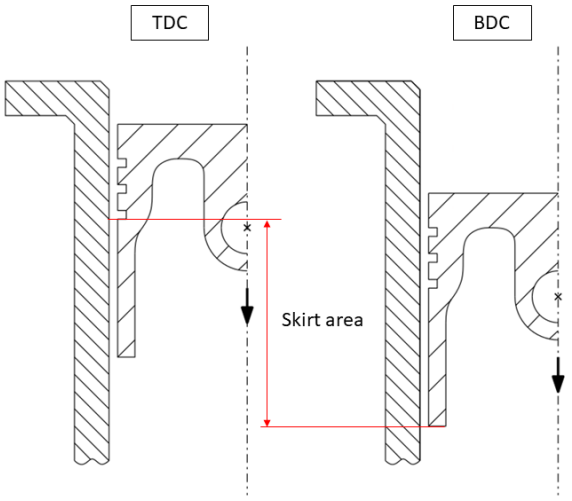

Figure 3.9. The region of application of the flux from the skirt.

3.3.1.3 Heat Transfer Coefficient and Temperature of the gas

First, the HTC (Heat Transfer Coefficient) and the T (Temperature) of the gas for each crank angle have to be considered.

It is now estimated how many portions of the liner, from time to time, are in contact with the gases; in other words, for each crank angle, there is a different portion of the line exposed to the gases and, therefore, each height along the axis of the liner will undergo a different contact with the gases, consider Figure 3.10.

Below, there are the steps useful for defining the effect of gases on the surface of the cylinder liner in terms of gas temperature and HTC. First, the HTC and T value for each crank angle has to be retrieved. The total HTC is then calculated for each coordinate along the axis of the liner. It is obtained as the sum of all the trapezoids of HTC recorded at the different crank angles. The formula is the one already seen above. In this way, for each vertical height of the barrel, the total of the HTC developed by the contact of the gases for the whole engine cycle is calculated. Similarly, the average gas temperature must also be calculated for each axial height of the cylinder. Now it is possible to calculate the heat flux per area for each *i-th* motor angle:

$$\frac{\Delta Q}{Area} = \frac{HTC_i \cdot T_i + HTC_{i+1} \cdot T_{i+1}}{2} \cdot (\theta_i - \theta_{i-1}) \tag{3.29}$$

To get the heat flux that affects the specific axial coordinate, the contributions of all the crank angles relative to the single height have to be summed together. Finally, to obtain the temperature, this sum is divided by this total HTC, which affects that particular height.

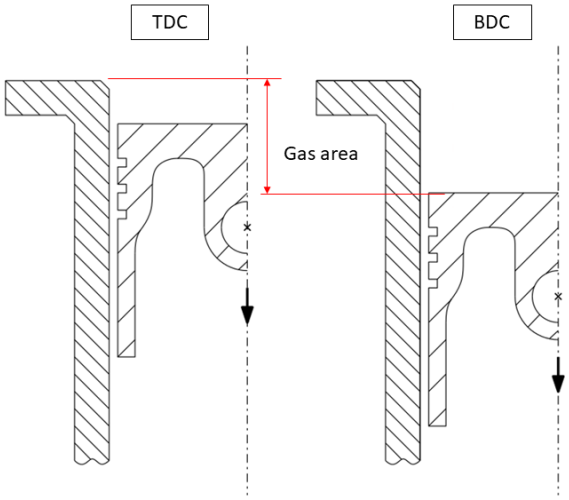

Figure 3.10. The region of application of the effect of the gas.

3.3.1.4 Heat Transfer Coefficient of oil

First, the area of the liner affected by the contact with the skirt is identified (Figure 3.11 (a)) and the area where contact occurs only with the rings is retrieved (Figure 3.11 (b)). For each portion, an HTC profile of the oil is identified for each axial coordinate of the cylinder.

The HTC value of the splashing oil in the crankcase is 0.0003 W/mm^{2}K; this could also be the value of the HTC on the walls of the liner in contact with the oil, but since not all areas of the liner are always in contact with the oil due to the movement of the piston, this value (0.0003 W/mm^{2}K) must be commensurate with the degree of exposure of the liner to oil. Only where the piston never covers the liner, the HTC of the oil exhibits the maximum value of 0.0003 W/mm^{2}K. Naturally, the lower areas of the barrel are constantly in contact with the oil, while those in the upper part are exposed to the cooling oil for less time, as shown in Figure 3.9.

The difference between the area that is not swept by the skirt and the one swept by the skirt lies in the first axial coordinate obtained geometrically and then increased for each crank angle using the displacement of the piston. Therefore, it is appropriate to apply different boundary conditions for each zone when creating the Finite Element model.

It must be considered that a large part of the barrel is lapped by gas and cooled by oil. Many Finite Element software are unable to combine two different pairs of HTC and temperature, so it is worth understanding how they can be combined using a simple spreadsheet.

The equivalent HTC is obtained by simply adding the HTC gas and oil for each axial coordinate as if considering the convective contributions of the two fluids to heat transmission summed together.

The equivalent temperature is obtained by making a balance on the incoming heat flow at each axial coordinate:

$$T_{eq} = \frac{HTC_{gas} \cdot T_{gas} + HTC_{oil} \cdot T_{oil}}{HTC_{gas} + HTC_{oil}} \cdot (\theta_i - \theta_{i-1}) \tag{3.30}$$

The formula (3.30) corresponds to the weighted average of the temperature on the HTC. It is immediate to understand that the temperature is more influenced by the fluid that has the highest HTC.

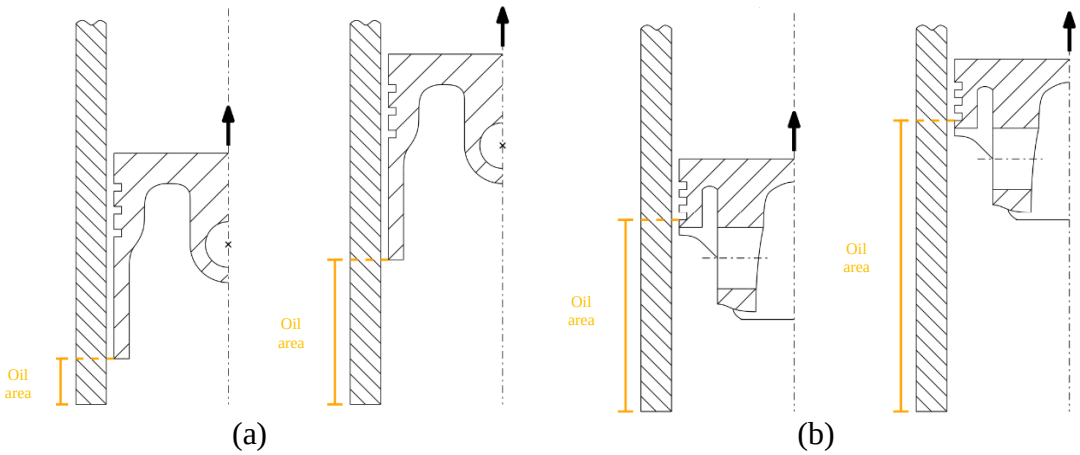

Figure 3.11. The region of application of the effect of the oil.

3.3.1.5 Heat flux due to friction

First, the heat fluxes generated by friction from the first pressure ring and the skirt are calculated, with the same approach seen in the piston section. The percentage of heat transferred to the barrel through an evaluation of the heat paths with lower resistance is taken into account, as already explained above in the piston section (3.2.7 Heat flux due to friction).

Considering the rings, the force, with which the rings are pressed on the liner through 70% of the gas pressure, is calculated and thanks to this force, multiplied by the friction coefficient, it is obtained the tangential force to the liner. Multiplying this value by the speed of the piston at each crank angle, the dissipated power is obtained. Using the trapezoid integration method, it is possible to find the compensation ordinate and therefore the average power dissipated value per cycle. By dividing this value by the area swept by the segment, I get the dissipated power value per area to be applied to the internal surface of the cylinder.

A similar procedure is followed for calculating the heat generated by friction from the skirt. Obviously, it is advisable to assign this incoming heat only to the cylinder area affected by the sliding contact of the piston skirt.

It may be sufficient to apply the average values of the flows generated by friction, but it is preferable to consider the instantaneous speed of the piston and the lateral thrust force to obtain the flux profile depending on the axial coordinate of the cylinder, more faithful to the actual physical phenomenon.

Chapter 4: Additive Manufacturing techniques

4.1 Introduction

Additive Manufacturing technologies are very widespread in every field of mechanics and the automotive world is no exception [26–28], both in the chassis [29–31] and motor fields [32–34].

Additive Manufacturing is the correct term to identify what used to be called rapid prototyping and what is commonly referred to as 3D printing [35]. The term rapid prototyping is used in industry to describe a process for rapidly creating a representation of a system or part before its launch on the market. In other words, the important thing is to create something quickly: a prototype or a basic model, from which further models or the final product will be derived.

The term rapid prototyping is no longer suitable and, in particular, does not effectively describe the most recent applications. The improvements in the quality of the output of these machines have shortened the distance between prototyping and the finished product.

Wanting to summarize the characteristics of Additive Manufacturing, the underlying principle of this technology consists in being able to create a mechanical component, modelled with a CAD tool, directly without having to plan the manufacturing process.

The key to the operation of Additive Manufacturing consists in the creation of parts by depositing material by layers: each layer is a thin cross-section of the piece obtained from its CAD model. The thickness of each layer affects the final result and the thinner it is, the more similar the product will be to the original drawing. All the machines on the market use an approach of this kind and differ from each other for the material used, for the method of deposition of the layers and for the type of bond that is established between them. These differences determine some characteristics such as manufacturing precision and mechanical properties of the final component. These differences also affect the speed of production of the part, the cost of subsequent processing required, the size of the machinery and the overall cost of the equipment and process.

Initially, Additive Manufacturing technologies were used exclusively to create models to visualize the product during the stages of its development. These techniques then developed together with the improvement of the materials used, the precision achieved and the overall quality obtainable at the end of the process. In addition, the recent introduction of high-power lasers has allowed the use of metals, significantly extending the range of possible applications.

4.1.1 The steps of the Additive Manufacturing process

An Additive Manufacturing process always starts from a CAD model, which fully describes its geometry. A reverse engineering approach could also be used, using optical or laser scans it is possible to create CAD representations.

The second step is the conversion and generation of an STL (STereo Lithography interface format) file, this contains information about the closed outer surface of the component and provides the basis for the calculation of the layers.

The newly created file is transmitted to the machinery, according to the needs and characteristics of the instrument it is possible to set the size and position of the object and the orientation of the layered deposition.

Now it is necessary to set the machine parameters inherent to the production process, i.e. constraints given by the material, energy source, thickness of each layer and the processing time.

Afterwards, the part is built, it is a fully automated process.

Once the machine has completed its task, the product must be removed. The operator must be sure that the part is sufficiently cold and that there are no moving mechanisms yet.

Once this stage is complete, the component may need further processing, may be delicate or may have supports to remove.

The component may now be ready for use, although other processing such as painting and assembly may be required.

After listing the steps in the Additive Manufacturing process it is important to understand that many of these machines require careful maintenance, have lasers and delicate parts, and should not be used in dusty and noisy environments.

Not only does the instrumentation require adequate attention, but even the filler materials also require careful management, the raw materials used in some processes have a limited shelf life and must be protected from harmful chemical reactions, which can be caused for example by humidity or from excessive exposure to light. Furthermore, the reuse of a material may not be allowed, so it might be interesting to study effective recycling techniques.

4.1.2 The advantages of Additive Manufacturing

The main advantage of using this technology is the processing speed. This benefit does not only refer to the time taken to build the component, but is also found in the entire production process.

Furthermore, a drastic reduction of the steps of the production process is observed, regardless of the complexity of the product, the result is achieved in a single phase. For this reason, it is easier to predict the time required for model production, without having to consider design changes that may be required for product development.

With the use of Additive Manufacturing technologies, the number of resources and processes required can be drastically reduced. Making a prototype using traditional techniques may require a succession of various methods such as hand carving, shaping or chip removal with numerical control machines.

It should also be highlighted the enormous design freedom that Additive Manufacturing offers. The subdivision into thin slices at the base of this process does not place theoretical limits on the complexity of the forms that can be produced. Unfortunately, there are practical limitations related to the usable materials and the need to have a support for each layer of material.

4.2 Classification of Additive Manufacturing processes

There are many ways to classify Additive Manufacturing techniques. A comprehensive method involves a two-dimensional classification, illustrated in Figure 4.1. The first dimension indicates the construction method of the layers. Early technologies used a single source to draw on the surface of the base material. Subsequently, the number of sources used to increase the production volume increased. Another dimension is also introduced, which refers to the raw material: liquid polymer, discrete particles, molten material and laminated sheets.

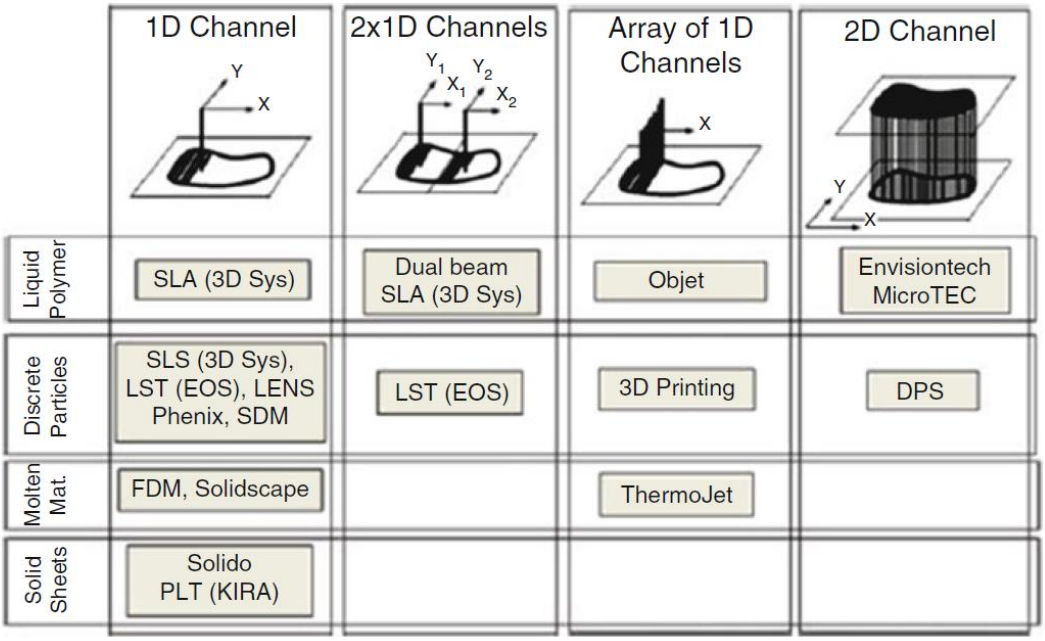

Figure 4.1. Classification of Additive Manufacturing processes. [35].

4.2.1 Powder Bed Fusion

Powder Bed Laser Fusion (PBF) processes were among the first Additive Manufacturing technologies to be commercialized. These have several basic characteristics, Figure 4.2: one or more heat sources to induce melting between powders, a method of limiting powder melting to a defined region of each layer, and mechanisms for adding and smoothing the dust. Lasers are the most common thermal source and are used in laser sintering machines.

These processes were initially developed to produce plastic prototypes using a point laser scanning technique. This approach extended to metal and ceramic powders; additional energy sources are now being used and variants of layered fusion are being marketed.

A laser sintering process melts layers of powder (typically between 0.075 and 0.1 mm thick), which have been distributed over the work area using a counter-rotating levelling roller.

The construction of the part takes place inside a closed chamber filled with nitrogen to minimize oxidation and degradation of the pulverized material. The dust on the work surface is kept at high temperatures just below its melting point (or glass transition point depending on the material used). Infrared radiators are installed above the platform to maintain a high temperature in the part that is forming and to preheat the powder before it is distributed on the work area. In some cases, the build platform is heated by resistors arranged around it. The powder and the bed are preheated and kept at high temperatures to minimize the laser power required by the process and to prevent distortion of the piece during production caused by non-homogeneous thermal expansion.

Once a suitable powder layer has been laid and preheated, a CO2 laser beam is directed onto the powder and moved using galvanometers to melt the material and form a cross-sectional layer. The dust around it acts as a support for subsequent layers, eliminating the need for secondary supports. After completing a layer, the platform drops by the thickness of the layer and a new layer of powder is placed, which is levelled by the counter-rotating roller. The beam scans the next cross-section. This sequence is repeated until the entire part is created. Typically a cooling period is required before exposing the component to ambient temperature and the atmosphere. If this time is not respected, the powders could degrade and the part could deform due to an irregular thermal contraction. Finally, the part is removed, cleaned of remaining dust and subsequent finishing operations are performed if necessary.

In principle, all materials, which can be melted and then solidified, can be used in a PBF process.

If you want to focus on metals, most of them are suitable. Usually, those that can be welded can be found suitable for a PBF process. The metals currently used are steels, stainless and for tools, titanium and its alloys, nickel-based alloys, some aluminium alloys and cobalt-chromium-based alloys, silver and gold.

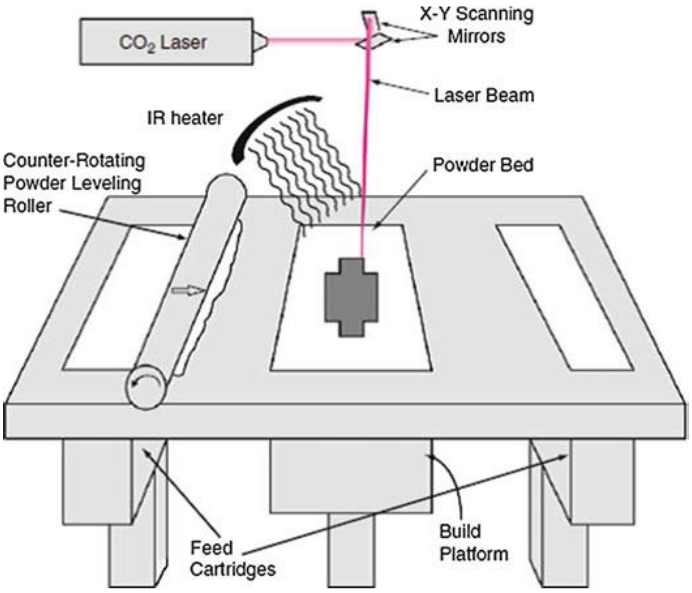

Figure 4.2. Scheme of a BED process [35].

4.2.2 Selective Laser Melting

One effective technique for creating metal components is selective laser melting (SLM). This process was studied in the late eighties and early nineties with little success. Some characteristics of metals, such as the high thermal conductivity, the propensity to oxidize, the high surface tension and the high reflectivity of the powders, have made these materials much more difficult to work with than polymers. The use of lasers with wavelengths better calibrated on the receptivity of metal powders was one of the keys to the rise of SLM technologies. Nd-YAG lasers were introduced instead of CO2 and then later the fibre lasers, which are cheaper, compact, efficient and have a better quality beam. Another turning point for the development of this process was the introduction of different scanning schemes, the use of *f-theta* lenses to minimize beam distortion and the adoption of inert atmospheres with low oxygen content.

A common practice is to bond the parts to a base plate on the bottom of the countertop. This is done to avoid distortions in the piece due to residual stresses. This entails a reduced design flexibility compared to the use of polymeric materials, because a process of removing the supports with machining is required.

Tolosa et al. [36] studied the influence that the SLM process could have on the mechanical properties of the AISI 316 steel alloy. The performance of many metals does not depend only on their chemical composition, but also on their microstructure. This is obtained from the processes used and therefore this means that the same alloy could show very different properties depending on the processes adopted. Tolosa carried out numerous tests on specimens, created with different deposition angles. He proved that the strength properties were always comparable, if not even superior, to those of specimens made with traditional technologies. The effort that leads to plasticization of the material is always higher than traditional specimens, while the elongation is lower, but always sufficient for the most common uses. The resilience test highlighted the inferior quality

of SLM products. The hardness tests showed no differences between the specimens of the different technologies. All these tests showed some degree of anisotropy of the models produced in SLM.

Kruth et al. [37] concentrated their studies on thermal stresses and on scanning strategies suitable for minimizing them. Both the properties of the powders used and the process parameters influence the thermal stresses to which the component is subject.

Generally, the cross-sections of the part are scanned with vectors parallel to each other, Figure 4.3. If an area is small, it requires a short vector, so neighbouring paths are drawn quickly in sequence, leaving little time for cooling. For larger areas, the laser beam travels longer distances and consequently or marked paths have more time to cool down. This leads to worse wettability and lower material density.

The different thermal conductivity of the powders and solidified material also influences the temperature trend in the manufacturing process. During laser melting, the density of the material increases. When scanning a small area, the powders surround and isolate it, keeping its temperature high, ensuring a high density of these areas.

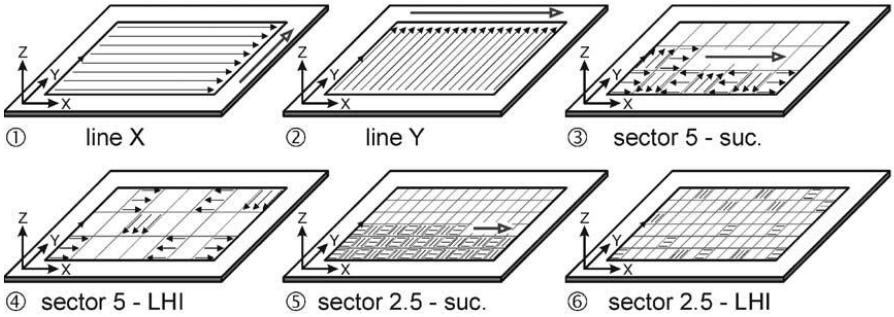

Figure 4.3. Different scanning strategies [37].

Chapter 5: Optimization Techniques

5.1 Introduction

The engine is equipped with an aluminium piston as standard, to test a steel piston it is not possible to maintain the same geometries as the original piston. A new steel piston has been then designed following the indications shown by topological optimizations. Before showing the design phases, it is necessary to expose what an optimization technique is, what structural optimization techniques are and then, finally, what Topological Optimization is.

5.2 Definition of optimization

In an optimization problem, the values of the variables that lead to an optimal value of the function to be optimized are looked for, Cavazzuti [38]. First of all, it is necessary to clearly define the optimization problem, that is the one to be optimized. Then some variables are needed, that is an appropriate parameterization of the problem, and a function to be optimized, that is to say, an objective. Finally, a procedure will be needed through which, for a given value of the variables (configuration or sample), the relative objective is calculated, this procedure can be an experiment or a simulation. An optimization process usually proceeds iteratively by generating a configuration and evaluating the value of the objective function. An optimization algorithm is basically a configuration generator to be tested that with different logics generates new configurations based on those previously tested, that is, the information collected.

The terminology in the field of optimization is not entirely uniform, the following terms are adopted below.

- Optimization problem: defines the object of the optimization.
- Input parameters: the set of parameters that characterizes the problem.
- Input variables (x_i): the subset of the input parameters that are actually taken into account in an optimization process. A variability field is usually associated with each input variable.
- Sample or configuration ($\boldsymbol{x}$): a set of input variables.
- Design space ($\boldsymbol{X}$): space of all possible configurations of the optimization problem.
- Experiment or simulation: the process by which information is extracted from a sample.
- Output parameters: the set of results collected through a simulation or experiment.
- The objective function ($f(\boldsymbol{x})$): the output parameter or a function of the output parameters that you want to maximize or minimize. If there is only

one objective function we speak of single-objective optimization, otherwise of multi-objective optimization.

- Constraints (*c(**x**)*): functions of the output parameters that must be respected by the optimal solution.
- Space of solutions (***Y***): the codomain of the project space.

The typical formulation of an optimization problem from the mathematical point of view is the following:

$$\begin{aligned} &\underset{\boldsymbol{x}\in\boldsymbol{D}}{\text{minimize}}\, f(\boldsymbol{x}) \\ &\text{subject to}\, c(\boldsymbol{x}) \leq 0 \end{aligned} \tag{5.1}$$

5.3 Optimization techniques

An optimization problem can be addressed in many ways and using different techniques. Five types of techniques can be distinguished:

- DOE - design of experiments;
- RMS- response surface modelling, o response surface methodology;
- Deterministic optimization;
- Stochastic optimization;
- RDA - robust design analysis, also called RED - robust engineering design.

The purpose of these types of techniques will be briefly discussed below.

5.3.1 Design of experiments

The DOE was born in the field of statistics around 1920. It was initially called "statistical experimental design". Its purpose is to properly plan the sequence of experiments to be carried out during a series of analyzes carried out in the laboratory so that, at the end of the experiment, the results can be statistically analyzed to determine the influence of the system variables on them. The DOE was then used in the context of optimization in order to find information on the project space through appropriate sampling.

A classic definition states that DOE techniques aim to plan experiments to gather the greatest amount of information on the problem under consideration using the least amount of resources.

5.3.2 Tecniche RMS

The RMS techniques have the purpose of interpolating or approximating the data collected through DOE by creating a metamodel that can then be used in optimization. An optimization process can take a lot of simulations and if these are particularly expensive, you have to wait a long time before you get the results. By appropriately

sampling and interpolating the data by combining DOE and RMS, a mathematical model can be obtained that estimates the response of the simulations with a smaller number of simulations. At this point, making optimizations based on the metamodel becomes computationally lighter. This approach, therefore, can be particularly advantageous in the case of very onerous optimization problems. On the other hand, relying on a metamodel is always risky: if the model is not reliable, due to an insufficient number of samples or because the real response of the system is particularly affected by noise, the results obtained can be almost unnecessary.

With RMS the output parameter $f(\boldsymbol{x})$ is approximated by a function $f^*(\boldsymbol{x})$:

$$f(\boldsymbol{x}) = f^*(\boldsymbol{x}) + \mathcal{E}(\boldsymbol{x}) \tag{5.2}$$

If the error $\varepsilon(\boldsymbol{x})$ in the sampled points x_i is zero ($\varepsilon(x_i)= 0$) the method is called interpolating, otherwise, it is called approximant.

5.3.3 Deterministic optimization

Deterministic optimization, also known as "mathematical programming", includes all the mathematically more rigorous optimization methods that do not have stochastic elements within them. These are mainly methods based on the calculation of the gradient and the Hessian of the functions of the output parameters, in large part deriving from the Newton-Raphson method.

If the gradients and the Hessian of a given function are not available directly from the simulation, as often happens, these must be approximated to the finite differences, which may require a large number of simulations. Generally, there is a tendency to distinguish, within deterministic optimization, between unconstrained optimization and constrained optimization, given the complications that the inclusion of constraints brings to traditional optimization algorithms.

Gradient optimization methods can use two different approaches.

- Line search: once the direction in which to move is identified, a sampling is carried out along the chosen direction until certain conditions are met by the sampled point. These are called Wolfe-Powell conditions [39] and serve to avoid that the improvement of the objective function between one step and another of the optimization is too small and, consequently, that the convergence of the method is too slow overall.
- Trust region: in these methods we iteratively proceed to a local quadratic approximation of the objective function by truncating the Taylor series. The minimum point of this function is then calculated around the point. The size of the surroundings is controlled adaptively. This technique can be seen as a relaxation procedure that tries to avoid too long steps between one iteration and another of the optimization process to favour its convergence.

5.3.4 Stochastic optimization

Stochastic optimization includes all those optimization techniques in which, to any extent, random or pseudo-random number generators are present. The strength of these algorithms lies in the fact that the tested samples can move in the design space more freely than what happens for deterministic optimization. For this reason, they do not suffer from the fact of being able to run into minimal rooms without being able to leave. Deterministic methods, in fact, being based on the calculation of the gradient, are local methods and are not able to leave the basin of attraction of the minimum point within which the point from which the optimization is started is located. Stochastic methods, being able to range quite freely in the design space, can explore it by reducing the probability of stopping at only locally optimal solutions. On the other hand, their nature necessarily implies an optimization process that usually has a much slower speed of convergence towards the optimum point.

Stochastic methods are also able to handle multi-objective optimization problems, which is impossible for a deterministic method. While the result of a single-objective optimization process is an optimal solution, in the case of multi-objective optimization this is not the case. In fact, a multi-objective optimization process results in a set of solutions that are called non-dominated. It is possible to consider an optimization problem with two objective functions f_1 and f_2 (figure 6.1) in which we want to minimize both f_1 and f_2. If we consider two samples x_1 and x_2 such that

$$f_1(x_1) \leq f_1(x_2) \text{ e } f_2(x_1) \leq f_2(x_2) \tag{5.3}$$

it is easy to understand that sample x_1 is better than sample x_2 as both objective functions relative to point x_1 are better than those of point x_2. In this case, sample x_1 is said to dominate sample x_2. In case, for example, it is instead

$$f_1(x_1) \leq f_1(x_2) \text{ e } f_2(x_1) \geq f_2(x_2) \tag{5.4}$$

there is no way to determine which of the two samples is better as one has a better performance concerning one goal, the other has a better performance than the other goal. In this case, the points are said to be mutually not dominated. At the end of an optimization process, all the evaluated samples that are not dominated by any other sample form the Pareto front. The points that belong to the Pareto front are therefore all optimal points. Some will lean more towards one objective function, others towards another, still others will be in the middle, but in any case, they are all points not dominated Figure 5.1. At this point, the designer can choose the preferred configuration among those of Pareto.

Therefore, by implementing suitable algorithms capable of identifying the Pareto front in a set of samples, it is possible to perform multi-objective optimizations.

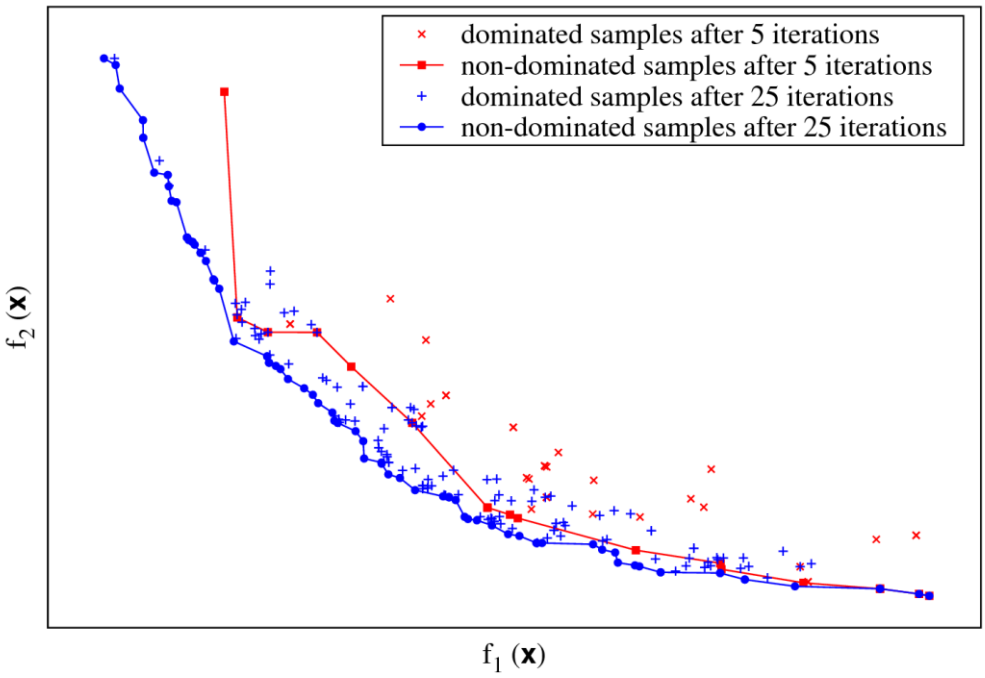

Figure 5.1. Dominated and non-dominated samples [38].

5.3.5 RDA

Although it may seem counterintuitive, it is not always a good idea to position oneself in the design phase on the overall optimal configuration; it is a good idea to check its robustness first. In fact, there may be parameters that cannot be controlled and that cause the real operation of the object of the optimization problem to deviate from the design conditions, significantly affecting its performance. For example, these disturbing factors may be due to:

- small errors in production or uncertainties due to tolerances;
- degradation of the object with use;
- variable operating conditions or in any case different from those of the project;
- other parameters that cannot be controlled.

If the performance of the optimal configuration is strongly affected by uncertainties, it may be a more conservative choice to position oneself on a sub-optimal configuration which, however, is less affected by uncertainties. Such a configuration is called robust. By robustness, it means precisely the ability not to lose too much in terms of performance due to uncertainties. The purpose of the RDA is precisely to evaluate the robustness of the configurations.

Figure 5.2 exemplifies the situation just described.

There are two different approaches to the RDA: the BIT and the RA. Both methods are based on a Montecarlo sampling around the configurations to be tested in terms of robustness.

To do this, of course, it is necessary to define a distribution for each variable affected by noise.

The weakness of these analyzes is that the extent of uncertainty, which can be expected for each variable, is not always known and therefore it is not easy to define a correct dispersion of the data.

MORDO transforms the *p*-objective optimization problem into a *2p* objective problem in which one aims to maximize or minimize the mean μ of the objective functions, and to minimize their standard deviation σ^2. The determination of robustness by biting, therefore, requires the use of multi-objective optimization algorithms (the acronym stands for multi-objective robust design optimization). In the case of $p = 1$ the optimization problem is modified as follows:

$$\begin{aligned} &\underset{\boldsymbol{x}}{\text{minimize}}\, f(\boldsymbol{x}) \\ &\text{subjected to}\, c(\boldsymbol{x}) \leq 0 \end{aligned} \quad \Rightarrow \quad \begin{aligned} &\underset{x}{\text{minimize}}\, \mu(\boldsymbol{x}) \\ &\underset{x}{\text{minimize}}\, \sigma^2(\boldsymbol{x}) \\ &\text{subjected to}\, c(\boldsymbol{x}) \leq 0 \end{aligned} \tag{5.5}$$

The RA (reliability analysis), on the other hand, defines for each objective a performance target below which one does not want to go down. The probability that the tested configurations do not respect the set targets is then estimated through Montecarlo sampling. If this probability is very low (as it is to be hoped that it will be) the Montecarlo sampling is however particularly inefficient. In fact, the coefficient of variation is defined as

$$\nu = \frac{\sigma}{P_f} = \sqrt{\frac{1 - P_f}{nP_f}} \tag{5.6}$$

and identifies an estimate of the error that occurs in the evaluation of uncertainty. P_f stands for the probability of failure and *n* for the number of samples. If we want to have an estimate whose error is within ± 10% ($\nu = 0.1$) and the probability of failure is $P_f = 3 \times 10^{-3}$, we can see that the number of samples to be carried out is at least $n = 33234$.

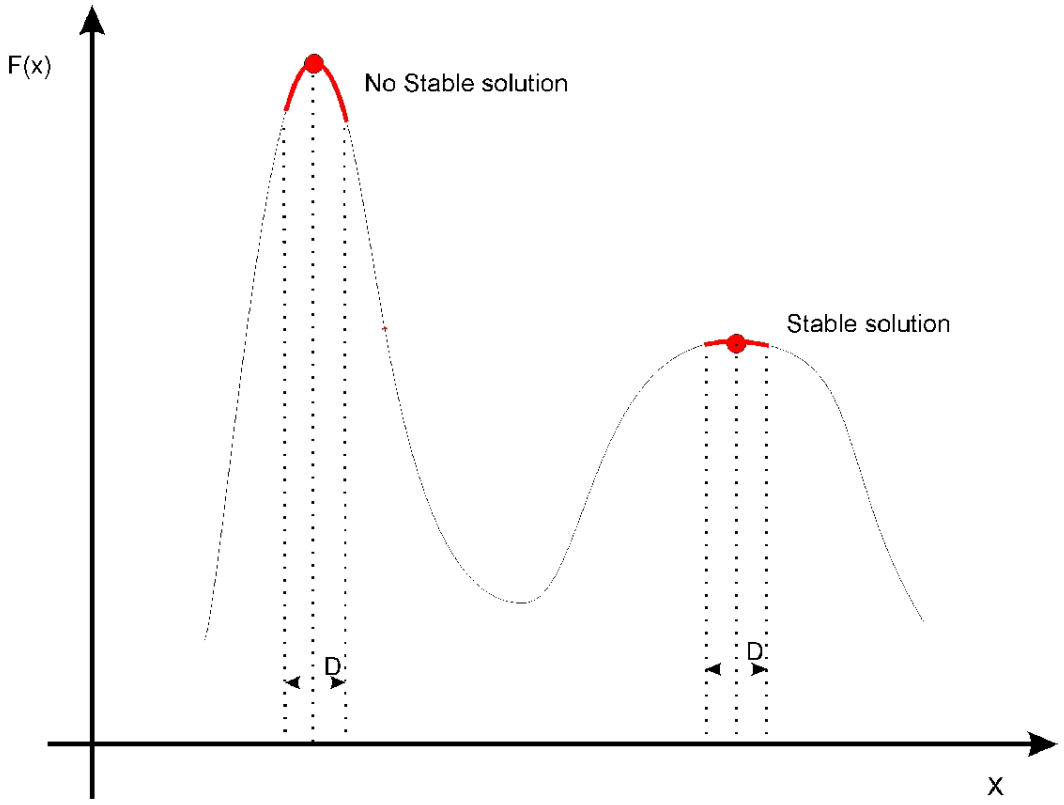

Figure 5.2. The robustness of the configurations [38].

5.1 The optimization process

Several techniques that can be used to solve an optimization problem have been listed. Each of them has its own characteristics, its own strengths and weaknesses. It is important to consider that optimization is never a single-step process in which only a given algorithm is chosen. Depending on the problem, it is good practice to use multiple techniques, although this can be expensive in terms of the number of simulations required to complete the optimization process.

For example, DOE sampling can be used to create a response surface using RSM techniques. A stochastic optimization method can be applied to the resulting metamodel in order to explore the design space, and then refine the optimal solution found through a deterministic optimization method. Finally, the robustness of the solution found can be evaluated employing a reliability analysis (RA). Such an approach defines what can be called a complete optimization process, in which all available techniques are used within the same process.

The individual algorithms that can be chosen at each step of the process may then be more suitable for one type of problem rather than another. Setting up an optimization process is therefore not always immediate and requires knowledge of the various techniques by the designer and experience.

5.2 Structural optimization

In the structural field, there are various *ad hoc* optimization techniques such as:

- topology optimization;
- topometry optimization;
- topography optimization;
- shape optimization;
- size optimization.

When we want to optimize the shape of an object, we generally resort to a parameterization of the shape and to the resolution of the optimization problem that derives from it through the techniques discussed above (shape optimization). However, a parameterization of the shape of an object made in this way does not allow to define its optimal topology.

5.3 Topology optimization

Identifying the optimal distribution of the material in a structure is a topological problem and requires that the problem be set up in the right way [40,41].

Consider a FEM model in which the following parameterization is applied: a variable of the optimization problem x_i corresponds to each element of the model. This varies continuously in the interval (0; 1] and represents the relative density of the element. The problem is solved in a continuous domain for the sake of simplicity since a discrete optimization presents greater difficulties in solving, even if an element whose relative density is not zero or one has no physical significance. The material density of the elements is then made to vary and with some stratagem, it is possible to obtain solutions with a limited number of elements at intermediate density. The main issue in solving an optimization problem of this type is that the number of variables is extremely high and therefore it is not easy to deal with it. For example, the construction of a metamodel is unthinkable, as is also the use of stochastic optimization techniques. or a robustness analysis. Deterministic optimization techniques are applicable but only if the gradients are not estimated using finite differences and are directly available from the FEM calculation. It is precisely the occurrence of this condition that makes topology optimization possible.

The optimization algorithm underlying the process is usually the MMA (method of mobile asymptotes) which is a deterministic gradient optimization algorithm. Each element of the domain is associated with a density and a stiffness function of the value of the variable x_i.

$$\begin{aligned} \rho_i(x_i) &= x_i \rho^* \\ E_i(x_i) &= x_i^p E^* \end{aligned} \tag{5.7}$$

Where ρ^* and E^* are the density and stiffness of the element at a relative density equal to one. Thanks to this choice, the derivative can be easily calculated

$$\frac{\partial E_i(x_i)}{\partial x_i} = p x_i^{p-1} E^* \tag{5.8}$$

Therefore, the choice of a link of this type between variable x_i and stiffness of the element allows the calculation of the gradients of the objective functions for each variable within the FEM analysis, avoiding the use of finite differences. Consider a problem of minimizing the compliance c of a structure (i.e. the external energy of the structure). Let E_i be the stiffness of the element, $\boldsymbol{K}_i\,(x_i) = x_i^p \boldsymbol{K}_i^*$ is the stiffness matrix of the element, $\boldsymbol{K} = \Sigma_i\, \boldsymbol{K}_i\,(x_i)$ is the stiffness matrix of the structure, $\boldsymbol{f}$ the vector of the applied forces and $\boldsymbol{u}$ the vector of the displacements. The considered optimization problem can be written as

$$\begin{aligned} &\underset{u,x_i}{\text{minimize}}\ \boldsymbol{f}^T\boldsymbol{u} \\ &\text{subject to}\ \boldsymbol{K}\boldsymbol{u} = \boldsymbol{f} \end{aligned} \tag{5.9}$$

where the constraint applied indicates the satisfaction of the equilibrium. Additional constraints such as the relative mass of the structure are usually applied alongside this to make sense of the optimization and prevent the solution from degenerating. By applying the adjoint method for calculating the gradient, compliance c can be rewritten as

$$c(x_i) = \boldsymbol{f}^T\boldsymbol{u} = \boldsymbol{f}^T\boldsymbol{u} - \tilde{\boldsymbol{u}}^T(\boldsymbol{K}\boldsymbol{u} - \boldsymbol{f}) \tag{5.10}$$

By deriving we obtain

$$\frac{\partial \mathrm{c}(x_i)}{\partial x_i} = -\boldsymbol{u}^T \frac{\partial}{\partial x_i}\left(\sum_j x_j^p \boldsymbol{K}_j^*\right)\boldsymbol{u} = -p x_i^{p-1} \boldsymbol{u}^T \boldsymbol{K}_j^* \boldsymbol{u} \tag{5.11}$$

In this way, we see how, in the case of compliance minimization, the derivatives of the objective function concerning all the variables of the problem are calculated directly within a single FEM simulation. Similar reasoning applies to other types of objective function.

Two parameters govern the behaviour of the topological solver: the penalty parameter p and the sensitivity filter r. The effect of these parameters is null if they are set equal to one, while it becomes more and more important as the value of the parameter grows. The role of p is to make intermediate density elements disadvantageous. In fact, for example, for $p = 3$ an element with relative density $x_i = 0.5$ weighs relatively much ($0.5\rho^*$) if compared to the contribution it gives to the stiffness of the structure ($0.5^3E^* = 0.125E^*$). By applying a value of $p = 1$, in fact, this effect disappears and the optimization result is given by a cloud of intermediate density elements. As p grows up, the solutions become more and more "black and white". However, a phenomenon known as

checkerboarding [42] is established for which the solver moves towards checkerboard configurations in which low and high-density elements are alternately next to each other. In fact, these configurations give the structure a spurious stiffness, which has no physical significance. The purpose of the sensitivity filter is precisely to avoid checkerboarding. The filter acts by mediating, at each iteration, the density of each element with those of the neighbouring elements within a range of *r* times the average size of the element. In this way, the solver forces the final configuration to create beam-like structures with a diameter equal to at least *2r* times the average size of the elements. The effect of the two parameters on the result of topological optimization is exemplified in 5.3 in which the result is represented in the case of a two-dimensional bridge-like structure loaded in the middle and hinged at the ends.

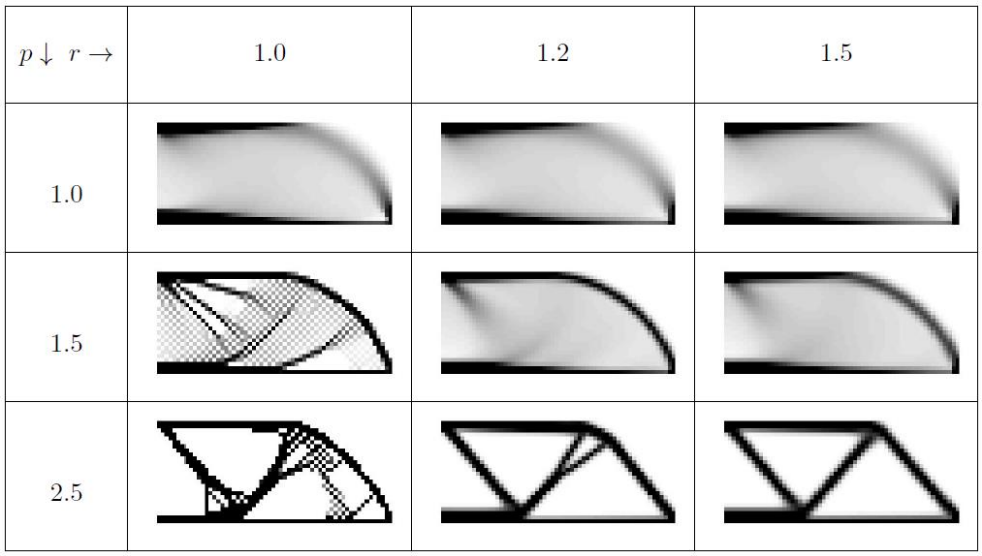

Figure 5.3. The effect of the *p* and *r* parameters [38].

5.3.1 Seize of mesh

The optimization results are always linked to the density of the mesh and therefore to its size. A different mesh density can lead to a different topological distribution.

Figure 5.4 shows the solution for a model of 600 elements. The same problem discretized with 5400 elements yields a much more detailed structure. Ideally, a refinement of the mesh should lead to a more defined model of the same optimal structure and a better description of its boundaries, not a more detailed and qualitatively different structure [43].

This problem can be divided into two categories: the need to refine the mesh to arrive at a solution and the problem of non-uniqueness of the result. In the first case, the refinement leads to a better value of the objective function. In the second case, a finer structure is always possible, but not necessary.

The non-uniqueness of the solution cannot be eliminated, but by introducing manufacturing constraints, such as a minimum size of the rib, a more stable result can be achieved.

Sigmund et al. [42] introduced three methods to solve this problem.

In the first procedure, the value of the perimeter is constrained, which for a discretized structure could be formulated as

$$P = \sum_{k=1}^{K} l_k \left(\sqrt{\left(\rho_i - \rho_j\right)^2 + \varepsilon^2} - \varepsilon\right) \tag{5.12}$$

where l_k is the length of the interface between two adjacent elements i and j. The parameter ε is a small positive number, which guarantees the differentiability of the perimeter.

A second method is to introduce a filter, which forces the generation of ribs with a characteristic dimension, such as thickness, greater than a value declared by the user. This system has the drawback of introducing elements of intermediate density.

The last way to stem the problem of the dependence of the solution on the mesh constrains the local gradient of the density slope of the elements. The formulation of this technique for a bidimensional n_x for n_y mesh is described as follows:

$$\begin{aligned} \left|\rho_{j+1,k} - \rho_{jk}\right| &\leq s \cdot h; \;\; j = 1, \dots, n_x - 1; \;\; k = 1, \dots, n_y \\ \left|\rho_{j,k+1} - \rho_{jk}\right| &\leq s \cdot h; \;\; j = 1, \dots, n_x; \;\; k = 1, \dots, n_y - 1 \end{aligned} \tag{5.13}$$

where the subscripts j and k identify the position of the element in the coordinate system, s is the upper limit of the density slope and h is the known mesh size; $s \cdot h$ should be less than 1/3.

Figure 5.4. A different mesh density can lead to a different topological distribution [43].

5.3.2 Manufacturing constraints

It can be very useful to force the solver to return solutions that are easily achievable with the most common subtractive technologies, and the design of a symmetrical component may also be required [44].

Zuo et al. [45] have proposed an analytical formulation for these constraints.

The production constraint can be expressed as follows:

$$\sum_{k=1}^{K1-1} |\left(x_{ij}^{e}\right)_{k+1} - \left(x_{ij}^{e}\right)_{k}|_{P} \leq \delta;\ i = 1, \dots, n_x;\ \ j = 1, \dots, n_y \tag{5.14}$$

where $(x^e_{ij})_k$ is the density of the k-th element positioned at (i, j) in the projection plane P, $K1$ is the number of elements in (i, j), n_x and n_y are the number of elements respectively in the x and y direction in the projection plane and δ is a small positive number.
The symmetry constraint can be formalized as follows:

$$\sum_{k=1}^{K2} |\left(x_{ij}^{e}\right)_{k} - \left(x_{ij}^{e}\right)_{-k}|_{M} \leq \delta;\ i = 1, \dots, n_x;\ \ j = 1, \dots, n_y \tag{5.15}$$

where $(x^e_{ij})_{-k}$ is the density of the symmetric element $(x^e_{ij})_k$ concerning the plane M, which in this formulation is the plane xy, and $K2$ is the number of elements positioned in (i, j).

5.1 Other types of structural optimization

The other types of structural optimization mentioned at the beginning of the section, except for shape optimization, are conceptually very similar to topological optimization.

Topometric optimization differs in that the variables of the problem are no longer given by the relative densities of the elements, but by the thicknesses of the shell elements. Same thing for size optimization in which, however, the thicknesses are not varied element by element, but component by component.

Topographic optimization considers the offsets of the shell elements from the median plane of the plate as variables, in this way, with appropriate precautions, it is possible to simulate the effect of adding ribs on a plate. Note how topological optimization can be applied to both three-dimensional and shell-type meshes, the concept of density, in fact, is valid for both types of elements. The topometric, topographic and size optimizations, on the other hand, are only applicable to shell-type elements.

On the other hand, shape optimization is a different thing. All that is needed is a parameterization of the shape of the object which can be done, for example, using Bézier curves or through the use of morphing procedures applied to the structure. The number of variables is therefore relatively low and generally, the problem can be solved by classical optimization procedures.

Chapter 6: FEM analysis of the aluminium piston

6.1 Introduction

The analysis developed in this work involves the use of Finite Element software for structural calculation and topological optimization and CAD programs for the design of the new steel piston.

The work began with a reverse engineering operation that involved the component made by Ducati Motorholdig S.p.A., this work made it possible to reproduce the geometry of the piece in a three-dimensional file necessary for subsequent analyzes. The software used in this phase is the SolidWorks2020 solid modeller.

The component used was then meshed with Altair HyperMesh2017 commercial software.

For the subsequent thermo-mechanical analyzes, the "MSC Marc Mentat" 2014.2 software was used.

6.2 3D mesh

The first step in creating the mesh is to import the files into the "Hypermesh" software from the solid modeller. The .iges format was used to transmit the information inherent to the geometry of the component (weighing 73 grams), this structure was used as the basis for the creation of the 2D mesh, a sort of skin on which the volume mesh is then created. Only one half of the system will be analyzed taking advantage of its symmetry plane. The first step is to divide the imported geometry into different sets, in order to work with less extensive and therefore more easily manageable geometries. Particular attention is given to the size of the 2D elements. A too coarse mesh results in a slim model and a short calculation time, but also a rather approximate analysis especially in the points with a high tension gradient; on the contrary, with a too fine mesh could be unmanageable by the computer. For this reason, a unitary size has been attributed to all the elements by adopting an R-trias mesh. Having a high quality of the 2D mesh is essential to obtain a good 3D mesh, so the shape and angles of the elements created were checked (in this specific case, the warpage, aspect and skew parameters) [46–48].

At this point it was possible to create the 3D mesh, choosing a CFD-type mesh, thanks to which it is possible to create a small thickness, called a boundary layer, consisting of prismatic 3D elements based on those of the skin mesh and a core made entirely of from tetragonal elements. Figure 6.1 clearly shows the boundary layer (in purple) and the core (in orange) just described. This meshing methodology guarantees the presence of at least 3 elements along the thickness. Therefore, for any thickness considered there will be at least 3 stress values, which are essential to try to be able to grasp the flexural butterfly profile and have results that are minimally representative of reality.

The procedure described above was also carried out for the connecting rod, Figure 6.2, only the part in contact with the pin is discretized in order not to make the calculation unnecessarily heavy. In particular, the part of the connecting rod with mass corresponding to the alternating mass of the same was considered, which is essential for properly evaluating the lateral thrust exerted by the piston on the cylinder liner. Also in this case a CDF type mesh has been created.

To discretize the pin, hexa8 elements were chosen (hexagonal elements with 6 knots). A longitudinal section of this component was made with quadrangular elements, then the 3D elements were obtained by revolution around the axis of the pin, Figure 6.3.

The files were then imported into Marc thanks to the conversion into .bdf format, compatible with both programs.

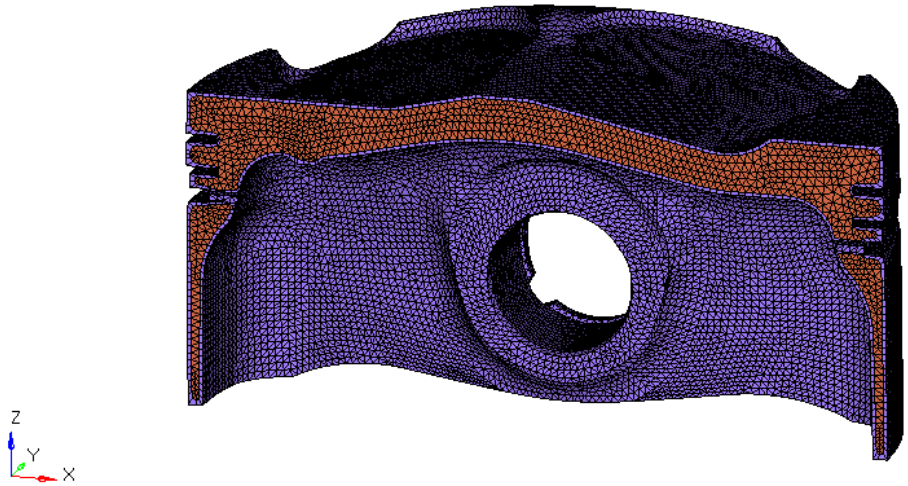

Figure 6.1. The mesh of the piston.

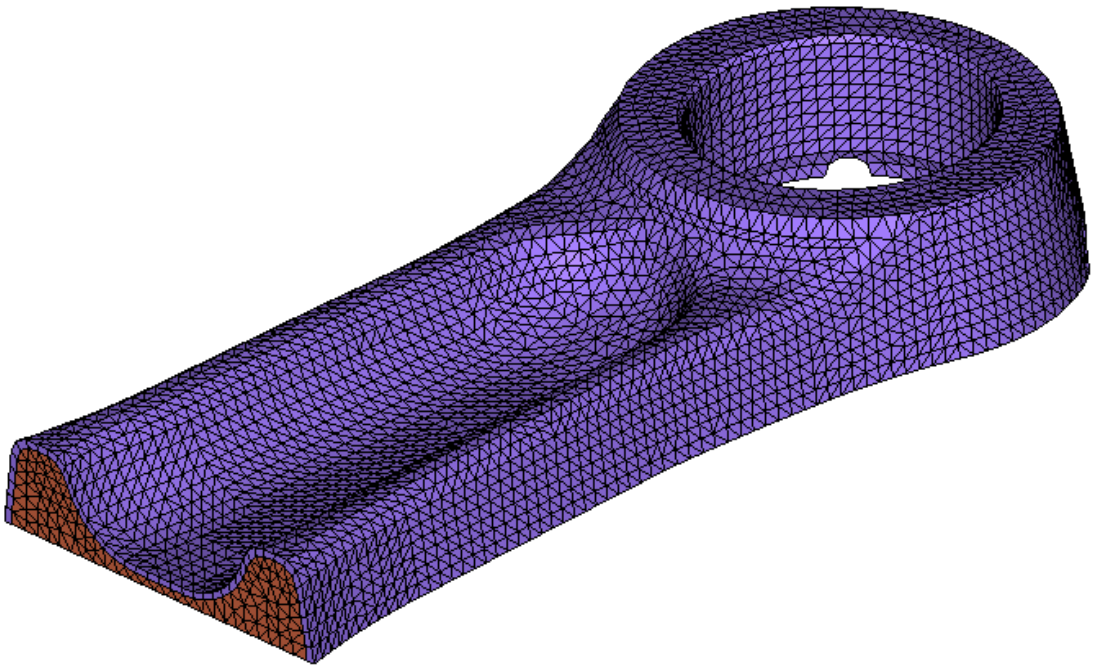

Figure 6.2. The mesh of the connecting rod.

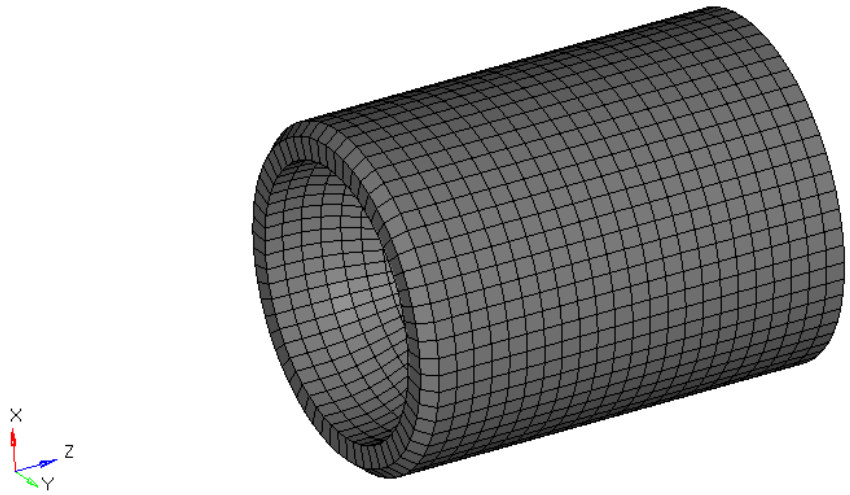

Figure 6.3. The mesh of the gudgeon pin.

6.1 Thermal analysis of the crank mechanism

A thermal analysis of the original assembly was performed which includes piston, pin and the upper part of the connecting rod. The full speed of 11000 rpm was considered, which corresponds to the speed at which the maximum pressure in the chamber is found.

The materials used, with their respective characteristics, are described in table 6.1.

Table 6.1. The materials employed.

Component	Material	Thermal conductivity
Piston	AlSi9Cu3(Fe)	0.115 W/(mm K)
Gudgeon Pin	Generic steel	0.039 W/(mm K)
Conrod	Generic steel	0.039 W/(mm K)

The contacts have been set and a contact conductivity of 0.1 W/(mm^{2}K) has been entered, this value may seem high, but it must be considered that high contact pressures arise due to the loads to which the crank mechanism is subjected. Piston and connecting rod were considered discrete, while the piston pin was declared analytical [49].

A Fortran subroutine has been inserted to obtain, at the end of the calculation and with some operations, a .bin file containing information on the temperatures of the integration points.

The specific settings and their results are now explained.

6.1.1 Thermal boundary conditions

An initial temperature of 20 ° C has been entered.

The incoming fluxes on the two sides of the skirt and on the first pressure ring groove have been set, the values in table 6.2 are shown.

Table 6.2. Face flux boundary conditions.

Application area	Value
Skirt (intake side)	0.2076 W/(mm^{2}K)
Skirt (exhaust side)	0.1355 W/(mm^{2}K)
First compression ring	0.0350 W/(mm^{2}K)

The other boundary conditions are of the thermal face film type, table 6.3 shows the settings used.

Table 6.3. Face film boundary conditions.

Application area	HTC [W/ mm^2°C]	T [°C]
Piston top	0.000667	1014
Piston crown (lateral)	0.000175	90
First compression ring up	0.002300	90
First compression ring down	0.005798	90
Second compression ring up	0.003574	90
Second compression ring down	0.003977	90
Oil ring up	0.002966	90
Oil ring down	0.002775	90
Skirt	0.008478	90
Oil jet	0.005320	120
Splashing oil (internal)	0.001856	120
Splashing oil (external)	0.000928	120
Splashing oil (rod and pin)	0.000773	120

6.1.2 Results of the thermal analysis

Figure 6.4 shows the thermal field of the crank mechanism calculated by the software. It can be seen how the lowest point is recorded on the piston crown, while the lowest temperature is reached by the connecting rod, which is abundantly wetted by the splashing oil. Figure 6.5 shows the piston in detail. The hottest point reaches and slightly exceeds 300° C. This is the threshold beyond which the mechanical properties of aluminium drop drastically and the aluminium used for the pistons is no exception. However, it should be noted that this area is limited to massive areas, where the exchange area with hot gases is large, but the exchange area with the refrigerant liquid is few.

Fortunately, these areas are not subject to high voltages, as the mantle could be, which fortunately is one of the coldest areas of the piston.

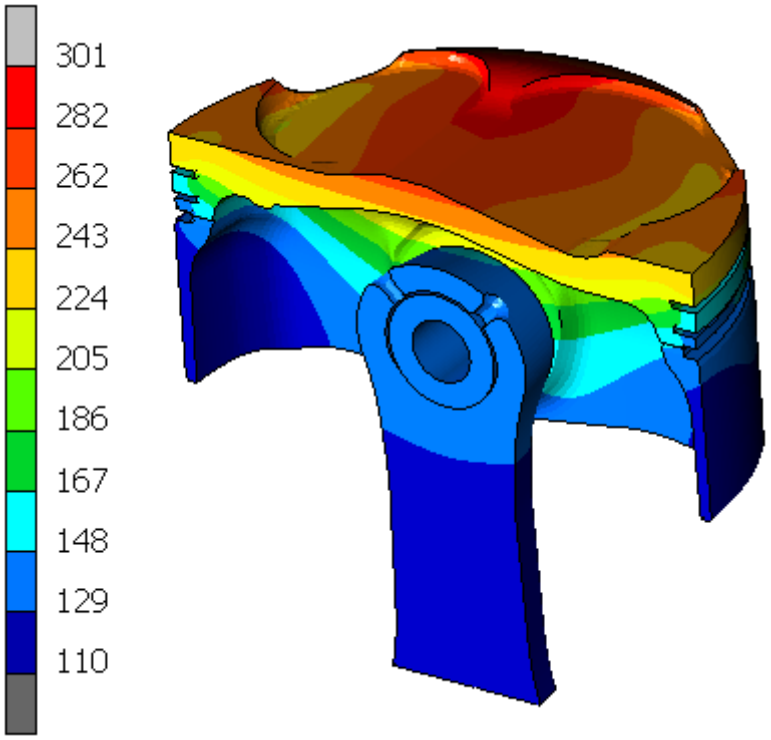

Figure 6.4. Temperature contour plot of the crank mechanism [°C].

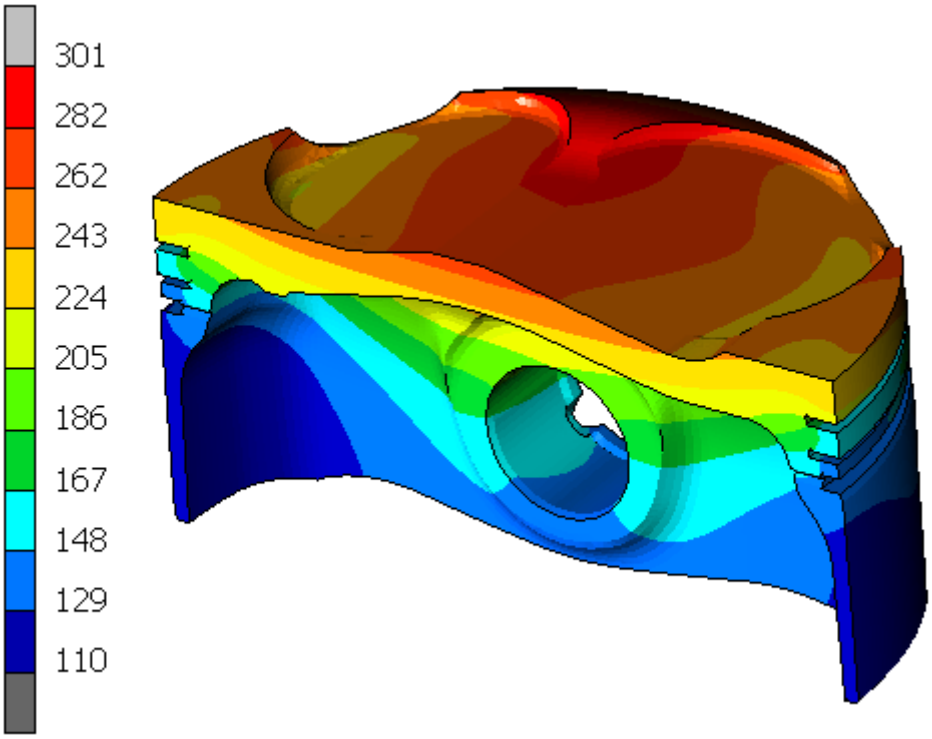

Figure 6.5. Temperature contour plot of the piston [°C].

6.1 Thermo-mechanical analysis of the crank mechanism

Two types of analyses were performed to achieve two different purposes. First, a thermal-structural calculation of the piston alone has been performed to evaluate in detail the deformation of the skirt and crown. This analysis will be used to obtain a first attempt profile to be assigned to the piston that will be designed in steel. Secondly, thermo-mechanical simulations of the entire crank mechanism have been performed with two purposes: to structurally verify the original aluminium piston and to define local stiffness targets and constraints that the new steel piston must satisfy.

The materials used, with their respective characteristics, are described in table 6.4.

Table 6.4. Materials employed.

Component	Material	Density [t/mm^3]	Young Modulus [MPa]	Poisson's ratio	Thermal expansion coefficient [°C^{-1}]
Piston	AlSi9Cu3(Fe)	2.68e-9	73575	0.3	2.1e-5
Gudgeon pin	Generic steel	7.8e-9	210000	0.3	1.1e-5
Conrod	Genetic steel	7.8e-9	210000	0.3	1.1e-5

The piston-pin and pin-connecting rod touching (i.e. single-sided) contacts have been set, indicating a contact tolerance of 0.01 mm and a friction coefficient of 0.2 for both cases. Even if the contacts are obviously lubricated, a very high friction coefficient

has been chosen which does not affect the goodness of the results in the static calculations that have been performed, but at the same time greatly speeds up the calculation time and fix the position of the pin. Piston and connecting rod were considered discrete, while the piston pin was declared analytical.

A Fortran subroutine has been inserted to enter the information regarding the temperatures of the integration points contained in the .bin file.

The specific settings and their results are now explained.

6.1.1 Analysis of the profile of the piston

For this analysis, only the piston has been considered, because the effects of the piston pin and connecting rod on the shape of the hot piston profile are considered negligible.

This calculation requires very simple settings.

The piston is constrained in space by exploiting its plane of symmetry, two vertical supports are then added to the base of the skirt and finally, a horizontal support is added to a node that belongs to the plane passing through the axis of the pin and the axis of the piston. and orthogonal to the plane of symmetry, Figure 6.6.

Finally, the previously calculated thermal field is added through a specific solver function called Map Temperature.

Figure 6.7 and 6.8 show the simulation results. The piston deformation has been amplified by 10 times and the undeformed piston profile is represented by a thin pink line. It is easy to see how the truncated conical shape of the crown is deformed under the effect of the thermal field, while to appreciate the deformation of the mantle it is necessary to process the output through a spreadsheet. The contour plot of Figure 6.7 shows the displacements in the x-direction, the legend has been filtered in a narrow neighbourhood of zero to highlight the fact that the piston has not rotated during deformation and it is, therefore, possible to analyze the output more simply. In fact, the rotation linked to the deformation corresponds to a rigid motion of the piston which will rotate accordingly to better adapt to contact with the cylinder, this rotation should be appropriately considered in the processing of the results. Figure 6.8 shows the same results, but with an unfiltered displacement field, it is evident that the deformation is sufficiently symmetrical and therefore the piston will behave in the same way in the two banks of the L-twin engine of the Panigale 959.

Figure 6.8 shows in detail the difference between the undeformed and the deformed profile. In particular, it shows the average of the deformation of the profile considering both sides of the skirt. It can be seen how the truncated cone shape of the crown is partially recovered under thermal stresses. While the barrel shape of the skirt opens, it still offers only one ideal contact point with the barrel. These deformed profile details will be used later to derive a first attempt profile of the steel piston that will be designed.

Figures 6.9 and 6.10 show the stress field according to von Mises, it can be seen how the stress state induced by the thermal gradient almost exclusively affects the land zones for the segments, where the stiffness of the zones changes abruptly in a restricted zone. Fortunately, the mechanical loads added to the thermal ones do not stress these areas.

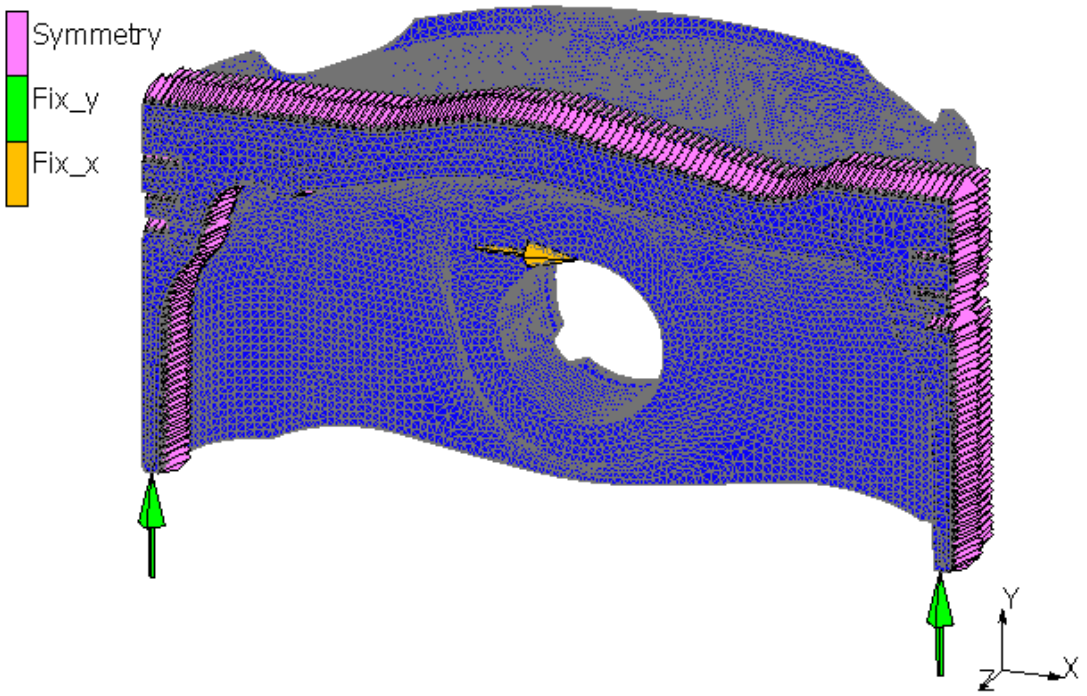

Figure 6.6. The boundary conditions.

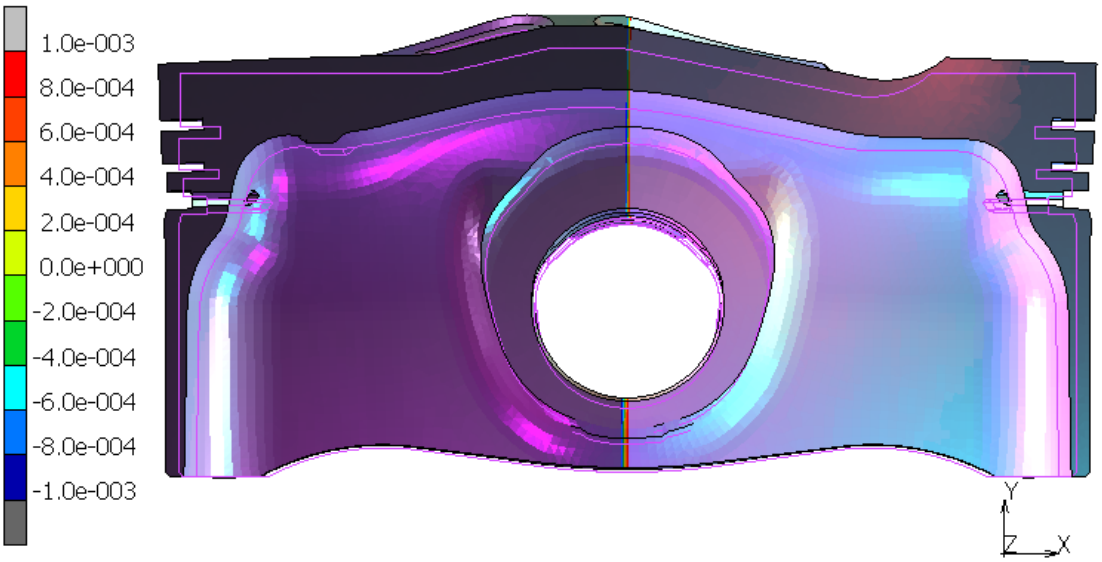

Figure 6.7. The deformed piston [mm].

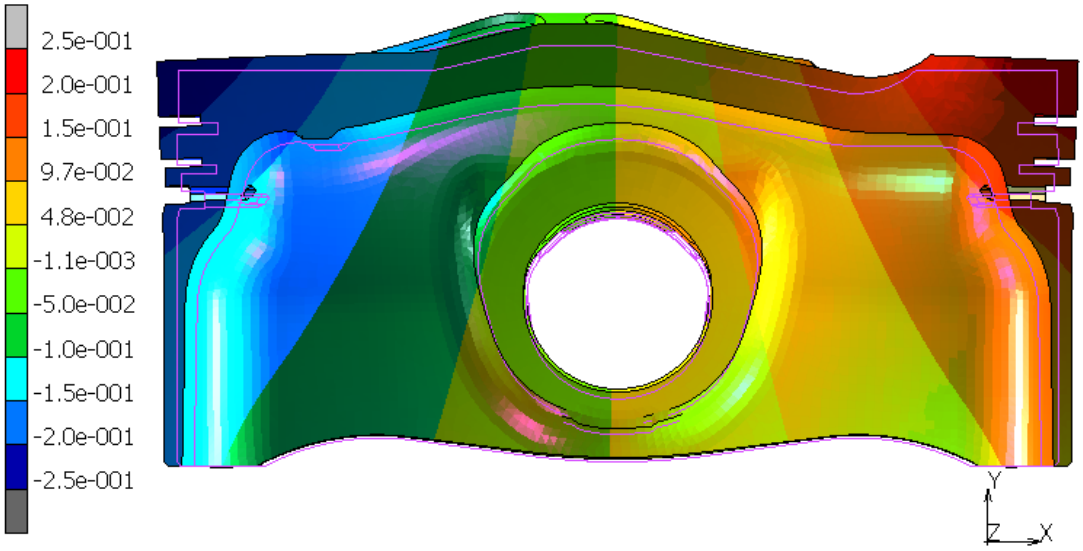

Figure 6.8. The deformed piston [mm].

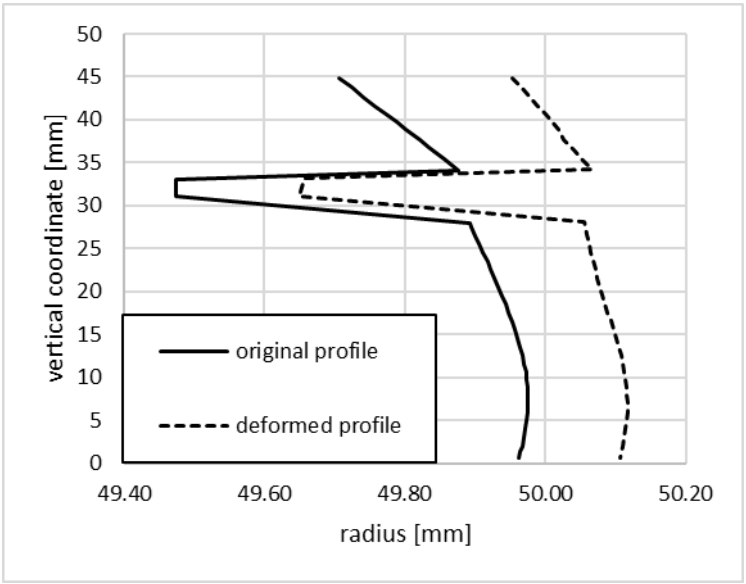

Figure 6.9. Comparison of the cold and hot piston profile.

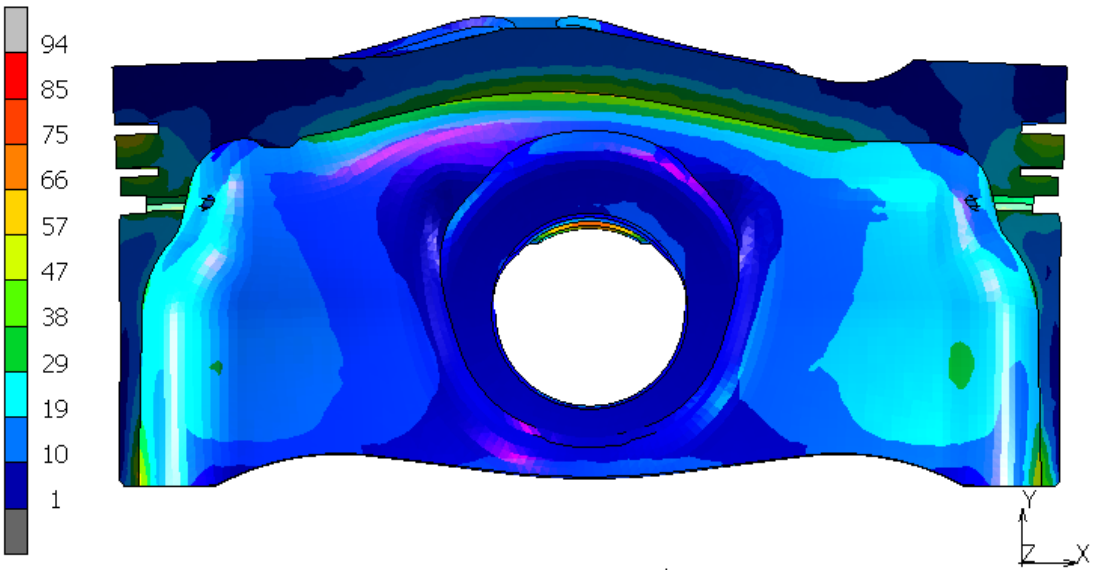

Figure 6.10. Von Mises stress contour plot [MPa].

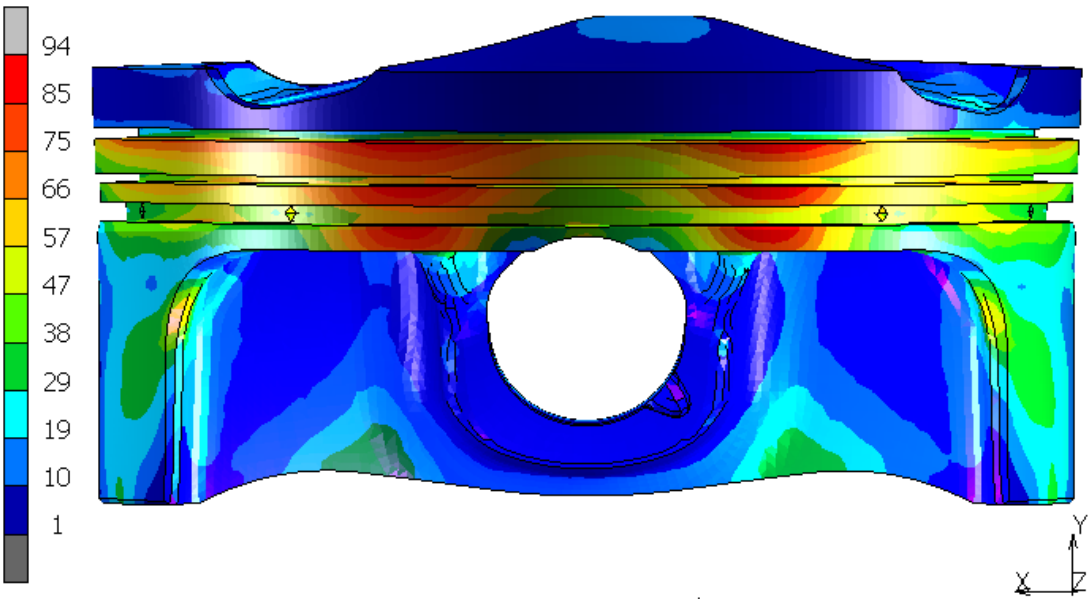

Figure 6.11. Von Mises stress contour plot [MPa].

6.1.2 Structural thermo-mechanical analysis of the crank mechanism

A thermo-mechanical analysis of the assembly has been performed which includes piston, pin and the reciprocating part of the connecting rod.

Four cases have been considered:

- combustion, that is the instant in which the chamber pressure reaches its maximum value;
- top dead centre at the beginning of the induction phase;
- maximum lateral piston thrust force;
- maximum lateral piston anithrust force.

These instants have been identified through a spreadsheet, these four different conditions influence the reciprocal position of the components involved and the loads that are generated. For each of these positions, a FEM analysis was performed at 11000 rpm, the case of maximum power.

The materials employed and their properties are shown in the previous Table 6.4.

The piston-pin and pin-connecting rod touching (single-sided) contacts have been set, indicating a contact tolerance of 0.1 mm for both cases. Piston and connecting rod were considered discrete, while the piston pin was declared analytical.

A Fortran subroutine has been inserted to enter the information regarding the temperatures of the integration points contained in the .bin file.

The specific settings and their results are now explained.

6.1.2.1 Cases of the top dead centre during combustion and at the beginning of the induction phase

An initial temperature of 20° C has been set for each element of the system.

Fixed displacement boundary conditions have been added. The z-direction displacements of the nodes lying on the xy symmetry plane of the entire crank mechanism have been prevented (Figure 6.12). The nodes lying on the cutting plane of the connecting rod have been constrained not to move in the y-direction (Figure 6.13). To block the displacements in the x-direction, the central node of the section just examined has been constrained, Figure 6.14. The pressure has been applied to the top, lateral crown and the top of the first ring groove, Figure 6.15. Finally, the acceleration of the reciprocating masses has been imposed, obtained with the aid of a spreadsheet for the whole model. The values of these loads, summarized in Table 6.5, were applied gradually in 4 increments according to a ramp trend to facilitate the convergence of the calculation.

Table 6.5. Values of pressure and acceleration.

Loadcase	Pressure [MPa]	Acceleration [mm/s^2]
Combustion	9.10	4.88e^7
PMSI	0.69	5.12e^7

In addition, a general state variable boundary condition has been created for the whole computational domain to apply the temperature values of the .bin file.

It must be specified that in the case of TDS (top dead centre) during combustion the maximum pressure value recorded in the chamber has been applied even if this value occurs after a few engine degrees the TDC. In this way, it is not necessary to tilt the rod and the resulting numerical complexities of the model. However, it was necessary to insert a high coefficient of friction in the contacts between the piston, piston pin and connecting rod to prevent the piston and piston pin from rotating and making the system labile.

Figure 6.16 and 6.17 show the results of the simulations in terms of von Mises stresses. In the case of TDC during combustion and at the beginning of the induction phase, the stresses are lower than 125 MPa and 150 MPa respectively, except for some localized contact areas with the pin. It should be noted that these stress values are not particularly critical because they occur in low-temperature areas of the piston, where the properties of aluminium are high enough to withstand the applied loads.

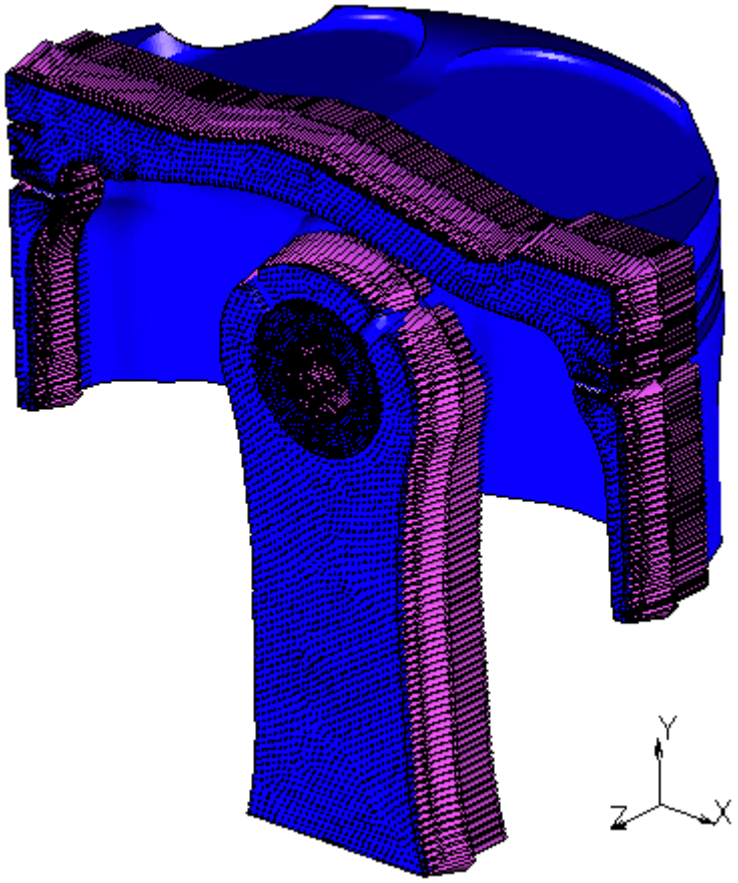

Figure 6.12. Symmetry boundary condition.

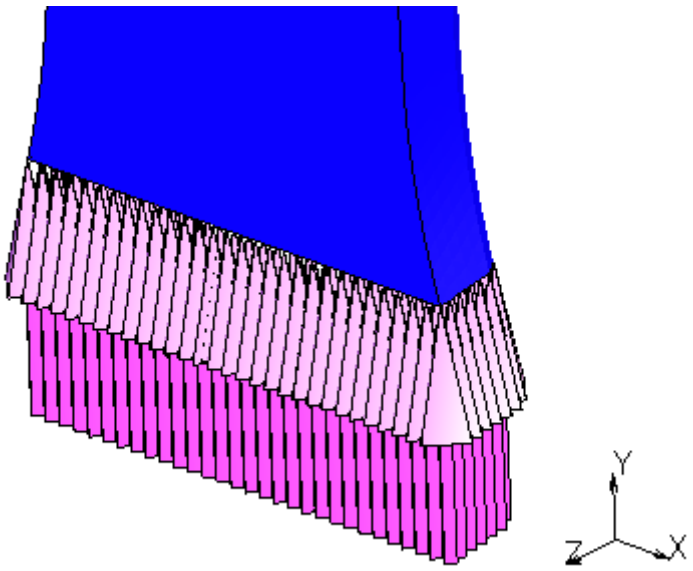

Figure 6.13. Fixed displacement boundary condition.

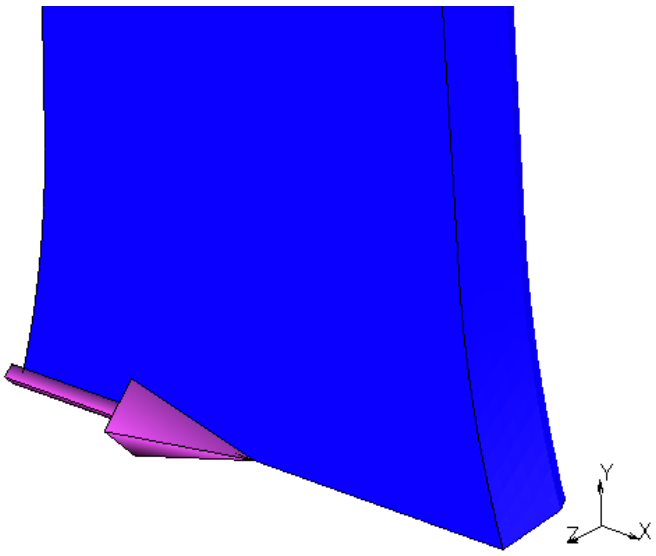

Figure 6.14. Fixed dispalcement boundary condition.

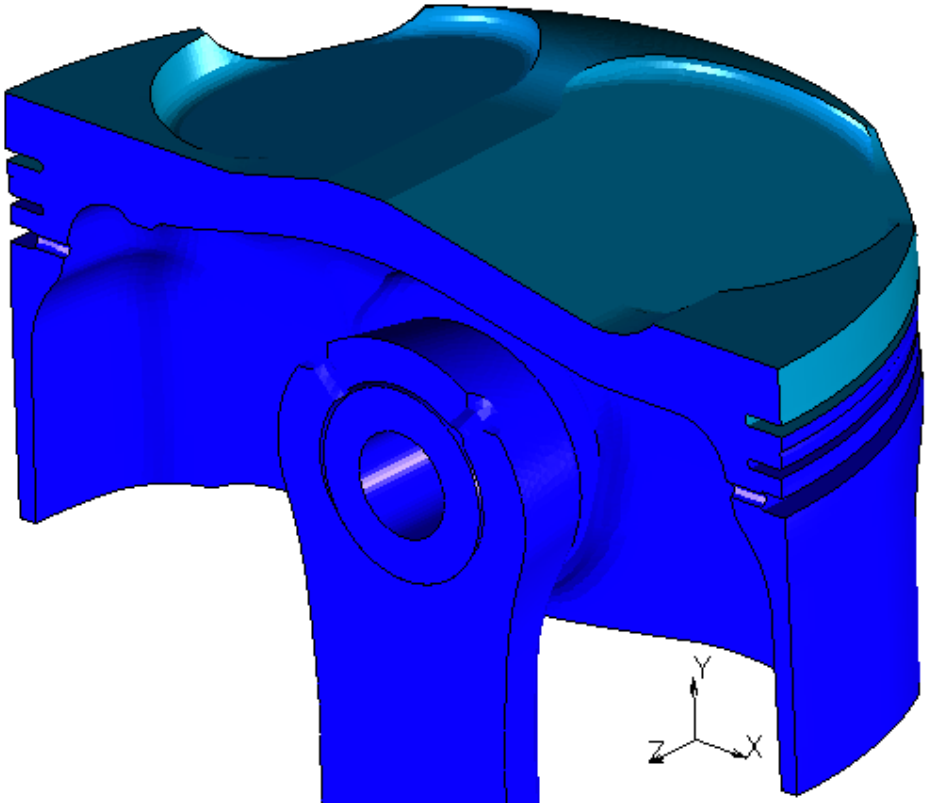

Figure 6.15. Pressure boundary condition.

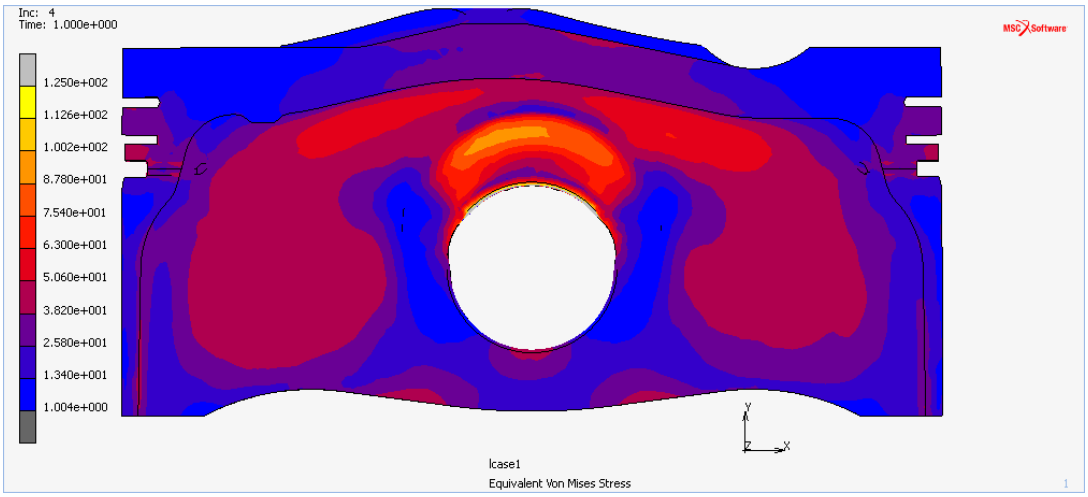

Figure 6.16. TDC during combustion, von Mises contour plot [MPa].

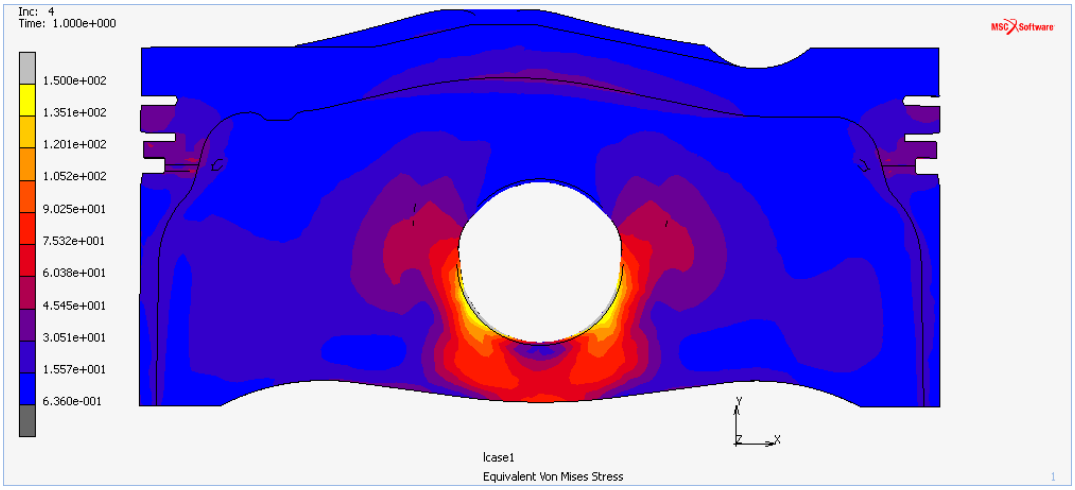

Figure 6.17.TDC at the beginning of the induction phase, von Mises contour plot [MPa].

6.1.2.2 Cases of maximum piston thrust and counterthrust force

In cases of lateral thrust and counter-thrust force, a cylindrical surface has been inserted to simulate the contact between piston and cylinder liner. The diameter of this surface has been suitably modified to take into account the thermal expansion caused by a uniform temperature range of 120° C. Furthermore, the connecting rod has been properly tilted by an angle φ of 14.52° (which corresponds to a crank angle of 472°) in the first case, Figure 6.18(a), and by -13.4° (which corresponds to an engine angle of 239°) in the second one, Figure 6.18(b). The underside of the connecting rod was modelled with a series of RBE2s having the master node in the centre of the head, Figure 6.18(c). The calculation setting is completely equivalent to that of the previous cases. An initial temperature of 20° C has been set. The symmetry boundary conditions have been inserted preventing the displacements in the z-direction of the nodes lying on the xy symmetry plane of the entire frame. The nodes lying on the cutting plane of the connecting rod have been constrained to the master node of RBE2 (figure 6.18(c)), this node can only rotate around a z-direction axis.

Table 6.6 shows the applied pressure and alternate acceleration values (directed downwards), which have been applied gradually in 4 increments according to a ramp trend to facilitate the convergence of the calculation.

Table 6.6. Values of pressure and acceleration.

Loadcase	Pressure [MPa]	Acceleration [mm/s^2]
Thrust	0.80	-2.30e^7
Counterthrust	1.61	-2.59e^7

In addition, also in this case, the thermal field has been applied to the components.

Figures 6.19 and 6.20 show the results of the simulations in terms of von Mises stresses. In the instants of thrust and counterthrust force, the stresses are lower than 140 MPa and 120 MPa respectively. Also in these cases, stress peaks are recorded in areas with temperatures below 130°C. In fact, the lower part of the skirt is the coldest area of

the piston: it offers a large exchange surface for the cooling oil and exchanges heat with water, encountering little resistance.

It is necessary to underline that the loads applied to the crank mechanism in this static analysis have been obtained simply using the laws of motion and a spreadsheet. In the reality, dynamic phenomena also arise [50–55] which amplify the loads affecting the crank mechanism in general and the piston in particular. It is possible to use multi-body software to quantify the loads also considering the dynamic effects [56].

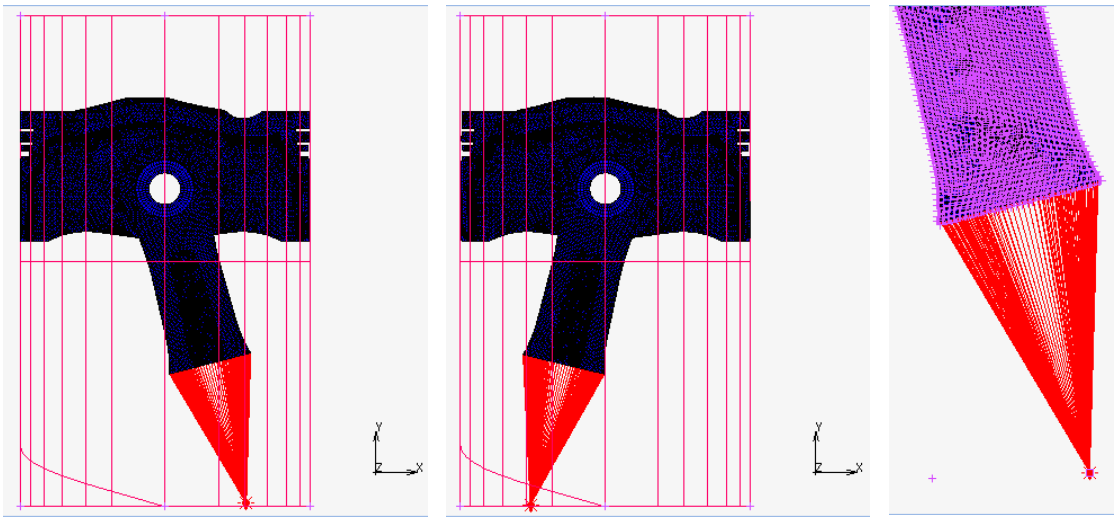

(a) (b) (c)

Figure 6.18. Maximum thrust and antithrust force cases.

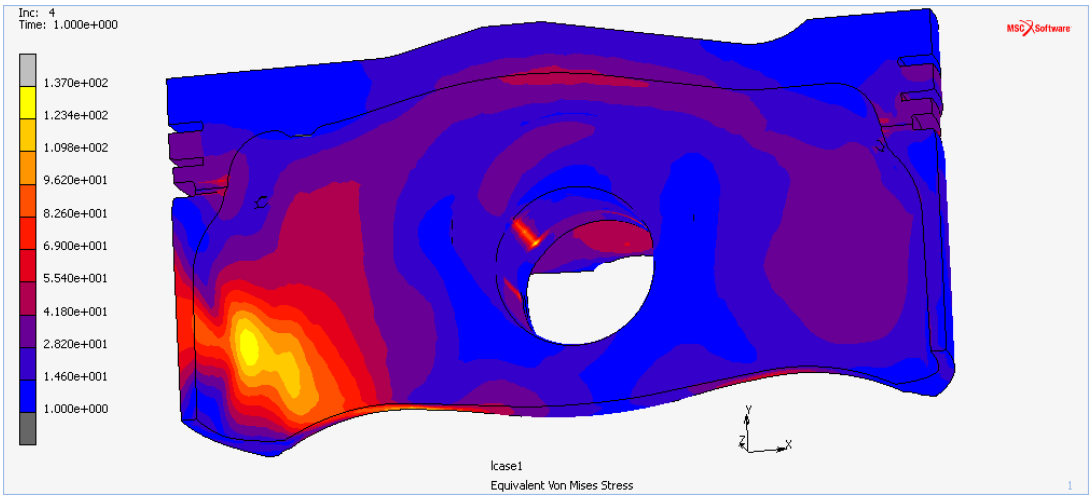

Figure 6.19. Maximum thrust force, von Mises contour plot [MPa].

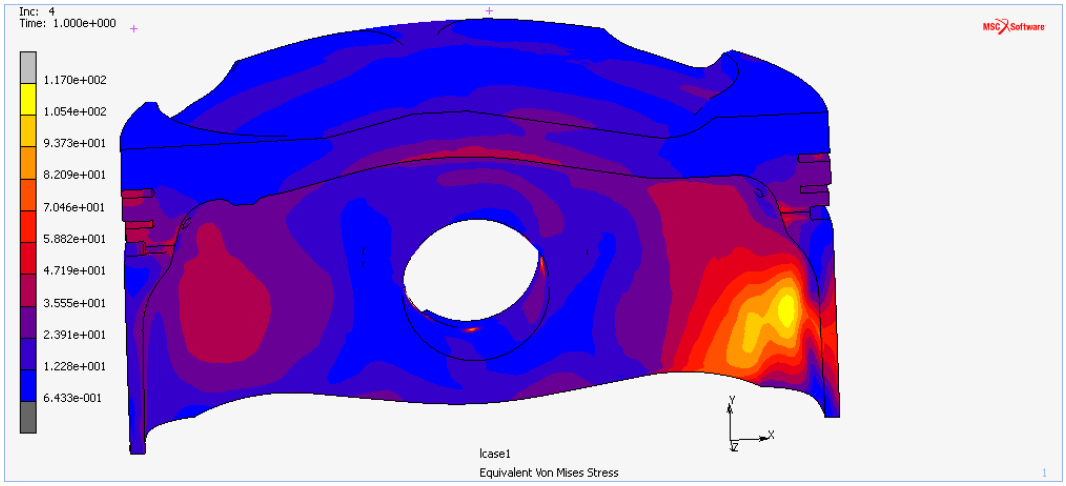

Figure 6.20. Maximum antithrust force, von Mises contour plot [MPa].

Chapter 7: Topology Optimization

7.1 Introduction

The piston is the main alternating mass in an internal combustion engine crank mechanism. Therefore, the minimization of piston mass is fundamental to contain inertial loadings. Because of its low density, aluminium is the most common material employed for piston manufacturing. Unfortunately, aluminium exhibits low mechanical properties, which further decrease when it is exposed to high temperatures [17,57–61]. In this scenario, aluminium may not represent the best choice and steel may be considered as a valid alternative for piston manufacturing [62–64]. Schreer et al. [10] analysed the consequences of employing a steel piston: a better kinematic behaviour of the crank mechanism, a comparable weight, more homogeneous surface temperatures, a lower dead volume at the top land, a lower blow-by and a more efficient combustion process are the main advantages registered. Nevertheless, traditional manufacturing technologies cannot be employed when steel is considered as the material for pistons. In fact, in order to obtain components with a comparable weight when compared with those produced by aluminium, the thickness of the different parts of a steel piston has to be reduced up to one millimetre. Additive Manufacturing represents a promising technology to obtain thin features. Bendsøe and Kikuchi [41] related optimization techniques to structural design, noting that the resulting complex shapes could be easily reproduced by Additive Manufacturing. Du and Tao [65] and Zhao et al. [66] adopted the topology optimization for an engine piston lightening, but they used the results only to understand which parts of the piston were redundant, without ascribing any focused design validity. Brackett et al. [67] analysed the main challenges and opportunities for topology optimization for Additive Manufacturing. The importance of mesh resolution, manufacturing constraints and the post-processing have been highlighted.

In this thesis, topology optimization analyses are coupled with Finite Element analyses in order to reach an optimum steel piston configuration. In particular, the minimum mass of the component is considered as the objective function and the displacements of specific nodes on the piston skirt, crown and bosses are employed as design constraints. Different load cases are considered and the results of the topology optimization are revised and discussed with the prospective to employ Additive Manufacturing as the production technique.

7.2 Model set up

The objective of this chapter is the design of a steel piston for the four-stroke motorcycle engine of the Ducati Panigale 959.

For setting up a topology optimization problem, both the domain of the structure (design space) and the governing parameters, i.e. the objective and the constraints of the optimization, have to be defined.

The domain of the structure should be as wide as possible, according to the project restriction, in order to guarantee maximum freedom to the optimization process in choosing the optimal material distribution.

Thus, the starting point in this study is a massive steel half cylinder representing a simple piston with a transversal hole and a parallelepiped pocket, useful to host the piston pin and the upper part of the connecting rod, see Figure 7.1.

The adoption of a geometry as simple as possible is very important to achieve a regular high quality mesh. Sigmund and Petersson [42] and Zuo et al. [43] studied the mesh dependency of topology optimization results noting that different structural solutions can be obtained if different mesh size and quality are considered. Wankhade and Zolekar [68] used a more complex geometry of the piston, but in this case, the ring belt belonged to the non-design space, so that this feature did not aggravate the analysis.

Figure 7.1 shows the domain of the topology optimization. Purple elements describe the crown, the ring belt, the skirt and the pin boss and they are fixed so that their density cannot be modified (non-design space). This layer is one millimetre thick and consists of about 187 thousand pentahedral elements (first order, 6 nodes, 6 Gaussian integration points). Orange elements form the bulk of the piston and represent the design space. The design space consists of 1.87 million tetrahedral elements (first order, 4 nodes, one Gaussian integration points), the average element size being one millimetre.

The material considered for the analysis is generic steel: Young modulus equal to 210000 MPa, density equal to 7.8 kg/dm^3 and Poisson's ratio equal to 0.3. It could seem wrong to use the property of a bulk isotropic material because Additive Manufacturing techniques always produce anisotropic components due to their lay-up style process. Nevertheless, Tolosa et al. [36] obtained selective laser molten steel with properties very close to the ones of the classic bulk material, even if an anisotropic behaviour was always reported. Kruth et al. [37] studied the scanning strategies of Selective Laser Melting techniques. A thin wireframe structure, similar to the one typically resulting from optimization calculations, requires a short scan vector. Hence, adjacent tracks are scanned rapidly one after the other, leaving little cool-down time in between, thus resulting in high temperatures. Consequently, suitable wetting conditions are present, leading to a high density of the material. Kahlen and Kar [69] determined the yield and ultimate strength of laser-fabricated parts. The interface of two consecutive layers is not found to be the weakest joint. However, the maximum strength is found to occur in a direction, which is inclined at an angle with the direction of material deposition. This angle is influenced by the temperature gradient during the solidification of the melt pool. Gardan et al. [70] presented a numerical optimization method for improving the internal structure of models produced by additive manufacturing. They developed a system to manage the additive manufacturing process and the material characterization for a better integration with the topological optimization technique.

In the present section, the objective of the optimization is the minimization of the mass of the piston.

Several optimization constraints have been imposed, based on the deformations registered with Finite Element analysis of the original aluminium piston. In particular, three different load cases have been taken into account:

- top dead centre during combustion (TDCC)
- top dead centre at the beginning of the induction stroke (TDCI)

- instant of maximum piston thrust force (PT)

The objective of these Topology Optimizations is to minimize the mass and the scope of this section is to obtain a new piston characterized by a similar stiffness if compared to the original aluminium one. So, for each static simulation performed in the previous section, the displacement of some particular nodes has been retrieved and employed as a design constrain in the Topology Optimizations. Different nodes and constraints have been selected for each case, according to the specific loadings involved and to the specific portion of the component affected by the most important deformation.

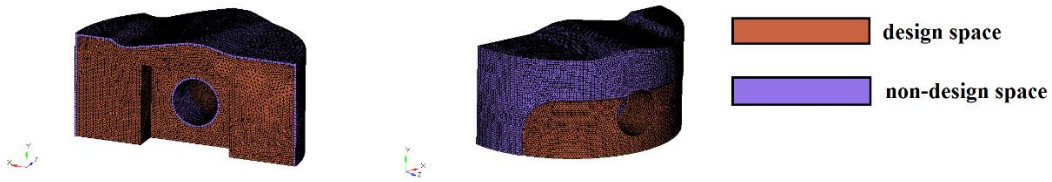

Figure 7.1. The design and non-design space of the optimization.

7.2.1 Top dead centre during combustion (TDCC)

At TDCC the total force acting on the piston is about 40800 N. As a consequence, a pressure of about 5.23 MPa has been applied on the piston top while a pressure of about 71.8 MPa has been applied on the top half of the pin boss, see Fig. 7.2 (a) and (b). In this way, the piston results self-balanced. Proper symmetry constraints have been also applied.

Table 7.1 reports the design constraints limiting the deformation of the piston crown, see Fig. 7.2 (c), and considered to guide the process of optimization. These values have been acquired from a preliminary FEM analysis of the original aluminium piston to reach the same stiffness in the new component. The solver has been then forced to give a symmetrical relative density distribution with reference to the piston yz plane.

Table 7.1. Values of design constraints at *TDCC*.

Nodes selected	Group 1	Group 2	Group 3
Lower bound [mm]	-0.02	-0.015	-0.01
Upper bound [mm]	0.001	0.001	0.001

Obviously, the lower bound refers to a deformation in the negative direction of the *y*-axes. However, it is important to notice that considering only the lower bound could have been enough, anyway, the computing process has shown that adding an upper bound accelerated the analysis by guiding the Optimization process towards a smaller range of solutions.

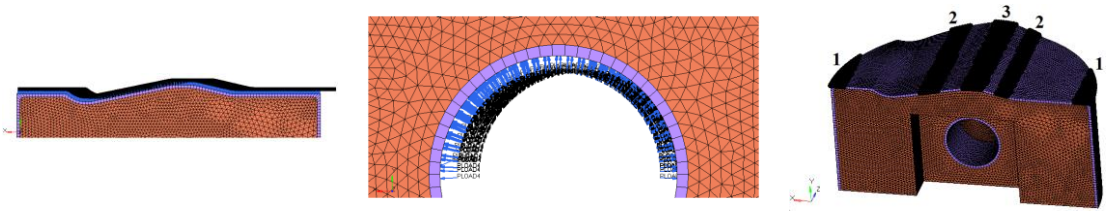

(a) (b) (c)

Figure 7.2. TDCC optimization settings.

7.2.2 Top dead centre at the beginning of the induction phase (TDCI)

At *TDCI* the total force acting on the piston is about 18600 N. As a consequence, a pressure of about -2.4 MPa has been applied on the piston top while a pressure of about 27.17 MPa has been applied on the bottom half of the pin boss, see Fig. 7.3 (a) and (b). In this way, the piston results self-balanced. Proper symmetry constraints have been also applied.

Table 7.2 reports the design constraints limiting the deformation of the piston crown, see Fig. 7.3 (c), and considered to guide the process of optimization. The solver has been then forced to give a symmetric relative density distribution with reference to the piston *yz* plane.

Table 7.2. Values of design constraints at *TDCI*.

Nodes selected	Group 1	Group 2	Group 3
Lower bound [mm]	0.01	0.01	0.05
Upper bound [mm]	0.02	0.015	0.01

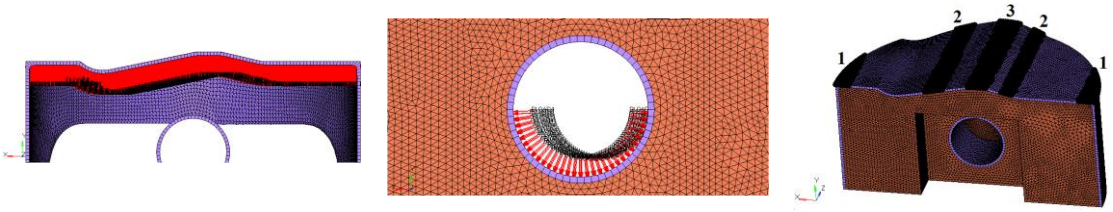

(a) (b) (c)

Figure 7.3. TDCI optimization settings.

7.2.3 Instant of maximum piston thrust force (PT)

At PT the total force acting on the piston is about 4200 N. As a consequence, a pressure of about 42.2 MPa has been applied on the piston skirt while a pressure of about 7.9 MPa has been applied on a half side of the pin boss, see Fig. 7.4 (a) and (b). In this way, the piston results self-balanced. Proper symmetry constraints have been also applied.

Table 7.3 reports the design constraints limiting the deformation of the piston skirt, see Fig. 7.4 (c), and considered to guide the process of optimization. The solver has

been then forced to give a symmetric relative density distribution with reference to the piston *yz* plane.

Table 7.3. Values of design constraints at *PT*.

Nodes selected	Group 1	Group 2	Group 3	Group 4	Group 5	Group 6	Group 7	Group 8	Group 9
Lower bound [mm]	-0.045	-0.04	-0.052	-0.057	-0.06	-0.075	-0.083	-0.09	-0.1
Upper bound [mm]	-0.035	-0.03	-0.042	-0.052	-0.05	-0.065	-0.073	-0.08	-0.09

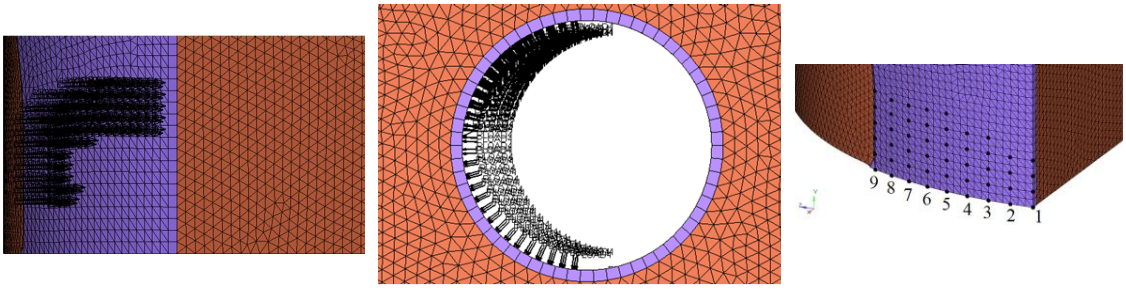

(a) (b) (c)

Figure 7.4. PT optimization settings.

7.3 The optimization process

The software package employed for the optimization is Altair OptiStruct, while the model set up has been made using Altair HyperMesh. To better tune the process, a sensitivity analysis on the optimization parameters DISCRETE (corresponding to the penalty factor, p) and MINDIM (related sensitivity filter, r) has been performed. The choice of the parameters has been driven by the following considerations:

- the solution achieved is more clearly defined;
- the number of intermediate density elements is lower;
- the convergence is achieved more easily;
- the topology of the piston is considered more interesting, innovative, and easier to be manufactured by the designer.

After the sensitivity analysis, it has been chosen to set the optimization parameters to DISCRETE=3 and MINDIM=2.

The DISCRETE parameter influences the tendency for elements in a topology optimization to converge to a material density of 0 or 1. Low values of this parameter help the solution to converge but results could be too sparse in terms of density distribution. Figure 7.5 shows the results for top dead centre during combustion. Only the elements with a relative density higher than 0.1 are shown. In this preliminary analysis, a DISCRETE value of 1 has been set. The structural features are not easy to be interpreted and some elements are detached from the rest of the structure even a low relative density value is considered (see the highlighted region in Figure 7.5).

The MINDIM parameter specifies the minimum diameter of members formed in a topology optimization. A minimum dimension of 2 millimetres for each feature of the steel piston has been chosen with the prospective to employ Additive Manufacturing as a manufacturing technique. Unnecessary high values of the MINDIM parameter could lead to suboptimal solutions. Figure 7.6 shows the results for the top dead centre during combustion. Only the elements with a relative density higher than 0.1 are shown. In this preliminary analysis, a MINDIM value of 4 has been set. This parameter forces the solver to converge to a low material density solution, which cannot lead to an easily interpretable result. Useful topology optimization results should display structural features at high values of relative density.

Besides, also the choice of the constraints has a crucial role in the model set up. For instance, Figure 7.7 shows the results for the top dead centre at the beginning of the induction stroke condition. In this analysis, the constraints in terms of fixed displacements have been applied to the nodes of the upper side of the piston bosses. Only the elements with a relative density higher than 0.1 are shown. Results do not allow the structure to be interpreted since only a small portion of the design space is interested by the optimization process. To obtain good results, different constraints have to be adopted.

Despite the sensitivity analysis, the results of the topology optimization are still far from being ready-to-made solutions for the piston design: even if a suitable choice of the parameters is made, a certain number of elements having intermediate density always characterizes the results and there are no perfectly black-and-white solutions. Moreover, due to the domain discretization, the solution presents non-smooth surfaces. Therefore, the results have always to be interpreted to create new models, which have to be manually re-drawn using CAD software. It could be possible to implement a proper filter to prevent the mesh-dependency and checkboard patterns, as reported by Hu et al. [71].

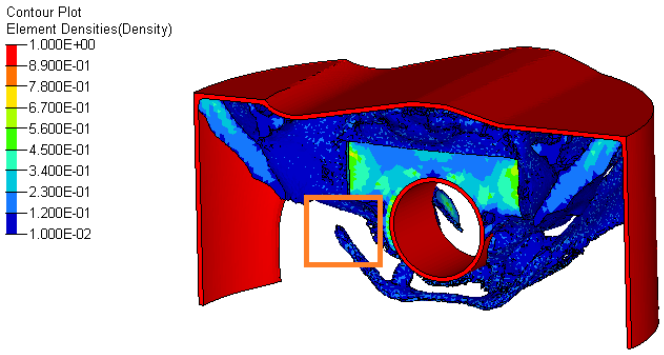

Figure 7.5. Contour plot TDCC 0.1 density, DISCRETE=1.

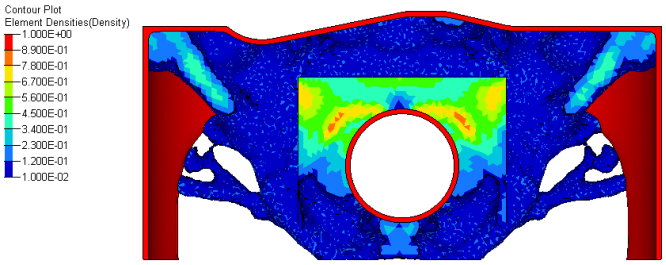

Figure 7.6. Contour plot TDCC 0.1 density, MINDIM=4.

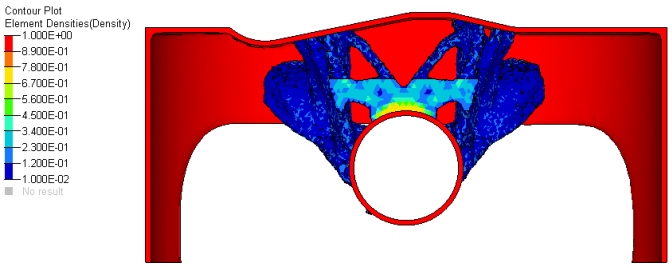

Figure 7.7. Contour plot TDCI 0.1 density, different constraints.

7.1 The Topology Optimization results

The results of the optimization process have been discussed in terms of relative density contour plots. Each load case has been analysed independently in order to better understand how the density distribution is influenced by the load path and by the design constraints. Different values of lower bound relative density, namely 0.1, 0.4 and 0.5 have been set to highlight the structural features proposed by the optimization analysis and let the reader clearly understand the consequent redesign process.

7.1.1 Top dead centre during combustion (TDCC)

Figure 7.8 (a) shows the results for top dead centre during combustion phase condition. It displays only the elements with a relative density higher than 0.1. Ribs linking the pin boss to the crown are visible. Besides, a wireframe structure is present in the area below the pin boss, where the presence of high-density elements far from the crown increases the global bending stiffness of the piston. Increasing the lower bound of the relative density up to 0.4, Figure 7.8 (b), supports that are fundamental for the stiffness of the piston are clearly identified.

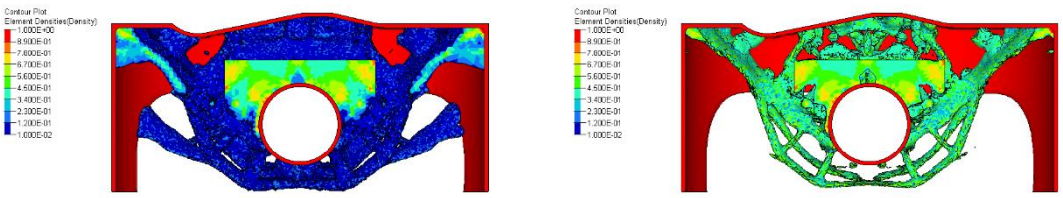

(a) (b)

Figure 7.8. Contour plot TDCC 0.1 (a) and 0.4 (b) relative density.

7.1.2 Top dead centre at the beginning of the induction phase (TDCI)

Figure 7.9 (a) shows the results for top dead centre at the beginning of induction stroke condition. Only the elements with a relative density higher than 0.1 are shown. Ribs linking the pin boss to the crown are visible. Moreover, a wireframe structure is present in the area below the pin boss, where the presence of high-density elements far from the crown increases the global bending stiffness of the piston. Increasing the lower bound of the relative density up to 0.5, Figure 7.9 (b), supports that are fundamental for the stiffness of the piston are clearly identified.

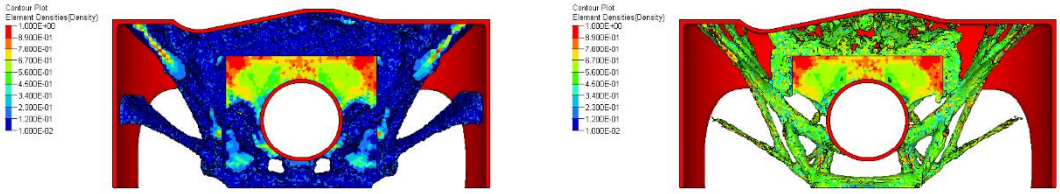

(a) (b)

Figure 7.9. Contour plot TDCI 0.1 (a) and 0.4 (b) relative density.

7.1.3 Instant of maximum piston thrust force (PT)

Figure 7.9(a) shows the results for the maximum piston thrust force condition. Only the elements with a relative density higher than 0.1 are displayed. Ribs linking the pin boss to the skirt are visible. Increasing the lower bound of the relative density up to 0.4, Figure 7.9(b), supports that are fundamental for the stiffness of the piston are clearly identified.

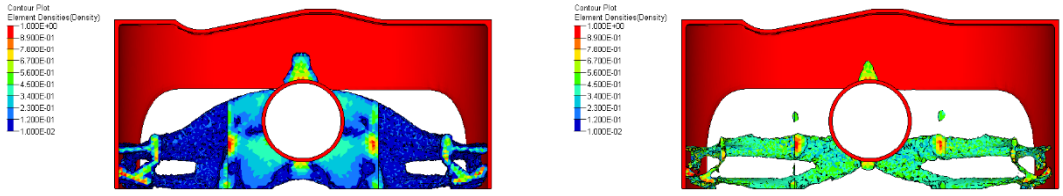

(a) (b)

Figure 7.9. Contour plot PT 0.1 (a) and 0.4 (b) relative density.

7.1 The redesign process

The software employed for the piston redesign is Solidworks. The geometry of the piston top, of the ring land, of the pin bosses and of the skirt has not been modified with respect to the original aluminium piston, in order to allow the new steel piston to

immediately fit the actual engine, Figure 7.10. The three different contours plots of Figures 7.7-7.9 have been interpreted and the main structural features from each load case have been identified. In particular, the geometries under the crown and below the pin bosses (highlighted with blue in Figure 7.11(a)) have been designed following the topology optimization results of TDCC and TDCI. The material linking the skirt and the pin bosses (highlighted with yellow in Figure 7.11(a)) have been designed to trace the optimization results corresponding to the piston thrust force load case. The optimization analysis produced a geometry abundant of small fillets. These features have been implemented accurately in the first steel piston proposal, Figure 7.12. These geometries (highlighted in Figure 7.11(b)) produced excessively high values of stress. Therefore, greater radii have been used and a slightly heavier component has been obtained. Using a greater value of the MINDIM parameter has been thought to obtain a clearer solution without small fillets. Unfortunately, this expedient has been useless: a contour plot rich of low-density elements has been obtained without providing an effective guide to the design process.

The new steel piston has a mass of 415 g. If compared to the original aluminium piston (380 g), a limited increase of 9% is registered.

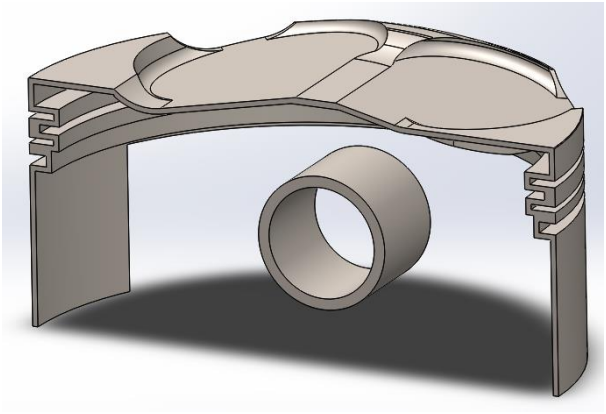

Figure 7.10. The geometrical boundaries of the piston.

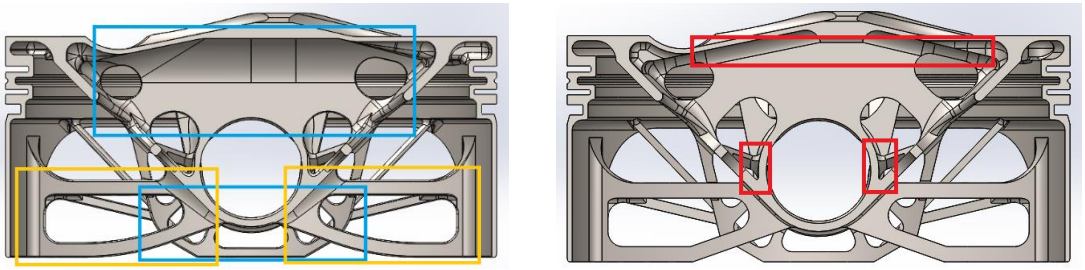

(a) (b)

Figure 7.11. The steel piston.

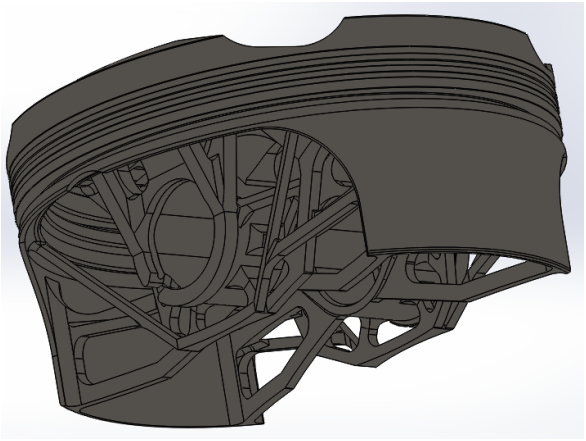

Figure 7.12. The steel piston.

Chapter 8: FEM analysis of the steel piston

8.1 Introduction

This chapter shows the thermal and structural analyses performed on the new piston made of steel. It is necessary to specify that the geometry of the proposed piston is the result of numerous iterations of calculation and subsequent improvement of the geometry. Thermal analyses have been also performed, but their results only marginally affected the geometry of the component. In fact, Topological Optimization considered mechanical loads and not thermal ones.

In this chapter, therefore, only the results relating to the last geometry reached by the piston are shown.

The thermo-structural analyses presented have the purpose of structurally verifying the designed component and obtaining the first proposal for a profile to be used to shape the steel piston to have a behaviour similar to that shown by the aluminium piston.

The settings of the thermo-structural simulations performed for the steel piston faithfully follow the methodology used for the aluminium piston. However, all variations used to test the new steel piston will be reported.

8.2 Mesh 2D e 3D

The models used involve the use of piston, pin and the upper part of the connecting rod, the mass corresponding to the reciprocating part of the connecting rod. The connecting rod and pin are exactly the same components used previously and therefore only the new steel piston had to be discretized. Figure 8.1 shows the discretization of the half of the piston used in the analyses. A CFD Tetramesh mesh was also used here to ensure the presence of at least three elements along any thickness of the component. About 192 thousand elements have been employed: 66 thousand pentahedral elements (bilinear, 6 nodes, 6 Gaussian integration points), and 126 thousand tetrahedral elements (first order, 4 nodes, one Gaussian integration points), the average element size being 1 millimetre.

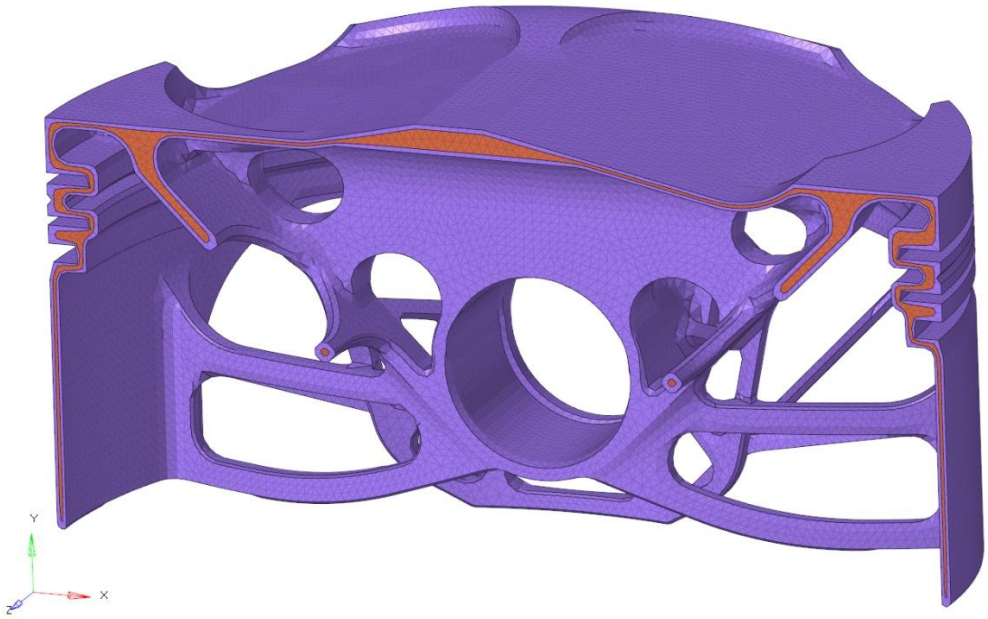

Figure 8.1. The 3D mesh of the piston.

8.3 Thermal analysis of the crank mechanism

A thermal analysis of the crank mechanism has been performed using the new steel piston. The same speed at 11000 rpm has been considered as used in the case of the aluminium piston.

A generic steel was used for all components, table 8.1.

Table 8.1. Materials employed.

Component	Material	Thermal conductivity
Piston, pin, conrod	Generic steel	0.039 W/(mm K)

The contacts have been set and a contact conductivity of 0.1 W/(mm^{2}K) has been entered. Piston and connecting rod were considered discrete, while the piston pin was declared analytical.

A Fortran subroutine has been inserted to obtain, at the end of the calculation and with some operations, a .bin file containing information on the temperatures of the integration points.

The specific settings and their results are now explained.

8.3.1 Thermal boundary conditions

The boundary conditions were calculated in the same way as it was done for the aluminium piston. The values of the boundary conditions may differ slightly because in the calculation of some quantities the mass of the piston and the areas of some areas of

the piston that have changed slightly are considered. In fact, the steel piston does not yet have the typical truncated cone shape of the crown and the barrel shape of the mantle. It is the purpose of this chapter to determine a first proposal for the definition of the piston profile.

An initial temperature of 20 ° C has been entered.

The incoming fluxes on the two sides of the casing have been set, the values are collected in table 8.2.

Tabella 8.2. Face flux boundary conditions.

Application area	Value
Skirt (intake side)	0.2306 W/(mm^{2}K)
Skirt (exhaust side)	0.1505 W/(mm^{2}K)
First compression ring	0.0329 W/(mm^{2}K)

The other boundary conditions belong to the thermal face film type, table 8.3 shows the settings used. No distinction has been made between the HTC of the oil that wets the internal part of the piston pin and the one that wets the external part. The average value between the two was assigned, in fact, the very branched geometry of the piston flows does not justify a different HTC value for the various areas.

Tabella 8.3. Face film boundary conditions.

Application area	HTC [W/ mm^2°C]	T [°C]
Piston top	0.000667	1014
Piston crown (lateral)	0.000175	90
First compression ring up	0.002143	90
First compression ring down	0.005490	90
Second compression ring up	0.003436	90
Second compression ring down	0.003436	90
Oil ring up	0.002291	90
Oil ring down	0.002291	90
Skirt	0.009583	90
Oil jet	0.005320	120
Splashing oil	0.001392	120
Splashing oil (rod and pin)	0.000773	120

8.3.2 Results of the thermal analysis

Figure 8.2 shows the thermal field of the crank mechanism calculated by the software. It can be seen how the highest temperature is recorded on the piston crown, while the lowest temperature is reached by the connecting rod, which is abundantly wetted by the splashing oil. Figure 8.3 shows the piston in detail. In particular, these high values of temperature are confined to a small angular portion of the valve pocket

peripheries, while the rest of the top surface exhibits a comparable temperature distribution with respect to the aluminium piston (ranging from 250°C to 300°C). Such a result has been obtained properly designing very thin geometrical features of the piston top (Figure 8.4), thus minimizing the thermal resistance through the piston top thickness. In fact, the thermal conductivity of steel can be up to five times lower than the aluminium one. Unfortunately, it has not been possible to remove material under the identified critical portions of the valve pockets periphery without modifying the non-design space (Figure8.5). A smoother temperature gradient could be obtained softening the geometry of these keen-edged features, but it will simultaneously increase the combustion chamber volume, thus reducing the compression ratio and the maximum power of the engine. Cooling galleries could be designed in order not to modify the geometry of the crown. Furthermore, an integrated in-cylinder/CHT analysis should be performed in order to guide the redesign process and to predict possible abnormal combustion occurrence related to these concentrated peaks of temperature [72].

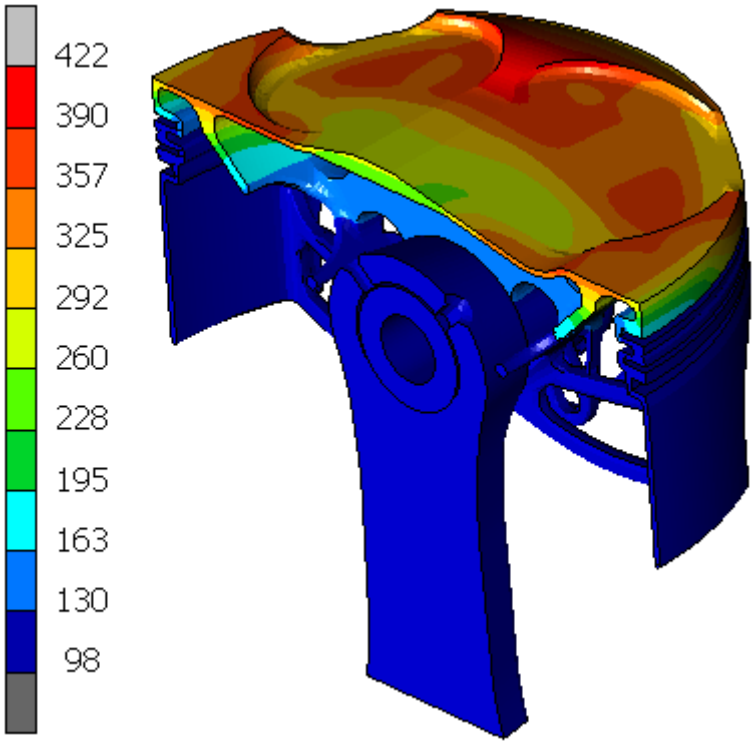

Figure 8.2. Temperature contour plot of the crank mechanism [°C].

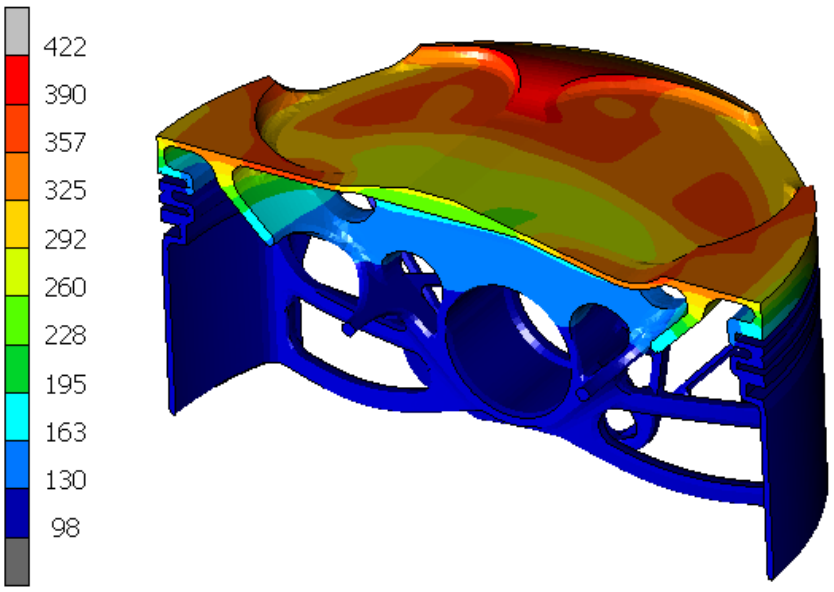

Figure 8.3. Temperature contour plot of the piston [°C].

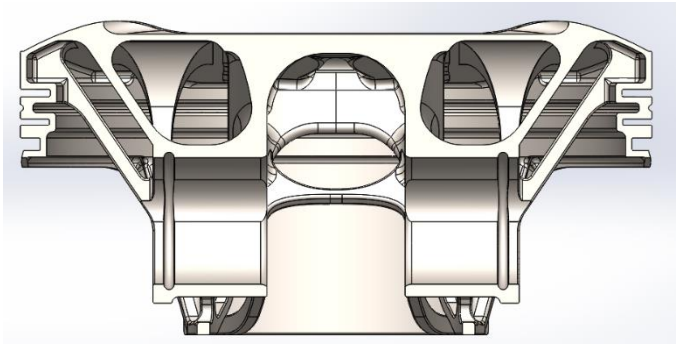

Figure 8.4. Detail of the new steel piston.

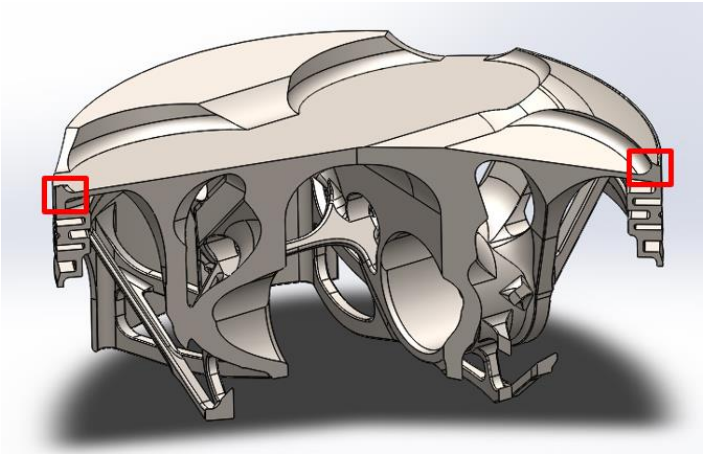

Figure 8.5. Detail of the new steel piston.

8.4 Thermo-mechanical analysis of the crank mechanism

Three different types of analyzes have been performed to achieve two different purposes. First, a thermo-structural calculation of the piston alone has been performed to evaluate in detail the deformation of the skirt and lateral crown. This analysis is used to obtain a first attempt profile to be assigned to the piston to obtain the same hot deformation of the aluminium piston. Second, thermomechanical simulations of the entire crank mechanism have been performed to structurally verify the steel piston and guide the design iterations.

Generic steel was used for all components of the crank mechanism, table 8.4.

Table 8.4. Material employed.

Component	Material	Density [t/mm^3]	Young Modulus [MPa]	Poisson's ratio	Thermal expansion coefficient [°C^{-1}]
Piston, pin, conrod	Generic steel	7.8e-9	210000	0.3	1.1e-5

The piston-pin and pin-connecting rod touching (i.e. single-sided) contacts have been set, indicating a contact tolerance of 0.01 mm and a friction coefficient of 0.2 as for the cases with the aluminium piston. Piston and connecting rod were considered discrete, while the piston pin was declared analytical.

A Fortran subroutine has been inserted to add the information regarding the temperatures of the integration points contained in the .bin file.

The specific settings and their results are now explained.

8.4.1 Analysis of the profile of the piston

To analyze the steel piston profile deformed by the thermal field, the same steps employer for the analysis of the aluminium piston have been followed.

Figure 8.6 and 8.7 show the simulation results. The piston deformation has been amplified by 10 times and the undeformed piston profile is represented by a thin pink line. The most important deformation is that involving the crown, which is the hottest part of the piston. The contour plot of Figure 8.6 shows the displacements in the x-direction, the legend has been filtered in a small range around zero to understand if the piston rotates during deformation and if it is legitimate to analyse the output more simply. In fact, the rotation linked to the deformation corresponds to a rigid motion of the piston which will rotate accordingly to better adapt to contact with the cylinder, this rotation should be appropriately considered in the post-processing of the results. Figure 8.7 depicts the same results, but with an unfiltered displacement field, it is evident that the deformation is sufficiently symmetrical and therefore the piston will behave in the same way in the two banks of the L-twin engine of the Panigale 959.

Figure 8.8, 8.9 and 8.10 show the stress field according to von Mises, it can be seen how the stress state induced by the thermal gradient affects not only the seats for the

elastic rings, but also all those areas in which the stiffness of the component varies in abruptly. Figure 8.10 shows high values of tension on the piston top, the beams that connect it to the boss for the pin have very different stiffness.

The piston examined has a perfectly cylindrical crown and mantle geometry (diameter of 100mm). The steps to obtain a first attempt profile for the piston, truncated cone for the lateral crown and barrel for the skirt are illustrated below. The goal is to obtain a steel piston that has a heat-deformed crown and skirt similar to that of the aluminium piston.

Figure 8.11 shows the radius profile undeformed and then thermally deformed. The average between the radii on the intake and exhaust side is shown, even if the two sides of the piston have almost the same deformation. The radius of the cold piston has a homogeneous profile of 50mm, while the radius profile of the hot piston has an evident deformation of the crown, while the skirt has a much more modest deformation. Figure 8.12 compares the deformed profile of the aluminium piston, taken as a reference, and that of the steel piston. The profile of the steel piston was determined by calculating the difference between the deformed profile of the steel and the aluminium piston (Figure 8.12). The result shows the need to adopt a nominal diameter of 100.13 mm (considering 99.95 mm for the aluminium piston).

By comparing the profile values of the new steel piston (figure 8.12) with the values used for the original piston (Figure 8.13), it can be seen that they are not too far from each other. Since the nominal diameter of the steel piston is significantly greater than that of the aluminium piston, it can therefore be said that the steel piston will have a cold shape more similar to the hot one if compared to the aluminium piston, which is very predictable given the smaller coefficient of thermal expansion of steel compared to aluminium. From this consideration, it can be assumed that the steel piston will have better cold behaviour than the aluminium one.

Now it is necessary to obtain the oval shape of the piston. The plane that is perpendicular to the symmetry plane of the piston and that passes through the pin axis and that of the piston has been considered. The deformed radius has been collected along a node of the crown and one of the skirt, the same nodes for both pistons. The radius of the steel piston has therefore been reduced to achieve the same radius. For the intermediate values of the angles, the same proportionality has been used as the original aluminium piston, to try to have the same type of ovality. Figure 8.15 shows the oval profile of the steel piston, while Figure 8.16 shows the oval profile of the aluminium piston. Figure 8.17 shows the overlap of the profiles for each angle between 0 ° and 90 °, Figure 8.17(a) refers to the steel piston, while Figure 8.17(b) refers to the original aluminium piston. It is important to note that the crown has a greater slope than the aluminium piston, this derives from the greater thermal gradient between the upper and lower parts of the steel piston compared to the aluminium one. Finally, Figure 8.18 and 8.19 collect all the data that are necessary to model the original aluminium piston and the new steel one.

Figure 8.20 shows the new profile assigned to the steel piston (solid line) and the thermally deformed profile (dashed line).

Figure 8.21compares the thermally deformed profile of the steel piston (solid line) and the thermally deformed profile of the original aluminium piston (dashed line), a more than acceptable match has been reached.

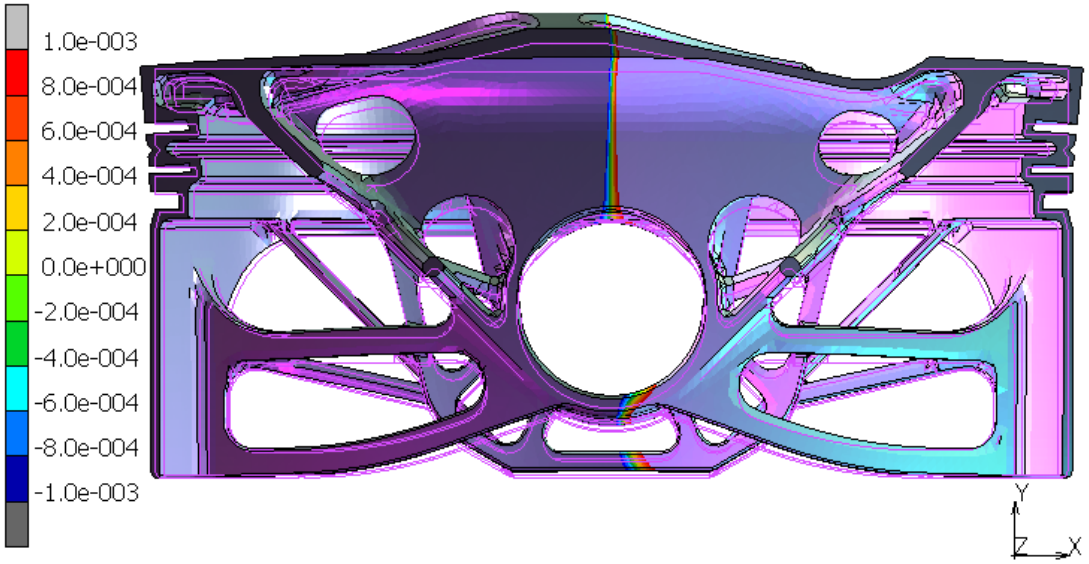

Figure 8.6. X-dispalcement contour plot, filtred [mm].

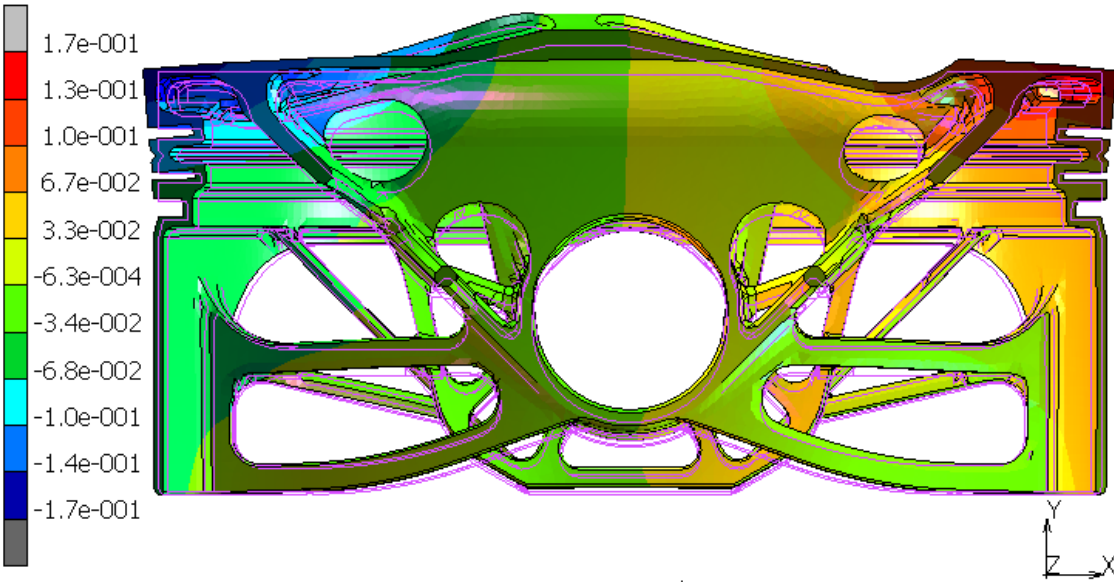

Figure 8.7. X-dispalcement contour plot [mm].

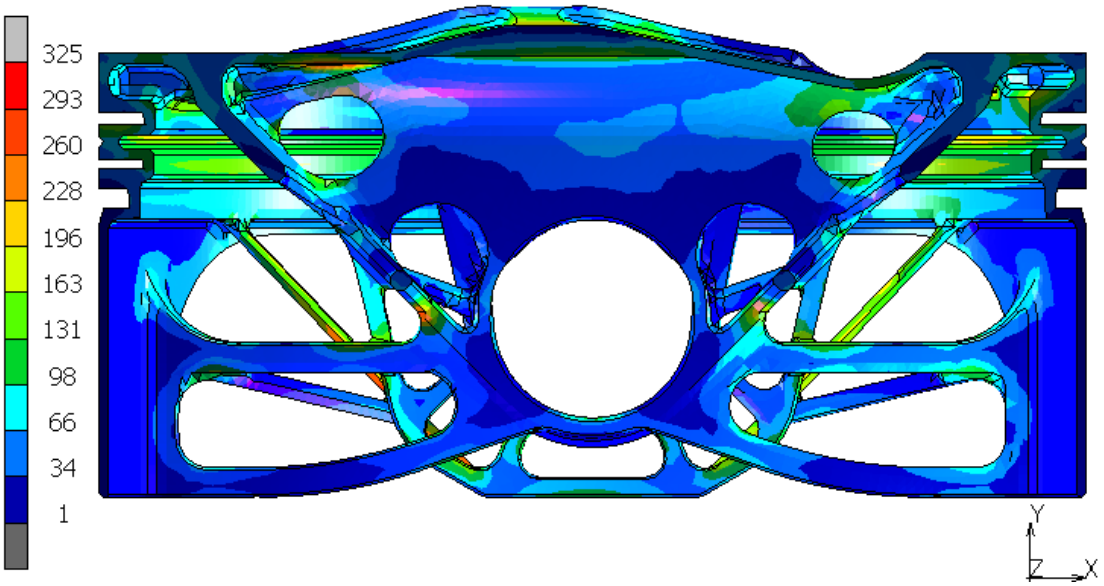

Figure 8.8. Von Mises stress contour plot, thermal loadings [MPa].

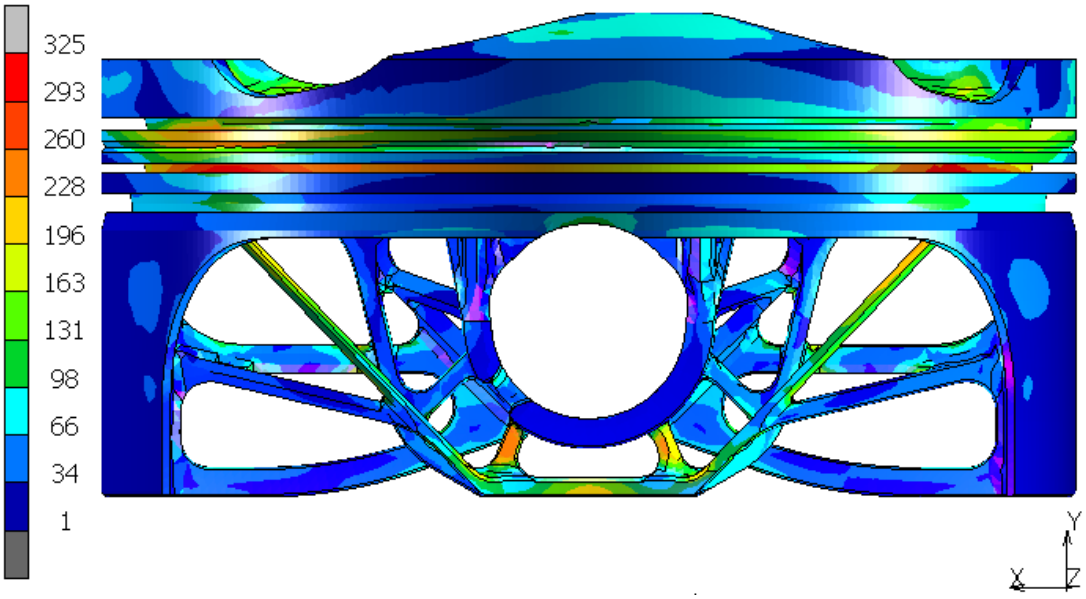

Figure 8.9. Von Mises stress contour plot, thermal loadings [MPa].

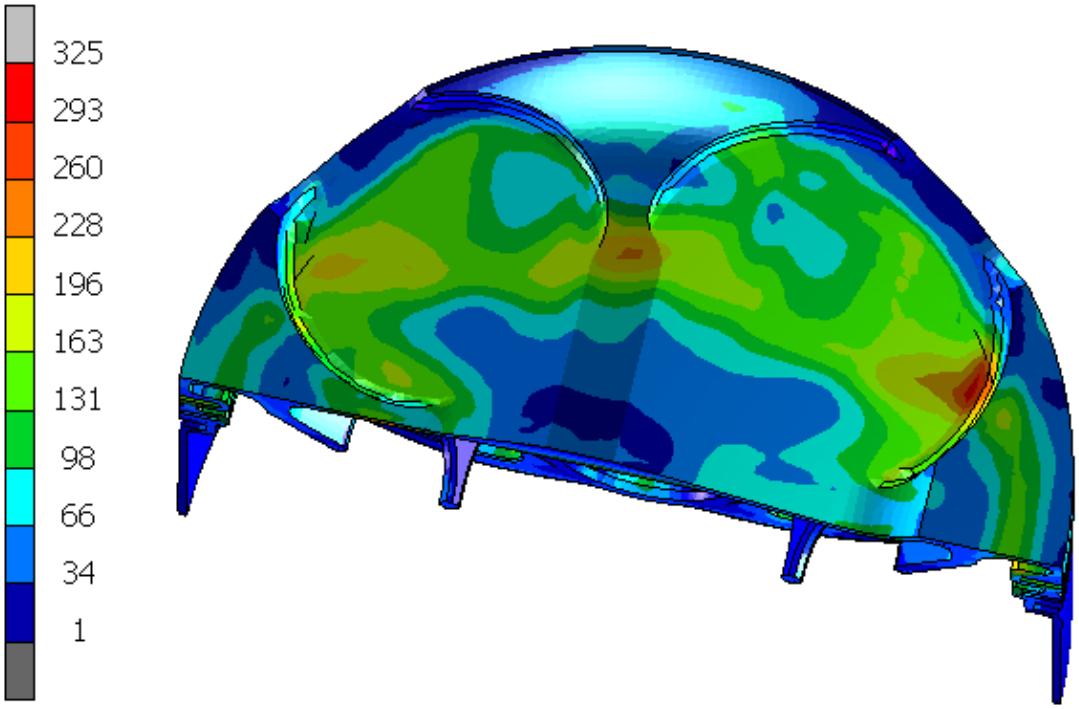

Figure 8.10. Von Mises stress contour plot, thermal loadings [MPa].

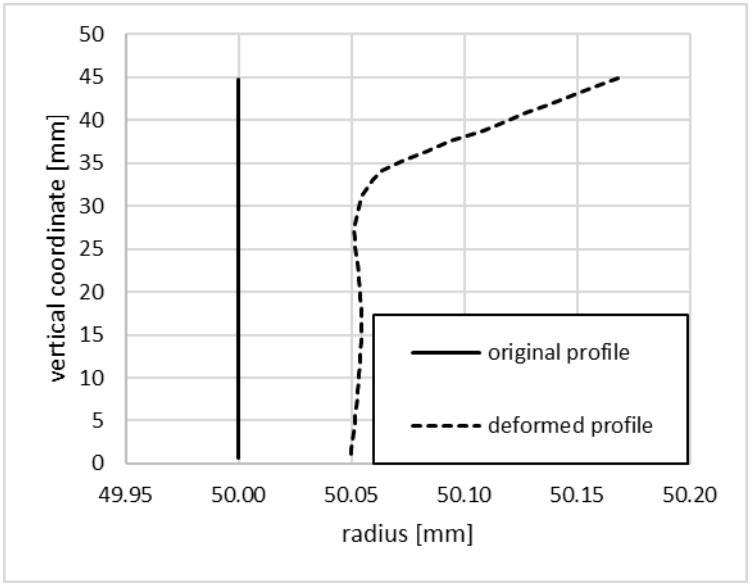

Figure 8.11. Steel piston profile [mm].

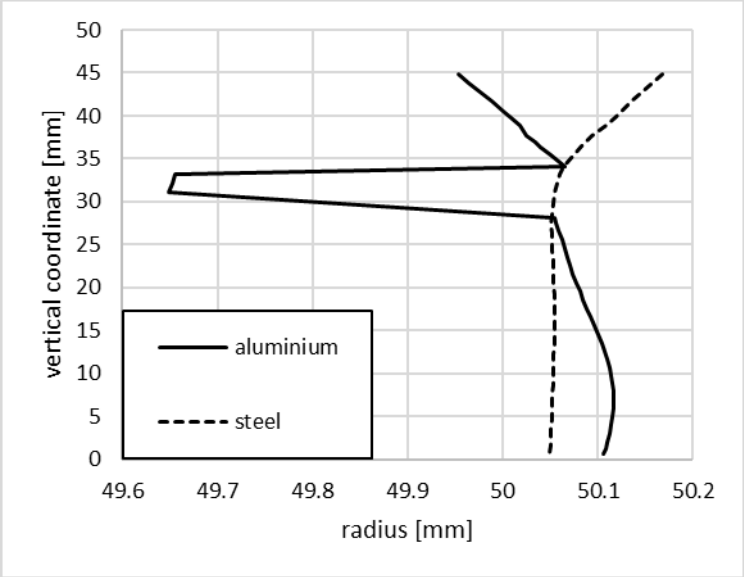

Figure 8.12. Aluminium and steel piston profiles [mm].

Nominal diameter	D_n	100.13	mm
Point	Coordinate z	Tolerance	Actual radius
z_1	46	-0.619097561	49.75545122
z_2	44.6	-0.559	49.7855
z_3	40.5	-0.383	49.8735
z_4	38.9	-0.309	49.9105
z_5	36.8	-0.227	49.9515
z_6	34	-0.117666667	50.00616667
z_7	33.5	-1	49.565
z_8	31	-1	49.565
z_9	30	-0.1305	49.99975
z_10	27.5	-0.118	50.006
z_11	22.5	-0.093	50.0185
z_12	17.5	-0.06	50.035
z_13	12.5	-0.021	50.0545
z_14	7	0	50.065
z_15	5	0	50.065
z_16	2	-0.009	50.0605
z_17	0	-0.017	50.0565
z_18	-1	-0.021	50.0545

Figure 8.13. Steel piston data [mm].

Nominal diameter	D_n	99.95	mm
Point	Coordinate z	Tolerance	Actual radius
z_1	46	-0.575073171	49.68746341
z_2	44.6	-0.53	49.71
z_3	40.5	-0.398	49.776
z_4	38.9	-0.345	49.8025
z_5	36.8	-0.28	49.835
z_6	34	-0.193333333	49.87833333
z_7	33.5	-1	49.475
z_8	31	-1	49.475
z_9	30	-0.19	49.88
z_10	27.5	-0.16	49.895
z_11	22.5	-0.1	49.925
z_12	17.5	-0.053	49.9485
z_13	12.5	-0.015	49.9675
z_14	7	0	49.975
z_15	5	0	49.975
z_16	2	-0.01	49.97
z_17	0	-0.03	49.96
z_18	-1	-0.04	49.955

Figure 8.14. Aluminium piston data [mm].

Angular coordinate		Oval_1 (Tapered)		Oval_2 (up barrel)		Oval_3 (low_barrel)	3th land
0	tol_O1_0	0	tol_O2_0	0	tol_O3_0	0	0.000
10	tol_O1_10	-0.006	tol_O2_10	-0.012	tol_O3_10	-0.017	0.000
20	tol_O1_20	-0.021	tol_O2_20	-0.065	tol_O3_20	-0.073	0.000
30	tol_O1_30	-0.054	tol_O2_30	-0.141	tol_O3_30	-0.152	0.000
40	tol_O1_40	-0.089	tol_O2_40	-0.229	tol_O3_40	-0.237	0.000
50	tol_O1_50	-0.117	tol_O2_50	-0.324	tol_O3_50	-0.327	0.000
60	tol_O1_60	-0.142	tol_O2_60	-0.406	tol_O3_60	-0.406	0.000
70	tol_O1_70	-0.165	tol_O2_70	-0.465	tol_O3_70	-0.468	0.000
80	tol_O1_80	-0.189	tol_O2_80	-0.518	tol_O3_80	-0.519	0.000
90	tol_O1_90	-0.214	tol_O2_90	-0.541	tol_O3_90	-0.541	0.000

Figure 8.15. Steel piston ovality data [mm].

Angular coordinate		Oval_1 (Tapered)		Oval_2 (up barrel)		Oval_3 (low_barrel)	3th land
0	tol_O1_0	0	tol_O2_0	0	tol_O3_0	0	0.000
10	tol_O1_10	-0.003	tol_O2_10	-0.01	tol_O3_10	-0.015	0.000
20	tol_O1_20	-0.011	tol_O2_20	-0.055	tol_O3_20	-0.065	0.000
30	tol_O1_30	-0.028	tol_O2_30	-0.12	tol_O3_30	-0.135	0.000
40	tol_O1_40	-0.046	tol_O2_40	-0.195	tol_O3_40	-0.21	0.000
50	tol_O1_50	-0.06	tol_O2_50	-0.275	tol_O3_50	-0.29	0.000
60	tol_O1_60	-0.073	tol_O2_60	-0.345	tol_O3_60	-0.36	0.000
70	tol_O1_70	-0.085	tol_O2_70	-0.395	tol_O3_70	-0.415	0.000
80	tol_O1_80	-0.097	tol_O2_80	-0.44	tol_O3_80	-0.46	0.000
90	tol_O1_90	-0.11	tol_O2_90	-0.46	tol_O3_90	-0.48	0.000

Figure 8.16. Aluminium piston ovality data [mm].

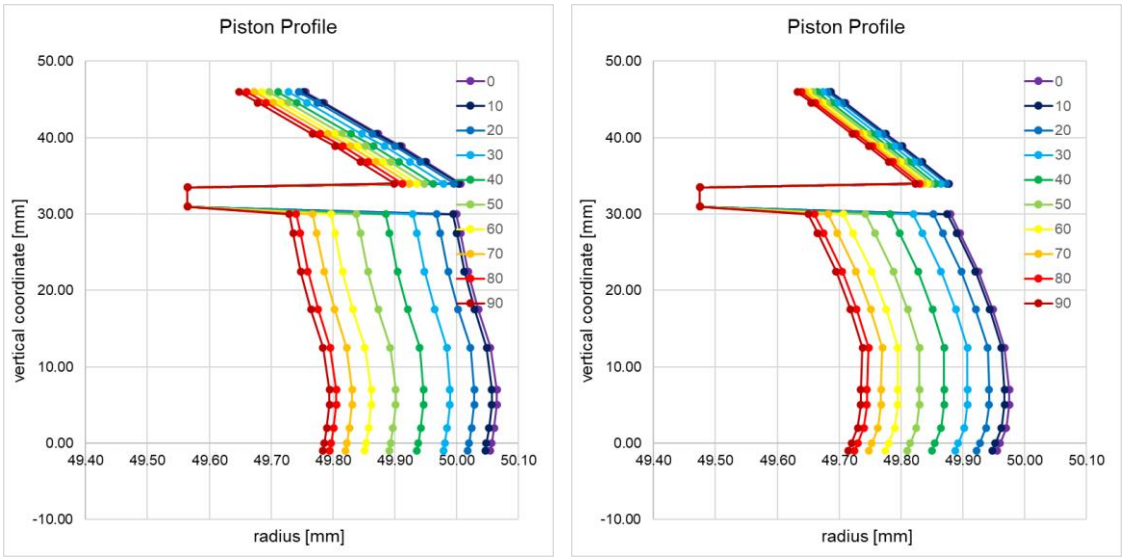

(a) steel (b) aluminium

Figure 8.17 Steel and aluminium piston profile.

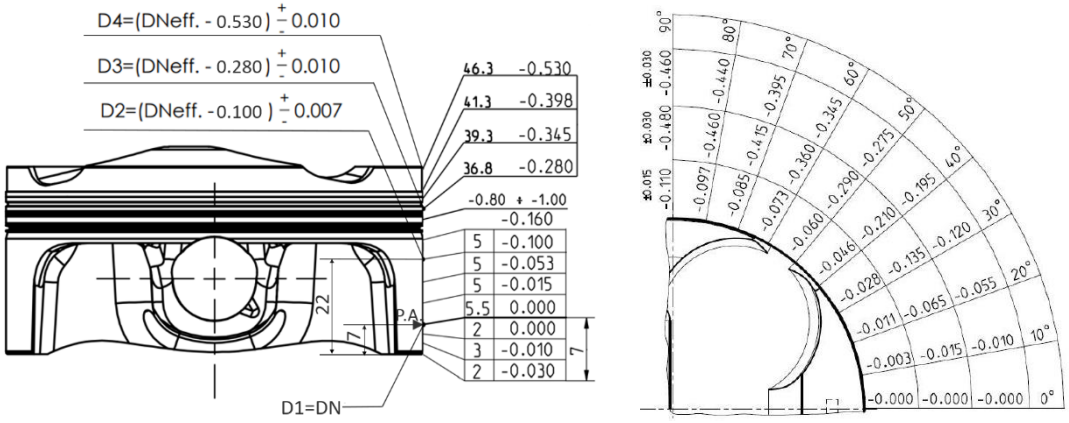

(a) (b)

Figure 8.18. Drawing of the aluminium piston profile.

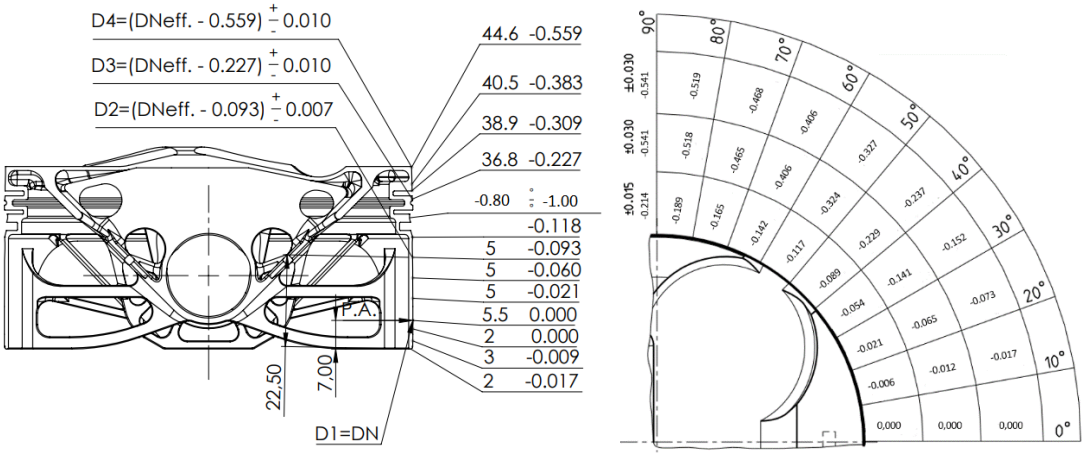

(a) (b)

Figure 8.19. Drawing of the steel piston profile.

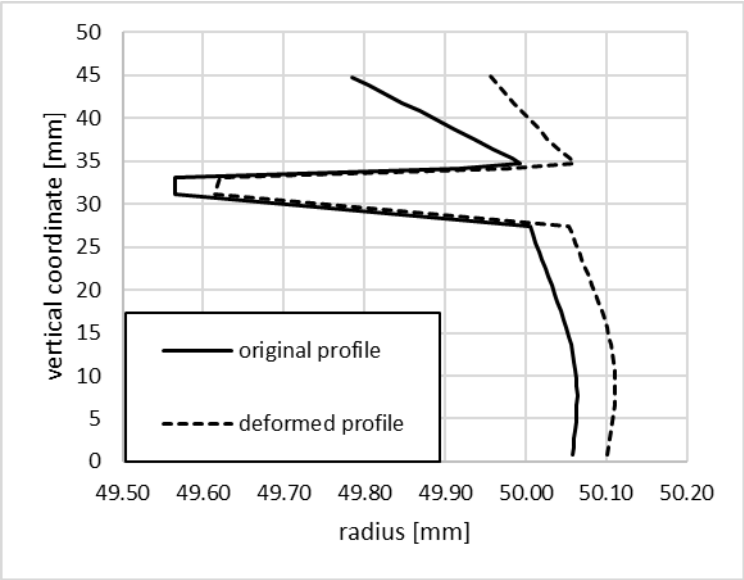

Figure 8.20. Steel piston profile [mm].

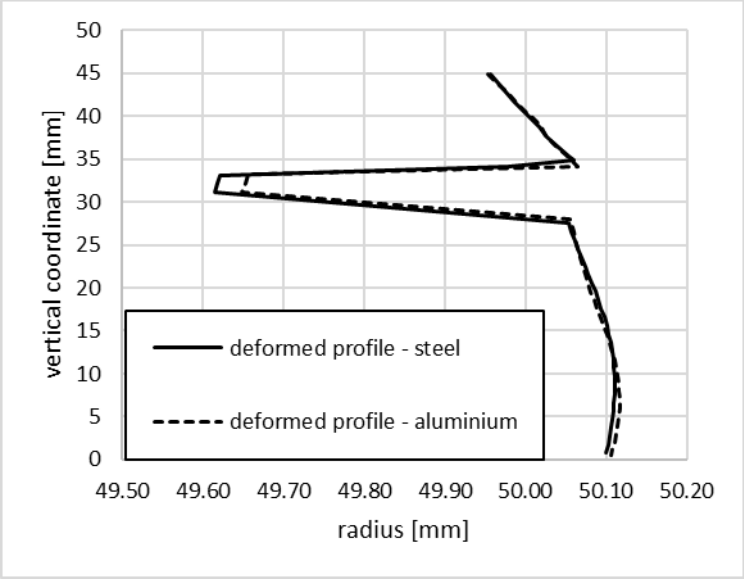

Figure 8.21. Comparison between the steel and aluminium deformed profile [mm].

8.4.2 Structural thermo-mechanical analysis of the crank mechanism

A thermo-mechanical analysis of the assembly has been performed which includes piston, pin and the alternating portion of the connecting rod.

Three cases have been considered:

- combustion, the instant of maximum combustion pressure;
- top dead centre at the beginning of the induction phase;
- maximum piston lateral thrust.

The case of maximum lateral counter-thrust is not considered, it is more correct to consider the case of maximum thrust for both sides of the piston. However, the numerous structural calculations carried out have shown that the steel piston exhibits an almost identical behaviour on both sides of the skirt. It will therefore be considered only for the sake of brevity.

These instants have been identified through a spreadsheet that influences the reciprocal position of the components involved and the loads that are generated. For each of these positions, a FEM analysis has been performed at 11000 rpm, in the case of maximum power.

The materials used, with their respective characteristics, are described in Table 8.4.

The piston-pin and pin-connecting rod touching (single-sided) contacts have been set, indicating a contact tolerance of 0.1 mm for both cases. Piston and connecting rod were considered discrete, while the piston pin was declared analytical.

A Fortran subroutine has been inserted to insert the information regarding the temperatures of the integration points contained in the .bin file.

Given the thin geometry of the beams that describes the pin bosses, it is advisable to check that buckling failure phenomena do not occur. In this case, it is necessary to simulate the whole components and it is no longer possible to exploit the symmetry of the components.

The specific settings and their results are now explained.

8.4.2.1 Cases of top dead centre during combustion and at the beginning of the induction phase

The boundary conditions have been set in a completely equivalent way to how it was done for the aluminium piston. Figure 8.20 shows the model used.

Table 9.2 summarizes the chamber pressure and vertical acceleration values assigned.

Table 9.2. Values of pressure and acceleration.

Loadcase	Pressure [MPa]	Acceleration [mm/s^2]
Combustion	9.10	4.88e^7
PMSI	0.69	5.12e^7

Figure 8.21 displays the von Mises stress contour plot. The material distribution computed by the topology optimization correctly supports the external loads. A maximum value of 385 MPa is registered on the diagonal beams linking the external areas of the top to the pin bosses. Figure 8.22 shows the buckle model results. The most critical beam of the wireframe structure collapse with a combustion pressure of about 800 MPa, 88 times greater than the load actually applied by the gas combustion.

Figure 8.23 displays the von Mises stress contour plot for the case of TDCI. The piston exhibits a lower level of stress if compared to the TDCC case. A maximum value

of 320 MPa is registered on the diagonal beams linking the external areas of the top to the pin bosses.

The analysis also returns that the buckle mode collapse will be triggered only by a negative acceleration. This result can be easily understood considering that at TDCI, the thinnest beams of the structure are subjected to a tensile load.

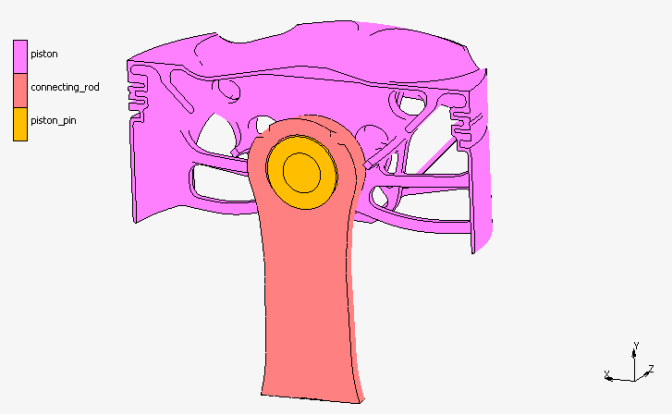

Figure 8.20. The model emplyed.

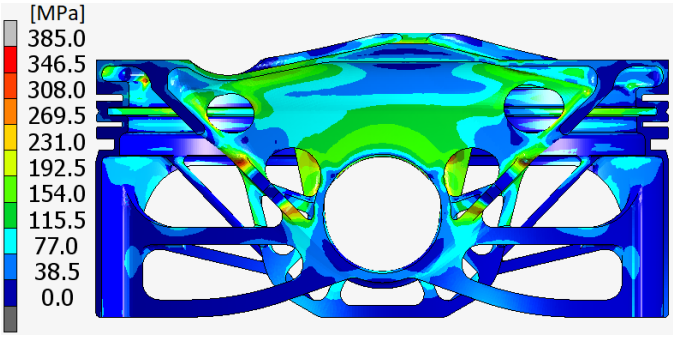

Figure 8.21. TDCC, von Mises contour plot [MPa].

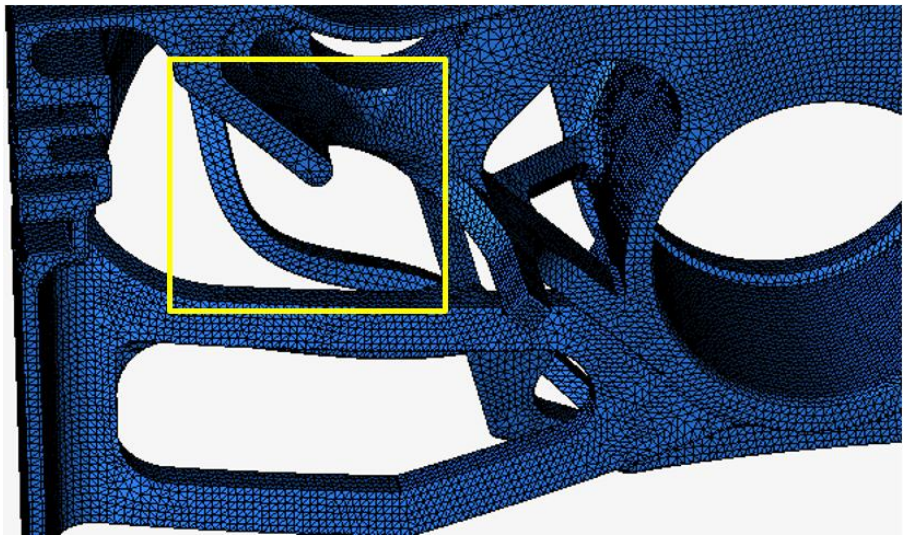

Figure 8.22. TDCC, buckling collapse.

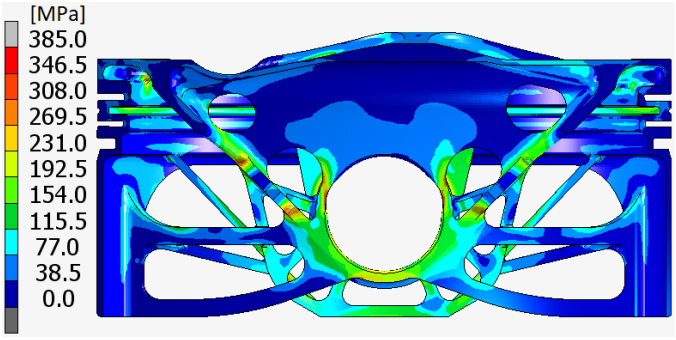

Figure 8.23. TDCI, von Mises contour plot [MPa].

8.4.2.2 Case of maximum piston force

Figure 8.24 shows the model employed to mimic the maximum piston thrust force condition. In this case, the connecting rod has been correctly tilted and a rigid surface has been introduced in order to simulate the cylinder liner reaction. Boundary conditions have been set which are completely similar to those used for the aluminium piston, in particular, table 9.3 shows the applied pressure and alternating acceleration values (directed downwards).

Figure 8.25 displays the von Mises stress contour plot. A maximum value of 300 MPa is registered on the material linking the skirt to the pin bosses. Figure 8.26 shows the buckle model results. The most critical beam of this wireframe structure collapse with a contact normal force 1000 times greater than the load actually applied to the piston. The buckling model results show that the piston is not subjected to Eulerian instability.

Table 9.3. Values of pressure and acceleration.

Loadcase	Pressure [MPa]	Acceleration [mm/s^2]

Maximum thrust force	0.80	$-2.30e^{7}$

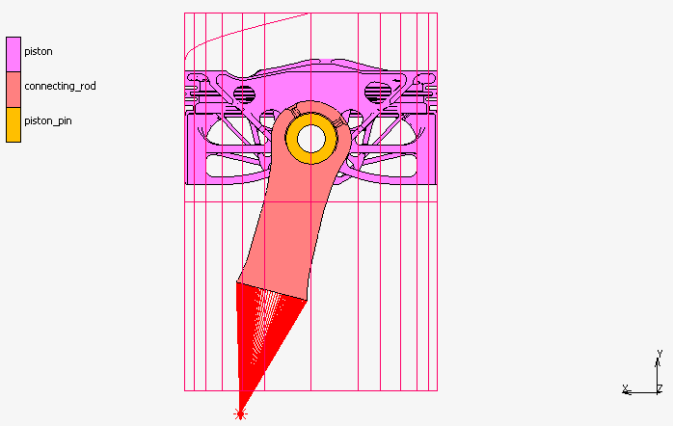

Figure 8.24. The model emplyed.

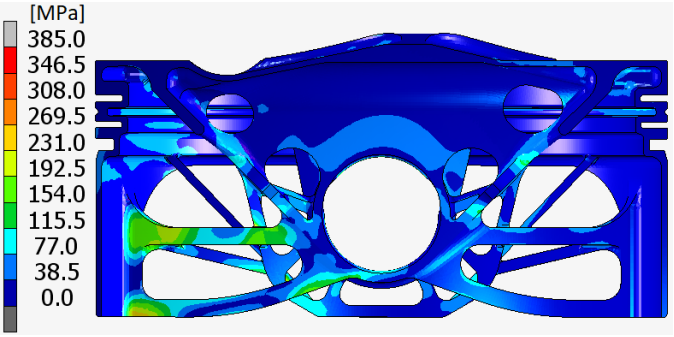

Figure 8.25. PT, von Mises contour plot [MPa].

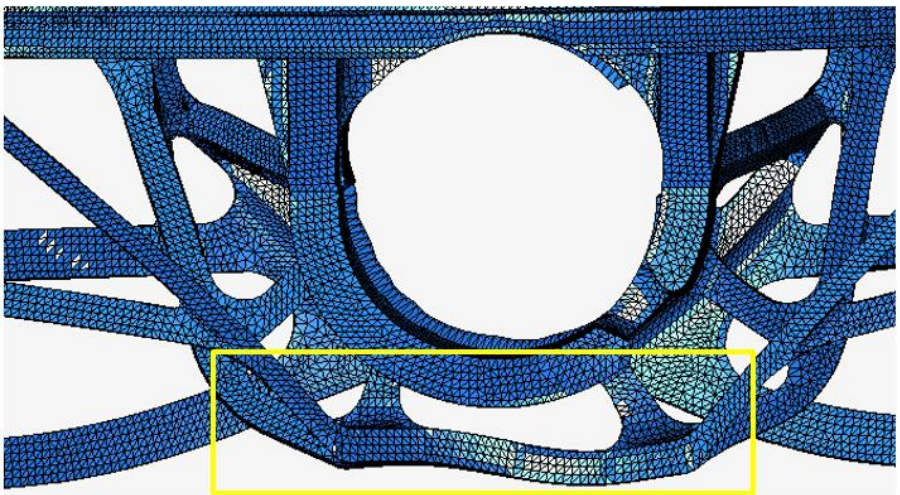

Figure 8.26. PT buckling collapse.

8.4.3 Fatigue analysis of the steel piston

A fatigue analysis has been performed, based on Dang Van criterion [73,74]. This is a stress-based multi-axial criterion employed to compute a fatigue safety factor by taking into account a certain load history. A reverse fatigue limit of 400 MPa has been considered [75–80]. Figure 8.27 shows the Dang Van safety factor contour plot. The whole component presents a minimum factor greater than one. The most critical areas are restricted and placed on the diagonal beams linking the external areas of the piston top to the pin bosses.

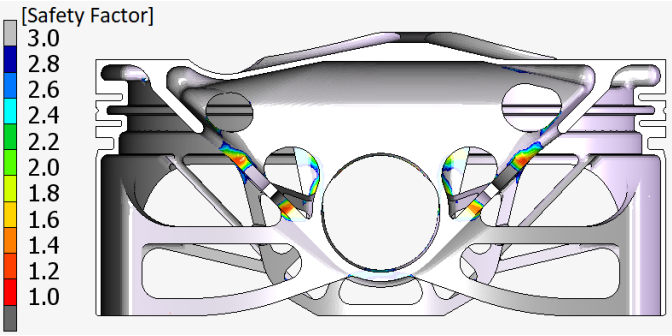

Figure 8.27. Dang Van safety factor contour plot.

Chapter 9: FEM analysis of the original engine

9.1 Introduction

The cylinder liner/piston rings coupling plays a crucial role in engine performance and pollution emission [81–83].

The piston rings have to seal the combustion pressure gas, to control the lubricant oil consumption and to transfer heat from the piston to the liner [17,18,84]. To fulfil these tasks, the whole ring periphery should keep the contact with the liner in engine operating conditions. However, because of mechanical and thermal distortions, the liner is not perfectly cylindrical and it is fundamental to study the piston rings conformability in a distorted liner [85–87].

In the first part of this chapter, a methodology aiming at simplifying the Finite Element evaluation of the liner bore distortion is described. In the second part, a methodology aiming at simplifying the Finite Element evaluation of cylinder liners fatigue behaviour is proposed, in fact, damage mechanisms due to fatigue loading are universally recognized to play an important role for engine liners durability [88]. First, the aluminium piston and a cylinder liner made of aluminium are considered, then the steel piston and a cylinder liner are considered, therefore, three more cases are studied, based on the other three different configurations of the piston-cylinder liner coupling. Table 9.1 collects the main data of the engine under investigation: it is L-twin high performance four stroke engine for motorcycle application.

Table 9.1. Engine data.

Engine Configuration	L-twin
Displacement	955 cm^3
Bore	100 mm
Stroke	60.8 mm
Maximum power	157 HP @ 11000 rpm
Maximum torque	107 Nm @ 9000 rpm
Maximum combustion pressure	91 bar @ 11000 rpm

Loenne [89] categorized the causes of cylinder distortion. The nominal cylindrical shape can be eventually modified by the production process, by the assembly of the engine head, gasket and bolts, by the gas forces, and by friction-related sliding movements in the sealing plane. This sliding phenomenon is caused by different thermal expansions of the cylinder head and engine block. In our work, we have taken into account each of these aspects. We have simulated different geometries of the liners within the range of tolerance. A complex model considering liners, gasket, engine head and block has been set up. Furthermore, thermo-structural simulations have been performed to evaluate the liner deformation under mechanical and thermal loadings.

Loenne et al. [90] employed the GOETZE bore deformation measurement system to correlate the liner bore distortion to different design strategies. In this paper, we have

measured the same experimental data in terms of Fourier coefficients amplitude considering the shape of the water jacket.

Fujimoto et al. [91] described the methodology and the tools necessary to measure the cylinder bore deformation during actual operating engines. The operating condition has been simulated with Finite Elements models obtaining comparable cylinder liner bore distortions.

Koch et al. [92] analysed the cylinder liner deformation using both experimental measurements and Finite Element simulations. In this thesis, a similar Finite Element model has been employed refining the mesh in order to better describe the regions of interest.

Maassen et al. [93] and Yang et al. [94] explained a methodology to optimize the cylinder bore distortion. Using our results, this iterative process of design and verification could be probably quickened.

In 2017 Liang et al. [95] investigated cylinder bore deformation using a complex Finite Element model including the cylinder block, cylinder head, liners and cylinder gasket. In this paper, we design a simplified methodology that needs only the Finite Model of the engine block, liners and bolts. Besides, Liang et al. [95] compared their results with experimental tests on the actual engine. Similarly, in our study, we set up a specific test bench employing a simplified engine head to better measure the cylinder bore distortion. Furthermore, an ad hoc Finite Element model has been properly tuned to compare the simulation with the experimental evidence and to validate the model.

Marathe et al. [96,97] pointed out the importance of head bolt cross pattern tightening and its effect on gasket sealing performance and bore deformation. Therefore, in this work, a sensitivity analysis of the consequences of the bolt tightening on the gasket contact pressures has been taken into account.

9.2 3D Mesh

The software employed are Altair Hypermesh for components discretization and Msc Marc for Finite Element non-linear solution. Only a single engine bench has been considered for this analysis. Figure 9.1-9.5 show the discretized components: the engine head, the bolts, the gasket, the liner and a half of the engine block (taking advantage of the symmetry plane).

About 1554 thousand elements have been employed: 177 thousand pentahedral elements (bilinear, 6 nodes, 6 Gaussian integration points), 295 thousand hexahedral elements (bilinear, 8 nodes, 8 Gaussian integration points) and 1082 thousand tetrahedral elements (first order, 4 nodes, one Gaussian integration point). The average element size changes along the model in order to better describe the regions of interest: one millimetre for gasket and elements in contact with it, two millimetres for the liners and four millimetres for the other areas. Particular attention has been adopted for the modelling of the engine gasket: Figure 9.3 shows the multi-layer steel gasket employed in the analyses: actual non-linear loading and unloading curves have been considered of the different sealing parts.

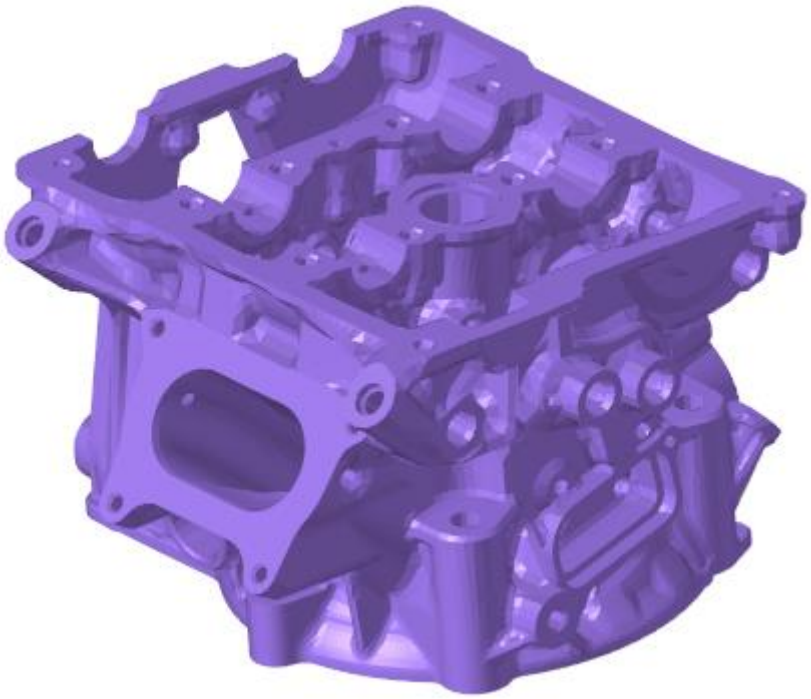

Figure 9.1. Discretized engine head.

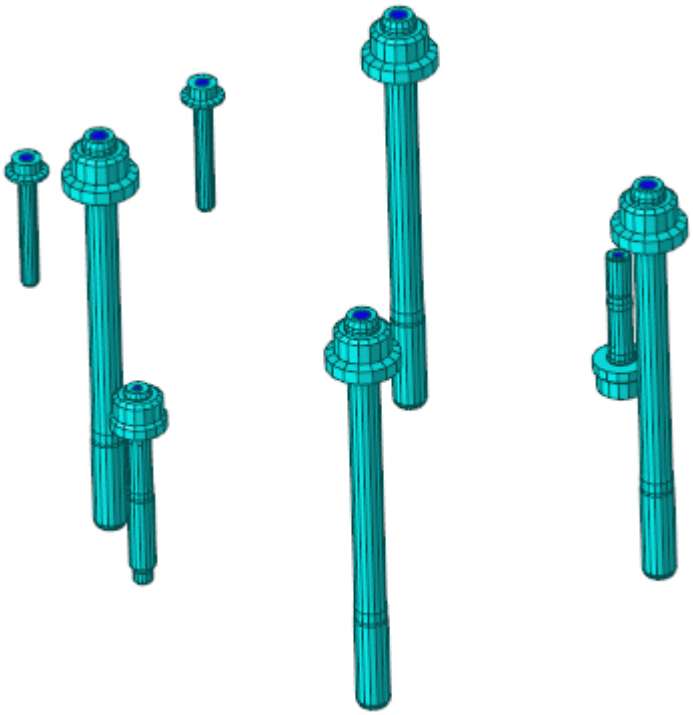

Figure 9.2. Discretized bolts.

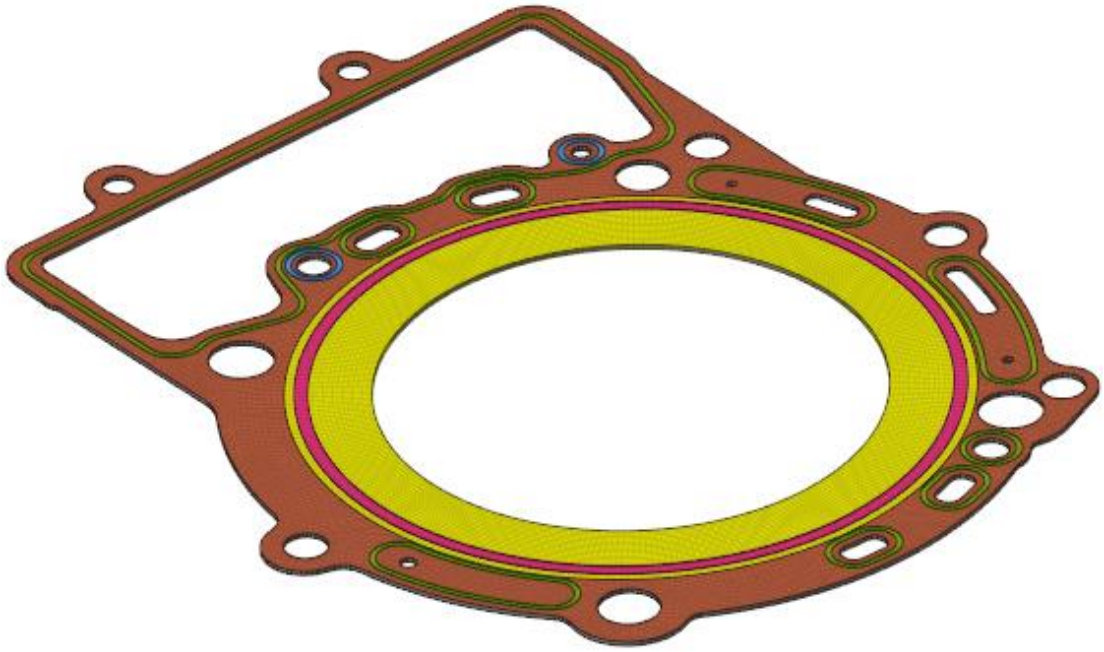

Figure 9.3. Discretized gasket.

Figure 9.4. Discretized cylinder liner.

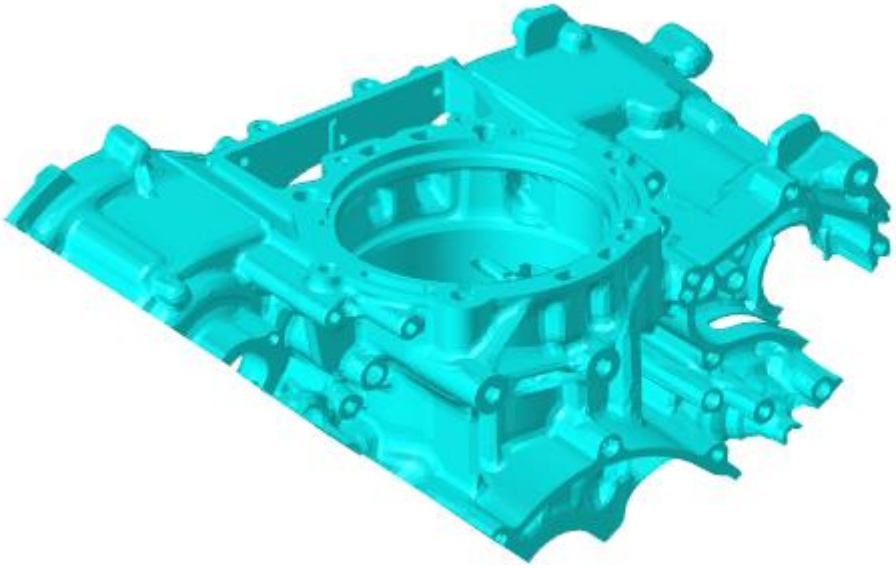

Figure 9.5. Discretized engine block.

9.3 Thermal analysis, aluminium liner

A static thermal model has been set up using boundary conditions averaged over the engine cycle. Because of the high thermal inertia of metals, the oscillations of walls temperatures due to the cyclic variation of entering heat fluxes have been considered to be negligible [98].

The material considered for the modelling of the bolts is a generic steel, while the material considered for the modelling of the engine head, the engine block and the liner is a generic aluminium, whose characteristics are reported in Table 9.2.

Table 9.2. Materials employed.

Component	Material	Thermal conductivity
Engine block	AlSi7Mg06	0.165 W/(mm K)
Liner	AS120	0.157 W/(mm K)
Bolts (M10, M8)	SCM435	0.042 W/(mm K)
Bolts (M6)	Steel	0.039 W/(mm K)
Engine head	GKAlSi10MgCU	0.17 W/(mm K)
Gasket	Steel	0.039 W/(mm K)

Homogeneous boundary conditions have been applied to the oil circuit, to the water jacket and to the external surface of the engine in terms of heat transfer coefficient (HTC) and reference temperature, whose values are specified in Table 9.3.

Table 9.3. Face film boundary conditions.

Application area	HTC [W/ mm^2°C]	T [°C]
Water jacket	0.002	90
Oil circuit	0.0003	120
Combustion chamber	0.001201	1144
Intake duct	0.00014	32
Exhaust duct	0.00026	727
External air	1.5e-5	40

The other boundary conditions have been evaluated using more complex methods, see Chapter 3.

The piston alternating motion has been taken into account for the correct estimation of the boundary conditions applied to the liner. Thus, the effect of the combustion, of the oil and of the heat flux exchanged between the piston and the liner have been inserted using space-dependent tables.

Regarding the contribution of the combustion gases, the HTC and temperature distribution during a single engine cycle has been considered, Figure 9.6 shows the profiles of these values. Each axial-coordinate of the liner has been studied and the values of HTC and temperature involved in this point have been identified as a function of the piston stroke. For instance, a face at the top of the liner receives the effect of gases during the whole engine cycle, while a face at the end of the stroke is subject only to the HTC and temperature at the bottom dead centres. Once these proper values have been identified, a mean value has been applied as a function of the axial coordinate, Figure 9.7 shows the tables applied in the FE model.

The boundary condition related to the oil has been identified following a similar procedure. Figure 9.8 shows the thermal oil contribution applied in the FE model: the faces of the elements of the top part of the liner are not exposed to the oil, because they are always shielded by the piston crown or exposed to gases. The maximum value of the HTC of oil has been applied to the lowest part of the liner, these faces are always exposed to the splashing oil. Therefore, the HTC of centrifuged oil in the sump corresponds to the maximum value of the chart. The maximum and the minimum value of the chart have been connected to each other based on the velocity of the piston. The faster the piston is, the lower the HTC is.

The heat flux related to the contact between the piston and the liner has been composed by the heat transfer by conduction from the piston to the liner and by the effect of friction.

The heat transfer by conduction has been quantified as a certain portion (30%) of the heat flux that enters the piston top and exits from the piston skirt and rings. In addition, this effect has been applied considering the piston stroke and the velocity of the reciprocating components: the more the piston is slow, the more the heat is transferred to the liner, Figure 9.9 shows the table applied to the FE model to modulate the heat flux.

The effect of the friction has been taken into account by estimating the heat flux generated by the piston and the ring for each axial-coordinate of the stroke. Figure 9.10 shows these values, they have been properly assigned to the liner by summing for each coordinate the corresponding heat fluxes. The heat flux that enters the liner and exits from

the water jacket has been quantified as a certain portion (85%) of the heat flux generated by friction. This portion has been quantified considering the different thermal resistance produced by the liner and by the piston. The difference between the values of HTC and the temperature of the water surrounding the liner and of the oil splashing the piston has been proved to be the most important parameter in this analysis.

Figure 9.11 and 9.12 show the results of the thermal analysis. In particular, Figure 9.13 and 9.14 represent the temperature contour plot of the liner. The uneven HTC distribution of the water jacket and the different heat fluxes produced by the piston at the thrust and at the antithrust areas strongly condition the cylinder liner. Therefore, this temperature distribution is non-axisymmetric.

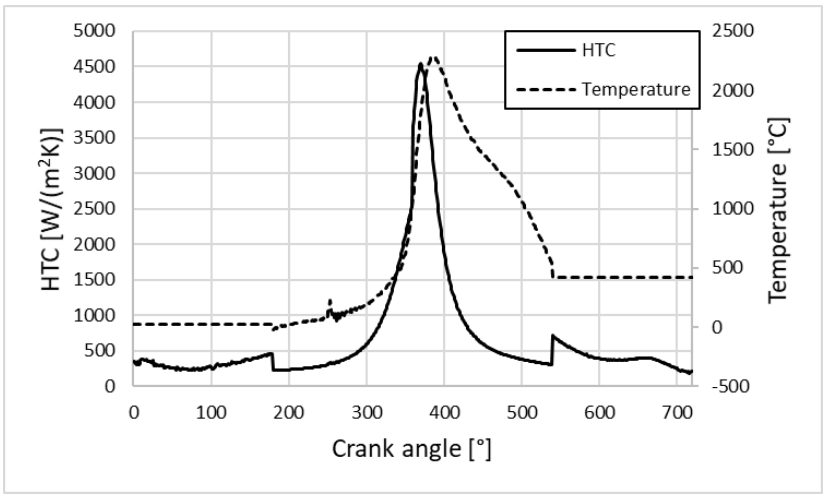

Figure 9.6. HTC and temperature distribution in an engine cycle.

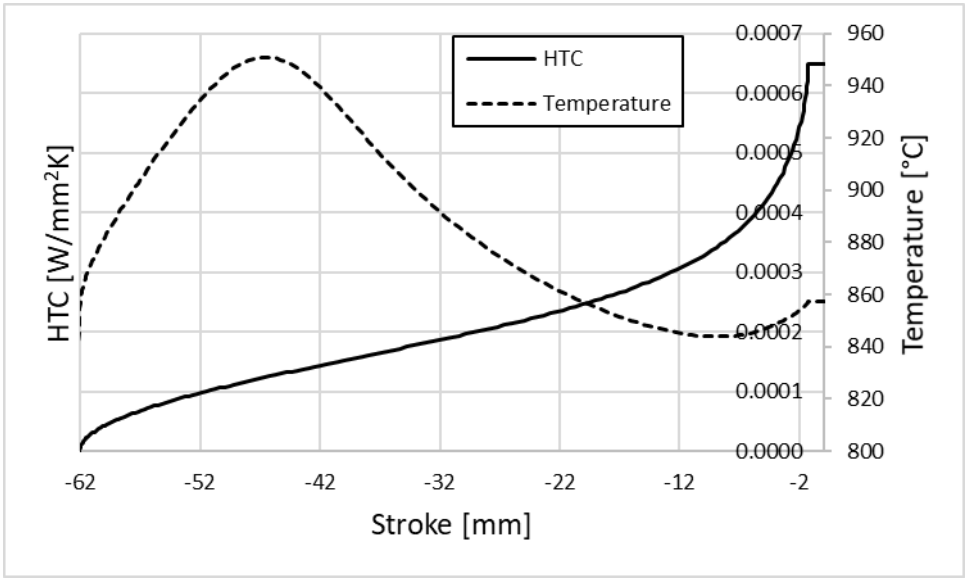

Figure 9.7. axial-coordinate HTC and temperature distribution of gases along the liner.

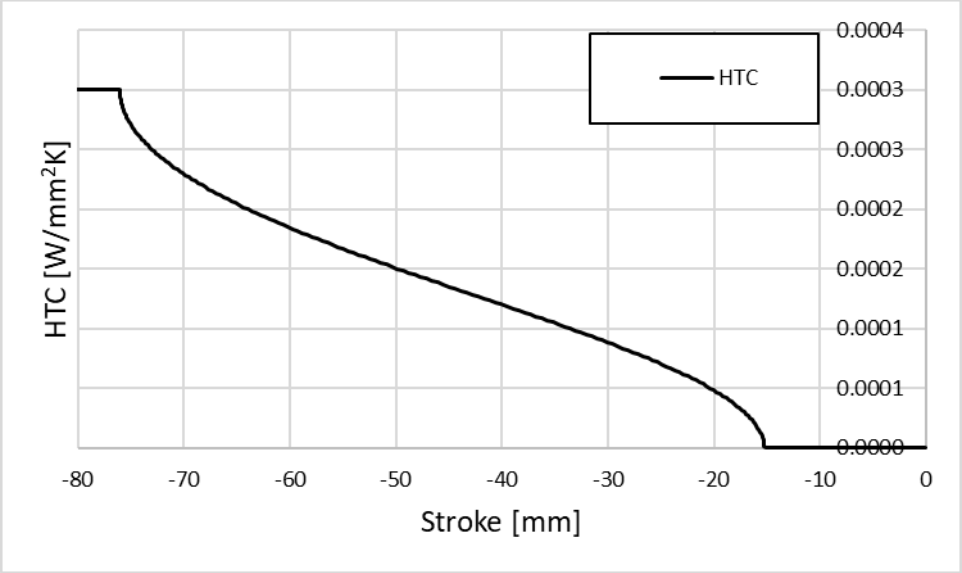

Figure 9.8. Axial-coordinate HTC distribution of oil along the liner.

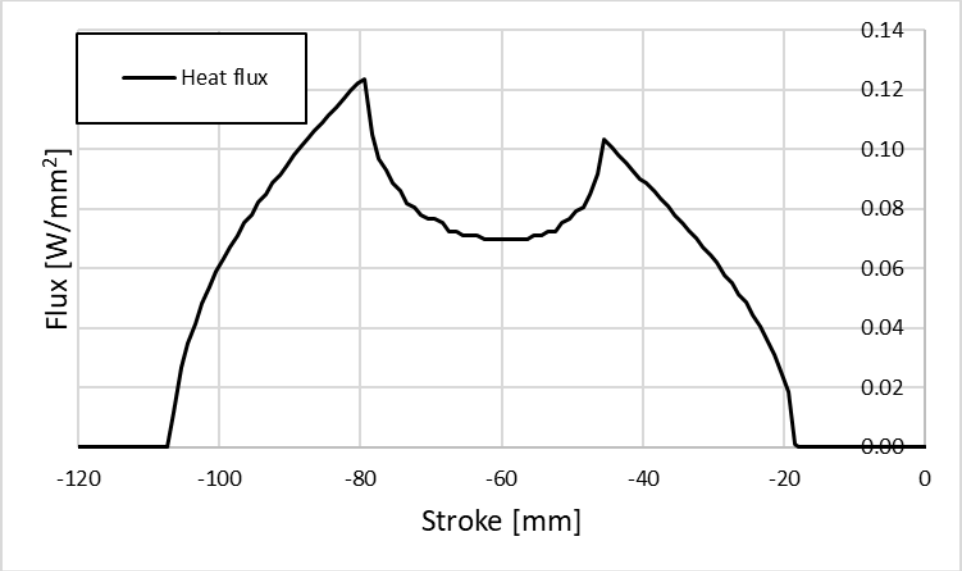

Figure 9.9. Axial-coordinate distribution of heat flux due to conduction along the liner.

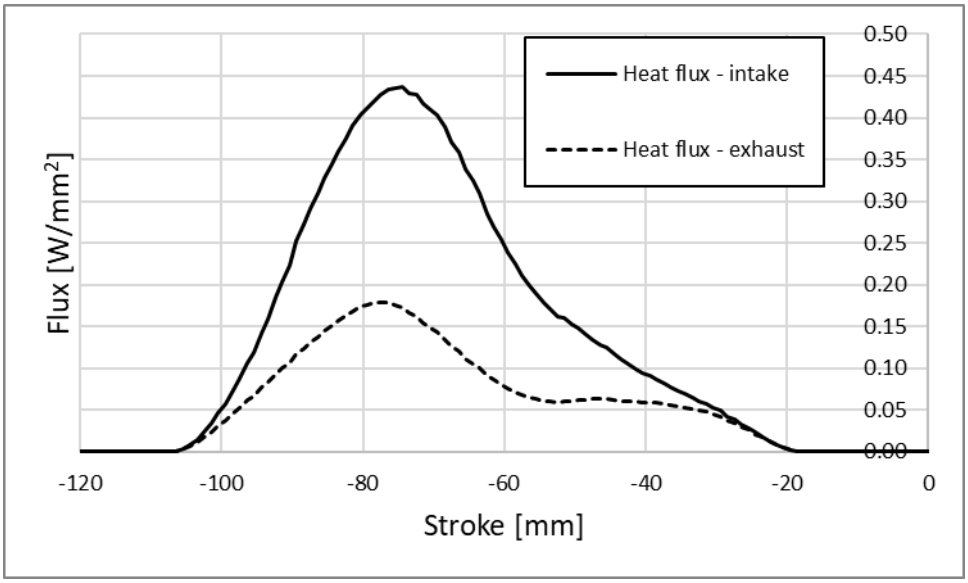

Figure 9.10. Axial-coordinate distribution of heat flux due to the friction forces along the liner.

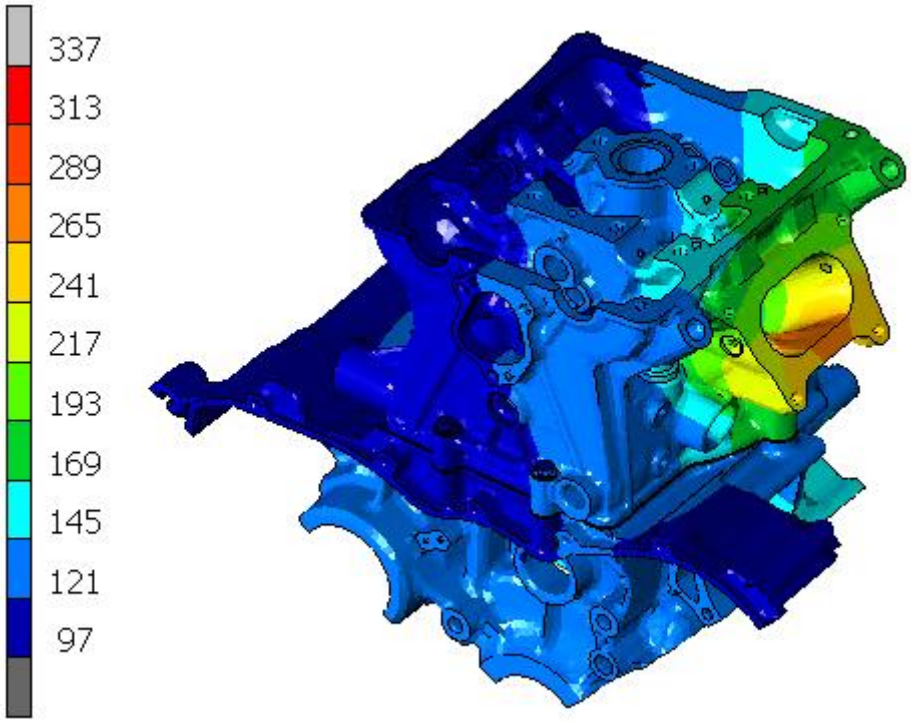

Figure 9.11. Temperature contour plot of the engine [°C].

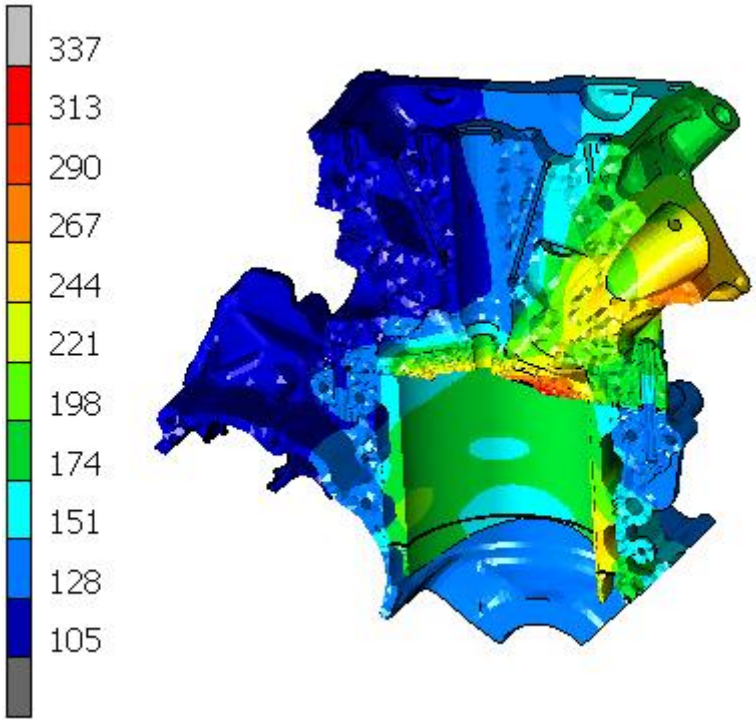

Figure 9.12. Figure 9.11. Temperature contour plot of the engine [°C].

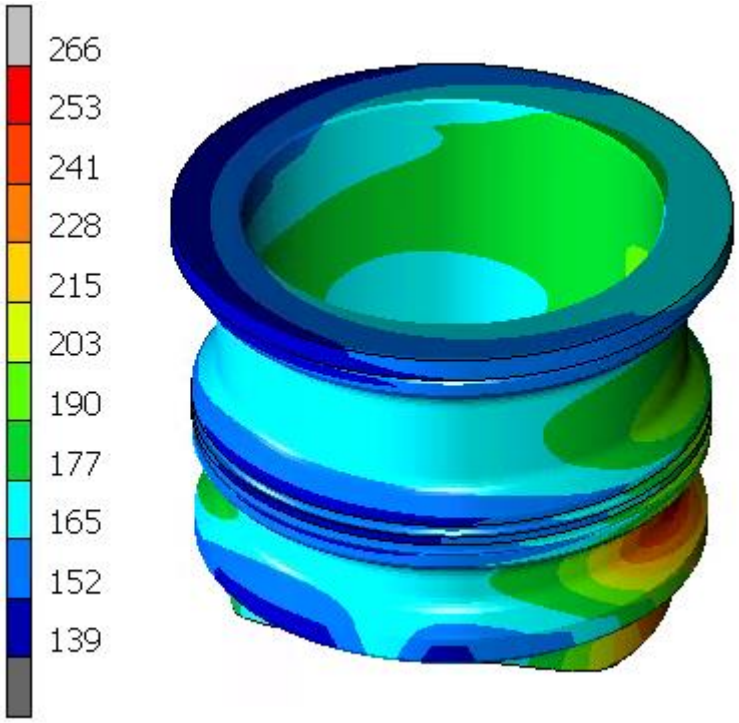

Figure 9.13. Figure 9.11. Temperature contour plot of the liner [°C].

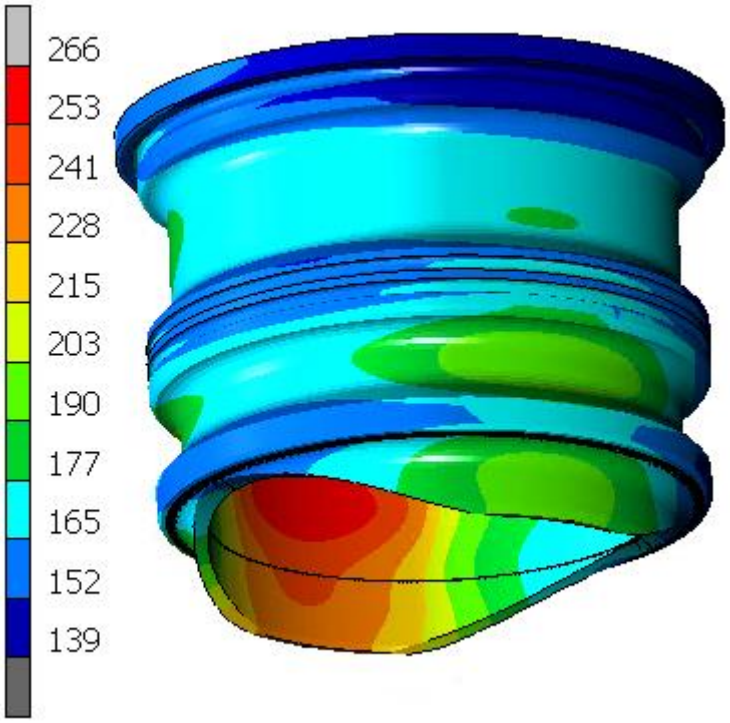

Figure 9.14. Temperature contour plot of the liner [°C].

9.4 Structural thermo-mechanical analysis, aluminium liner

The thermo-structural model mimics two different instants. The bolts have been tightened and the temperature field has been applied, first, the condition of no pressure in the combustion chamber has been simulated, then, the condition of maximum pressure has been simulated. The most important result to take into account is the bore distortion, Figure 9.15 shows the inner profile of the liner has been measured every 10 mm along an axial coordinate. In particular, the deformed bore profile has been expanded in term of Fourier series and the amplitude of the single orders have been considered, Figure 9.16. The evaluation of the liner bore distortion in terms of Fourier coefficients is fundamental for the choice of the most suitable piston ring pack. In fact, each ring is usually designed to ensure perfect sealing of the combustion chamber within a certain range of amplitudes of the Fourier coefficients.

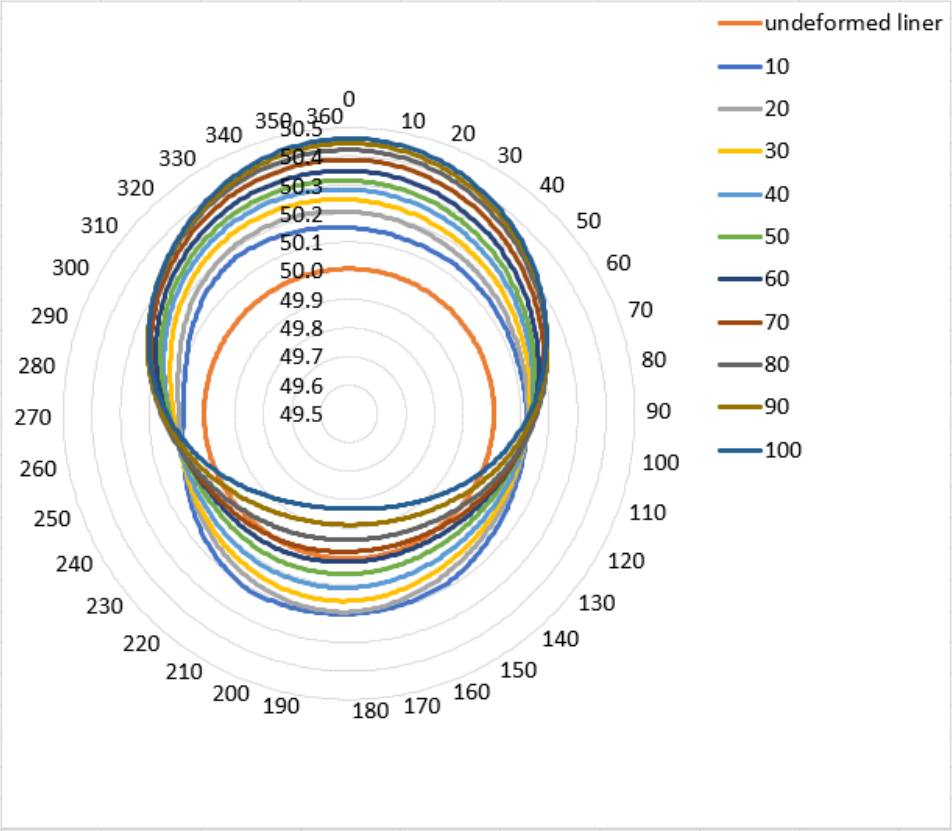

Figure 9.15. Cylinder- liner bore distortion plot [mm].

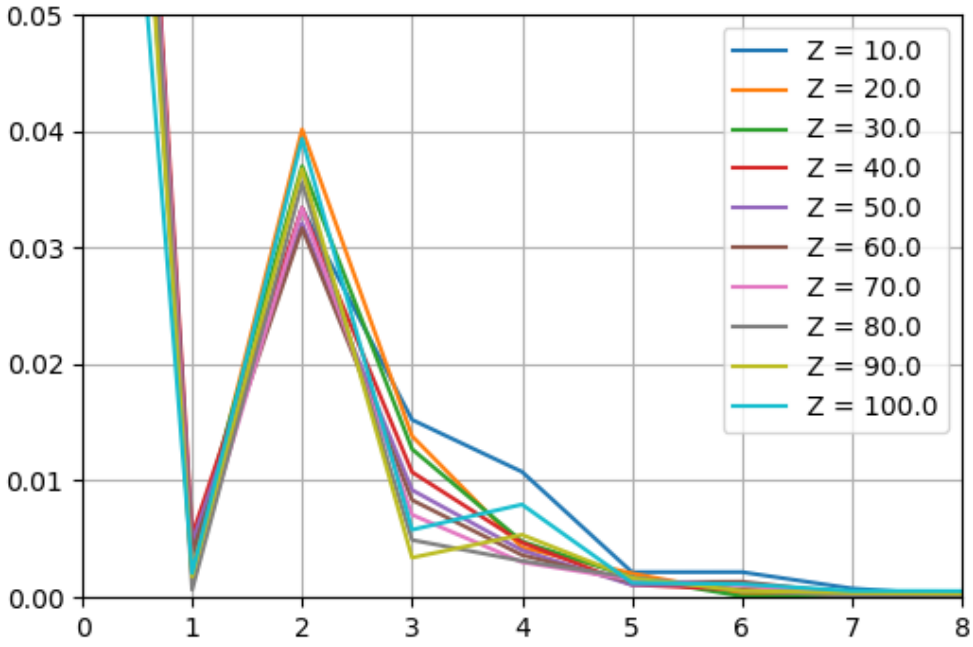

Figure 9.16. Fourier decomposition plot [mm].

9.4.1 The simplified Finite Element model

In [99], a methodology aiming at simplifying the Finite Element model employed to evaluate the cylinder liner bore distortion is presented. In this thesis, the same steps have been applied. In fact, a simplification of the model is crucial to study the piston – liner contact interaction. The decrease in the number of elements and in the sources of non-linearity can surely reduce the computational effort. The number of elements should not be limited by using a coarser mesh, but by removing all unnecessary elements. Consequently, the head, the gasket and the upper part of the bolts have been removed, while the liners and the block have been kept with the same mesh resolution. In this way, three different sources of contact non-linearity have been removed. On the other hand, the contact interaction between the liners and the block, which strongly affects the bore distortion, has been kept. Figure 9.17 shows the simplified Finite Element model employed in this analysis. The removed components have been then replaced with suitable loadings.

In particular, Figure 9.18 shows the simplification adopted for the bolts. The upper part of each bolt has been removed and a tensile force has been applied to each node of these sections. The sum of the forces of each section is equal to the tightening force applied to each bolt in the complete model.

Considering the liner, the contact interaction between the flange and gasket has been simplified. The gasket has been removed the contact forces have been applied directly to the liner flange. It is important to notice that the flange is in contact with both the structural layer (yellow) and the full bead (pink) of the gasket, Figure 9.19. These two contact interactions have been considered in two different ways. The structural layer softly touches the flange and a quite homogeneous low value of the contact force is generated between these components. So, in the simplified model, the resultant contact pressure has been converted into a perfectly homogeneous pressure applied directly to the flange (light blue in Figure 9.20).

The pressure applied by the full bead on the liner flange has been applied directly on the liner in a more detailed way (the white region in Figure 9.20) because it strictly affects the liner bore distortion. Figure 9.21 shows the contact pressure of the full bead acting on the liner flange. These results have been adopted to refine the simplified model. The distribution of the contact pressure between the full bead and the liner flange has been analysed using a Fourier decomposition until the 12^{th} order, Figure 9.22 shows the actual profile of the contact pressure moving along the liner flange (solid) and the Fourier decomposition of this profile (dashed). Finally, the Fourier series has been properly assigned to the liner flange. It is easy to guess that the most important order of the pressure profile of the complete engine is the 6^{th} one, in fact, figure 9.22 shows 6 peaks and 6 valleys, and this surely depends on the six bolts that surround the liner. However, Figure 9.23 shows the Fourier decomposition until the 6^{th} order, this profile could seem too inaccurate. For this reason, it has been necessary to use a higher order (12) to catch some features, such as the “double valley” of the second big valley showed between 1 and 2 radians. In fact, this feature of the profile could have been caught only by doubling the orders considered.

Finally, the contact interaction between the deck and the half beads and between the deck and the structural layer has been considered to have little influence on the

deformation of the liner, since these contact pressures have a low value and the distribution is quite scattered on the deck of the block. For this reason, the resultant force has been applied via a homogeneous pressure distribution directly on the deck, Figure 9.24.

Table 9.4 collects the value of pressures and forces applied to the simplified model. Please consider Figure 9.25 for the numbering of the bolts.

Table 9.4. Pressure and forces for the simplified model.

Application area	Value
Chamber pressure	0.00 MPa
Liner flange pressure	12.13 MPa
Engine deck pressure	14.09 MPa
Bolt 1	12913 N
Bolt 2	12734 N
Bolt 3	50726 N
Bolt 4	26073 N
Bolt 5	52288 N
Bolt 6	55558 N
Bolt 7	28695 N
Bolt 8	53249 N

Figure 9.26 and Figure 9.27 compare the deformed shape of the liner. The inner shape of the liner has been post-processed, the deformed shape bore has been retrieved every 10 mm along the axial coordinate. Figure 9.26 and 9.27 display the deformed bore at 10 mm and 20 mm from the top of the liner flange. These profiles are very close to each other, therefore the refined simplified model has been validated and this obtained tuning will be employed in the following steps.

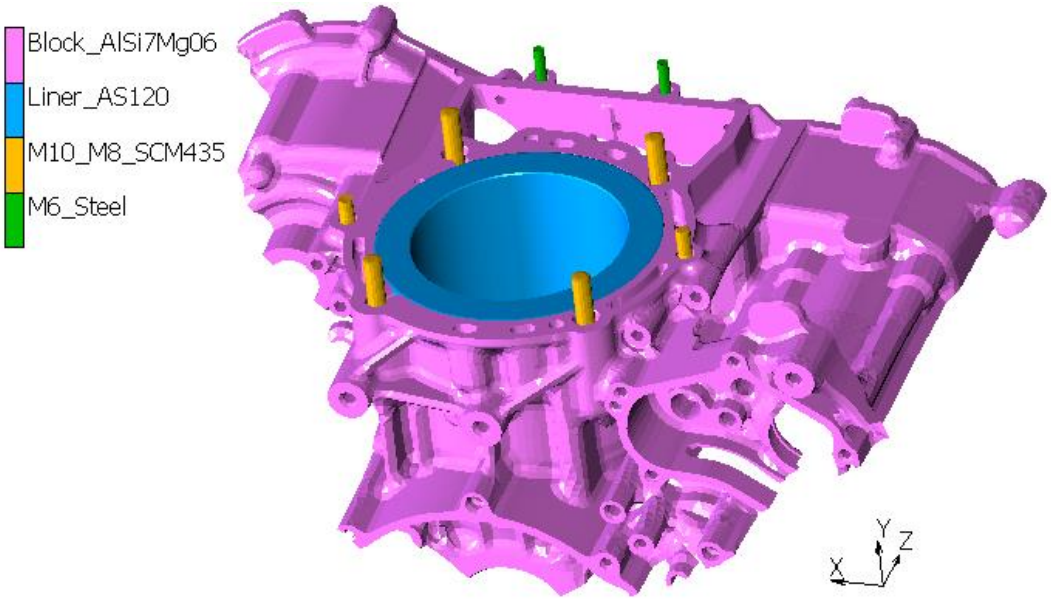

Figure 9.17. The simplified model.

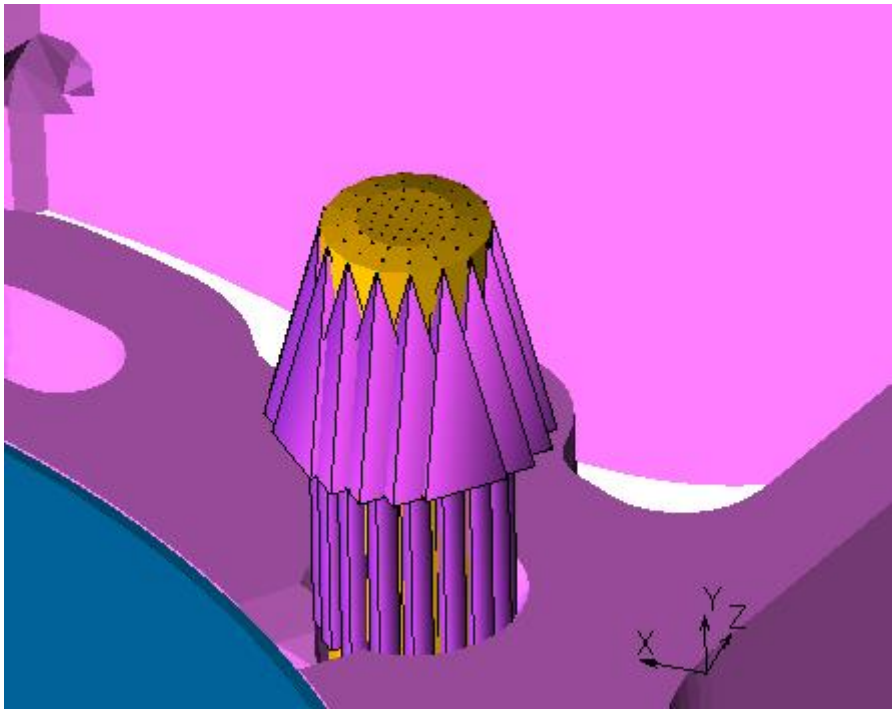

Figure 9.18. Detail of the cross-section of the bolts.

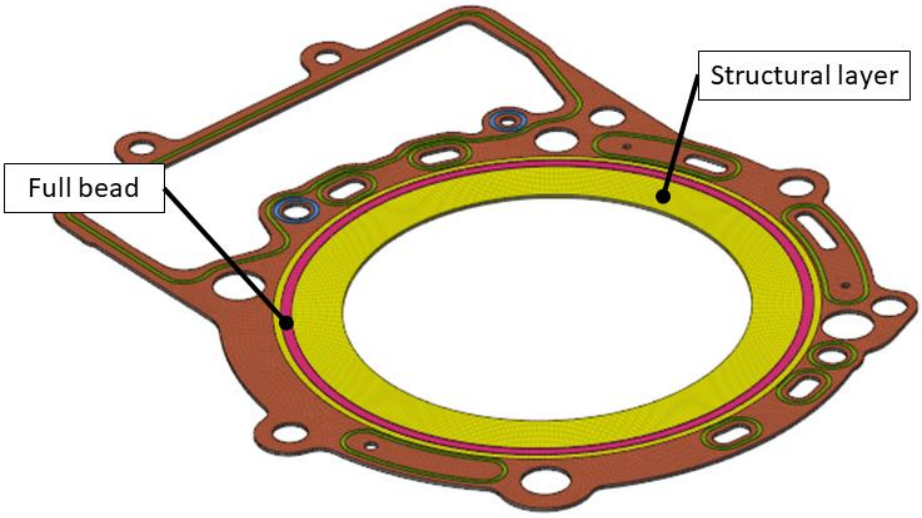

Figure 9.19. The gasket.

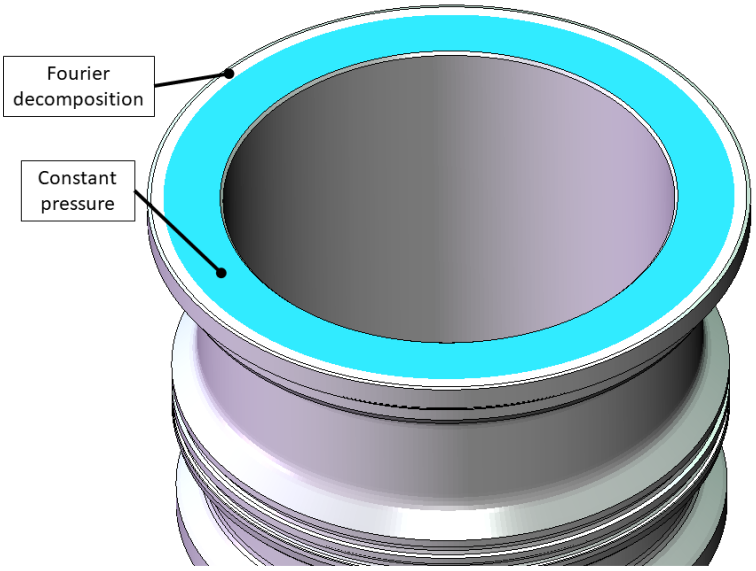

Figure 9.20. Detail of the liner flange.

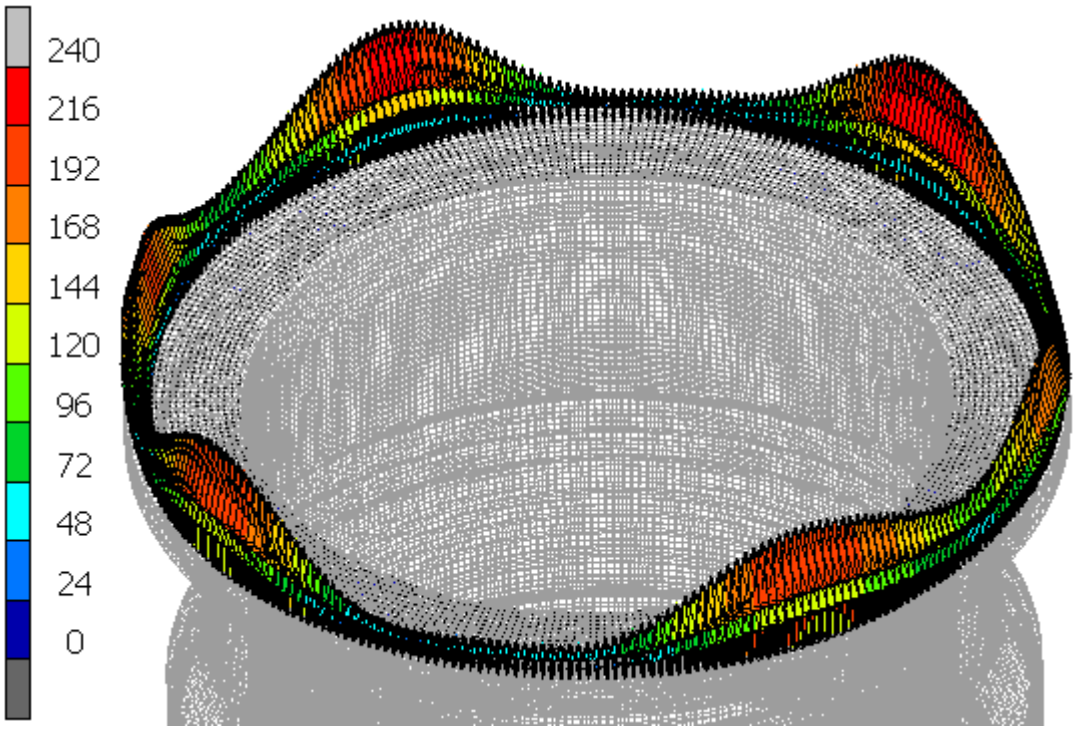

Figure 9.21. Contact normal forces of the flange [N]

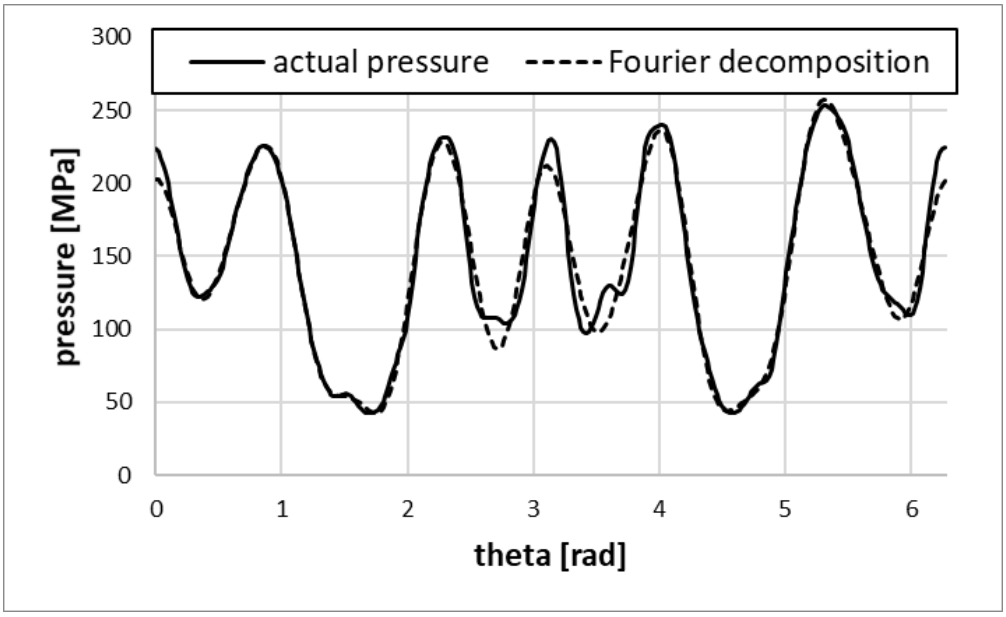

Figure 9.22. Contact normal pressure profile.

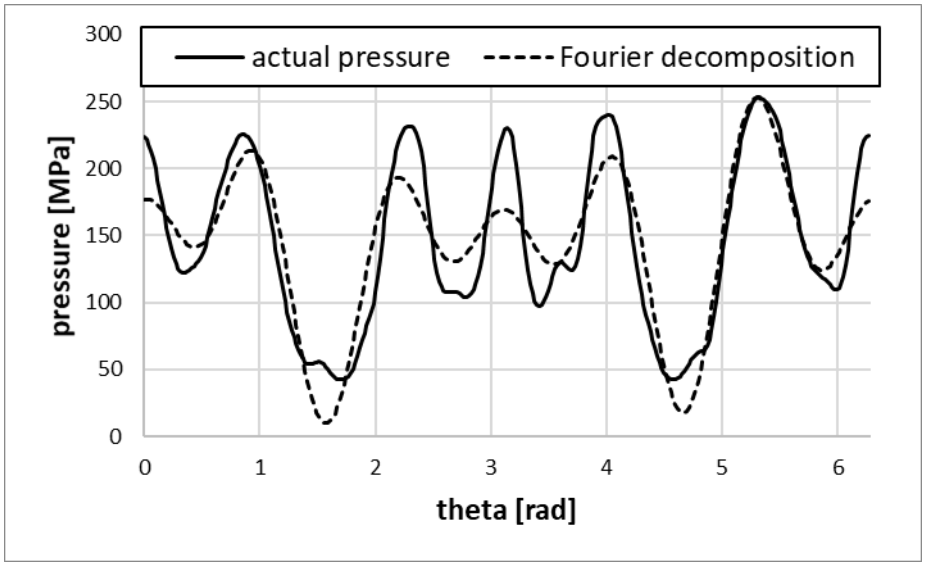

Figure 9.23. Contact normal pressure profile.

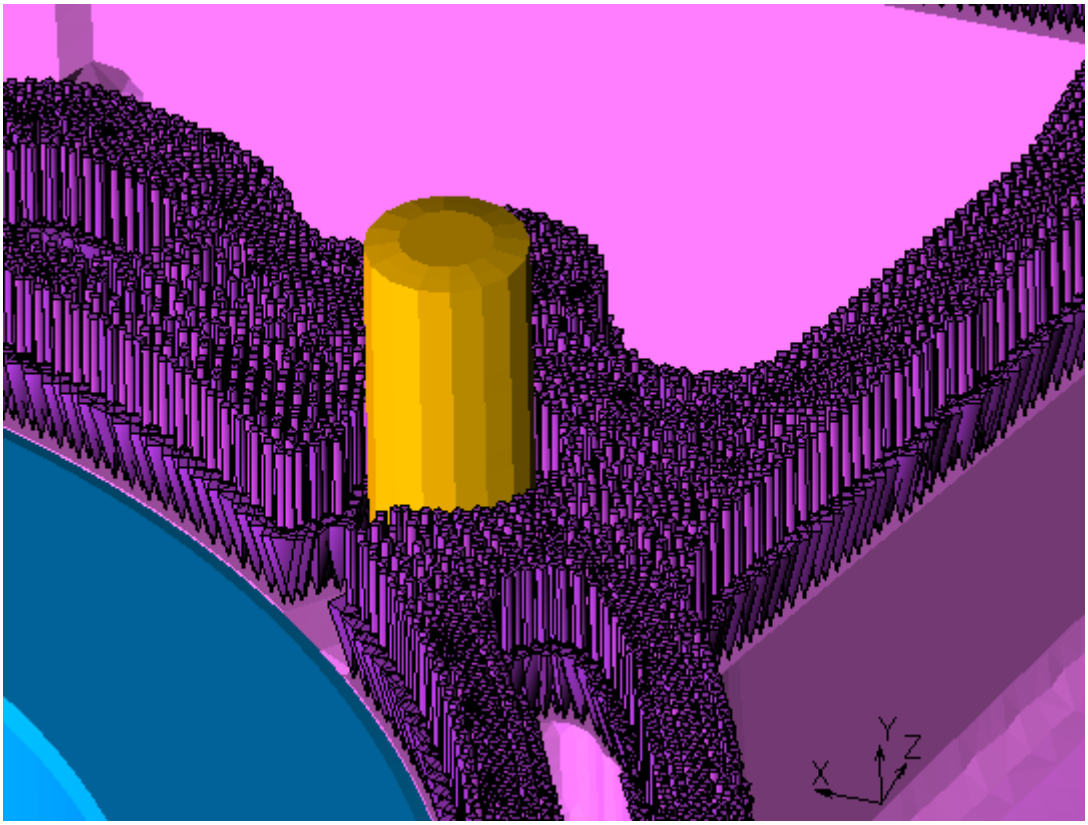

Figure 9.24. Detail of the deck surface.

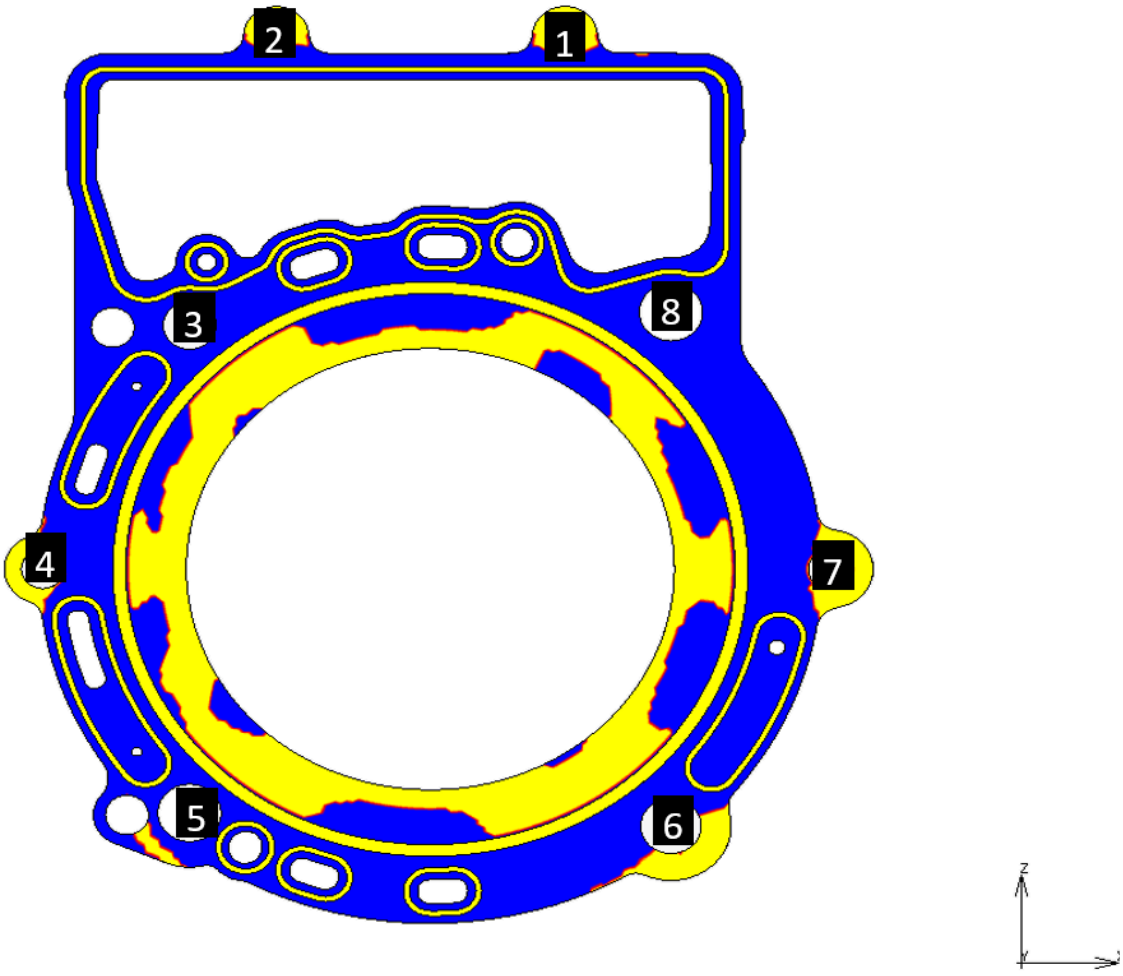

Figure 9.25. Contact status contour plot, the numbering of the bolts.

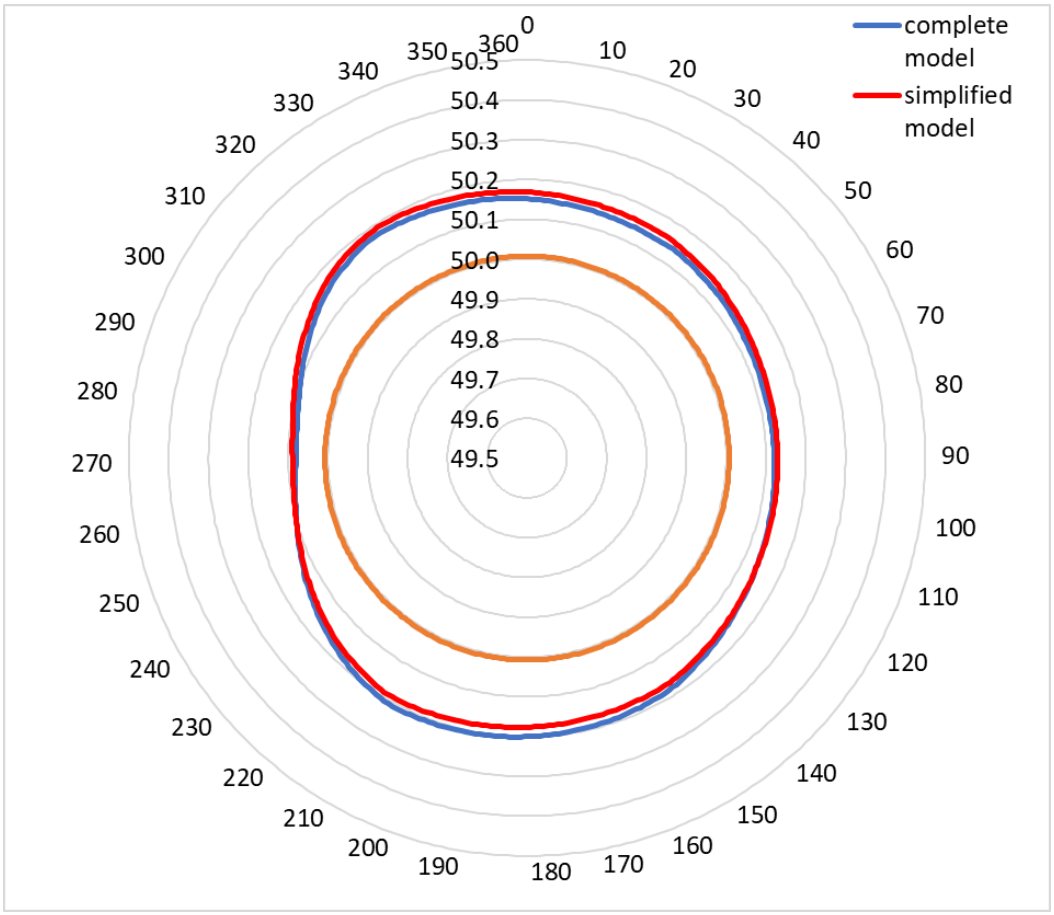

Figure 9.26. Comparison of the deformed bore at 10 mm from the flange. [mm]

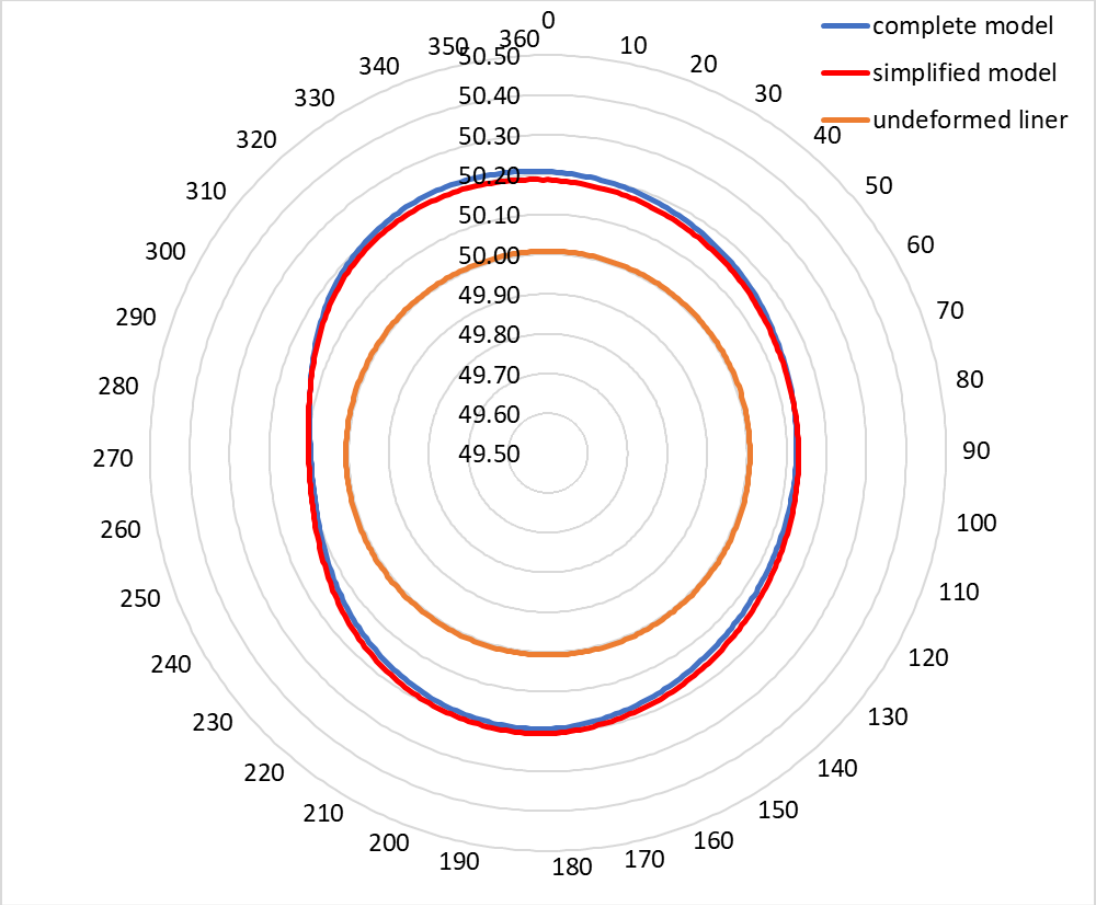

Figure 9.27. Comparison of the deformed bore at 20 mm from the flange. [mm]

9.5 Fatigue analysis, aluminium liner

In [100], a methodology aiming at simplifying the Finite Element evaluation of cylinder liners fatigue behaviour is described. In this thesis, the same methodology has been applied.

The cyclic thrust force of the crank mechanism may cause the fatigue failure of the cylinder liner. The piston thrust profile has been analysed to identify the extremes of the fatigue cycle and to minimize the computational effort by reducing the simulations necessary to compute the resulting fatigue safety factor distribution. The value of thrust force alone cannot identify the fatigue cycle, since the stress status of the liner depends on the instantaneous position of the piston for each different crank angle. Thus, the liner layout has been considered as two simply supported beams between its interference fit supports, Figure 9.28, and the bending moment profile has been estimated, Figure 9.29. Five different local maxima or minima have been identified, Figure 9.29, and employed to identify the corresponding static mechanical analysis to be performed.

Two disconnected simply supported beams have been considered instead of a hyperstatic one based on the coupling of the liner with the block. In fact, there is a small

gap between the blue figures in Figure 9.28 so that it is plausible that only two of these three features are in contact at the same time.

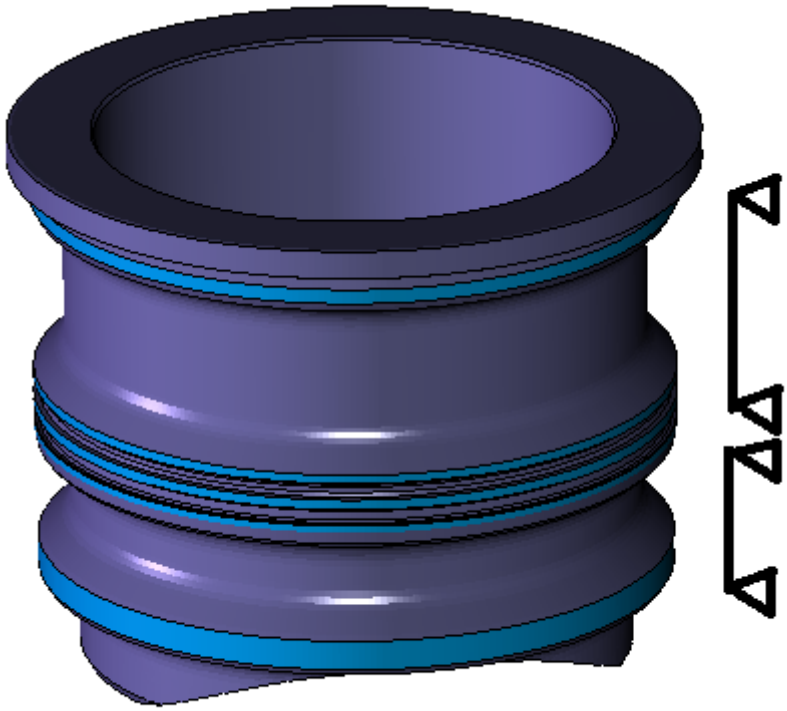

Figure 9.28. Culinder liner semplification.

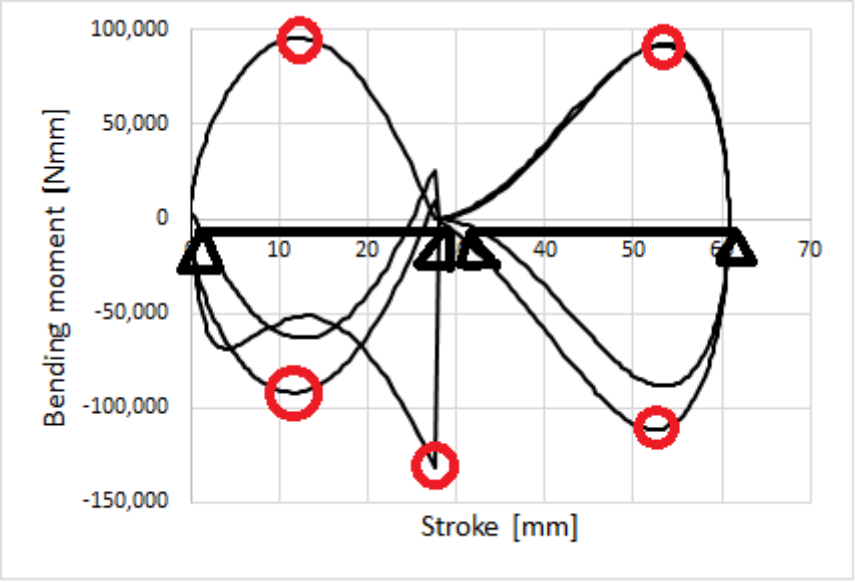

Figure 9.29. Bending moment profile.

9.5.1 Fatigue analysis

The crank mechanism has been added to the previous model. The components involved (piston, piston pin, and the connecting rod small end) have been discretized: about 560000 elements have been employed, the average element size being 1 millimetre, figure 9.30. The material considered for the modelling of the connecting rod and of the piston pin is generic steel, while the material considered for the modelling of the piston is generic aluminium.

A static thermo-mechanical model has been set up for each load case.

The connecting rod has been correctly tilted and positioned and different mechanical loads have been applied depending on the piston position during the operating cycle. In particular, the alternating inertial acceleration has been evaluated as a function of the crank angle θ by the classical formula

$$a(\theta) = \omega^2 r[cos\theta + \lambda \cos(2\theta)] \tag{9.1}$$

where ω is the angular velocity, r is the crank radius and λ is the connecting rod ratio. The inertial acceleration has been applied to all the elements of the crank mechanism, considering that the portion of the connecting rod that has been modelled approximately corresponds to its reciprocating part.

The proper combustion gas pressure has been applied based on the referring crank angle in terms of pressure value and application region.

The other boundary conditions (bolt tightening, pressure applied to de deck, Fourier decomposition of the pressure applied to the outer part of the liner flange and pressure applied to the inner part of the liner flange) have been obtained considering their value at the condition of null and maximum chamber pressure. Therefore only two complete simulations have been necessary and the five obtained load cases have been simplified

In particular, a linear interpolation has been employed. The value of each necessary boundary condition has been extracted using the following formula:

$$a_\theta = (a_{max} - a_{min}) \frac{p_\theta - p_{min}}{p_{max} - p_{min}} + a_{min} \tag{9.2}$$

where p_θ is the chamber pressure of the specific load-case, p_{max} and p_{min} are the maximum and minimum chamber pressure registered along the whole engine cycle, a_θ represents any physical quantity to compute (the pressure acting on the liner flange, on the deck, on the bolts or a coefficient of the Fourier decomposition for the full bead) and a_{max} and a_{min} are the values of the same physical quantity registered at the condition of maximum and minimum chamber pressure respectively, Figure 9.31.

Table 9.5 collects the values of pressures and forces applied in each load case. It is easy to notice that all boundary conditions applied to the engine are similar to the ones of the condition of null chamber pressure (table 9.4) so that it is also easy to understand that Figure 9.31 is only for a didactic purpose. On the other hand, the position and the acceleration of the crank mechanism have had a remarkable influence on the results.

Table 9.5. Pressure and forces for the simplified model.

Load case	Maximum pressure	1	2	3	4	5
Application area	Value	Value	Value	Value	Value	Value
Crank angle	/	47 CA	228 CA	437 CA	491 CA	674 CA
Chamber pressure	9.81 MPa	0.05 MPa	0.15 MPa	1.45 MPa	0.64 MPa	0.13 MPa
Liner flange pressure	3.10 MPa	12.08 MPa	11.98 MPa	10.70 MPa	11.50 MPa	12.00 MPa
Engine deck pressure	12.59 MPa	14.09 MPa	14.07 MPa	13.85 MPa	13.99 MPa	14.07 MPa
Bolt 1	12922 N	12913 N	12913 N	12915 N	12914 N	12913 N
Bolt 2	12737 N	12734 N	12734 N	12734 N	12734 N	12734 N
Bolt 3	51856 N	50732 N	50745 N	50906 N	50805 N	50743 N
Bolt 4	26224 N	26074 N	26075 N	26097 N	26083 N	26075 N
Bolt 5	53752 N	52296 N	52312 N	52521 N	52390 N	52310 N
Bolt 6	56495 N	55563 N	55573 N	55707 N	55624 N	55572 N
Bolt 7	28950 N	28696 N	28699 N	28735 N	28713 N	28698 N
Bolt 8	55570 N	54256 N	54270 N	54459 N	54341 N	54268 N
Reciprocating acceleration	/	$26E^3 m/s^2$	$-28E^3 m/s^2$	$-0.72E^3 m/s^2$	$-28E^3 m/s^2$	$0.28E^3 m/s^2$

A fatigue analysis has been performed, based on Dang Van criterion [73,74,101,102]. Figure 9.32 and 9.33 show the Dang Van safety factor contour plot, an alternating fatigue stress limit of 125MPa has been applied. The most critical area is restricted and located on the lower part of the liner, on the thrust side (Figure 9.32). Figure 9.33 shows the upper part of the liner, where the flange is subjected to a heavy fatigue loading.

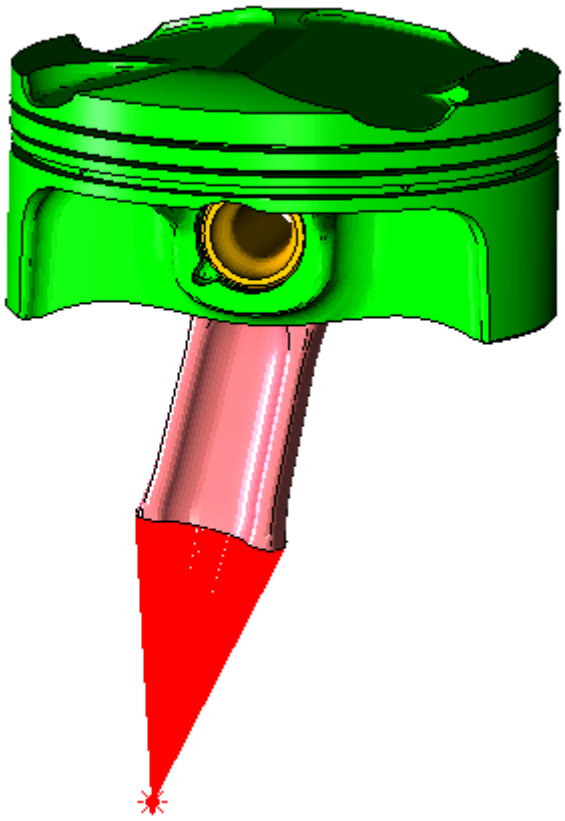

Figure 9.30. The crank mechanism.

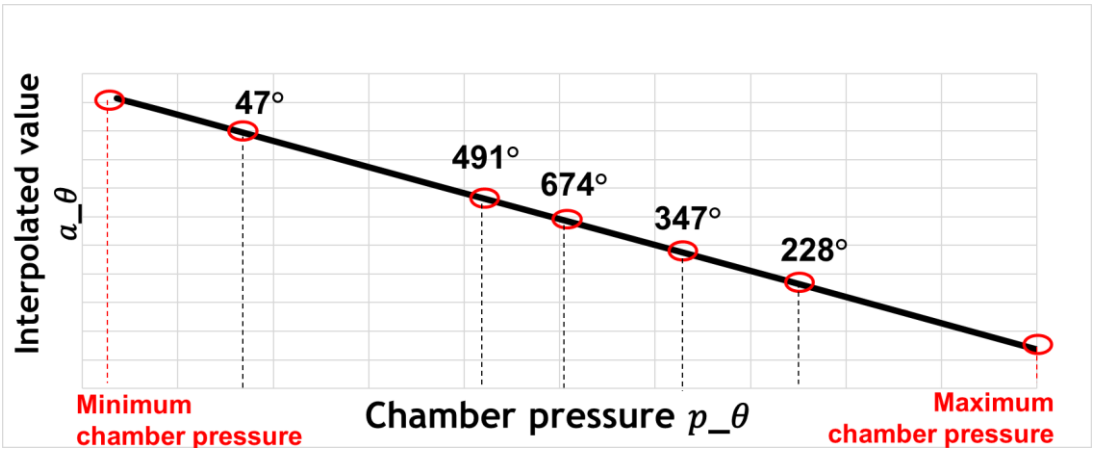

Figure 9.31. The linear interpolation.

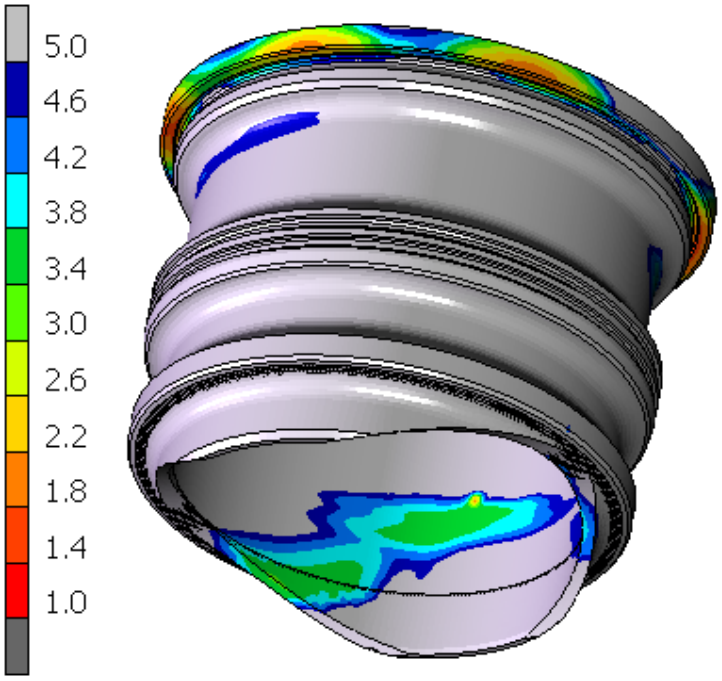

Figure 9.32. Dang Van safety factor contour plot.

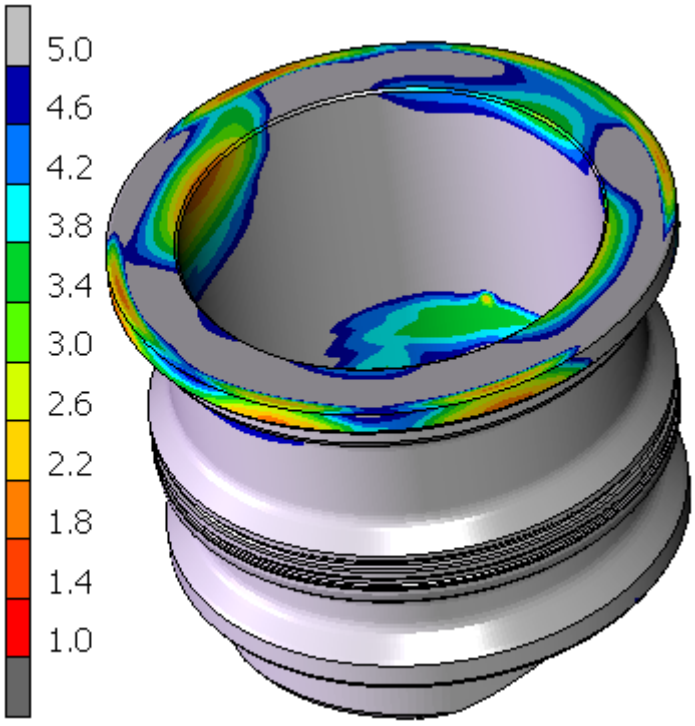

Figure 9.33. Dang Van safety factor contour plot.

9.5.2 The simplified model of the fatigue analysis

If the analysis is focused on the cylinder liner, it is possible to remove one more source of non-linearity.

The crank mechanism has been substituted by a suitable pressure distribution acting on the liner, mimicking the piston-liner interaction, in order to further simplify the model. The distribution of the contact pressure on the piston has been analysed for the load case of absolute maximum bending moment, Figure 9.34. Thus, the resulting force has been applied to the liner using a simple and homogenous pressure distribution, Figure 9.35. A static analysis has been computed for each identified load-case and a fatigue analysis has been performed. Figure 9.36 and 9.37 show the Dang Van safety factor contour plot obtained employing this simplified approach. The minimum safety factor distribution is similar to that obtained by the complete model described in the previous section with a maximum relative deviation of 10% and a reduction of the computational time of 90%.

It is necessary to specify that the contact area between the piston and the cylinder liner varies with the crank angle based on a different value of piston lateral thrust force so that it could be more precise to change the shape of the constant pressure applied directly to the liner. However, the results show that this further refinement of the model is not necessary.

In addition, these results show that these calculations are not naive because of the lack of the influence of the lubricant. In fact, the lubricant, in static analyses, could only smooth the peaks of contact pressure and not change the value of the resultant contact forces generated between the piston and the cylinder liner. In this simplified fatigue analysis, a perfectly homogeneous pressure distribution is applied and a safety factor contour plot fully compatible with the complete model is obtained. So that it is easily imaginable that the presence of lubricant in these static analyses is not necessary. However, the correct modelling of lubricant is a key factor in dynamic and multi-body analyses. The application of a coupled methodology using static and multi-body simulation could be found in [103], the multi-body software has been employed to find the border of the fatigue cycle and to retrieve the actual values of the axial and lateral acceleration of the piston considering the dynamic effects, while static simulation has been set up to obtain the stress and strain field and, consequently, the safety factor contour plot.

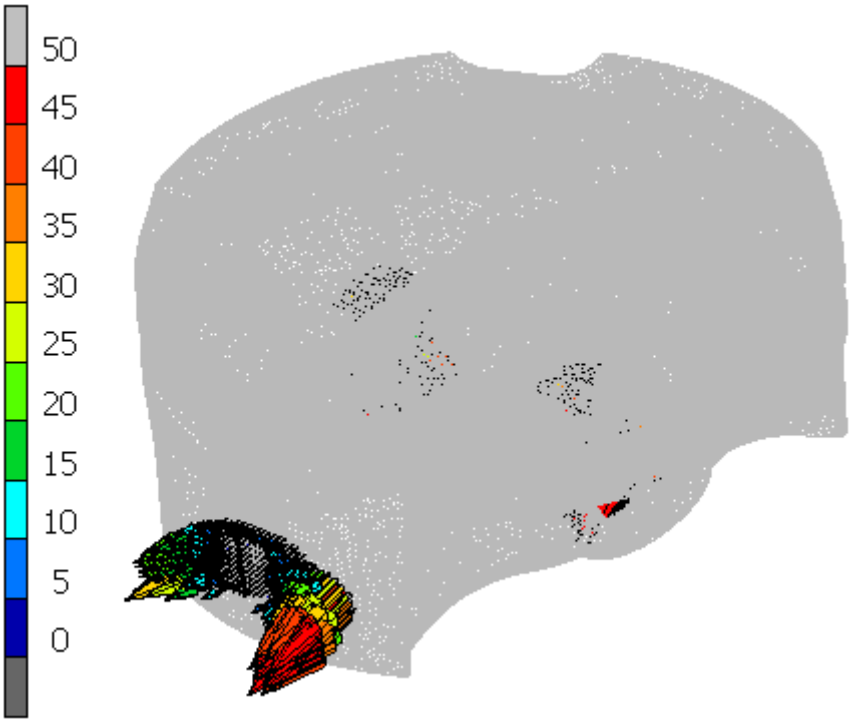

Figure 9.34. Contact normal force vector plot [N].

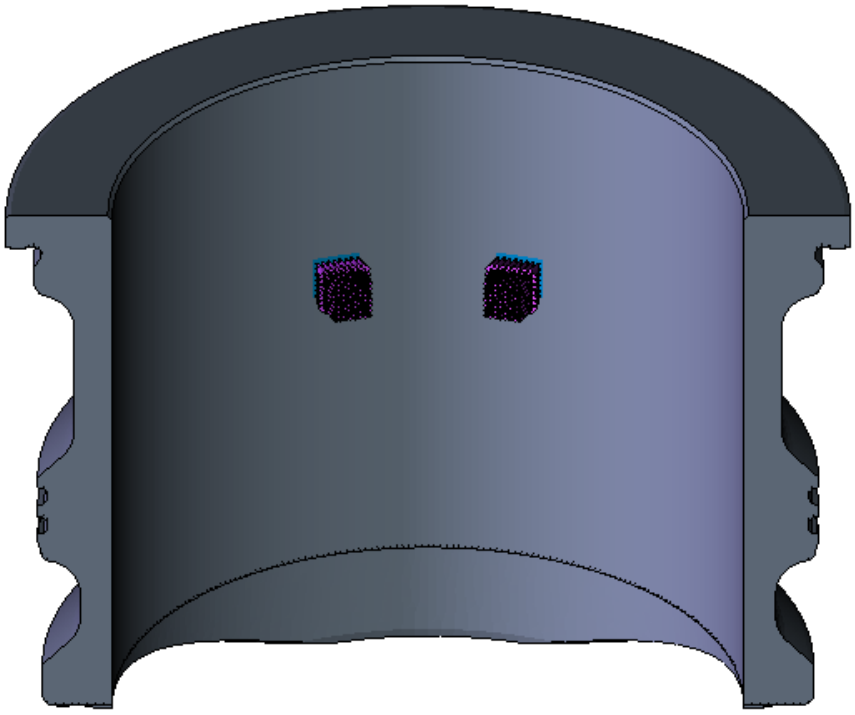

Figure 9.35. Homogeneous pressure mimicking the contact interaction.

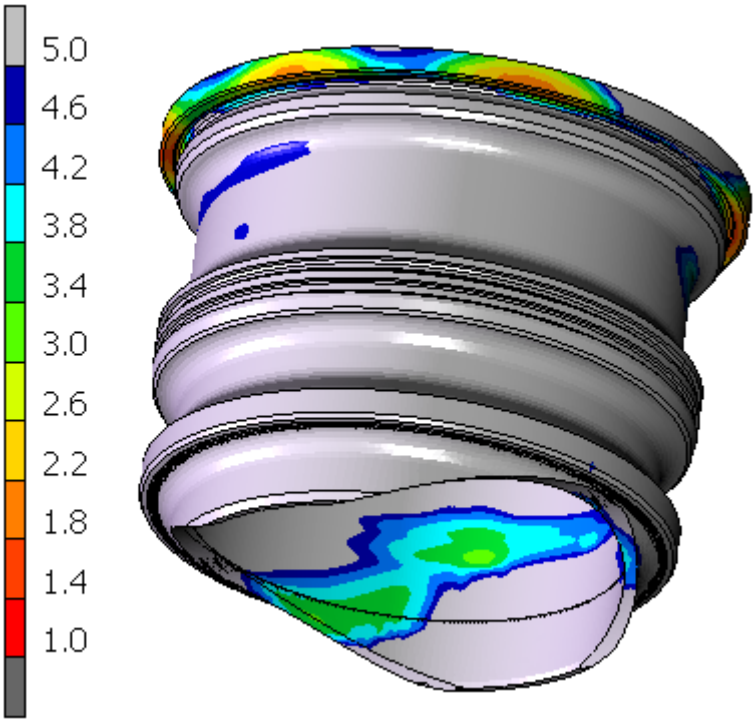

Figure 9.36. Dang Van safety factor contour plot.

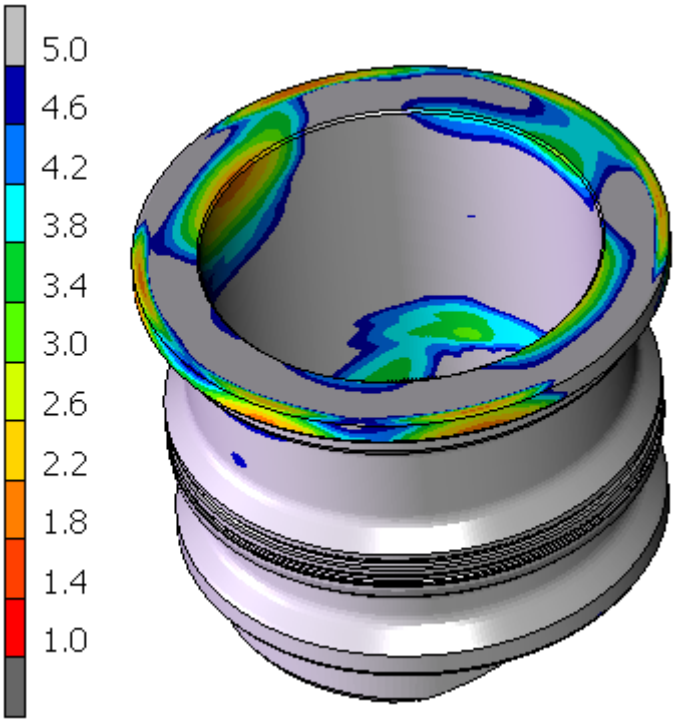

Figure 9.37. Dang Van safety factor contour plot.

Chapter 10: FEM analyses of the different engine configurations

10.1 Introduction

In this chapter, three different engine configurations are taken into account:

- aluminium piston and steel cylinder liner;
- steel piston and aluminium cylinder liner;
- steel piston and steel cylinder liner.

For each configuration, the contact interaction between these components is studied and the fatigue analysis of the cylinder is performed. The geometry and the profile of the steel piston have been already defined in the dedicated chapter, but the geometry of the steel cylinder liner has to be defined yet.

10.2 The steel cylinder liner

The geometry of the cylinder liner is simply defined by the thickness of the liner itself. In fact, the same inner nominal diameter of the aluminium piston should be kept. However, to obtain a proper gap between the piston and the liner, the actual inner radius will be slightly modified.

Starting from the consideration that the aluminium liner and the steel one should exhibit the same fatigue safety factor and that bending moment causes the highest stress values, the thickness of the liner is defined as follow. Considering the liner as a simply supported beam of section b*h (b=1 mm and h=t)

$$t_{steel} = \sqrt{t_{Al}{}^2 \frac{\sigma_{\lim\_Al}}{\sigma_{\lim\_steel}}} \tag{10.1}$$

where t_{steel} is the thickness of the new liner made of steel, t_{Al} is the thickness of the original aluminium liner (3 mm), σ_{lim_Al} is the stress limit of aluminium (288 MPa) and σ_{lim_steel} is the stress limit of steel (1260 MPa). The resulting t_{steel} is 2.87 mm, but a thickness of 3 mm will be employed.

Figure 10.1 compares the geometries of the original aluminium liner (a) and of the new steel one (b). The thickness of the liner has been thinned according to the previous calculations, but the interference fit features have been left untouched to allow an easy replacement of the liner. Then the shape of the liner results in a quite massive component.

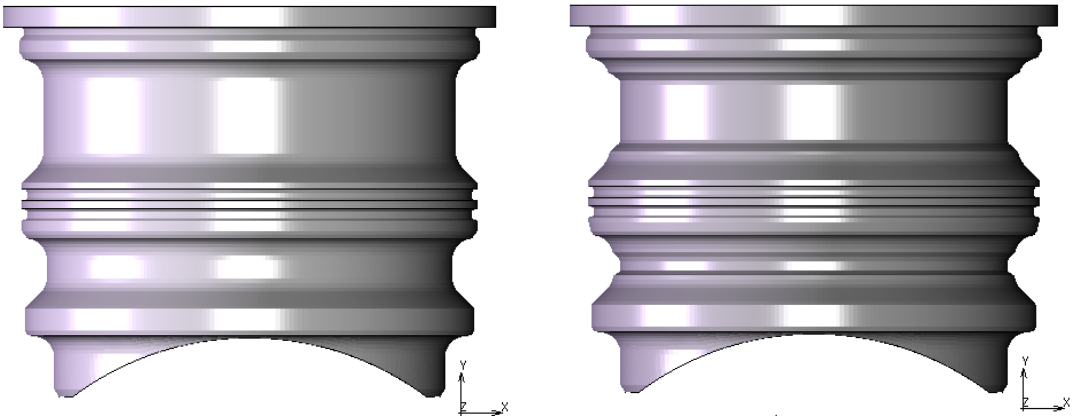

(a) (b)

Figure 10.1 (a) aluminium liner; (b) steel liner.

10.3 Thermal analysis of the engine - steel cylinder liner

A thermal analysis of the engine with the cylinder liner made of steel has been performed. In particular, the same methodology explained in Chapter 9.3 has been employed.

Figures 10.2 and 10.3 compare the temperature contour plot of the original aluminium liner (a) and of the new steel one (b). The steel liner reaches a very high temperature on its lower part. It is important to underline that the new liner has been designed on a structural basis without taking into account the amplified thermal resistance of the steel liner. The temperature field of the remaining part of the engine resulted to be almost unchanged from the previous configuration.

Besides, it has been necessary to find a proper inner diameter of the steel liner based on the mean temperature retrieved on the inner surface of the cylinder liner:

$$d_{steel} = d_{Al}\frac{1 + \alpha_{Al}\Delta T_{Al}}{1 + \alpha_{steel}\Delta T_{steel}} \tag{10.2}$$

where d_{Al} is the diameter of the aluminium liner (100.01433 mm), α_{Al} and α_{Al} are the thermal expansion coefficient of aluminium ($2.1e^{-5}$) and steel ($1.1e^{-5}$) respectively, ΔT_{Al} and ΔT_{steel} are the computed average delta temperature of the inner surface of the aluminium (156°C) and steel (206°C) liner respectively. d_{steel} results out to be 100.11612 mm.

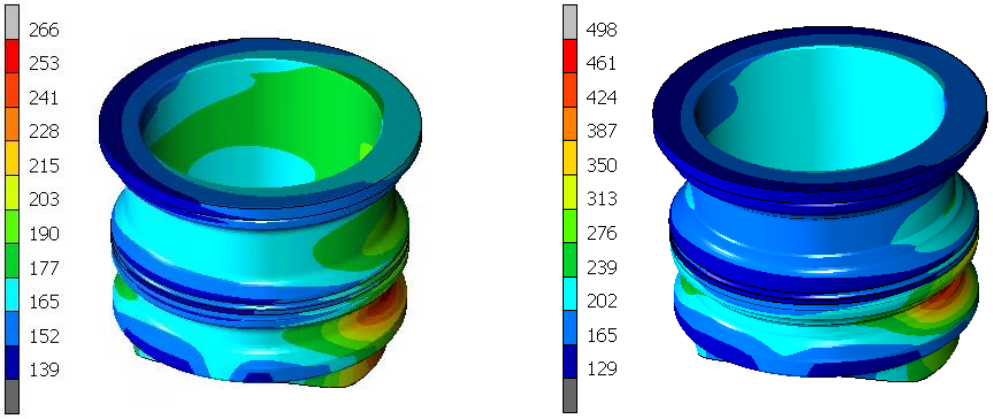

(a) (b)

Figure 10.2 (a) aluminium liner; (b) steel liner.

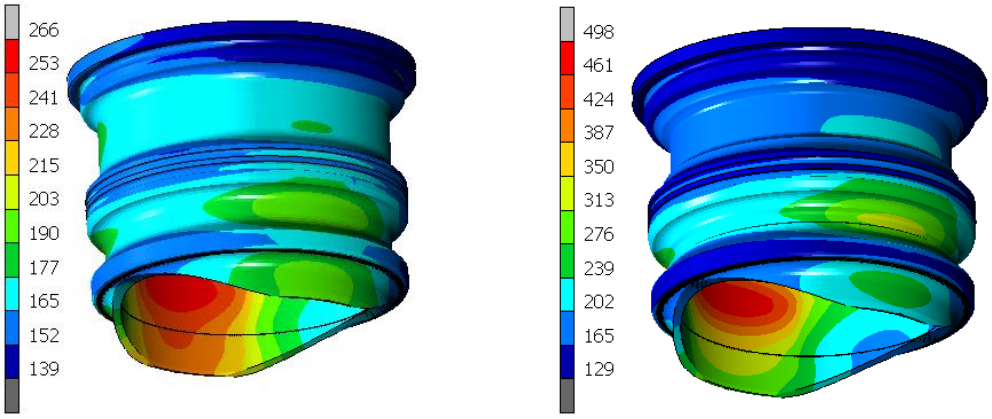

(a) (b)

Figure 10.3 (a) aluminium liner; (b) steel liner.

10.4Thermo-structural analyses, different configurations

Now, the results of the three different configurations will be exposed: aluminium piston – steel liner, steel piston – aluminium liner and steel piston – steel liner.

The same methodologies exposed previously for the aluminium piston – aluminium liner case have been employed. In particular, some thermal boundary conditions have been slightly adapted considering the specific material involved and the new geometry of the components. However, the same five configurations, that describe the fatigue border, of the classical configuration have been considered also for the steel piston, even if, the slightly different mass of the piston would have modified the exact position of the fatigue border. For each different configuration of materials employed, a fatigue analysis has been performed and some consideration on the coupling will be provided in terms of contact area, contact normal forces and the gap or interference fit. Figure 10.4 shows the safety factor contour plot of the aluminium piston – aluminium liner case, Figure 10.5 (a) and (b) show the contact area and the vector plot of the contact

normal forces respectively for the 491 CA case, which is a border of the fatigue cycle and it is quite near to the instant of maximum piston thrust. These images are provided to help the reader to understand the following results.

It is important to specify that the lubricating oil between the piston and the liner has not been considered in the structural simulation. However, the effect of the oil should result only in a slight redistribution of the high value of contact normal forces, while the contact area should remain essentially unchanged, thus confirming the reliability of the fatigue calculations.

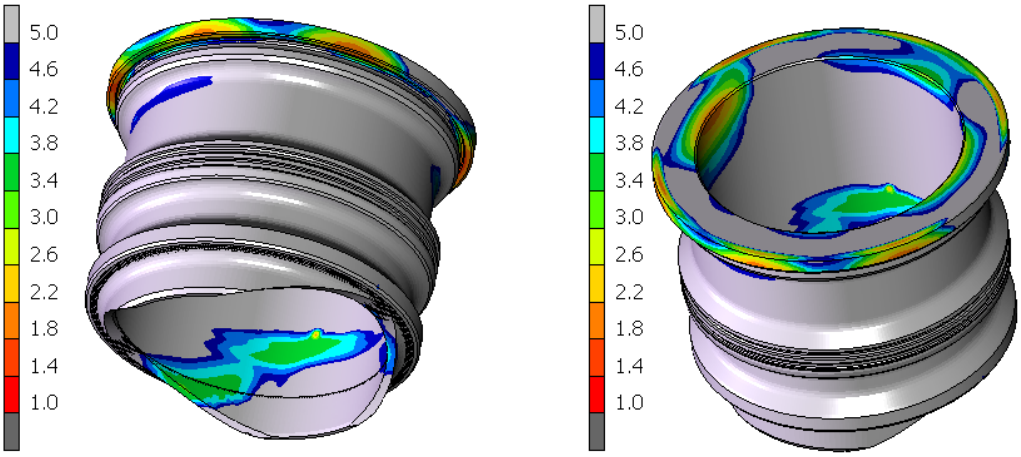

(a) (b)

Figure 10.4 Dang Van safety factor contour plot.

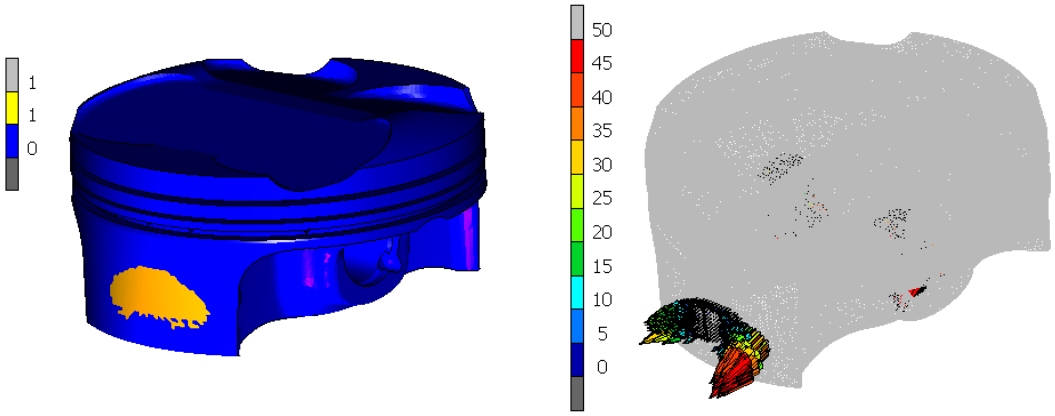

(a) (b)

Figure 10.5 (a) contact status contour plot; (b) contact normal force vector plot [N].

10.4.1 Aluminium piston – steel liner

The nominal cold diameter of the aluminium piston is 99.95 mm while the inner surface of the steel liner has a cold diameter of 100.11612 mm, so that a small gap is present at ambient temperature, the simulations have shown that a small gap is also present at the temperature of the working conditions.

Figure 10.6 show the Dang Van safety factor contour plot of the fatigue analysis, a stress limit of 540 MPa has been set for the steel liner. The minimum value is located in the lower area of the liner, where a maximum value of bending moment has been computed in Chapter 9. The figure displays very high values of the safety factor, in fact, also the flange has not been thinned to obtain a liner that could replace easily the original aluminium one.

Figure 10.7 (a) show the contact status at 491CA, the contact area a bit less wide than is the case of the aluminium liner. This could be ascribed to the more stiff behaviour of the steel liner. The liner has been thinned, but the regions in contact with the block show a massive geometry.

Figure 10.7 (b) shows the vector plot of the normal contact forces. The maximum value (80N) of the contact forces is higher than the maximum value (50N) retrieved in the previous configuration because of the less wide contact area involved. High values of contact force are correctly located near the region of the skirt bosses.

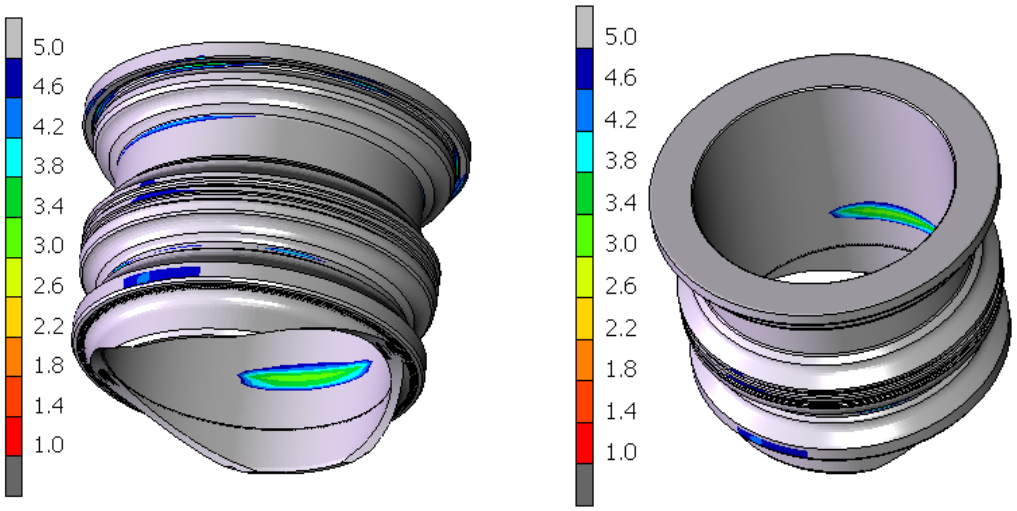

(a) (b)

Figure 10.6 Dang Van safety factor contour plot.

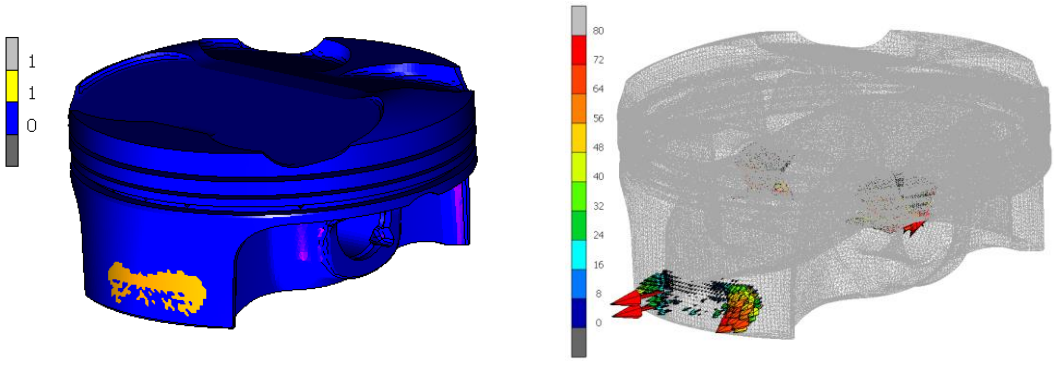

(a) (b)

Figure 10.7 (a) contact status contour plot; (b) contact normal force vector plot [N].

10.4.2 Steel piston – aluminium liner

The nominal cold diameter of the steel piston is 100.13 mm while the inner surface of the aluminium liner has a cold diameter of 100.01433 mm so that interference is present at ambient temperature, however, the simulations have shown that a small gap is present at the temperature of the working conditions, also the structural deformation of the skirt and of the liner has facilitated the occurrence of the gap.

Figure 10.8 show the Dang Van safety factor contour plot of the fatigue analysis, a stress limit of 125 MPa has been set for the aluminium liner. The minimum value is located in the lower area of the liner, where a maximum value of bending moment has been computed in Chapter 9. The figure displays almost the same safety factor shown in the configuration with the aluminium liner (Figure 10.4). So it could be possible to use the steel piston in the aluminium liner, after a thorough warm-up of the engine, as it is possible to see in the Formula One competitions.

Figure 10.9 (a) show the contact status at 491CA, the contact area is very wide and involves the upper area of the skirt. It should be necessary to redesign this area of the steel piston, maybe a less stiff lateral crown and a more stiff skirt should be designed

Figure 10.9 (b) shows the vector plot of the normal contact forces. The value of the contact forces in the upper area of the skirt is quite low so that it could be correct to slightly correct the profile of the skirt without trying to redesign the lateral crown of the piston. In fact, the maximum values (80N) of contact forces are correctly located near the area of the skirt bosses.

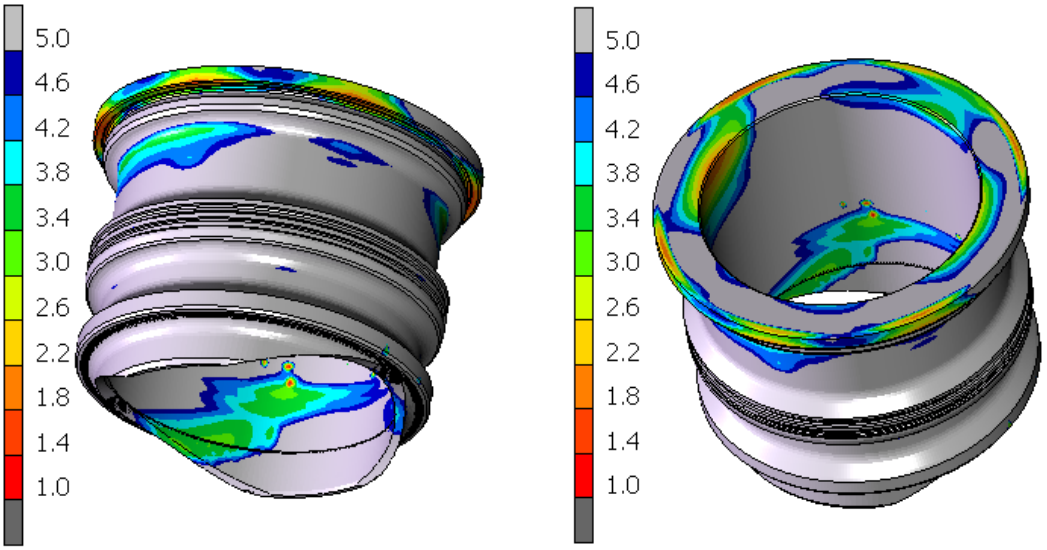

(a) (b)

Figure 10.8 Dang Van safety factor contour plot.

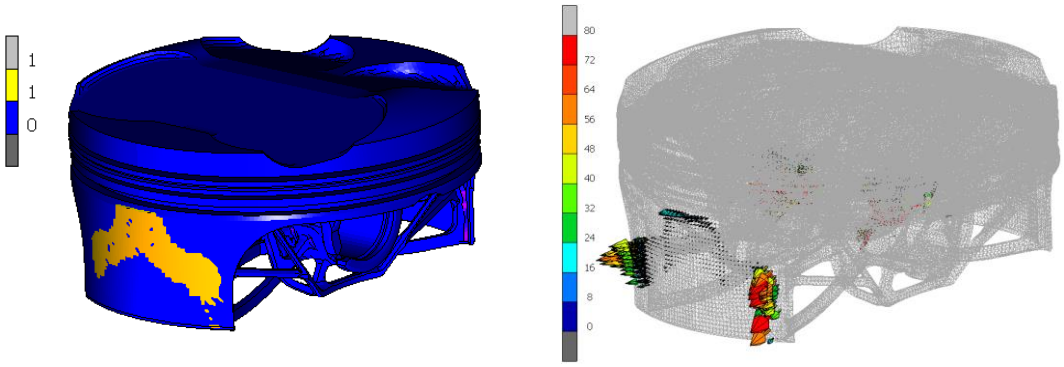

(a) (b)

Figure 10.9 (a) contact status contour plot; (b) contact normal force vector plot [N].

10.4.3 Steel piston – steel liner.

The nominal cold diameter of the steel piston is 100.13 mm while the inner surface of the aluminium liner has a cold diameter of 100.11612 mm so that a very small interference is present at ambient temperature, however, the simulations have shown that a small gap is present at the temperature of the working conditions, also the structural deformation of the skirt and of the liner has facilitated the occurrence of the gap.

Figure 10.10 show the Dang Van safety factor contour plot of the fatigue analysis, a stress limit of 540 MPa has been set for the steel liner. The minimum value is located in the inner and outer area of the feature for the correct sealing in the lower area of the liner, see also Figure 10.11. This result should be ascribed to high compressive stress in this region of the liner.

Figure 10.12 (a) show the contact status at 491CA, the contact area seems to be correct and involves only the lower area of the skirt.

Figure 10.12 (b) shows the vector plot of the normal contact forces. The maximum values (85N) are correctly located near the area of the skirt bosses.

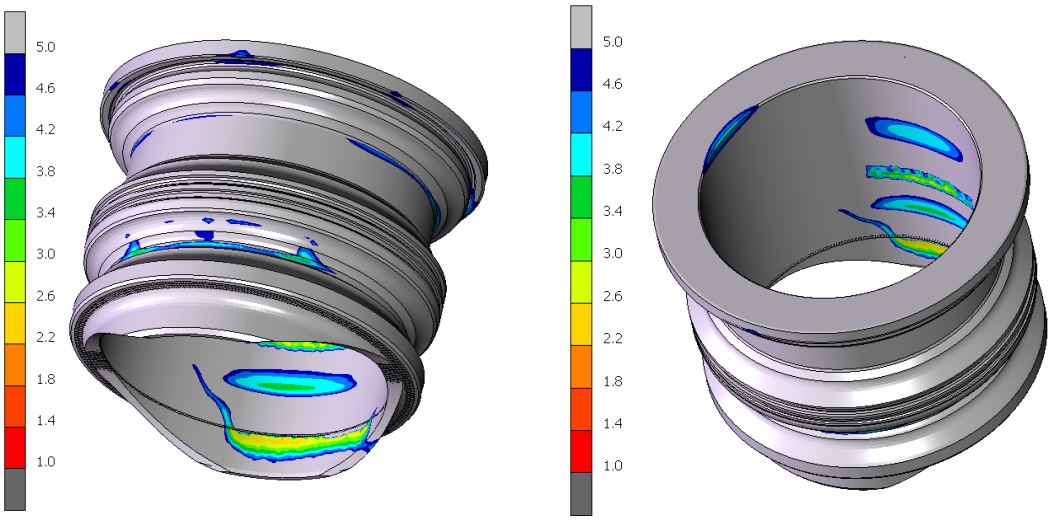

(a) (b)

Figure 10.10 Dang Van safety factor contour plot.

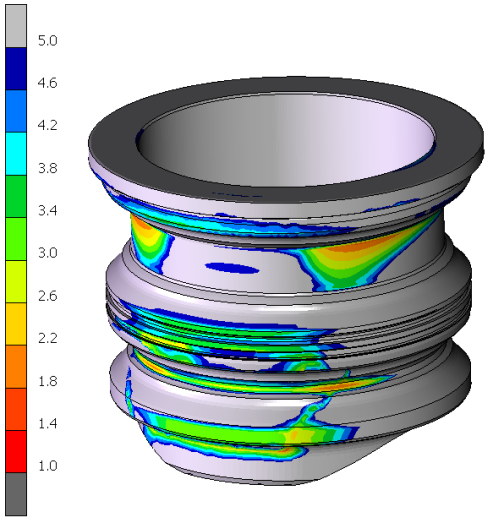

Figure 10.11 Dang Van safety factor contour plot.

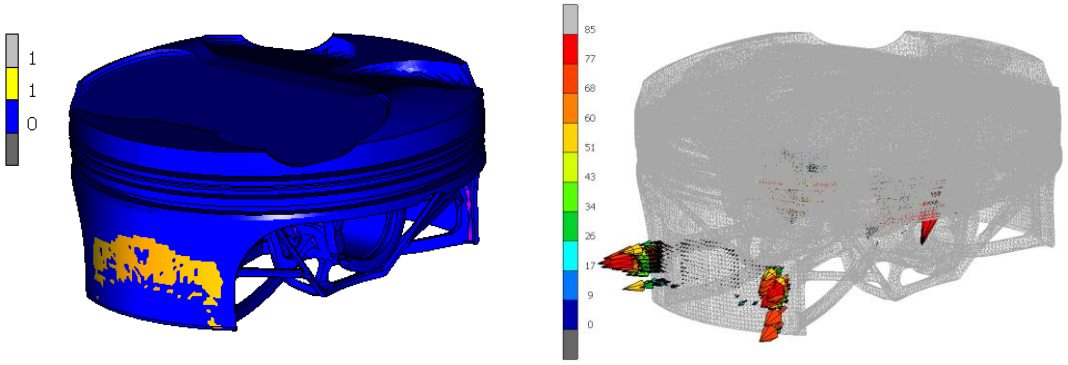

(a) (b)

Figure 10.12 (a) contact status contour plot; (b) contact normal force vector plot [N].

10.4.4 Details of the aluminium and steel pistons

Two last simulations have been performed to compare the aluminium piston to the steel one in the condition of maximum lateral thrust force. In particular, only one half of the crank mechanism has been considered (taking advantage of the symmetry plane) and a rigid cylindrical surface has been employed to mimic the liner. The diameter of this cylinder is 100.342 mm, since the thermal field has been taken into account. Only one cylinder has been considered to mimic both the aluminium and the steel liner (see section 10.2).

The simulations display the instant of maximum piston lateral thrust, this load case is the clearest one to understand the is the profile applied to the skirt is correct and if the skirt bosses can support correctly the interaction with the liner.

Figure 10.13 displays the results concern the aluminium piston. Figure 10.13 (a) shows the contact status contour plot. The contact area is correctly located in the lower part of the skirt and it covers both the regions of the skirt bosses. Figure 10.13 (b) depicts the vector plot of the contact normal forces, the highest values are located in the area of the skirt bosses, as it should always be in the instant of maximum thrust force.

Figure 10.14 displays the results concern the steel piston. Figure 10.14 (a) shows the contact status contour plot. The contact area is quite wide, from the area of the skirt bosses to the upper area of the skirt. Figure 10.14 (b) depicts the vector plot of the contact normal forces, the highest values are correctly located in the area of the skirt bosses, even if quite negligible values are located also in the upper part of the skirt, thus denoting the possibility to further investigate the barrelled profile of the skirt of the new steel piston.

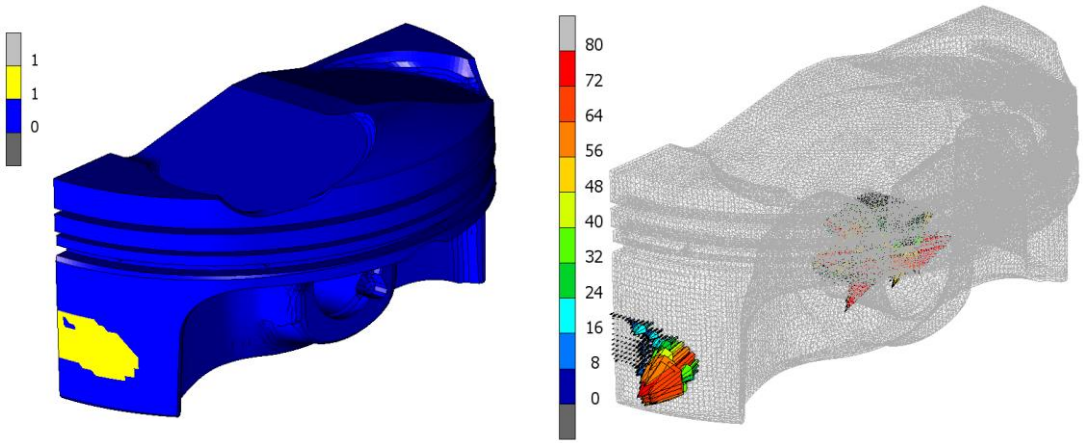

(a) (b)

Figure 10.13 (a) contact status contour plot; (b) contact normal force vector plot [N].

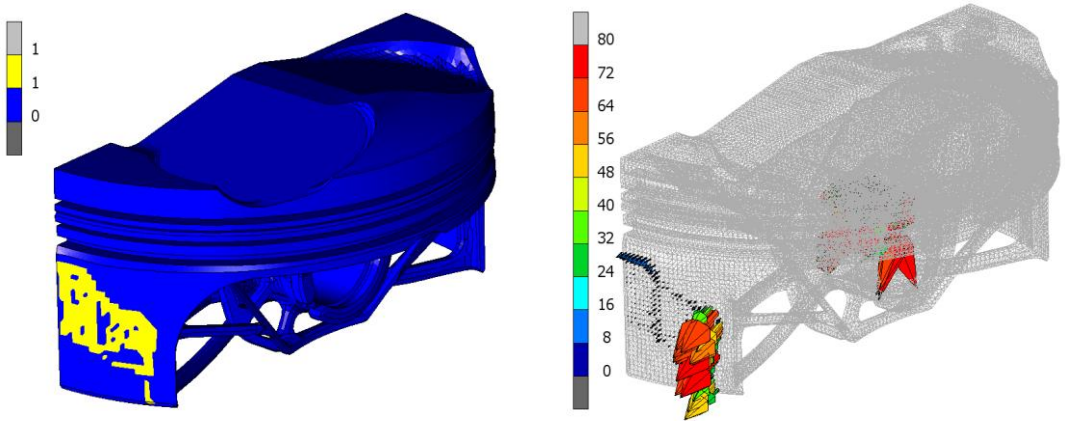

(a) (b)

Figure 10.14 (a) contact status contour plot; (b) contact normal force vector plot [N].

10.5 Experimental validations

The last phase of this work should include an experimental validation of the results obtained. Unfortunately, it has not been possible to carry out these latest studies yet for reasons of cost and time.

First, the static and fatigue strength of the designed steel piston must be checked. It could be possible to insert the new piston directly into the engine with the original aluminium cylinder liner, but there would be an unnecessary risk of seriously damaging the entire engine. Instead, an ad hoc test rig could be built in which the crank mechanism moves inside a simplified cylinder liner and the pressure exerted by combustion is simulated by a compressible body placed on the top of the cylinder liner. In particular, it could be possible to use sand enclosed in a container of elastic and resistant material in order to be adapted to the shape of the piston crown and simulate a constant pressure. Furthermore, this sand should be constrained to a non-linear spring to have the same

pressure trend that has been recorded in the original engine. However, using this test rig it would not be possible to faithfully simulate a fatigue cycle, in fact, it would not be possible to simulate the instant of top dead centre in crossing. Therefore, it is necessary to alternate an adequate number of cycles using the sand to compress the piston to other engine cycles by removing the sand to simulate the absence of pressure in the camera at the top dead centre at the beginning of the induction phase. In particular, if we consider the instant of maximum thrust, it is immediately clear how important it is to use a piston with a correct profile, since this test would be carried out at an ambient temperature, it is necessary to make a piston with the cold profile equal to the hot one defined through simulations (section 8.4.1).

Now it is necessary to test in detail the contact interaction between piston and cylinder liner in the four configurations according to the different materials used. The previously used test rig could be used for some preliminary tests, but care must be taken to machine the internal bore of the cylinder to obtain a diameter equivalent to that obtained considering the thermal expansion, a consequence of the thermal field that shows the engine in operation (section 10.4.4).

Finally, it is necessary to try the four possible configurations in the actual engine and investigate in detail the cylinders and pistons in looking for breakages, damage or polishing of the components that could be the consequence of too high contact pressures and therefore a probable symptom of not sufficiently suitable piston profiles.

However, all this considered, it has been possible to analyse visually the piston and the cylinder liner of the actual engine of the Panigale 959. Figure 10.15 shows details of the piston skirt, scratches on the surface are visible as a consequence of the high values of contact pressure involved. The area is located on the skirt, in the area corresponding to the skirt bosses, as the Finite Element results have clearly highlighted.

Figure 10.16 shows the most damaged area of the aluminium liner. This area is located on the lower internal surface of the liner. This is the same area shown by the Finite Element forecasts, see Figure 10.4.

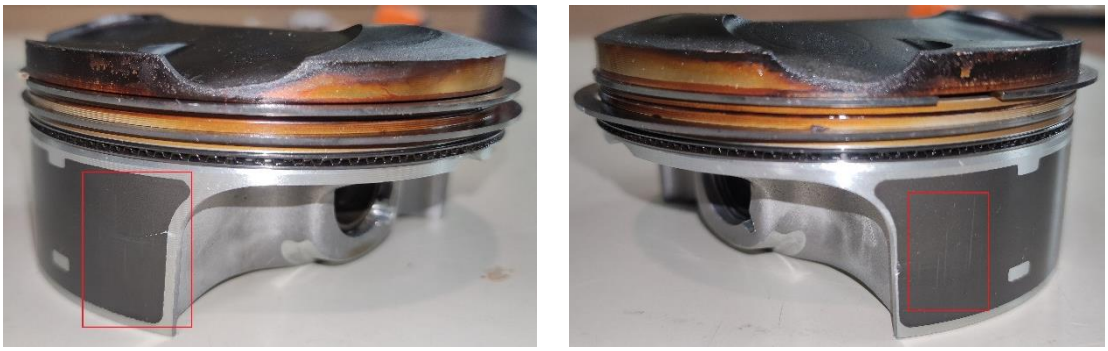

(a) (b)

Figure 10.15 detail of the piston.

(a) (b)

Figure 10.15 detail of the piston.

Conclusions and future works

In this thesis, a wide overview of the FEM calculations on the piston and liner for a high-performance engine has been presented.

A method for a computer-aided steel piston design has been proposed. In particular, the presented methodology aimed at finding more efficient layout solutions for the piston framework feasible with Additive Manufacturing techniques. Topology optimizations have been employed to define the optimal structural topology. Special care has to be taken in setting up the optimization process since the choice of the constraints, i.e. the performance targets, of the mesh size and quality and of the optimization parameters directly affect the outcome of the process. The topology optimization results have guided the redesign process towards a wireframe structure abundant of small fillets. The structural analyses have revealed high values of von Mises stress in localized areas, thus larger radius fillets have been adopted. The fatigue analysis underlined the need to review the geometry of the diagonal beams linking the external areas of the piston top to the pin bosses. Preliminary thermal analyses have shown the requirement to modify the geometry of the piston top in order to remove/reduce concentrated peaks of temperatures arising at sharped geometrical features inherited from the original aluminium piston configuration. Such a modification has to be guided by ad hoc integrated in-cylinder/CHT analysis necessary to avoid undesired and detrimental abnormal (knocking) combustion processes that may arise. The new steel piston exhibits a mass of 415 g. If compared to the original aluminium piston (380 g), a limited increase of 9% is registered. The new steel piston could allow high mechanical and thermal loadings to be reached; therefore a wider redesign of the engine components will be necessary in order to totally take advantage of the steel piston adoption.

A first profile for the lateral crown and skirt of the new steel piston has been proposed, based on the comparison between the thermal deformation of the original aluminium piston and the new steel piston.

Experiments will be mandatory to validate the detailed drawing of the new steel piston.

In the present thesis, a simplified methodology for the structural analysis of the assembly of an internal combustion engine has been proposed. Both structural and thermo-structural analyses have been performed and a very close match has been obtained between complete and simplified model, proving the method to be suitable for reducing the computational effort. This methodology could be employed to lighten all the Finite Element model of engines when a deep study of the head is not necessary. For instance, this methodology could quicken the study of the interaction between the piston and the liner and its fatigue analysis.

On the other hand, this methodology could be slightly modified in order to keep the engine head and replace the effect of the gasket, block and liners with suitable contact pressures. This model could be employed to lighten the computational effort when the focus of the analysis is to study the cam carrier or the whole engine timing.

In addition, in the present thesis, a methodology aiming at simplifying the fatigue analysis of the cylinder liner of an internal combustion engine has been proposed.

The decrease of the number of elements and of the sources of non-linearity has reduced the computational effort. The number of elements has not been limited by using a coarser mesh, but by removing all unnecessary components. Consequently, the head, the gasket, the upper part of the bolts and the crank mechanism have been removed, while the liners and the block have been kept with the same mesh resolution. In this way, several different sources of contact non-linearity have been removed. On the other hand, the contact interaction between the liners and the block, which strongly affects the liner bending stress, has been kept. The removed components have been then replaced with suitable loadings. The simplified methodology has revealed itself to be well correlated with the complete analyses thus reducing the computational effort necessary for the numerical component approval.

In future works, the pressure distribution chosen to mimic the piston-liner interaction will be further analysed. In particular, the contact pressure distribution will be correlated to the stiffness and geometry of the piston skirt taking into account the instantaneous load applied. Therefore, it will be possible to modulate the shape of the contact distribution during the engine cycle. Besides, it is possible to consider the dynamic effects that involve the crank mechanism, employing multi-body software, it will be possible to compute more precisely the contact interaction between the piston and the liner.

In the last chapter of this thesis, four different configurations have been taken into account. The simulations showed that all the possibilities could be suitable, even if gaps and interferences have to be carefully managed. The fatigue analyses derived from the composition of different quasi-static analyses. In future works, dynamic analyses could be employed or a coupled FEM - multi-body methodology could be employed, as it is described in [56].

Finally, all the methodologies presented must be validated through experiments as the last section of chapter 10 describes. In particular, it is crucial to build the new steel piston and the new steel cylinder liner and they must be tested using a specific test rig and then employing the actual engine.

References

1. MAHLE, “Pistons and enigne testing,” ISBN 9783834815903, 2012.
2. Aljaberi, H.A., Aziz Hairuddin, A., and Abdul Aziz, N., “The use of different types of piston in an HCCI engine: A review,” *Int. J. Automot. Mech. Eng.* 14(2):4348–4368, 2017, doi:10.15282/ijame.14.2.2017.17.0346.
3. Sadiq Y, R. and Iyer, R.C., “Experimental investigations on the influence of compression ratio and piston crown geometry on the performance of biogas fuelled small spark ignition engine,” *Renew. Energy* 146:997–1009, 2020, doi:10.1016/j.renene.2019.06.140.
4. Kumar, V., “Experimental investigation of piston bowl geometry effects on performance and emissions characteristics of diesel engine at variable injection pressure and timings,” *Int. J. Ambient Energy* 39(7):685–693, 2018, doi:10.1080/01430750.2017.1333041.
5. Wickman, D.D., Senecal, P.K., and Reitz, R.D., “Diesel engine combustion chamber geometry optimization using genetic algorithms and multi-dimensional spray and combustion modeling,” *SAE Tech. Pap.* 110:487–507, 2001, doi:10.4271/2001-01-0547.
6. Morris, A.J., “Internal combustion engine with piston having combustion cavity in its head,” United States: 7–12, 1959.
7. Christensen, M., Johansson, B., and Hultqvist, A., “The Effect of Piston Topland Geometry on Emissions of Unburned Hydrocarbons from a Homogeneous Charge Compression Ignition (HCCI) Engine,” *SAE Technical Papers*, 2001, doi:10.4271/2001-01-1893.
8. Rabute´, R. and Tian, T., “Challenges Involved in Piston Top Ring Designs for Modern SI Engines,” *J. Eng. Gas Turbines Power* 123(2):448–459, 2001, doi:10.1115/1.1364520.
9. Regolamento (CE) N. 715/2007 del Parlamento Europeo e del Consiglio del 20 giugno 2007 relativo all’omologazione dei veicoli a motore riguardo alle emissioni dai veicoli passeggeri e commerciali leggeri (Euro 5 ed Euro 6) e all’ottenimento di informazioni.
10. Schreer, K., Roth, I., Schneider, S., and Ehnis, H., “Analysis of Aluminum and Steel Pistons—Comparison of Friction, Piston Temperature, and Combustion,” *J. Eng. Gas Turbines Power* 136(10):101506, 2014, doi:10.1115/1.4027275.
11. MAHLE, “Cylinder components Properties, applications , materials,” ISBN 9783834807854, 2008.
12. Thomson, Wi., “IV. On the elasticity and viscosity of metals,” *Proc. R. Soc. London* 14:289–297, 1865, doi:10.1098/rspl.1865.0052.
13. Li, G., Gong, J., Tan, J., Zhu, D., and Jia, W., “Stress relaxation behavior and life prediction of gasket materials used in proton exchange membrane fuel cells,” *J. Cent. South Univ.* 26(3):623–631, 2019, doi:10.1007/s11771-019-4033-7.
14. Lee, C.C., Chiang, K.N., Chen, W.K., and Chen, R.S., “Design and analysis of gasket sealing of cylinder head under engine operation conditions,” *Finite Elem. Anal. Des.* 41(11–12):1160–1174, 2005, doi:10.1016/j.finel.2004.12.007.

15. Kandreegula, S.K., Gupta, U., and Vyas, S., “Investigation of gasket sealing behavior of cylinder head and block under engine operating conditions and its experimental verification,” *SAE Tech. Pap.* (1), 2015, doi:10.4271/2015-26-0029.
16. Woschni, G., “A Universally Applicable Equation for the Instantaneous Heat Transfer Coefficient in the Internal Combustion Engine,” 1967, doi:10.4271/670931.
17. Giacopini, M., Sissa, S., Rosi, R., and Fantoni, S., “Influence of different temperature distributions on the fatigue life of a motorcycle piston,” *Proc. Inst. Mech. Eng. Part D J. Automob. Eng.* 229(9):1276–1288, 2015, doi:10.1177/0954407014560201.
18. Cantore, G., Giacopini, M., Rosi, R., Strozzi, A., and Engineering, C., “Validation of a combined CFD / FEM methodology for the evaluation of thermal load acting on aluminum alloy pistons through hardness measurements in internal combustion engines,” 29, 2011.
19. Congiu, C., Barbieri, S.G., Giacopini, M., and Marmorini, L., “Development of simplified numerical methods for the thermomechanical analysis of an innovative automotive injector,” Università degli Studi di Modena e Reggio Emilia, 2020.
20. Barbieri, S.G., Giacopini, M., and Mangeruga, V., “Tecniche di ottimizzazione topologica per la definizione di un pistone in acciaio realizzato tramite Additive Manufacturing,” Università degli Studi di Modena e Reggio Emilia, 2016.
21. French, C.C.J., “Piston Cooling,” *SAE Transacctions* 81:148–164, 1972.
22. Ma, C.F., Zheng, Q., and Ko, S.Y., “Local heat transfer and recovery factor with impinging free-surface circular jets of transformer oil,” *Int. J. Heat Mass Transf.* 40(18):4295–4308, 1997, doi:10.1016/S0017-9310(97)00054-9.
23. Stevens, J. and Webb, B.W., “Local Heat Transfer Coefficients Under an Axisymmetric, Single-Phase Liquid Jet,” *J. Heat Transfer* 113(1):71–78, 1991, doi:10.1115/1.2910554.
24. Liu, Y.C., Guessous, L., Sangeorzan, B.P., and Alkidas, A.C., “Laboratory Experiments on Oil-Jet Cooling of Internal Combustion Engine Pistons: Area-Average Correlation of Oil-Jet Impingement Heat Transfer,” *J. Energy Eng.* 141(2):1–11, 2015, doi:10.1061/(ASCE)EY.1943-7897.0000227.
25. Easter, J., Jarrett, C., Pespisa, C., Liu, Y.C., Alkidas, A.C., Guessous, L., and Sangeorzan, B.P., “An Area-Average Correlation for Oil-Jet Cooling of Automotive Pistons,” *J. Heat Transfer* 136(12):1–5, 2014, doi:10.1115/1.4027835.
26. Leal, R., Barreiros, F.M., Alves, L., Romeiro, F., Vasco, J.C., Santos, M., and Marto, C., “Additive manufacturing tooling for the automotive industry,” *Int. J. Adv. Manuf. Technol.* 92(5–8):1671–1676, 2017, doi:10.1007/s00170-017-0239-8.
27. Böckin, D. and Tillman, A.-M., “Environmental assessment of additive manufacturing in the automotive industry,” *J. Clean. Prod.* 226:977–987, 2019, doi:10.1016/j.jclepro.2019.04.086.
28. Juechter, V., Franke, M.M., Merenda, T., Stich, A., Körner, C., and Singer, R.F., “Additive manufacturing of Ti-45Al-4Nb-C by selective electron beam melting for automotive applications,” *Addit. Manuf.* 22(November 2017):118–126, 2018, doi:10.1016/j.addma.2018.05.008.

29. Kumar Dama, K., Kumar Malyala, S., Suresh Babu, V., Rao, R.N., and Shaik, I.J., "Development of Automotive FlexBody Chassis Structure in Conceptual Design Phase using Additive Manufacturing," *Mater. Today Proc.* 4(9):9919–9923, 2017, doi:10.1016/j.matpr.2017.06.294.
30. Marchesi, T.R., Lahuerta, R.D., Silva, E.C.N., Tsuzuki, M.S.G., Martins, T.C., Barari, A., and Wood, I., "Topologically Optimized Diesel Engine Support Manufactured with Additive Manufacturing," *IFAC-PapersOnLine* 48(3):2333–2338, 2015, doi:10.1016/j.ifacol.2015.06.436.
31. Mantovani, S., Barbieri, S., Giacopini, M., Croce, A., Sola, A., and Bassoli, E., "Synergy between topology optimization and additive manufacturing in the automotive field," *Proc. Inst. Mech. Eng. Part B J. Eng. Manuf.* 235(3):555–567, 2021, doi:10.1177/0954405420949209.
32. Gray, J. and Depcik, C., "Review of Additive Manufacturing for Internal Combustion Engine Components," *SAE Int. J. Engines* 13(5):03-13-05–0039, 2020, doi:10.4271/03-13-05-0039.
33. Haba, S.A. and Oancea, G., "Digital manufacturing of air-cooled single-cylinder engine block," *Int. J. Adv. Manuf. Technol.* 80(5–8):747–759, 2015, doi:10.1007/s00170-015-7038-x.
34. Posser, T. and Freitas de Oliveira, B., "Design for additive manufacturing applied for mass reduction of a two-stroke engine cylinder for portable machine," *Int. J. Interact. Des. Manuf.* 14(2):709–717, 2020, doi:10.1007/s12008-019-00596-1.
35. Gibson, I., Rosen, D., and Stucker, B., "Additive Manufacturing Technologies," Springer New York, New York, NY, ISBN 978-1-4939-2112-6, 2015, doi:10.1007/978-1-4939-2113-3.
36. Tolosa, I., Garciandía, F., Zubiri, F., Zapirain, F., and Esnaola, A., "Study of mechanical properties of AISI 316 stainless steel processed by 'selective laser melting', following different manufacturing strategies," *Int. J. Adv. Manuf. Technol.* 51(5–8):639–647, 2010, doi:10.1007/s00170-010-2631-5.
37. Kruth, J.P., Froyen, L., Vaerenbergh, J. Van, Mercelis, P., Rombouts, M., and Lauwers, B., "Selective laser melting of iron-based powder," *J. Mater. Process. Technol.* 149(1–3):616–622, 2004, doi:10.1016/j.jmatprotec.2003.11.051.
38. Emerson, R.W. and Cavazzuti, M., "Optimization Methods: From Theory to Design," ISBN 9783642311871, 2013.
39. Davis, C.S., "Line search methods for extended penalty function environments," *Int. J. Numer. Methods Eng.* 15(6):867–888, 1980, doi:10.1002/nme.1620150607.
40. Bendsøe, M.P. and Sigmund, O., "Topology Optimization," Springer Berlin Heidelberg, Berlin, Heidelberg, ISBN 978-3-642-07698-5, 2004, doi:10.1007/978-3-662-05086-6.
41. Bendsøe, M.P. and Kikuchi, N., "Generating optimal topologies in structural design using a homogenization method," *Comput. Methods Appl. Mech. Eng.* 71(2):197–224, 1988, doi:10.1016/0045-7825(88)90086-2.
42. Sigmund, O. and Petersson, J., "Numerical instabilities in topology optimization: A survey on procedures dealing with checkerboards, mesh-dependencies and local minima," *Struct. Optim.* 16(1):68–75, 1998, doi:10.1007/BF01214002.
43. Zuo, K.T., Chen, L.P., Zhang, Y.Q., and Yang, J., "Study of key algorithms in topology optimization," *Int. J. Adv. Manuf. Technol.* 32(7–8):787–796, 2007,

doi:10.1007/s00170-005-0387-0.
44. Mantovani, S., Presti, I. Lo, Cavazzoni, L., and Baldini, A., "Influence of Manufacturing Constraints on the Topology Optimization of an Automotive Dashboard," *Procedia Manuf.* 11(June):1700–1708, 2017, doi:10.1016/j.promfg.2017.07.296.
45. Zuo, K.T., Chen, L.P., Zhang, Y.Q., and Yang, J., "Manufacturing- and machining-based topology optimization," *Int. J. Adv. Manuf. Technol.* 27(5–6):531–536, 2006, doi:10.1007/s00170-004-2210-8.
46. Knupp, P.M., "Algebraic Mesh Quality Metrics," *SIAM J. Sci. Comput.* 23(1):193–218, 2001, doi:10.1137/S1064827500371499.
47. Knupp, P.M., "Algebraic mesh quality metrics for unstructured initial meshes," *Finite Elem. Anal. Des.* 39(3):217–241, 2003, doi:10.1016/S0168-874X(02)00070-7.
48. Knupp, P.M., "Remarks on mesh quality," *46th AIAA Aerosp. Sci. Meet. Exhib.* 8–11, 2008.
49. Marc, M., "Volume A: Theory and user information," *Msc. Software, Palo Alto, USA*, 2001.
50. Dursunkaya, Z., Keribar, R., and Ganapathy, V., "A model of piston secondary motion and elastohydrodynamic skirt lubrication," *J. Tribol.* 116(4):777–785, 1994, doi:10.1115/1.2927332.
51. Cho, S.H., Ahn, S.T., and Kim, Y.H., "A Simple Model to Estimate the Impact Force Induced by Piston Slap," *J. Sound Vib.* 255(2):229–242, 2002, doi:10.1006/jsvi.2001.4152.
52. Koizumi, T. and Tsujiuchi, N., "Reduction of piston slap excitation by optimizing piston profiles," *Proceedings of IMAC-XX: A Conference on Structural Dynamics*, Los Angeles, CA; United States: 107–113, 2002.
53. Okubo, M., Kanda, H., and Yonezawa, T., "Analysis and Reduction of Piston Slap Noise in Diesel Engines," *SAE Technical Papers*, 1989, doi:10.4271/890127.
54. Prata, A.T., Fernandes, J.R.S., and Fagotti, F., "Dynamic Analysis of Piston Secondary Motion for Small Reciprocating Compressors," *J. Tribol.* 122(4):752–760, 2000, doi:10.1115/1.1314603.
55. Haddad, S.D. and Tjan, K.-T., "An analytical study of offset piston and crankshaft designs and the effect of oil film on piston slap excitation in a diesel engine," *Mech. Mach. Theory* 30(2):271–284, 1995, doi:10.1016/0094-114X(94)00035-J.
56. Barbieri, S.G., Bianco, L., Mangeruga, V., and Giacopini, M., "A simplified finite element methodology for the structural assessment of an engine piston under dynamic loadings," 020014, 2020, doi:10.1063/5.0033956.
57. Haque, M.M. and Sharif, A., "Study on wear properties of aluminium-silicon piston alloy," *J. Mater. Process. Technol.* 118(1–3):69–73, 2001, doi:10.1016/S0924-0136(01)00869-X.
58. Haque, M.M. and Sharif, A., "Study on wear properties of aluminium–silicon piston alloy," *J. Mater. Process. Technol.* 118(1–3):69–73, 2001, doi:10.1016/S0924-0136(01)00869-X.
59. Oñoro, J., Salvador, M.D., and Cambronero, L.E.G., "High-temperature mechanical properties of aluminium alloys reinforced with boron carbide particles," *Mater. Sci. Eng. A* 499(1–2):421–426, 2009,

doi:10.1016/j.msea.2008.09.013.
60. Coër, J., Bernard, C., Laurent, H., Andrade-Campos, A., and Thuillier, S., "The Effect of Temperature on Anisotropy Properties of an Aluminium Alloy," *Exp. Mech.* 51(7):1185–1195, 2011, doi:10.1007/s11340-010-9415-6.
61. Cottrell, A.H. and Stokes, R.J., "Effects of temperature on the plastic properties of aluminium crystals," *Proc. R. Soc. London. Ser. A. Math. Phys. Sci.* 233(1192):17–34, 1955, doi:10.1098/rspa.1955.0243.
62. Gnanavel, C., Saravanan, R., and Chandrasekaran, M., "Investigation of appropriateness of coated steel piston for aluminium alloy piston for small engines," *Int. J. Ambient Energy* 41(11):1293–1298, 2020, doi:10.1080/01430750.2018.1507945.
63. Buyukkaya, E., "Thermal analysis of functionally graded coating AlSi alloy and steel pistons," *Surf. Coatings Technol.* 202(16):3856–3865, 2008, doi:10.1016/j.surfcoat.2008.01.034.
64. Binder, C., Abou Nada, F., Richter, M., Cronhjort, A., and Norling, D., "Heat Loss Analysis of a Steel Piston and a YSZ Coated Piston in a Heavy-Duty Diesel Engine Using Phosphor Thermometry Measurements," *SAE Int. J. Engines* 10(4), 2017, doi:10.4271/2017-01-1046.
65. Du, F.R. and Tao, Z., "Study on Lightweight of the Engine Piston Based on Topology Optimization," *Adv. Mater. Res.* 201–203:1308–1311, 2011, doi:10.4028/www.scientific.net/AMR.201-203.1308.
66. Zhao, J., Du, F., and Yao, W., "Structural Analysis and Topology Optimization of a Bent-bar-frame Piston Based on the Variable Density Approach," *ASME 2014 Dynamic Systems and Control Conference*, ISBN 9780791846193: 1–7, 2014, doi:10.1115/DSCC2014-6118.
67. Brackett, D., Ashcroft, I., and Hague, R., "Topology optimization for additive manufacturing," 67(6):14–21, 2011.
68. Zolekar, V., "Finite Element Analysis and Optimization of I . C . Engine Piston Using RADIOSS and OptiStruct," *Altair Technol. Conf.* 1–8, 2013.
69. Kahlen, F.-J. and Kar, A., "Tensile Strengths for Laser-Fabricated Parts and Similarity Parameters for Rapid Manufacturing," *J. Manuf. Sci. Eng.* 123(1):38, 2001, doi:10.1115/1.1286472.
70. Gardan, N., Schneider, A., and Gardan, J., "Material and process characterization for coupling topological optimization to additive manufacturing," *Comput. Aided. Des. Appl.* 13(1):39–49, 2016, doi:10.1080/16864360.2015.1059192.
71. Hu, S.B., Chen, L.P., Zhang, Y.Q., Yang, J., and Wang, S.T., "A crossing sensitivity filter for structural topology optimization with chamfering, rounding, and checkerboard-free patterns," *Struct. Multidiscip. Optim.* 37(5):529–540, 2009, doi:10.1007/s00158-008-0246-3.
72. Fontanesi, S., Cicalese, G., Cantore, G., and D'Adamo, A., "Integrated in-cylinder/CHT analysis for the prediction of abnormal combustion occurrence in gasoline engines," *SAE Tech. Pap.* 1, 2014, doi:10.4271/2014-01-1151.
73. Dang Van, K., Griveau, B., and Message, O., "On a New Multiaxial Fatigue Limit Criterion: Theory and Application," in: Brown, M. W. and Miller, K. J., eds., *Mechanical Engineering Publications*, London: 479–496, 1989.
74. Dang Van, K., Cailletaud, G., Flavenot, J.F., Douaron, A. Le, and Lieurade, H.P.,

Criterion for High Cycle Fatigue Failure Under Multuiaxial Loading, *Biaxial and Multiaxial Fatigue* 459–478, 1989.

75. Meneghetti, G., Rigon, D., Cozzi, D., Waldhauser, W., and Dabalà, M., "Influence of build orientation on static and axial fatigue properties of maraging steel specimens produced by additive manufacturing," *Procedia Struct. Integr.* 7:149–157, 2017, doi:10.1016/j.prostr.2017.11.072.
76. Meneghetti, G., Rigon, D., and Gennari, C., "An analysis of defects influence on axial fatigue strength of maraging steel specimens produced by additive manufacturing," *Int. J. Fatigue* 118(May 2018):54–64, 2019, doi:10.1016/j.ijfatigue.2018.08.034.
77. Gordon, J.V., Haden, C.V., Nied, H.F., Vinci, R.P., and Harlow, D.G., "Fatigue crack growth anisotropy, texture and residual stress in austenitic steel made by wire and arc additive manufacturing," *Mater. Sci. Eng. A* 724(December 2017):431–438, 2018, doi:10.1016/j.msea.2018.03.075.
78. Gordon, J., Hochhalter, J., Haden, C., and Harlow, D.G., "Enhancement in fatigue performance of metastable austenitic stainless steel through directed energy deposition additive manufacturing," *Mater. Des.* 168:107630, 2019, doi:10.1016/j.matdes.2019.107630.
79. Yadollahi, A. and Shamsaei, N., "Additive manufacturing of fatigue resistant materials: Challenges and opportunities," *Int. J. Fatigue* 98:14–31, 2017, doi:10.1016/j.ijfatigue.2017.01.001.
80. Spierings, A.B., Starr, T.L., and Wegener, K., "Fatigue performance of additive manufactured metallic parts," *Rapid Prototyp. J.* 19(2):88–94, 2013, doi:10.1108/13552541311302932.
81. Mastrandrea, L.N., Giacopini, M., Bertocchi, E., Strozzi, A., and Dini, D., "A complete 3-D description of the elastic behavior of a piston ring and its influence on the tribological behavior of the piston ring-cylinder liner interface," *Soc. Tribol. Lubr. Eng. Annu. Meet. Exhib. 2016* 121–124, 2016.
82. Anderberg, C., Dimkovski, Z., Rosén, B.-G., and Thomas, T.R., "Low friction and emission cylinder liner surfaces and the influence of surface topography and scale," *Tribol. Int.* 133(January 2018):224–229, 2019, doi:10.1016/j.triboint.2018.11.022.
83. Delprete, C. and Razavykia, A., "Piston ring–liner lubrication and tribological performance evaluation: A review," *Proc. Inst. Mech. Eng. Part J J. Eng. Tribol.* 232(2):193–209, 2018, doi:10.1177/1350650117706269.
84. Schneider, E.W., Blossfeld, D.H., Lechman, D.C., Hill, R.F., Reising, R.F., and Brevick, J.E., "Effect of Cylinder Bore Out-of-Roundness on Piston Ring Rotation and Engine Oil Consumption," *SAE Technical Paper Series*, 1993, doi:10.4271/930796.
85. Dunaevsky, V. V, "Analysis of distortions of cylinders and conformability of piston rings," *Tribol. Trans.* 33(1):33–40, 1990, doi:10.1080/10402009008981927.
86. Tomanik, E., "Piston Ring Conformability in a Distorted Bore," *SAE Technical Paper Series*, 1996, doi:10.4271/960356.
87. Kamat, P., Burns, J.R., Self, D.G., and Mckeough, B., "Cylinder Liner for an Internal Combustion Engine and Method of Forming," 2018.

88. Saeidi Googarchin, H., Sharifi, S.M.H., Forouzesh, F., Hosseinpour, G.H.R., Etesami, S.M., and Malek Zade, S., "Comparative study on the fatigue criteria for the prediction of failure in engine structure," *Eng. Fail. Anal.* 79(March):714–725, 2017, doi:10.1016/j.engfailanal.2017.05.016.
89. Loenne, K., "The Effects of Engine Operating Conditions on Static Cylinder Distortions," *GOETZE AG Technical Paper D7*, Muskegon Engineering Data (Goetze paper D7), 1972.
90. Loenne, K. and Ziemba, R., "The GOETZE Cylinder Distortion Measurement System and the Possibilities of Reducing Cylinder Distortions," *SAE Technical Paper Series*, Detroit, Michigan: 25–33, 1988, doi:10.4271/880142.
91. Fujimoto, H., Yoshihara, Y., Goto, T., and Furuhama, S., "Measurement of Cylinder Bore Deformation During Actual Operating Engines," *SAE Technical Paper Series*, 1991, doi:10.4271/910042.
92. Koch, F., Decker, P., Gülpen, R., Quadflieg, F., and Loeprecht, M., "Cylinder Liner Deformation Analysis - Measurements and Calculations," *SAE Technical Paper Series*, Detroit, Michigan, 1998, doi:10.4271/980567.
93. Maassen, F., Koch, F., Schwaderlapp, M., Ortjohann, T., and Dohmen, J., "Analytical and Empirical Methods for Optimization of Cylinder Liner Bore Distortion," *SAE Technical Paper Series*, 2001, doi:10.4271/2001-01-0569.
94. Yang, Z., Li, B., and Yu, T., "Distortion Optimization of Engine Cylinder Liner Using Spectrum Characterization and Parametric Analysis," *Math. Probl. Eng.* 2016:1–11, 2016, doi:10.1155/2016/9212613.
95. Liang, X., Wang, Y., Huang, S., Yang, G., Tang, L., and Cui, G., "Investigation on Cylinder Bore Deformation under Static Condition Based on Fourier Decomposition," *SAE Technical Paper Series*, 2017, doi:10.4271/2017-01-0366.
96. Marathe, A. V, Venkatachalam, G., Marathe, N. V, and Gadve, P.G., "Analysis of Cylinder Head Bolt Cross Pattern Tightening and Its Effect on Gasket Sealing Performance and Bore Deformation," 3(3):647–652, 2017.
97. Marathe, A. V., Venkatachalam, G., and Marathe, N. V., "Cylinder Head Bolt Tightening Strategies in Case of Multi-Cylinder Engines and Its Effect on Gasket Sealing Performance, Bore Deformation and Piston Ring Conformability," *Aust. J. Mech. Eng.* 00(00):1–19, 2018, doi:10.1080/14484846.2018.1523292.
98. Fontanesi, S. and Giacopini, M., "Multiphase CFD-CHT optimization of the cooling jacket and FEM analysis of the engine head of a V6 diesel engine," *Appl. Therm. Eng.* 52(2):293–303, 2013, doi:10.1016/j.applthermaleng.2012.12.005.
99. Barbieri, S.G., Mangeruga, V., Giacopini, M., Bianco, L., and Mastrandrea, L.N., "A simplified methodology for the analysis of the cylinder liner bore distortion : Finite Element analyses and experimental validations," *SAE Tech. Pap. Ser.*, 2019, doi:10.4271/2019-24-0164.Abstract.
100. Barbieri, S.G., Mangeruga, V., Giacopini, M., Laurino, C., and Lorenzini, M., "A finite element numerical methodology for the fatigue analysis of cylinder liners of a high performance internal combustion engine," *Key Eng. Mater.* 827:288–293, 2019, doi:10.4028/www.scientific.net/kem.827.288.
101. Van, K.D., Douaron, A. Le, and Lieurade, H.P., "MULTIAXIAL FATIGUE LIMIT: A NEW APPROACH," *Fracture 84*, Elsevier: 1879–1885, 1984, doi:10.1016/B978-1-4832-8440-8.50185-X.

102. Charkaluk, E., Bignonnet, A., Constantinescu, A., and Dang Van, K., "Fatigue design of structures under thermomechanical loadings," *Fatigue Fract. Eng. Mater. Struct.* 26(7):661–661, 2003, doi:10.1046/j.1460-2695.2002.00613.x-i1.
103. Barbieri, S.G., Bianco, L., Mangeruga, V., and Giacopini, M., "A simplified finite element methodology for the structural assessment of an engine piston under dynamic loadings," *AIP Conference Proceedings*, ISBN 9780735440456: 020014, 2020, doi:10.1063/5.0033956.